A DENSE PLASMA FOCUS DEVICE AS A PULSED NEUTRON SOURCE FOR MATERIAL IDENTIFICATION

by

AMGAD ELSAYED SOLIMAN MOHAMED

MSc., Zagazig University, 2007

AN ABSTRACT OF A DISSERTATION

submitted in partial fulfillment of the requirements for the degree

DOCTOR OF PHILOSOPHY

Department of Mechanical and Nuclear Engineering
College of Engineering

KANSAS STATE UNIVERSITY
Manhattan, Kansas

2015

Abstract

Dense plasma focus (DPF) devices are pulsed power devices capable of producing short-lived, hot and dense plasmas (~10^{19} cm^{-3}) through a fast compression of plasma sheath. A DPF device provides intense bursts of electrons and ion beams, X-rays, and 2.5 MeV neutrons when operated with deuterium through the fusion reaction $^{2}H(d,n)^{3}He$. The Kansas State University DPF machine was designed and constructed in early 2010. The device was characterized to determine its performance as a neutron source. The device was shown to produce 5.0×10^{7} neutrons/pulse using a tungsten-copper anode. Such machines have the advantages of being non-radioactive, movable, and producing short pulses (typically tens of nanoseconds), which allows rapid interrogation. The signature-based radiation-scanning (SBRS) method has been used to distinguish targets that contain explosives or explosive surrogates from targets that contain materials called "inert," meaning they are not explosive-like.

Different targets were placed in front of the DPF source at a distance of 45 cm. Four BC-418 plastic scintillators were used to measure the direct neutron yield and the neutrons scattered from various targets; the neutron source and the detectors were shielded with layers of lead, stainless steel, and borated polyethylene to shield against the X-rays and neutrons. One of the plastic scintillators was set at 70^{o} and two were set at 110° from the line of the neutron beam; a bare ^{3}He tube was used for detecting scattered thermal neutrons.

Twelve metal cans of one-gallon each containing four explosive surrogates and eight inert materials were used as targets. Nine materials in five-gallon cans including three explosive surrogates were also used. The SBRS method indicated a capability to distinguish the explosive surrogates in both experiments, although the five gallon targets gave more accurate results. The MCNP code was used to validate the experimental work and to simulate real explosives. The simulations indicated the possibility to use the time of flight (TOF) technique in future experimental work, and were able to distinguish all the real explosives from the inert materials.

A DENSE PLASMA FOCUS DEVICE AS A PULSED NEUTRON SOURCE FOR MATERIAL IDENTIFICATION

by

AMGAD ELSAYED SOLIMAN MOHAMED

MSc., Zagazig University, 2007

A DISSERTATION

submitted in partial fulfillment of the requirements for the degree

DOCTOR OF PHILOSOPHY

Department of Mechanical and Nuclear Engineering
College of Engineering

KANSAS STATE UNIVERSITY
Manhattan, Kansas

2015

Approved by:

Major Professor
Prof. William L. Dunn

Copyright

Abstract

Dense plasma focus (DPF) devices are pulsed power devices capable of producing short-lived, hot and dense plasmas (~10^{19} cm^{-3}) through a fast compression of plasma sheath. A DPF device provides intense bursts of electrons and ion beams, X-rays, and 2.5 MeV neutrons when operated with deuterium through the fusion reaction $^{2}H(d,n)^{3}He$. The Kansas State University DPF machine was designed and constructed in early 2010. The device was characterized to determine its performance as a neutron source. The device was shown to produce 5.0×10^{7} neutrons/pulse using a tungsten-copper anode. Such machines have the advantages of being non-radioactive, movable, and producing short pulses (typically tens of nanoseconds), which allows rapid interrogation. The signature-based radiation-scanning (SBRS) method has been used to distinguish targets that contain explosives or explosive surrogates from targets that contain materials called "inert," meaning they are not explosive-like.

Different targets were placed in front of the DPF source at a distance of 45 cm. Four BC-418 plastic scintillators were used to measure the direct neutron yield and the neutrons scattered from various targets; the neutron source and the detectors were shielded with layers of lead, stainless steel, and borated polyethylene to shield against the X-rays and neutrons. One of the plastic scintillators was set at 70^{o} and two were set at 110° from the line of the neutron beam; a bare ^{3}He tube was used for detecting scattered thermal neutrons.

Twelve metal cans of one-gallon each containing four explosive surrogates and eight inert materials were used as targets. Nine materials in five-gallon cans including three explosive surrogates were also used. The SBRS method indicated a capability to distinguish the explosive surrogates in both experiments, although the five gallon targets gave more accurate results. The MCNP code was used to validate the experimental work and to simulate real explosives. The simulations indicated the possibility to use the time of flight (TOF) technique in future experimental work, and were able to distinguish all the real explosives from the inert materials.

Table of Contents

List of Figures

List of Tables

Acknowledgements

I wish to express my sincere gratitude and appreciation to my advisor, Dr. Dunn for being an excellent mentor, for his guidance, and for providing the materials and detection tools which were needed to finish this work. I would like to express my deep thanking and appreciation to Dr. A. Abdou for his efforts in the construction of dense plasma focus device and his help in plasma diagnostics. My deep gratitude and appreciation to Mohamed Ismail who helped me along through this work. I would like to thank the faculties, and the staff in the program of nuclear engineering at Kansas State University for being helpful during my PhD studying. Finally I want to thank my supervising committee members for their time and advices.

Dedication

To Amira, Nouran, Mohamed, Omar, and Juairia.

Chapter 1 - **Dense Plasma Focus Theory**

1.1 Introduction

The dense plasma focus (DPF) device is a bi-directional accelerator for ions. The device uses the Lorentz force $F = J \times B$, where J is current density and B is magnetic field, to accelerate gas molecules swept by plasma sheath, axially with high speed to a certain position at which the flow is converted to a radial acceleration with higher speed to collapse and induce a high density filament of plasma called a plasma focus.

The device originally is a coaxial accelerator [1] that stores an induced magnetic field behind an ionized layer of gas. The plasma sheath moved under the effect of the magnetic field is referred as magnetic piston [2]; this ionized layer extends between an inner and outer electrodes (anode and cathode), and is responsible for transfer of the electric current between the two electrodes. The ionized layer that carries the current is called the current sheet (CS). The current sheet represents the J component, the electric current passes through the anode from its base to the position of the current sheet, hence induces an azimuthal magnetic B field around the anode in the azimuthal θ direction (B_θ), as shown in Figure 1.1. The magnetic field lies behind the current sheet, the J_r and B_θ components push the current sheet with a Lorentz force (F_z) to reach a high axial velocity, of the order of 10^7 cm/s, which is doubled in the radial direction [3].
The plasma focus device accelerates and compresses the gas in the radial direction to the range of 10^{19} /cm^3 to produce a hot filament with energy of a few keV [4]. The pinch formation is accompanied by plasma instability and high electric field, leading to the emission of ion and electron beams in opposite directions [5]. If the filling gas is deuterium, a d-d fusion reaction occurs in the pinch that continues for tens of nanoseconds [6-8].

1.2 Plasma focus device

The plasma focus device contains a metallic chamber that is filled with gas or a mixture of gases under vacuum pressure; the pressure ranges from a fraction of mbar up to tens of mbar. The chamber contains an inner electrode called the anode surrounded by a number of electrodes which comprise the cathode. The anode is insulated from the cathode at the base by an electrical

insulator (e.g., a glass tube). The anode is electrically connected to a triggered high current switch [9, 10]. The switch is connected to the positive connector of a capacitor, while the capacitor negative side is connected to the cathode and to ground. A high voltage power source supplies voltage (a few kilovolts up to a few hundred kilovolts) to the capacitor, and this step is called the *charging stage*. A controller is then used to start the trigger switch, which starts the discharge between the anode and cathode through the filling gas inside the vacuum chamber.

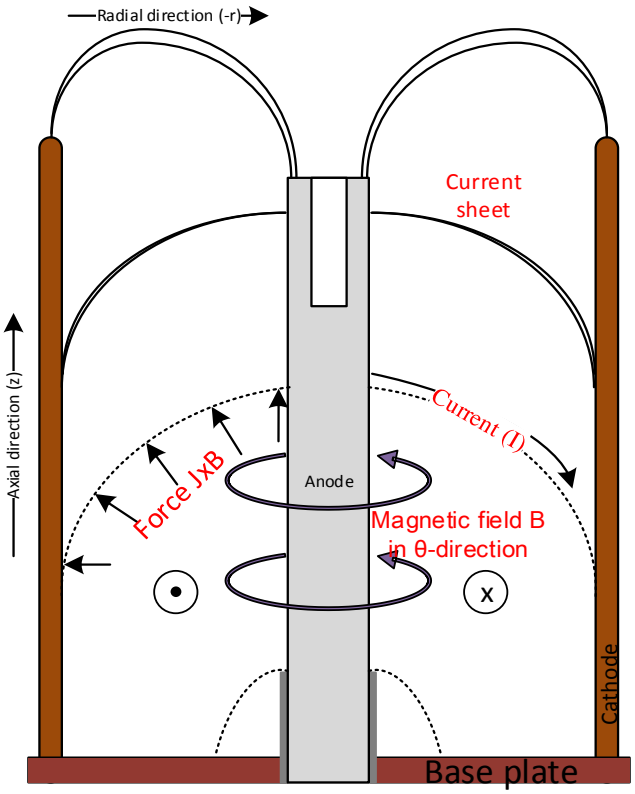

Figure 1.1: Axial and radial motion of the current sheet in a dense plasma focus device.

The working principal of the device is to transfer the stored energy inside the capacitor to the electrodes using the simple electric natural response of the DPF circuit. This response includes the transfer of very high electric current (in the range of tens of kilo amperes up to Mega amperes), which behaves as

$$I = I_o \exp(\alpha t)\sin(\omega t), \qquad (1.1)$$

where α is the exponential damping coefficient and ω is the natural radial frequency of the circuit. This current is responsible for generating a high magnetic field, and forces the ionized gas in the chamber to move under a Lorentz force $J \times B$. The *discharge stage* includes three main phases: the breakdown phase, the axial rundown phase, and the radial phase.

1.2.1 Breakdown phase

When the switch connects the high voltage to the anode, the ionization of the gas atoms/molecules starts on the sides of the anode insulator. The initial gas breakdown depends on the high voltage difference between the two electrodes, the gas type, and the vacuum pressure. There is an optimum pressure for the gas breakdown [11-13]. The breakdown voltage is usually less than 1 kV, while the voltage over the electrodes is equal to the charging voltage, which is higher by an order of magnitude or more. This breakdown leads to the ionization of the layer around the insulator [14-16]; when the current reaches the base of the anode above the insulator area, a current filaments is formed between the anode and the plate around (which is part of the cathode electrode), see Figure 1.1. Both electrodes are then electrically connected by the ionized filaments; the filaments' structure depends on the voltage, gas type and pressure. The plasma filaments lift off under the force of $J \times B$ (where $B=\mu_o I/2\pi r$, where μ_o is the permeability of free space $=4\pi \times 10^{-7}\ N\,A^{-2}$, I is the current that passes through the current sheet, and r is the distance from the anode surface). This forms a current sheath between the anode surface and the cathode rods. The current sheath then runs in axisymmetric form along the anode axis, this phase lasts for 50-300 ns depending on the device conditions. Experiments showed that the insulator type and surface play a big role in the breakdown phase and hence in the plasma sheath structure and strength, and in turn in the strength of the compression phase afterwards [17].

1.2.2 Axial acceleration phase

In the axial phase, a thin layer of compressed gas is formed in front of the current sheet, called the shock front, which precedes the magnetic piston. The shock front sweeps and ionizes the gas in the axial phase as it runs down the axial direction. Lorentz force is the highest near the anode surface and decreases by $(1/r)$ as it moves radially toward the cathode. As the current sheet slips, the curvature of the sheet increases slightly and takes the shape of an umbrella. The

current sheet thickness is less than 2 cm as investigated by previous experiments. This shock front followed by the current sheet pushes the plasma axially toward the end side of the anode [18, 19]. The velocity of the current sheet increases as the electric current increases in the first quarter of the cycle. The duration of the axial phase takes 0.5 to 4 μs in most machines to reach the tip of the anode with a velocity of about 10^7 cm/s. A fraction of total discharge current contributes to the plasma acceleration (this fraction is around 0.7) while the rest of the current diffuses through the electrodes. The current sheet pushes the gas and leaves a vacuum region behind. The snow plow is a good model to describe the motion of the current sheet. The equations of the model are discussed briefly in section 5.2.2. At the end of the axial phase, the inner side of the current sheet reaches the top end of the anode and changes to the radial direction to push the gas radially inward while the other side still pushes the gas in the axial direction. This causes a small fraction of the compressed gas to move into the radial phase.

1.2.3 Radial phase

The current sheet still sweeps in the inward radial direction under the Lorentz force, pushing a portion of the gas to collapse around the central axis of the anode. This action takes 10-200 ns. The velocity in the radial phase is higher by 2-4 times than the axial velocity depending on the device characteristics. During the radial phase, the collapse of the plasma column leads to a rapid increase of the plasma inductance, given by

$$L_p(t) = \frac{\mu_o z_p}{2\pi} \ln\left(\frac{b}{r_p(t)}\right), \qquad \textbf{(1.2)}$$

where b and r_p are the radii of the outer electrode and the moving plasma column respectively, and z_p is the plasma column length [20]. The resistance associated with the plasma column R_p is given by

$$R_p(t) = \frac{z_p}{\sigma \pi r_p^2(t)}, \qquad \textbf{(1.3)}$$

where σ is the electrical conductivity, the conductivity is subject to an anomalous term that suddenly changes the amount of resistance [21]. Previous experiments showed plasma column dimensions of 1-15 mm in diameter and 10-70 mm in length [22]. The discharge current changes

slightly during the radial phase and can be considered a constant. This leads to an induced electric field, the voltage of which across the plasma column is

$$V_p = I\frac{d}{dt}L(t) + R_p(t)I \ . \qquad \textbf{(1.4)}$$

All the device radiation is induced during this phase, including the ion and electron beams, and neutron production in case of deuterium or deuterium-tritium gas mixture.

The radial phase includes four stages; the *compression (collapse) phase* followed by a *quiescent phase*, the *instability phase*, and finally the *decay phase*.

- Due to the difference in acceleration of the current sheet between the anode and the cathode, the current sheet in the radial phase takes the shape of a funnel. The electron temperature of the sheath reaches 60 eV before the time of collapse; this temperature is gained through the collision with ions of ~100 eV (corresponding to deuterium at 1×10^7 cm/μs) [1, 23]. When the plasma column compresses, it reaches a radius r_{min}, and the shock wave then reflects back to meet the magnetic piston and recompresses again. The joule/ohmic heating then becomes the main source of heating the plasma column. The current dips as the impedance largely increases in a short time, and the voltage V_p sharply increases during the same period, see Figure 1.2. At the end of the phase, the plasma density reaches 10^{19} cm^{-3} and reaches a temperature of 0.2-1 keV [21].

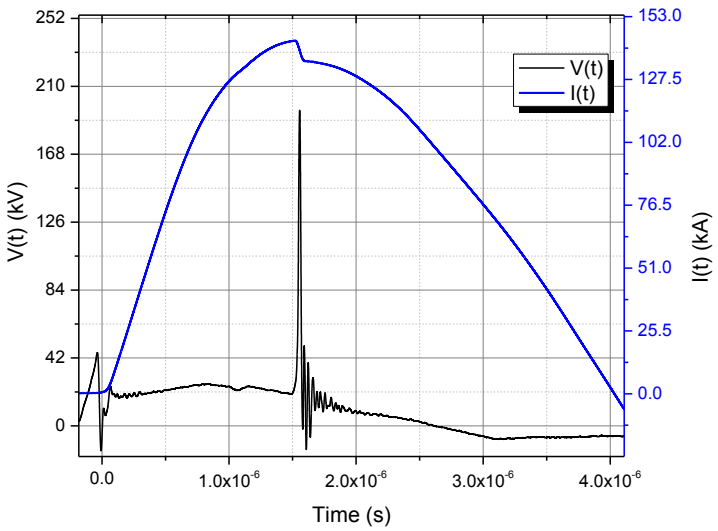

Figure 1.2: A current dip and a voltage spike occur within the pinch time; the case shown is for 3 mbar deuterium gas and a 17 kV charging voltage.

- The plasma column is magnetically confined, while the temperature increases by joule heating. The plasma column is unstable, and is subject to instabilities by any small perturbation. Two main kinds of instabilities affect the plasma, the *m*=0 is called the sausage instability, see Figure 1.3, and the *m*=1 is called the kink instability. The azimuthal magnetic field in the plasma pinch associated with the current flow through the plasma column is inversely proportional to the radius of the plasma column itself

$$B_\theta(r_p) = \frac{\mu_0 I}{2\pi r_p} \quad . \qquad \textbf{(1.5)}$$

That means the magnetic squeezing pressure ($B^2/2\mu_o$) over the plasma is proportional to (B^2) or ($1/r_p^2$) [24-27]. When the plasma column is subjected to any perturbation, the plasma column gets narrow at random positions where the magnetic field increases and squeezes the narrow region to form a neck. This phenomenon is called a sausage or flute instability. The perturbation may lead to a kink instability where the magnetic field lines bunch together from a side leading to a high pressure ($\propto B^2$), and spread apart from the other side.

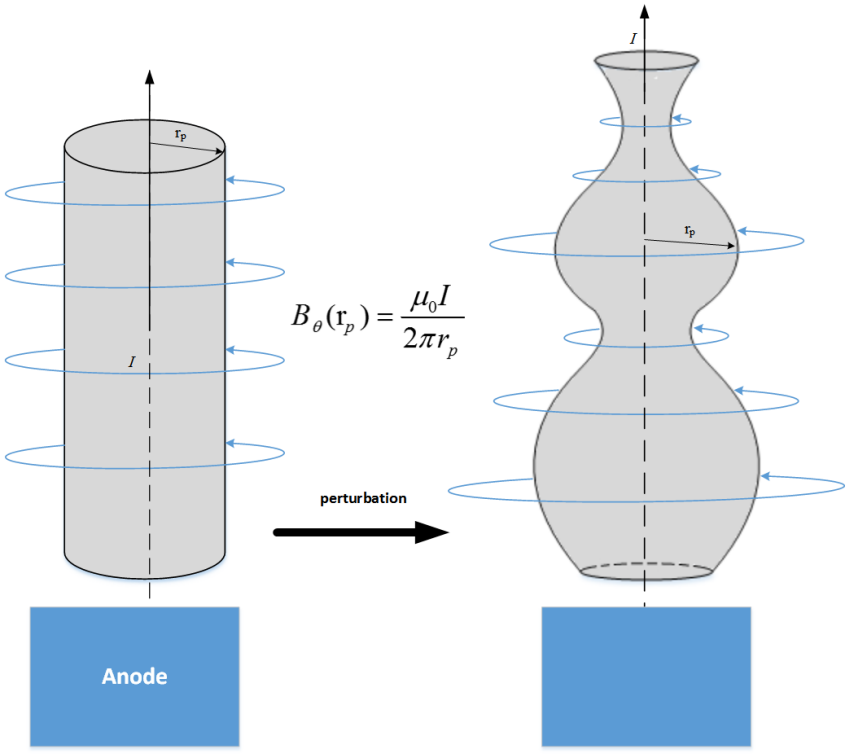

Figure 1.3: Plasma column sausage/flute instability propagation in the radial phase.

This leads to a smaller force from the other side, and a kink occurs in the column [28]. The growth time rate of the flute instability is faster than the kink instability because of the proportionality of the force to the $1/r_p^2$ in the first case [29]. These rapid changes of the magnetic field due to the flute instability lead to positions of weak magnetic fields and others with strong magnetic fields. This induces a large axial electric field that accelerates the ions in the plasma column against the anode and the electrons toward the anode to energies of hundreds of keV. The ion beam plays a big role in the emission of fusion neutrons, while the electron accelerated beam produces hard X rays according to the anode material. The main sources of X rays in DPF discharges are the plasma column, where energetic free electrons interact with the dense plasma, and accelerated electron beam collisions with the anode. The hard X-ray intensity and mean energy increases by using heavy filling gases like neon and high Z dense material for the anode like tungsten [30, 31]. The minimum pinch voltage for accelerating the electrons and to produce hard X-ray production was assumed to satisfy $3.9\times10^{-16} n_i z_p / T_e$ [32, 33], where T is the electron temperature, n_i is the ion density, and z_p is pinch height.

- The plasma column finally breaks into regions at the end of the instability phase and forms a hot and thin plasma cloud. After the dip, the discharge current continues to flow through the cloud of plasma to the cathode, and the voltage returns back to the ordinary capacitor voltage as the high electric field dissipates, and continues the discharge process through the closed circuit. [34]

1.3 Neutron production

The Coulomb barrier must be overcome in order for fusion to occur. In the d-d reaction, this barrier is 0.47 MeV; in the d-t reaction, the Coulomb barrier is 0.43 MeV [35]. Studies of the tunneling effect in quantum mechanics indicated that the nucleus does not need to reach an energy equal to the Coulomb barrier. At lower energies there is a probability for the nuclei to fuse together [36]. This probability is called the reaction cross section, the cross section for the two reactions are shown in Figure 1.4 [37].

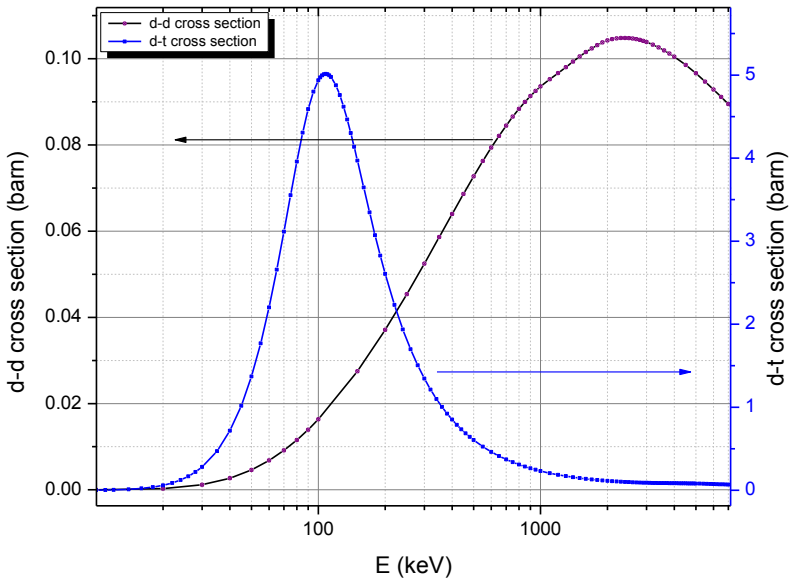

Figure 1.4: The d(d,n) and d(t,n) fusion cross sections.

The d-d fusion reaction occurs in two ways while the d-t fusion reaction has only one outcome

$$\begin{aligned} d+d &\xrightarrow{fusion} n(2.45MeV)+{}^{3}_{2}He(0.82MeV) \\ d+d &\xrightarrow{fusion} p(3.02MeV)+T(1.01MeV) \\ d+t &\xrightarrow{fusion} n(14.1MeV)+\alpha(3.49MeV) \end{aligned} \quad . \qquad \textbf{(1.6)}$$

The light nuclei need to gain energy in order to fuse. One of the mechanisms of producing neutrons in the DPF is the beam target mechanism; during the instability phase, the accelerated deuterons hit the deuterium nuclei in the plasma column with energies that reach hundreds of keV. Only the very hot deuterium gas in the plasma column can induce thermonuclear fusion. Normally the temperature of the pinch is of order 200 eV-1 keV, and the thermonuclear reaction is weak. For example, if we assume an average deuterium density in the plasma column of $N_D \approx 10^{19}$ cm^{-3}, a neutron production period of $\tau \approx 50\,\text{ns}$, a volume of the plasma column of $V_p \approx 0.063$ cm^3, the average of the reaction cross section times the velocity σv over a Maxwellian velocity distribution [38] is given by the approximation

$$\overline{\sigma_d v_d} = \frac{9\times10^{-15}}{T^{2/3}}\exp\left(-\frac{18.76}{T^{1/3}}\right) cm^3/s \,. \qquad \textbf{(1.7)}$$

Hence, the neutron yield in one DPF shot due to the thermonuclear reaction [39-41] will be

$$Y_{th} = \frac{1}{2} N_D^2 \overline{\sigma_d v_d} V_p \tau . \qquad \textbf{(1.8)}$$

If we assume a plasma temperature of 200 eV up to 1 keV, this leads to a neutron production of 10-10^6 n/pulse. That is why researchers attempt to overcome the plasma instabilities to confine the plasma column for longer times to extract more energy. Many researchers suggest the beam target mechanism as the main source of neutron production, as an anisotropy of the neutron production [42-47] was observed. The results indicated that the beam-target mechanism produces 90 to 96% of the total fusion yield in device [48]. By studying different plasma focus devises, researchers have tried to find a scaling law for neutron production from DPF machines. The plasma temperature, which is important in thermonuclear fusion, depends on the current I and the density N. The equilibrium relation between the plasma pressure and the magnetic pressure in the plasma column is indicated in the Bennet relation [24], which states that

$$Nk\,(ZT_e + T_i) = \frac{\mu_o}{8\pi} I^2 , \qquad \textbf{(1.9)}$$

where k is Boltzmann's constant, Z is the ionic charge number (equal to one in deuterium), N is the ion density, T_e and T_i are the electron and ion temperatures, respectively. The scaled neutron yield [40, 41, 49, 50] has been related to the peak discharge current or pinch current by the following

$$Y_n = A I_p^{\,B} , \qquad \textbf{(1.10)}$$

where I_p is the peak current at the pinch time, A is a constant ~ 1.8×10^{10}, and B varies from 3.8~ 4. To obtain the maximum neutron yield of the machine, the deuterium gas pressure is adjusted so that the pinch occurs at the time of peak discharge current. The filling pressure is proportional to the anode length; to get maximum current at the pinch time, the corresponding pressure should be chosen to match the anode length and the pressure in such a case is defined as the neutron optimum filling pressure. The total deuteron beam energy was found to be proportional to $I_{pinch}^2 L_p$ [51], where L_p is the plasma column inductance described by equation (1.2). The neutron yield from the beam-target mechanism was approximately calculated [52, 53] as

$$Y_{BT} = C_n n_i I_{pinch}^2 z_p^2 (\ln b / r_p)\sigma / V_{\max}^{1/2} , \qquad \textbf{(1.11)}$$

where C_n is a calibration constant for the experiment, n_i is the ion density in the plasma, b and r_p are the cathode diameter and plasma column radius, respectively, $V_{\max}$ is the maximum voltage induced by the current sheet that is compressing the plasma column, and σ is the cross-section of

the d-d fusion reaction. The total neutron yield is $Y = Y_{th} + Y_{BT}$. The mechanism of neutron production is not yet fully understood and still needs more research [21]. The ion energy and flux depend mainly on the capacitor stored energy supplied to the device ($0.5\ CV^2$). The ion energy ranges from tens of keV up to ~1 MeV. The ion and electron beam were found to obey the same acceleration, $dN/dE \propto E^{-x}$ where $x \approx 3.5 \pm 0.5$ [54]. Multiple spikes of the ion beam and neutron production were observed in the pinch period in some DPF devices, attributable to a severe sausage (m=0) instability [45, 55]. Researchers have tried to use the ion beam of the dense plasma focus in industrial applications, e.g., for surface modification, thin film deposition, and short-lived radioisotope production [56-60].

Chapter 2 - **Material Interrogation and Improvised Explosive Devices**

2.1 Introduction

Due to the world revolution in transportation and logistics services, millions of packages are shipped every day [61]. The worldwide shipping cargoes move everyday through ports and borders of countries, FedEx fact sheet [62] shows 10 million packages are delivered daily in 220 countries by the end of 2014. The USPS processes 500 million mail-pieces every day in the United Stated. Through this daily number of shipping, the material identification becomes an important requirement to check the large amounts of packaging passes through the borders or ports for the existence of smuggled drugs, explosives, weapons, nuclear or harmful materials.

The illegal usage of explosives is considered a severe danger especially if it is used in a crowded place. The explosives used for a terroristic attack are known as improvised explosive devices (IEDs). The IED is a homemade bomb or destructive device constructed to destroy, harass, or damage certain range. The IEDs can take different forms; (for example, one may be hidden in small cardboard mailing box, a pipe with detonator, or a car or a truck with hundreds to thousands of pounds of explosive. The IEDs have become one of the important causes for civilian deaths every year worldwide. Between 1985 and 1997, eight commercial aircrafts were lost or damaged due to IED threats, and approximately 1100 people died in such accidents [63].

Table 2.1: Examples of IED Explosive incidents worldwide

Explosive example	**Primary usage**	**Form of material**	**IED use**
Urea nitrate	Fertilizer	Solid	World Trade Center, 1993.
Ammonium nitrate, and fuel oil (ANFO)	Mining and fertilizing	Solid	Oklahoma City Government building bombing, 1995.
Ethylene glycol dinitrate (EGDN)	Manufacturing low freezing dynamite	Liquid	Los Angeles airport, 1999.

Semtex, and ammonium nitrate	Military use, And a fertilizer	Plastic solid	Irish Republican Army bombings attack (Manchester bombing), 1996.
Triacetone, Triperoxide (TATP)	n/a	Crystalline solid	London Bombings, 2005.
Pressure cooker bombs filled with explosive material	Housing purposes	Solid powder plus sharp nails and ball bearings	Boston Marathon bombings, 2013.

One of the most important issues for protecting civilians and reducing losses is to evacuate the distance in the radius of the suspicious IED as suggested in Table 2.2. The detection of IEDs presents a big challenge for security employees, police, or military personnel.

Table 2.2: the IED threat stand-off distance. (http://www.nctc.gov/site/technical/bomb_threat.html)

IED description	Explosive capacity as TNT equivalent.	Building evacuation distance	Outdoor evacuation distance
Pipe bomb	5 lbs/2.3 kg	70ft/21 m	1,200ft/366 m
Suicide vest	20 lbs/9.2 kg	110ft/34 m	1,750ft/518 m
Briefcase/suitcase bomb	50 lbs/23 kg	150ft/46 m	1,850ft/564 m
Sedan	500 lbs/227 kg	320ft/98 m	1,900ft/580 m
SUV/van	1,000 lbs/454 kg	400ft/122 m	2,400ft/732 m
Small delivery truck	4,000 lbs/1,814 kg	640ft/195 m	3,800ft/1159 m
Container/water truck	10,000 lbs/4,536 kg	860ft/263 m	5,100ft/1,555 m
Semi-trailer	60,000 lbs/27,216 kg	1,570ft/479 m	9,300ft/2,835 m

2.2 Composition of the IED

The IED assembly consists of an explosive compound which has a chemical formula like ammonium nitrate fuel oil (ANFO), or TNT. The mass of the explosive is critical in determining the damage it can cause. The TNT is used as a measure for the explosion power; one gram of TNT gives 4.18 kJ of explosion energy. The common explosives have around 0.5~1.5 times the power of TNT. The explosive material is assembled inside a container and connected to a detonator. A taggant is required to be added (by the manufacturer) to the explosive material which is absent in case of homemade bombs. Shrapnel such as nails or other small pieces of sharp metals, glass or plastics can be added, which greatly increase harm to humans. The incident at the Boston Marathon in 2013 is a good example of that case [64]. The density of explosives varies over a wide range, but the effective high performance IEDs have a total density of 1.2~1.9 g/cm^3 [65].

2.3 System of explosives detection

The system of explosives detection is a security program established to deny terrorists' access to civilians or buildings, to clear threats of military weapons such as landmines, or to the ability to construct IEDs. The system of detection is mainly used in airports, country borders, landmine areas, and in case of a threat of bombs or suspicious bodies in crowded areas.
The purpose of using a system for explosive detection is to give an alarm and in some cases a decision when there is a detected explosive threat. The system should give the fewest alarms when there is no threat. The explosive detection system should contains more than one detector/sensor because the more sensors used in the system of detection the better the chance of reducing false alarms. The major programs of explosive detection are bulk detection and vapor detection techniques [66]. The bulk detection aims to detect large quantities of explosives, while vapor detection looks for very small quantities emitted into the environment as an evidence of explosive presence. Table 2.3 lists the commonly used explosives, gives chemical formulas, and identifies the approximate chemical vapor pressure measured at 25 ^{o}C [67].

Generally, the methods of detection involve active and passive detection. The active detection requires subjecting the target under interrogation to a type of radiation (e.g., THz electromagnetics, X-rays), or a direct sample analysis to obtain the required data. The passive kind of

detection requires no interruption for the investigated target or a direct contact, (e.g., infrared imaging, or vapor detection). The system of explosive detection is divided into three main categories, described in the next section, (Figure 2.1).

Table 2.3: Explosives chemical formulas and approximate vapor at temp 25ºC.

Explosive	Chemical Name	Chemical Formula	Vapor Pressure (atm)
NM	Nitromethane	CH3NO2	0.0468
HP	Hydrogen peroxide	H2O2	0.00288
DADP	Diacetone diperoxide	C6H12O4	2.44E-04
TATP	Triacetone triperoxide	C9H18O6	6.31E-05
EGDN	Ethylene glycol dinitrate	C2H4N2O6	1.02E-04
P-MNT	P-Nitrotoluene	C7H7NO2	6.47E-05
DNT	Dinitrotoluene	C7H6N2O4	4.11E-07
NG	Nitroglycerin	C3H5N3O9	6.45E-07
TNM	Trinitromesitylene	C9H9N3O6	4.06E-09
TNT	Trinitrotoluene	C7H5N3O6	9.15E-09
TNB	Trinitrobenzene	C6H3NO6	2.00E-08
AN	Ammonium nitrate	NH4NO3	1.47E-08
TNC	Tri-nitro-m-cresol	C7H5N3O7	1.71E-09
Picric acid	Trinitrophenol	C6H3N3O7	9.71E-10
TNX	Trinitro-m-xylene	C8H7N3O6	1.61E-10
Styphnic acid	Tri-nitroresorcinol	C6H3N3O8	6.03E-11
UN	Urea nitrate	CH5N2ONO3	3.88E-10
PETN	Pentaerythritol tetranitrate	C5H8N4O12	1.07E-11
TETRYL	N-Methyl-n tetranitroaniline	C7H5N5O8	7.41E-12
TNA	Trinitroaniline	C6H4N4O6	1.51E-11
RDX	Cyclotrimethylene trinitramine	C3H6N6O6	4.85E-12
AP	Ammonium perchlorate	NH4 ClO4	4.01E-14
DATB	Di-amino-trinitrobenzene	C6H5N5O6	3.76E-14
Nitroguanidine	Nitroguanidine	CH4N4O2	1.86E-14
HMX	Cyclotetramethylenetetranitramine	C4H8N8O8	2.37E-17
TATB	Triamino-trinitrobenzene	C6H6N6O6	2.38E-18
HNS	Hexanitrostilbene	C14H6N6O12	6.09E-21
GN	Guanidine nitrate	CH6N3NO3	2.62E-23

2.3.1 Detection process

The detection process involves the use of certain sensors or detectors that obtain responses due to an explosive device [68]. The response detected from the explosive should be unique and different from other signals coming from the background and the ambient environment.

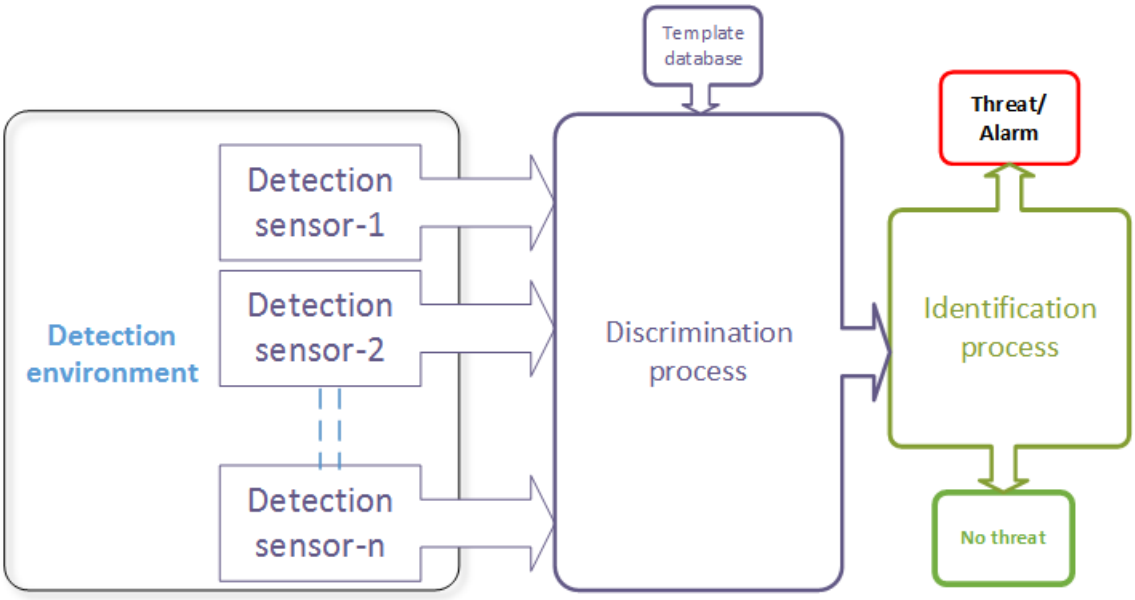

Figure 2.1: System of explosive detection flow chart.

2.3.2 The discrimination process

The discrimination process generally includes a comparison between the incoming signal and different pre-saved templates [69, 70]. For explosive discrimination, there should be a database of responses for real explosives or simulants [71-73].

2.3.3 The identification process

The identification of the existence of an explosive includes processing the responses to reach a conclusion wither there is a threat or not. Different kinds of detectors and sensors are able to detect events from the ambient environment and give corresponding signals; the signals of the detectors have to pass through the discrimination process to see if there is a match to one or more of the library templates. The discrimination process thus gives information about

whether the responses are close to (or match) a certain template. The identification process uses hardware/software techniques [73, 74] to decide if the collected data indicate the presence of a potential threat or if an item needs further investigation or if the item shows no sign of an explosive.

2.4 Common detection method

There are different kinds of detectors that are helpful in detecting the presence of explosive materials. One can attempt to detect the trace of an explosive, or non-reactive components (e.g., the detonator material, taggants, or the IED casing), or the bulk explosive. Traditional technologies are still used such as dogs or metal detection but these are time consuming, relatively expensive, and not always effective. New detection technologies including infrared, terahertz (THz), and microwaves imaging or spectroscopy have been tried to distinguish hazardous materials hidden in packages or the human body [73].

2.4.1 The metal detectors

The metal detection method was used in the early twenty century. It is one of the easiest and affordable methods to sense explosives with metal casing, like landmines [75] through the detection of metal contents of the object. The detector is simply a magnetic field source through a coil which is interrupted by the presence of metal [76]. This method is time consuming and unreliable for explosives with low metal casing or in areas where there are a lot of metal bodies. In some cases, the metal detectors need to be assembled on a robot/cart to keep humans away from the area of danger.

2.4.2 Infrared/ thermal imaging

Infrared (IR) sensors have the ability to sense the hidden pack on a human body (such as a suicide bomber) due to the difference in the thermal emission from the human and the package. Infrared techniques working best indoors, where there is less ambient thermal interruption. Normally explosive packages and other hidden materials in clothes are opaque to thermal radiation. The imaging IR cameras can easily identify these as dark spots on the scanned body, while the body itself has thermal emission brightness. The IR technique is not limited to hidden material

detection only; it may be used for identifying some body sickness syndromes especially when quarantine is essential for epidemic cases at airports [77].

2.4.3 Infrared spectroscopy

Molecules of materials can absorb low-energy photons at characteristic wavelengths. Many explosives show distinct absorption lines between, 5 and 11 μm [78, 79]. By examining the absorption spectrum, the chemical composition for a material can be identified. Because most nitrogenous explosives have -NO_2 groups, the absorption due to this group is taken as a signature for the explosive. The spectroscopy is obtained by the Fourier transform infrared (FTIR) method. For some measurements, the material is mixed with potassium bromide (KBr), which is transparent over wide range of optical wavelengths including the mid-range of IR. The ratio of mixed KBr to plain KBr spectra is calculated to give the required transmission spectrum [80]. Research in the field of infrared spectroscopy has enabled low detection limits that reached 160 ng/cm^2 for the TNT and 400 ng/cm^2 for HMX [81]. The disadvantage of the method is the requirement to be in touch with the material under investigation.

2.4.4 Terahertz imaging

The terahertz band lies within the range of frequencies ~ 0.1 to 1 THz, which ranges from the microwave to near the infrared. Terahertz radiation has the ability to detect concealed weapons because many of non-metallic materials are transparent to terahertz radiation. Terahertz imaging avoids exposure to ionizing radiation, which should be minimized especially for some people (e.g., radiation therapy patients) [82]. The image resolution ΔL at distance L is limited by $\Delta L/L > \lambda/D$ where λ and D are the wavelength of the wave and the aperture of the antenna used to form the image. This equation requires large dimension antennas to increase the resolution, and to work at higher wavelengths. Infrared imaging may be combined with terahertz imaging, in order to give more details about hidden materials [83, 84].

2.4.5 Terahertz spectroscopy

The terahertz spectroscopy is considered one of the promising technologies (started in the last decade) for explosive and drug detection. Explosives such as RDX, TNT, HMX, PETN, and

others show spectral features [85] that can used as fingerprints for concealed materials, (Table 2.4) [82]. For practical applications, a spectral matrix is constructed of the spectral frequencies and the chemical substances of known explosives or drugs. The terahertz spectral chart for an unknown substance is then compared to the matrices to determine if there is a fingerprint for a harmful material [86].

Table 2.4: Absorbance peaks for some explosives and drugs in the range of terahertz.

Material	Band center position frequency (THz)
Explosive	
Semtex-H	0.72, 1.29, 1.73, 1.88, 2.15, 2.45, 2.57
PE4	0.72, 1.29, 1.73, 1.94, 2.21, 2.48, 2.69
RDX/ C4	0.72, 1.26, 1.73
PETNa	1.73, 2.51
PETNb	2.01
HMXa	1.58, 1.91, 2.21, 2.57
HMXb	1.84
TNTa	1.44, 1.91
TNTb	1.7
TNT	5.6, 8.2, 9.1, 9.9
NH4NO3	4, 7
Drugs	
Methamphetamine	1.2, 1.7– 1.8
MDMA	1.4, 1.8
Lactose α-monohydrate	0.54, 1.20, 1.38, 1.82, 2.54, 2.87, 3.29
Icing sugar	1.44, 1.61, 1.82, 2.24, 2.57, 2.84, 3.44
Aspirin, caplets	1.4, 2.24
Acetaminophen	6.5
Terfenadine	3.2
Naproxen sodium	5.2, 6.5

2.4.6 Microwave spectroscopy

Microwaves lies in the region of 100 to 300 GHz, which overlaps the terahertz region. An imaging array of detectors can be used with relatively low noise. Fourier transform is used to obtain an image spectrum. Microwave spectroscopy provides information about the molecular structure of the tested sample. The signal strength is measured at certain frequencies and compared to the explosive calibrated data [87]. For heterogeneous samples, the image is divided into

segments of homogeneous regions; the procedure of spectroscopy is then applied to each region independently.

2.4.7 X-ray radiography

X-ray techniques are widely used in airports and other transportation portals for screening luggage and provide a reliable method for investigation. The X-ray system includes an X-ray tube that provides photons of energy up to typically 450 keV or an accelerator that can produce X rays in some cases to 1 MeV. The X-ray detection system is an array of small detectors that provides data of the transmitted or scattered X-ray photons [88, 89]. The X-ray screening can give information about the density and the effective atomic number which may be helpful in the material identification. Different X-ray imaging techniques include transmission, scattering dual energy screening, and tomography screening. The interaction of the X-ray photons with the material atoms determines the system response [90]. The linear interaction coefficient (μ), or mass interaction coefficient (μ/ρ) are used to express the interaction probability of the X-ray photons with electrons of the elements present [91]; for neutrons, such probability is commonly known as the cross-section of interaction (σ). The major components of the interaction coefficient are the photoelectric absorption (μ_{phe}), Compton scattering (μ_{Cs}), and pair production (μ_{pp}). The interaction coefficients are dependent on the primary X-ray photon energy. The photoelectric absorption coefficient is proportional to Z^n, where n=3~4, and inversely proportional to E^3 [92, 93], i.e.

$$\mu_{phe} \propto \rho \frac{Z^n}{A} \frac{1}{E^3}. \qquad \textbf{(2.1)}$$

The Compton scattering interaction coefficient is directly proportional to $(Z\rho / A)$ [94, 95], where Z is the atomic number, ρ is the elemental density, and A is the atomic weight. Normally Z≈A/2 (except for hydrogen); that makes μ_{Cs} directly proportional to the material density

$$\mu_{Cs} \propto \rho. \qquad \textbf{(2.2)}$$

In Compton scattering, the scattering angle can vary between 0 and π rad according to the Klein-Nishina formula [96], which is a function of photon energy. Pair production starts for photon energies > 1.022 MeV, which is equal to the rest mass energy of an electron-positron pair. The pair production coefficient varies as

$$\mu_{pp} \propto \rho \frac{Z^2}{A} \qquad \textbf{(2.3)}$$

Figure 2.2 shows the three coefficients for hydrogen, nitrogen, aluminum and iron.

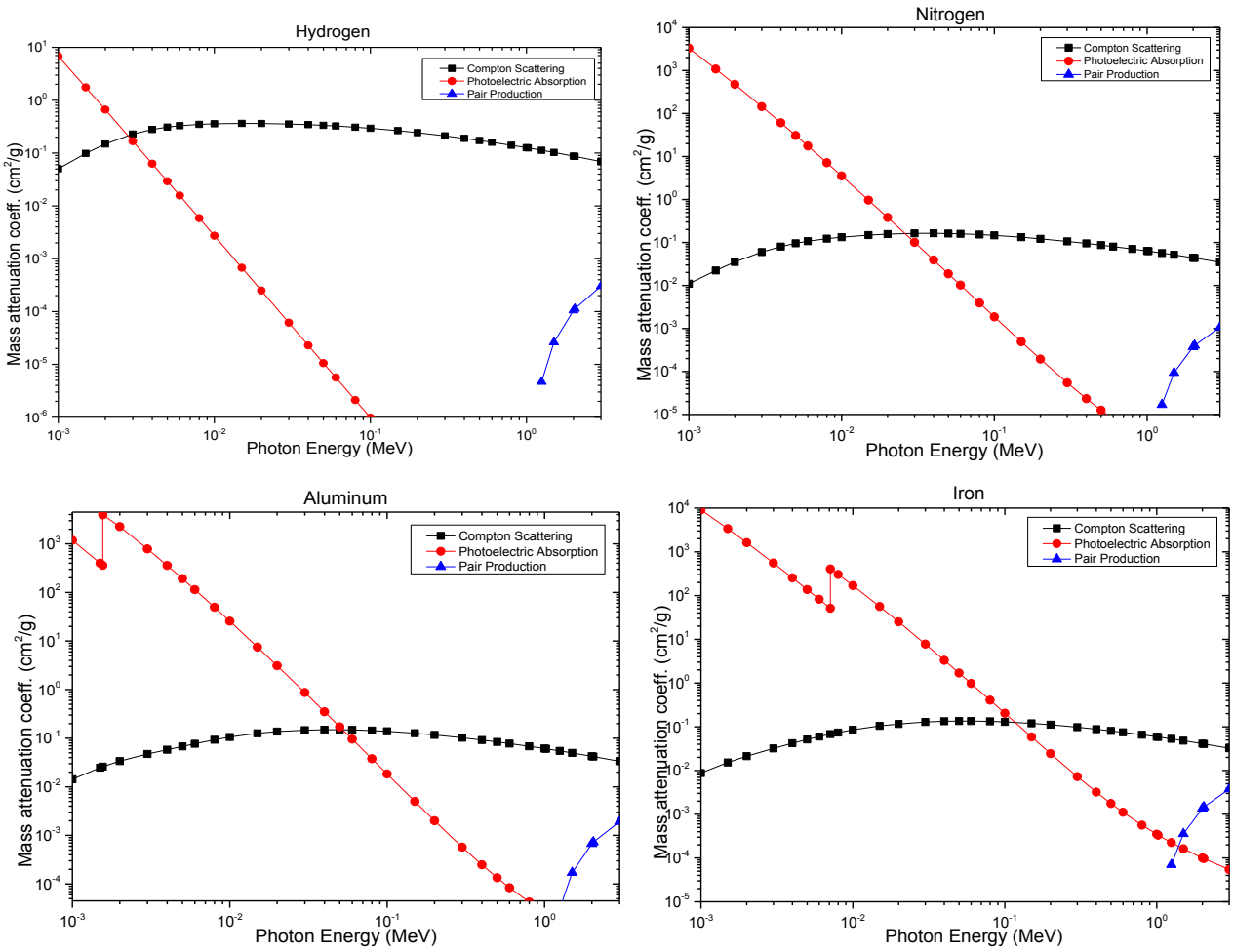

Figure 2.2: Mass attenuation coefficient as (μ/ρ) for different materials

2.4.7.1 The transmission imaging

In forward imaging, the screened object is placed between the X-ray source and the imaging screen. The screen detector array measures the X-ay photons that are transmitted through the

object (some are attenuated by the object, see Figure 2.3). Neglecting scattered radiation, the relative intensity simply complies with the law

$$(I / I_o) = \exp(-\mu \times t), \quad \textbf{(2.4)}$$

where I_o and I are the intensity of X-ray beam before and after penetrating the object in a certain direction Ω, μ is the linear interaction coefficient for the segment where the beam penetrates, and t is the length of segment the beam penetrates in the direction of Ω. The value of μ depends on the density and the effective atomic number of the object segment. The previous equation may be correct for a monoenergetic gamma source, but the situation for X-ray sources is different; the X-ray source emits a continuous spectrum of energy S(E) [97]. The flux transmitted through a body is calculated as

$$I = \int_{E_i}^{E_f} S(\mathrm{E}) \exp\left(-\int_{\ell} \mu(\mathrm{E}, \mathrm{x})\, \mathrm{dx}\right) dE, \quad \textbf{(2.5)}$$

where E_i and E_f are the minimum filtered energy and maximum energy of the X-ray spectrum. The linear attenuation coefficient μ is normally homogenized over the track length of the X-ray beam; for a hybrid medium of n different elements

$$\frac{\mu(E_o)}{\rho} = \sum_{i=1}^{n} w_i \frac{\mu_i(E_o)}{\rho_i}, \quad \textbf{(2.6)}$$

where w_i is weight fraction of component i. In equation (2.5) the homogenized attenuation coefficient is integrated over the path length of the X-ray scanning beam, and the transmitted flux is obtained by integrating the attenuated flux spectrum over the energy range.

Explosives are low atomic number materials, with generally higher density than the clutter materials in luggage (e.g., clothes). The problem of such a 2-D method is that the device can not differentiate between a thick object with low value of μ (e.g., plastic object) and a thin object of high μ (e.g. sheet of copper). For that reason the trained personnel are required to follow the screened objects and identify possible suspicious material. Backscatter imaging is often preferred in X-ray screening processes that are meant to be covert (see Figure 2.3).

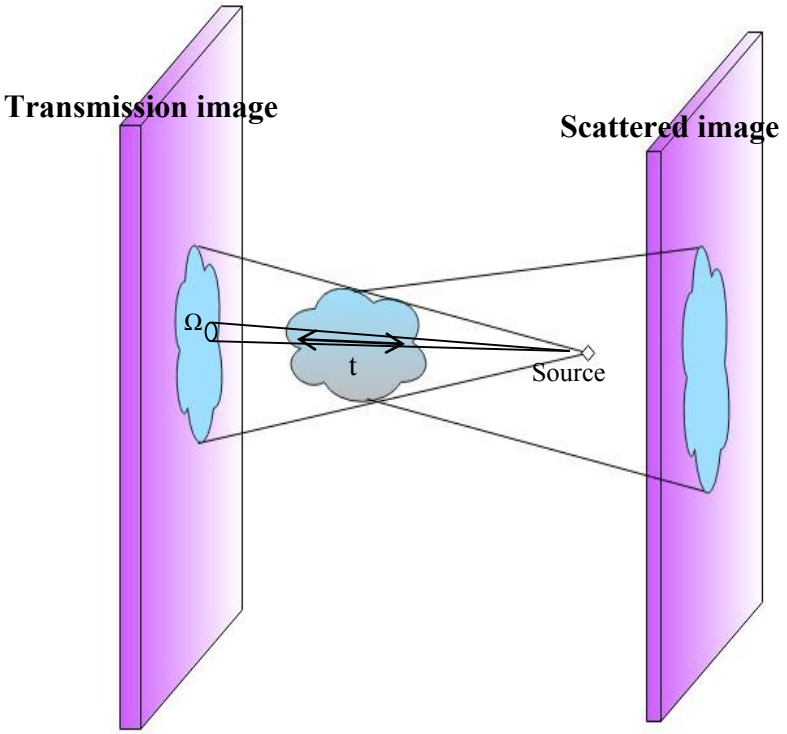

Figure 2.3: X-ray transmission and scattering imaging technique.

2.4.7.2 The X-ray scattering imaging

The plastic explosives contain low *Z*-elements with the majority of H-C-N-O components; they are also characterized by higher density than similar organic inert materials. As mentioned above in equation (2.2), the scattering coefficient is proportional to the material density. Setting a shielded X-ray detector on the same side of the source (Figure 2.3) and directed toward the target, the detector receives the scattered photons from the target at a certain angle [98]. The energy of the Compton scattered photon at angle θ can be predicted from

$$E_s(\theta) = \frac{E_o}{1+\alpha_c(1-\cos(\theta))}, \qquad \textbf{(2.7)}$$

where $\alpha_c = E_o / m c^2$, E_0 is the incident photon energy, m is the electron rest mass, and c is the speed of light. The differential cross section of scattering can be given [99] from the Klein Nishina formula

$$\frac{d\sigma}{d\Omega} = 3.971\times10^{-30}\left(\frac{1+\cos^2\theta}{\left(1+\alpha_c(1-\cos\theta)\right)^2}\right) \times\left(1+\frac{\left(\alpha_c(1-\cos\theta)\right)^2}{\left(1+\cos^2\theta\right)\left(1+\alpha_c(1-\cos\theta)\right)}\right). \quad \textbf{(2.8)}$$

It is clear that the differential cross section is angular-energy dependent, as shown in Figure 2.4. The photon with low energy (few keV) is somewhat isotropic. By increasing the energy of the photon scattering becomes more forward peaked [100]. Imaging techniques that use photon scattering can distinguish hidden metallic objects from low Z elements like hydrogen, carbon, nitrogen and oxygen. Thus, plastic explosives show up as a bright area on the imaging screen. The combination of transmission and scattered imaging provides more information than either one alone.

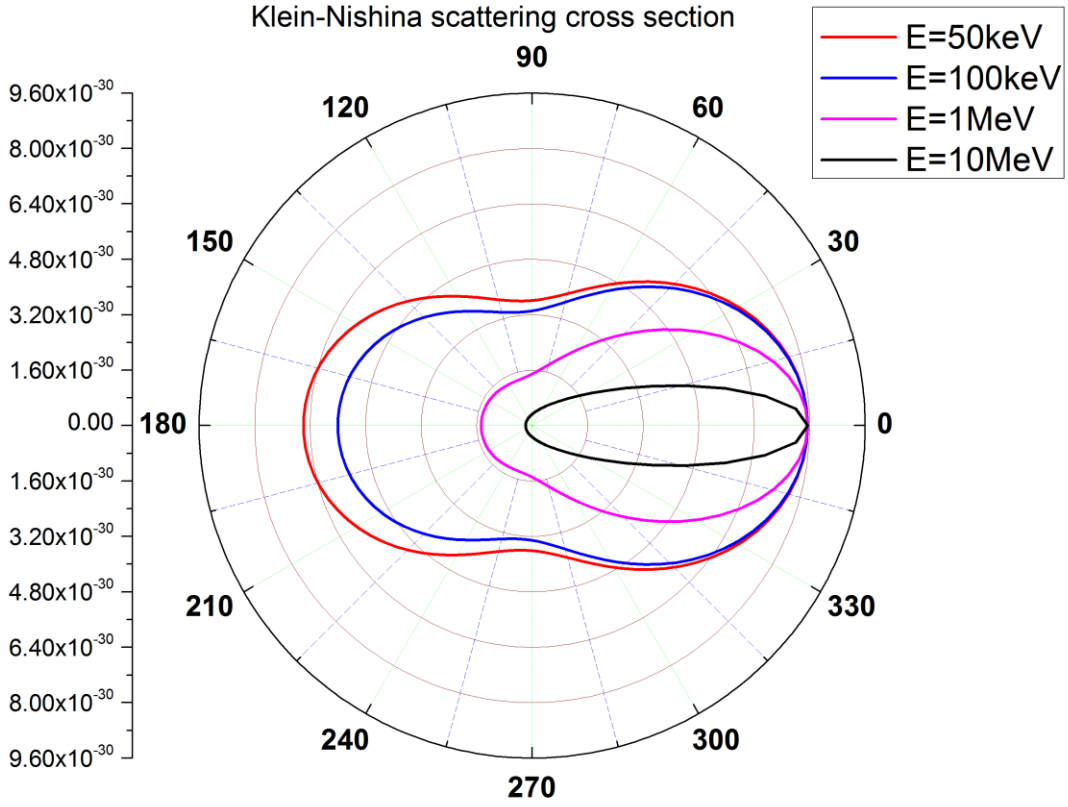

Figure 2.4 Klein Nishina Angular cross section at different photon energies.

2.4.7.3 Dual band energy screening

The dual energy X-ray technique is one of the better techniques used for material identification [101] even though it can only identify broad classes of materials. The object is screened by using two X-ray energy bands. One is low, around 80 keV, and the other is high, over 100 keV. The response of the high energy band depends on the material density, while for the low energy band, the response depends on the effective atomic number and the density of the material, [102]. It is worth mentioning that the method is well known in medical imaging to determine the bone density. For aviation purposes, the response of the high and low energy bands are compared to identify the existence of explosives. The materials of explosives look dark at the low energy band because of the existence of carbon, oxygen, and nitrogen, but appear transparent at the high energy, while the metal parts of the IED appears dark in both energy bands (see Figure 2.5).

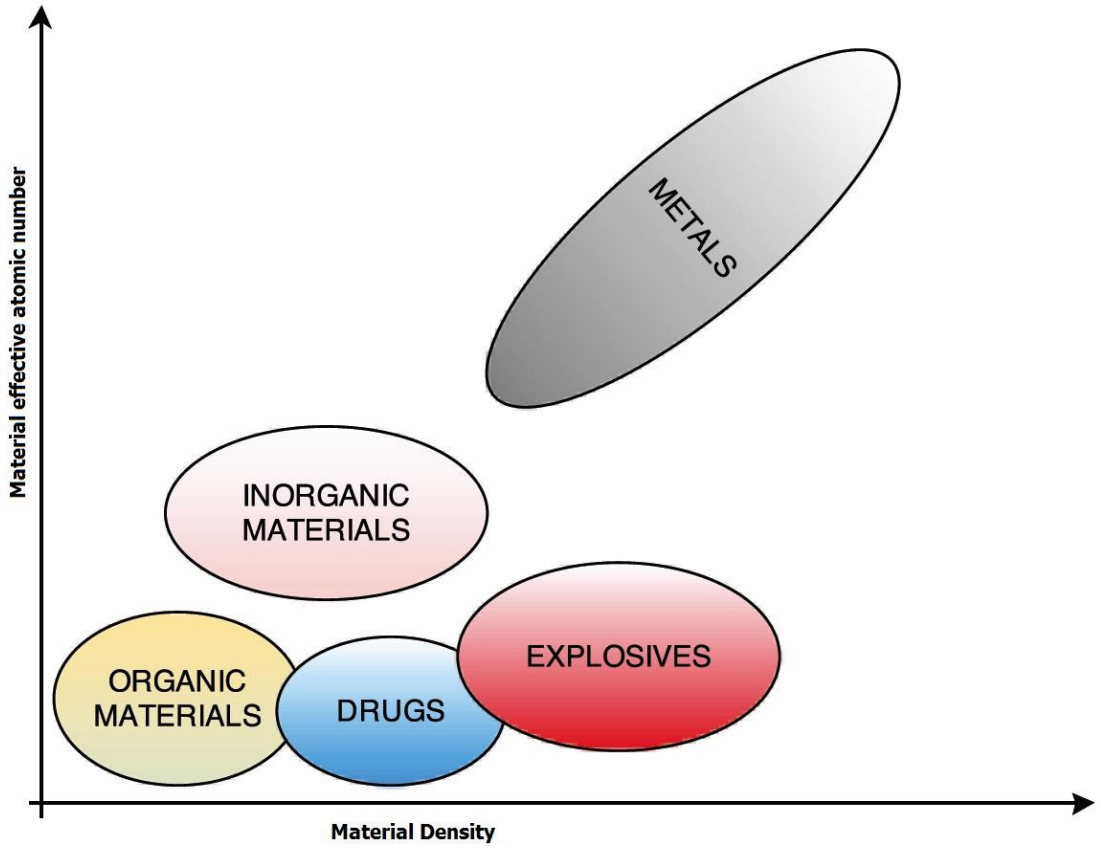

Figure 2.5: The chart for dual energy X-ray identification method.

2.5 Nuclear based explosive detection

The neutron, gamma ray, and X-ray techniques have been used for concealed contraband items over decades in different configurations [103]. The X-ray transmission or scattering has the capability to differentiate between the different densities of materials [94], this technology has the advantage of imaging materials from a distance up to 15 m. X-ray tomography has been developed to take images from different angles and provide 3-D configuration of objects under investigation. Neutron techniques have more varieties than the conventional X-ray techniques because neutrons have different interaction types with the nuclei of materials.
Gamma rays from neutron inelastic scattering are useful for investigating the contents of samples (Figure 2.6). The gamma ray interactions can be used for explosive detection by detecting the inelastic scatter gamma rays, the neutron energy at the time of interaction must be high enough to excite the nucleus to energy levels sufficient to emit the inelastic scatter gamma rays.

Table 2.5: HCNO content of explosive and narcotic materials; the neutron response to the elements using FNA and TNA methods.

Characteristic feature	**Explosive**	**Drugs**	**Nuclear signal strength**	
	Level of elemental density		**Thermal neutron analysis (TNA)**	**Fast neutron analysis (FNA)**
Hydrogen	Low-medium	High	Very high	High
Nitrogen	High-very high	Low	Low	Medium
Carbon	medium	High	Very low	Very high
Oxygen	Very high	Low	0	High
Total Density	High	Medium-low		
O/C	High-very high	low		

The method has the advantage of determining the H-C-N-O content ratios of the investigated material, which is vital information to determine the kind of the material under investigation (see Table 2.5). On the other hand, in the method of fast neutron analysis (FNA), measuring

the inelastically scattered gamma rays can take a relatively long time, depending on the source strength of the neutron source (e.g., Cf-252). Explosive materials should have high oxygen, nitrogen, and a low carbon elemental density. Unlike drugs, explosives have lower hydrogen density, whereas the narcotics contain high hydrogen density and high carbon to oxygen density ratio ~ 3 [104]. Gamma ray sources can be used for explosive detection as well by detecting the products of the interaction (e.g., (γ,n)), except that it needs high gamma ray energy to interact effectively with the H-C-N-O contents of material. The energy value should be around 20 MeV.

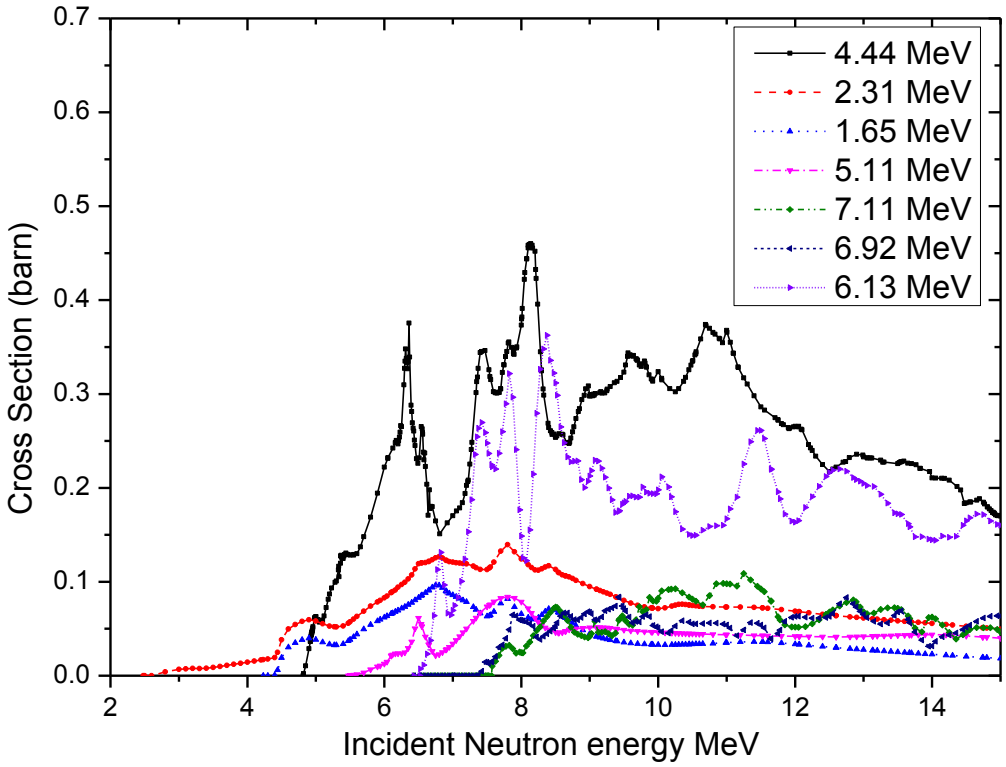

Figure 2.6: Inelastic gamma ray production cross sections for carbon (4.44 MeV), nitrogen (2.31, 1.65, 5.11 MeV), and oxygen (7.11, 6.92, 6.13 MeV).

2.6 Neutron based detection techniques

The neutron detection techniques are effective for identifying the elemental characteristics of a material; the neutron has a distinct interaction with the nucleus which depends on the neutron energy, and the element atomic number and mass [105]. However the neutron system is high in cost and takes more time for scanning, the neutron inspection is a kind of bulk detection that can find small amount of hidden explosive in a carrying bag, up to a large amount inside a

vehicle such as a van or truck. The basis is to find signatures for the major contents of explosives (i.e., nitrogen, oxygen, carbon, and hydrogen). The signatures come from different types of interactions, e.g., *(n,n)*, *(n,n')*, or *(n,γ)* [106]. The type of interaction depends mainly on the neutron energy. Detectors measure the products of the interactions, such as elastically or inelastically scattered neutrons and prompt and/or delayed gamma rays.

2.6.1 Neutron interactions with matter

Neutrons are neutral particles that can interact with nuclei in different ways. The cross sections of neutron interactions include the following:

$\sigma_{el} = \sigma(\mathrm{n},\mathrm{n})$ = elastic scattering cross section.

$\sigma_{i} = \sigma(\mathrm{n},\mathrm{n}')$ = inelastic scattering cross section.

$\sigma_{s} = \sigma_{el} + \sigma_{i}$ = total scattering cross section

σ_{a} = absorption / capture cross section

$\sigma_{t} = \sigma_{s} + \sigma_{a}$ = total cross section

$\sigma_{ne} = \sigma_{t} - \sigma_{el}$ = non-elastic cross section

$\sigma_{\gamma} = \sigma(\mathrm{n},\gamma)$ = radiative capture cross section

$\sigma_{f} = \sigma(\mathrm{n},\mathrm{f})$ = fission cross section

$\sigma(\mathrm{n},\mathrm{p})$ = proton production cross section

- The neutron may scatter elastically with the nucleus like billiard balls (*n,n*), this kind of interaction conserves the momentum and kinetic energy of the particles, Figure 2.7.
- The second kind of scattering is inelastic scattering (*n*, *n*'), in which the neutron leaves the nucleus in an excited state; the nucleus emits one or more inelastic gamma rays as it returns to the ground state. The gamma-ray energies are characteristic of the changes in energy levels within the nucleus.

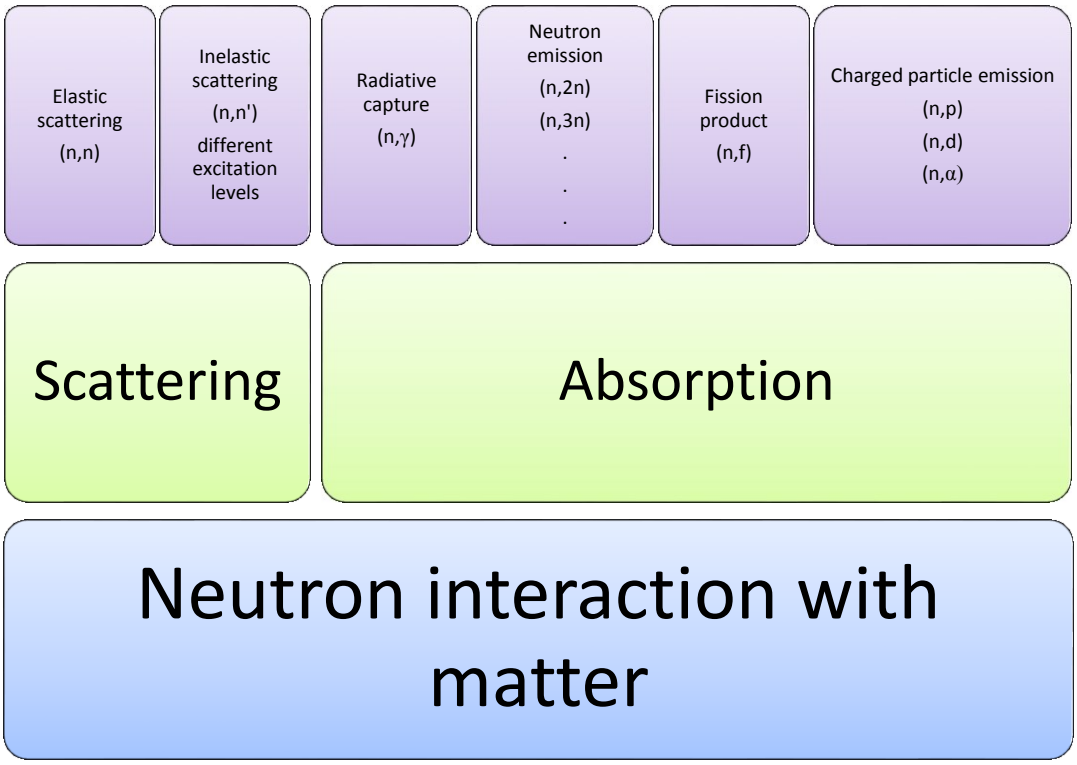

Figure 2.7: Neutron interactions with matter and cross sections.

- Absorption of a neutron accompanied by a gamma emission is called radiative capture (n,γ). In this interaction, the neutron is absorbed and the nucleus becomes the nucleus of a new isotope at some exited state. The new isotope emits one or more gamma photons with certain distinct energies trying to reach the ground state, (Figure 2.8).
- The neutron may be absorbed; the new isotope is excited to a certain energy level, leading to emission of two (or more) neutrons or a charged particle (e.g., a proton, a deuteron, an alpha, etc.).
- A neutron may be absorbed by a heavy nucleus and lead to a fission into two or more fission fragments.

2.6.1.1 Gamma emission from neutron interaction with explosives

The major contents of explosives are the H-C-N-O elements. Neutrons interact with the nuclei of these elements and sometimes produce distinct gamma rays that are characteristic of

these elements. Gamma emission from fast neutron interaction is a powerful method to identify the four H-C-N-O elements [37, 72, 107, 108], (see Table 2.6).

Table 2.6: High probability gamma ray emission from fast neutron interaction with H-C-N-O materials.

Element	*Interaction*	*Incident Neutron Energy*	*Measured Product*	*Energy of Gamma*	*Cross Section**
H	$H\left(n_{th},\gamma\right)d$	Thermal neutron, (requires moderator)	Prompt gamma capture	2.22 MeV	$\sigma_{th} = 0.332\ b$
C	$^{12}C\left(n,\mathrm{n}'\right)^{12}C$	$E_n > 4.8MeV$	Inelastic Gamma	4.44 MeV	$\sigma_{E14} = 0.100\ b$
N	$^{14}N\left(n,\mathrm{n}'\right)^{14}N$	$E_n > 2.6MeV$	Inelastic Gamma	2.313 MeV	$\sigma_{E14} = 0.055\ b$
		$E_n > 5.5MeV$		5.11 MeV	$\sigma_{E14} = 0.045\ b$
		$E_n > 4.4MeV$		1.635 MeV	$\sigma_{E14} = 0.032\ b$
O	$^{16}O\left(n,\mathrm{n}'\right)^{16}O$	$E_n > 7MeV$	Inelastic Gamma	6.13 MeV	$\sigma_{E14} = 0.145\ b$
	$^{16}O\left(n,\mathrm{p}\right)^{16}N$	$E_n > 7.6MeV$	Activation, 7.1 s decay time	6.13 MeV (67%), 7.12 MeV (5%)	$\sigma_{E14} = 0.062\ b$

** The neutron cross section either corresponds to th=thermal, or E_{14}=14 MeV.*

The method of measuring gamma emission is used for cargo screening, the method is however expensive, and hazardous because of the radioactivity of the neutron source and the products of screening [108]. Neutron capture usually occurs for thermal neutrons and is accompanied by prompt gamma emission. The new product may be radioactive and in most cases decays by beta decay delayed gamma emission (Figure 2.8). If the product is radioactive it has a distinct half-life. For example, following the ^{14}N $(n,2n)$ ^{13}N reaction, the ^{13}N is radioactive with a half-life of 9.97 min, and decays by positron emission. The prompt capture gamma energies emitted by different isotopes are listed in reference [109] along with measured spectra and cross sections.

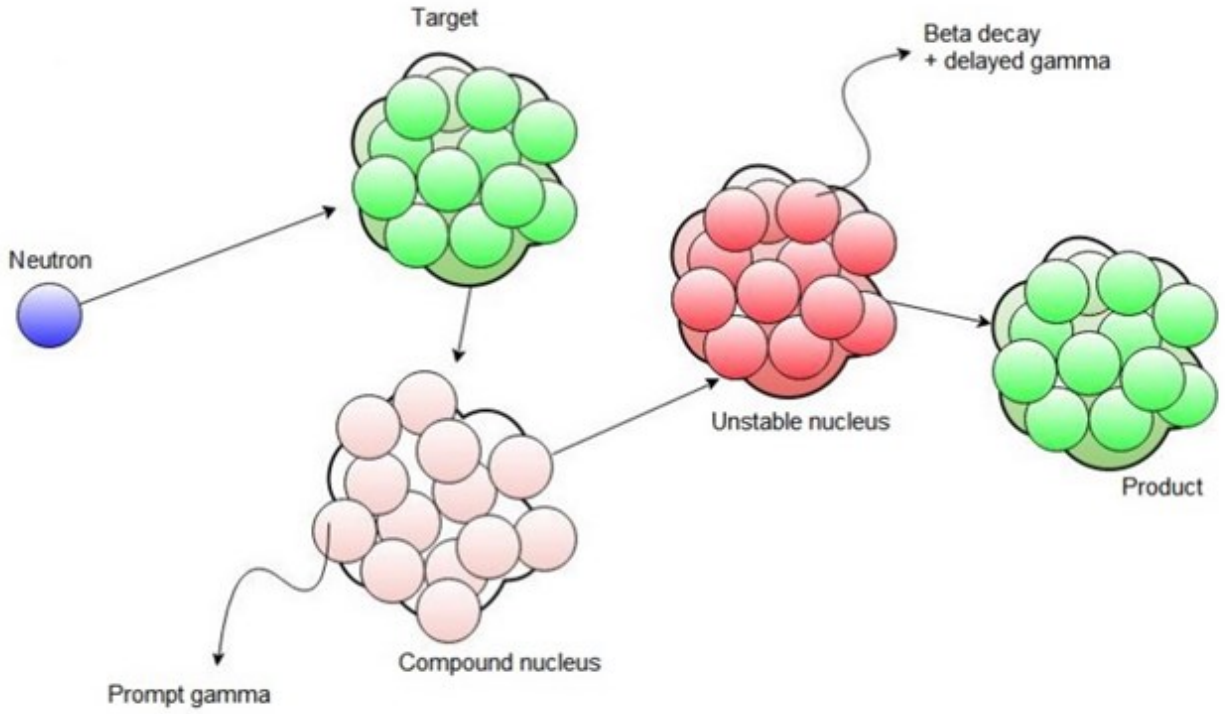

Figure 2.8: Neutron capture in matter, followed by prompt gamma, and beta decay.

2.6.1.2 Gamma detection based neutron detection systems

There are techniques of measuring the product radiation, namely gamma rays, as there are prompt and delayed gamma radiation; each kind should have different duration of measurement. Various gamma-ray-based detection schemes can be divided as follows.

I. Thermal Neutron Analysis (TNA) is a commonly used method; thermal neutrons have high capture cross sections for most elements. The neutrons from Cf-252 or other radioisotope sources [110] or from accelerator based sources, (e.g., d-d source) can be thermalized outside or within the sample. The TNA test is very helpful in detecting hydrogen contents of materials [111]. Gamma radiation from the radiative capture interaction are distinct for each element, and those for H-C-N-O are given in Table 2.7.

Table 2.7: Thermal neutron capture gamma ray characteristics of H-C-N-O elements

Element	Gamma-ray Energy (MeV)	Cross section (milli-barns)
H	2.22	332
C-12	1.26	1.24
	3.68	1.22
	4.95	2.61
N-14	5.27, 5.29	23.6, 16.8
	6.32	14.5
	4.51	13.2
	10.83	11.3
O-16	0.87	0.17
	1.09	0.16
	2.18	0.16
	3.27	0.035

II. Fast Neutron Analysis (FNA) begins with a source of fast neutrons, which may be generated from a D-T reaction in an accelerator device, which provides ~14 MeV neutrons. The fast neutron strikes the nucleus with energy E_n and in inelastic scattering interactions, raises it to an excited state. The nucleus de-excites by promptly emitting one or more gamma photon [112]. The test can determine C-N-O contents of a material. Sometimes a combination between TNA, and FNA are made by emitting a pulse of fast neutrons, then a pulse of thermal neutrons.

III. Pulsed Fast Neutron Analysis (PFNA) depends on emitting a short pulse of fast neutrons from a pulsed accelerator, such as a (d-t) or a (d-d) fusion device [113]. The technique allows separating the fast neutrons from thermalized ones by timing, because of the thermalization time. Often, the neutrons are collimated and the gamma products are measured by a detector array. The location of the interaction can be estimated from the time difference between the neutron emission and the gamma-ray detection.

IV. Associated Particle Imaging (API), where the alpha particle associated with neutron production (D-T) is measured and located [114], giving information about the neutron production time and direction; then the time of flight (TOF) may be used to determine the

interaction location [115]. The gamma rays produced are often measured by detector arrays around the target. The method has the advantage of detecting the interaction locations without the need to emit neutrons in ns pulses.

2.6.1.3 Fast Neutron Scattering Analysis (FNSA)

Unlike other techniques of measuring gamma ray production, the method of fast neutron scattering analysis (FNSA) is different in the product measurements, as it focuses on measuring the elastically scattered neutrons of the interrogated material. The type and amount of nuclides causing neutron scattering are determined based on the scattered neutron energy and the angle of scattering as well as the incident neutron energy [116]. The neutron source must be monoenergetic to relate the scattering neutron energy and scatter angle. The method uses neutrons in the energy range 0.1~14 MeV as this range energy allows the neutrons to penetrate relatively deeply into the sample. At this energy range the H-C-N-O elements have different cross sections for elastic interactions (see Figure 2.9).

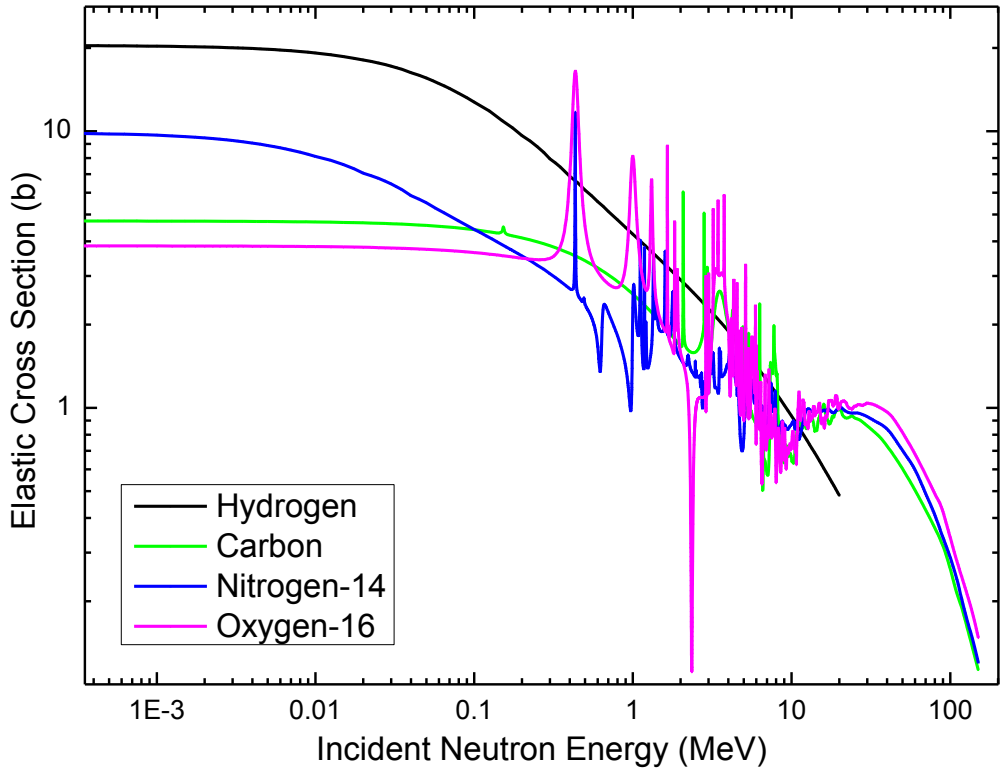

Figure 2.9: Elastic scattering cross section for the H-C-N-O elements. (Seen in color)

Several techniques may be used with the elastic scattering neutrons individually or combined.

I. The kinematic laws of collision may be used to predict the mass of the target nuclides by measuring the energy and direction of the neutron before and after a single collision.

II. If the incident energy is high enough, this will excite the nucleus energy levels through inelastic scattering, and adding a punch of low energy inelastically scattered neutrons, which by measuring can identify the target nuclei.

III. A portion of the neutrons slows down in the matter because of the successive collisions. This amount is very helpful for determining the hydrogen content of the material.

IV. The forward and backscattering neutrons may be measured by two detectors. The ratio of forward to backscattered neutrons can give an indication about the material contents.

V. Two neutron sources with different energies may be used, the scattered neutrons are then measured, and the ratio of the responses gives an indication about the material contents, as the neutron cross section differs as the energy changes.

Chapter 3 - **Signatures and Signature Based Radiation Scanning**

The signature based radiation scanning (SBRS) method depends on collecting different responses regarding the interactions of an ionizing radiation beam with a target [107, 114, 117]. If a target is subjected to a beam of X-rays, the photons of the beam interacts with target materials in three basic ways, photoelectric effect, Compton scattering, and pair production (for photon energy > 1.022 MeV). The responses from such interactions are Compton scattered photons, X-ray fluorescence [118, 119], and annihilation photons of 511 keV each. In the case of neutron beam interactions, the responses may be prompt gamma rays from thermal neutron capture, inelastic-scatter gamma rays, and neutrons that are elastically or inelastically scattered. Different filters may be applied to the signal response giving more responses. For example a cadmium sheet may be wrapped around a neutron detector preventing the thermal neutrons from getting to the detector.

3.1 Neutron elastic scattering

The scattered neutron flux at some position from a certain material that is hit by a monoenergetic neutron beam depends on the angle of scattering, the original energy of the incident neutrons, and the number of interactions inside the material volume. For d-d fusion neutrons with energy around 2.5 MeV, elastic scattering is dominant. Inelastic scattering is significant only above the energy range for the D–D fusion neutrons, for instance at 6-7 MeV for carbon and oxygen and at 3 MeV for nitrogen. Hence we may neglect the inelastic scattering regime for the case of a d-d neutron generator. It is worth to mention that for some accelerators, the energy of deuterons might reach few MeVs, which in its turn energizes the produced neutrons [116].

In elastic scattering, the neutron hits the material stationary nucleus with kinetic energy $E_l = \frac{1}{2} m \upsilon_l^2$, the neutron leaves the nucleus in the ground state in a reaction of zero Q value; this interaction conserves the momentum and kinetic energy of the two involved particles. Because the collision system under investigation involves two relative masses, it is often more convenient to mathematically work in the center of mass (COM) system rather than lab [120-122].

Let the relative neutron mass ≈1, and the relative nucleus mass ≈A, then the velocity of the center of mass, the neutron, and the nucleus areV_{cm} , v_c, and V_C respectively (see Figure 3.1). We can state the velocities as a function of the incident neutron velocity and relative masses as where v_l is the neutron velocity in the lab system.

$$V_{cm} = \frac{v_l}{1+A}$$

$$v_c = \frac{A v_l}{1+A} \quad , \qquad \textbf{(3.1)}$$

$$V_C = \frac{-v_l}{1+A}$$

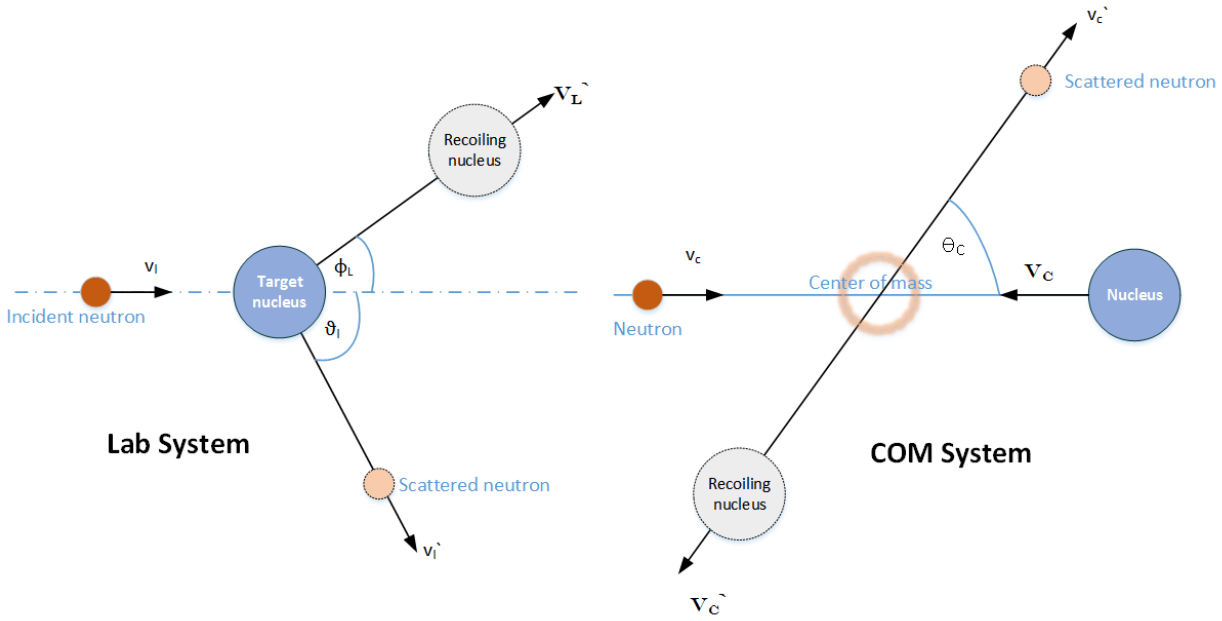

Figure 3.1: Neutron elastic scattering kinematics, the collision system is shown in COM and lab systems.

The summation of linear momentum before and after the collision in the COM system is zero, and $v_c = A V_C$, $v_c' = A V_C'$. This leads to fact that the velocities in the COM system are constant and are related to those of the lab system as follows

$$v_c = v_c' \ , \ V_C = V_C'$$

$$v_c' = \frac{A v_l}{1+A} \ , \ V_C' = \frac{-v_l}{1+A} \qquad \textbf{(3.2)}$$

The total energy in the COM system can be related to the energy in the lab system by

$$E_c = \frac{1}{2}(v_c^2 + A V_c^2) = \frac{1}{2} v_l^2 \left(\frac{A^2}{(1+A)^2} + \frac{A}{(1+A)^2}\right) = \frac{1}{2} v_l^2 \left(\frac{A^2 + A}{(1+A)^2}\right)$$
$$= \frac{1}{2} \frac{A}{(1+A)} v_l^2 = \frac{A}{(1+A)} E_l \,. \qquad \textbf{(3.3)}$$

The COM and lab velocities can be related to each other by considering the vector diagrams in Figure 3.2 from which the relation between the angles of neutron scattering in the lab and COM systems may be found.

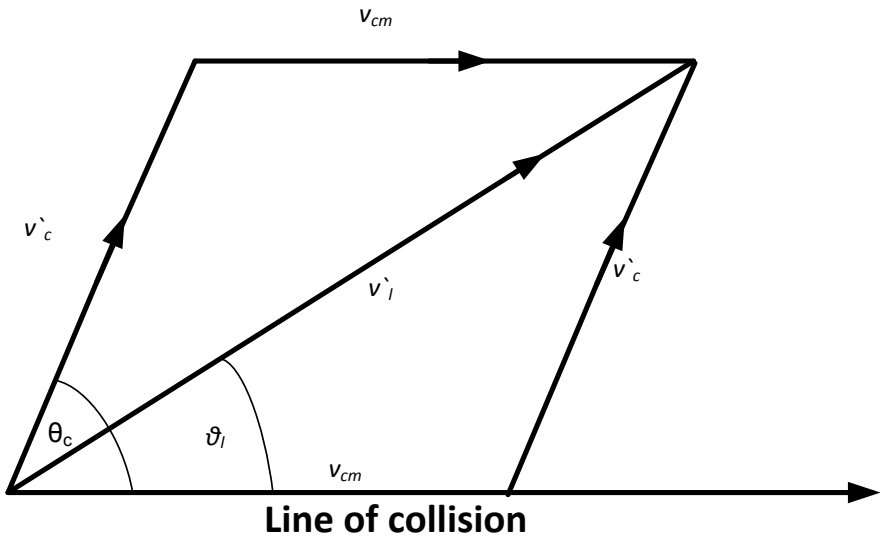

Figure 3.2: Relationship between lab and COM system

The velocity vectors in the lab and COM systems are related to the velocity of the center of mass in equation (3.1).

$$\vec{v}_{cm} \quad \vec{\cdot}_{l} \quad \vec{\cdot}_{c} \qquad \textbf{(3.4)}$$

The sin law relates angles to the velocities

$$\frac{v_l'}{\sin(\theta_c)} = \frac{v_c'}{\sin(\vartheta_l)}\,, \qquad \textbf{(3.5)}$$

and the cosine law can be written as

$$v_{cm} = v_l' \cos(\vartheta_l) - v_c' \cos(\theta_c)\,. \qquad \textbf{(3.6)}$$

An important relation from the parallelogram in Figure 3.2 is

$$v_l' = \sqrt{(v_c')^2 + (v_l')^2 + 2 v_c' v_l' \cos(\theta_c)} \qquad \textbf{(3.7)}$$

From equations (3.5), (3.6), and substituting from equation (3.2)

$$\tan(\vartheta_l) = \frac{A\,\sin(\theta_c)}{1 + A\,\cos(\theta_c)}. \qquad \textbf{(3.8)}$$

It also may be deduced that

$$\cos(\vartheta_l) = \frac{1 + A\,\cos(\theta_c)}{\sqrt{A^2 + 2A\,\cos(\theta_c) + 1}}$$

or

$$\cos(\vartheta_c) = \frac{1}{A}\left((\cos^2(\theta_l) - 1) + \cos(\theta_l)\sqrt{A^2 + \cos^2(\theta_l) - 1}\right). \qquad \textbf{(3.9)}$$

For a neutron-proton interaction, A≈1, and $\cos(\vartheta_c) = \cos^2(\theta_l) - 1$, for a single scatter θ_l is varying between 0 and π/2. For the collision with nuclei other than proton (A>1), the angle θ_l varies between 0 and π. That means the neutron is not allowed to have backscattering after a single collision with hydrogen nucleus, but can do with any other nucleus. The conservation of momentum equation in the lab system may be solved to get a relation between the scattered neutron energy and angle of scattering [123, 124]. For non-relativistic speeds, the momentum equation can be constructed from Figure 3.1 in the lab system. The particle momentum is $p = m\,v = \sqrt{2\,mE}$ and the momentum equation is

$$2AE_{nuc} = 2E_l + 2E_l' - 2\sqrt{E_l\,E_l'}\,\cos(\vartheta_l). \qquad \textbf{(3.10)}$$

By solving the quad equation, noting that $E_l = E_l' + E_{nuc}' - Q$ (Q=0 for elastic scattering)

$$E_l' = \frac{1}{(A+1)^2}\left(\sqrt{E_l}\,\cos(\vartheta_l) + \sqrt{E_l(\mathrm{A}^2 - 1 + \cos^2\vartheta_l)}\right)^2. \qquad \textbf{(3.11)}$$

This equation is very important as it is used to predict the single scatter neutron energy given the initial neutron energy and the scatter angle. The scatter angle θ_l may be expressed in terms of the initial and final energies of the incident and scattered neutron

$$\cos(\vartheta_l) = \frac{1}{2}\left((\mathrm{A}+1)\sqrt{\frac{E_l'}{E_l}} - (\mathrm{A}-1)\sqrt{\frac{E_l}{E_l'}}\right). \qquad \textbf{(3.12)}$$

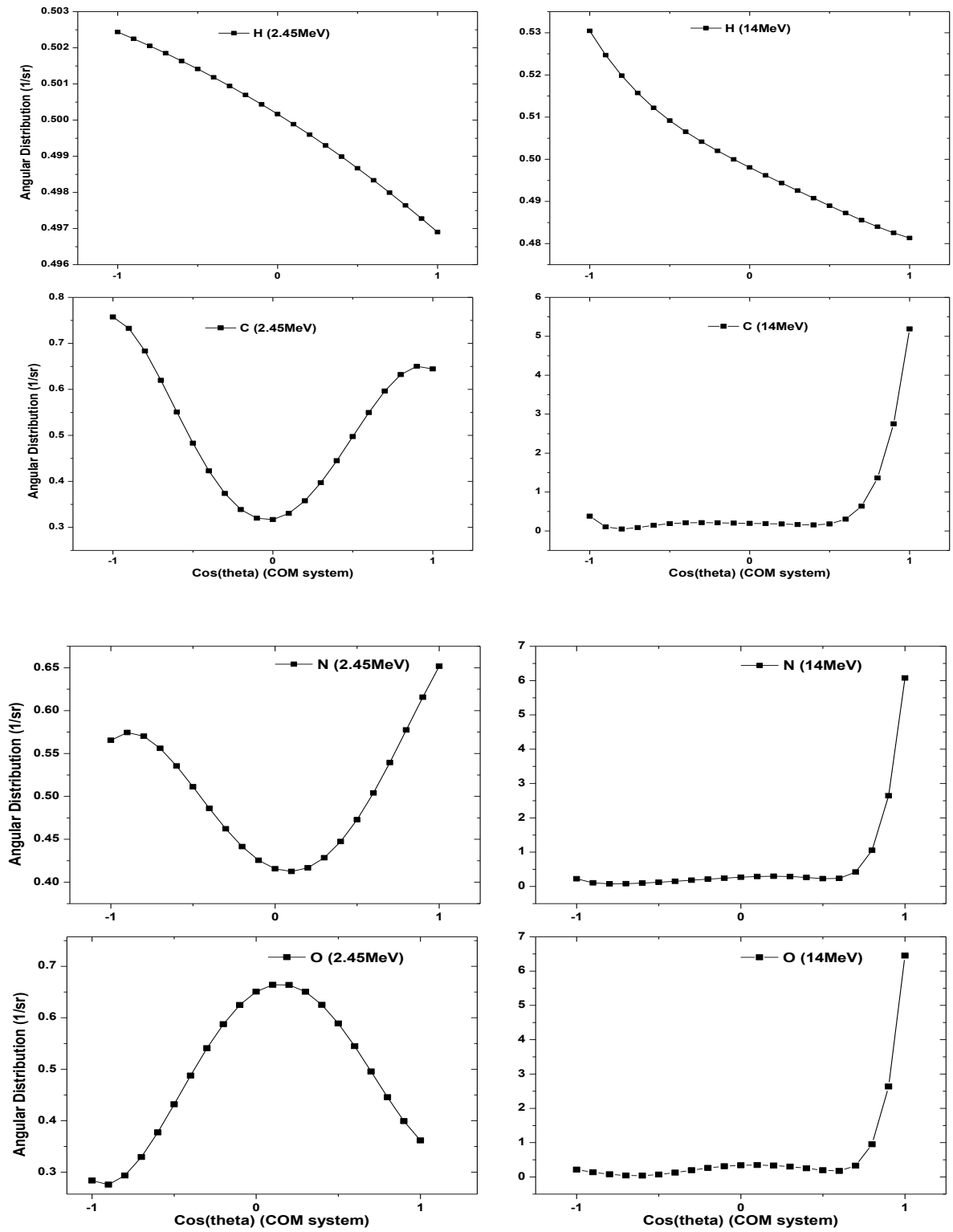

Figure 3.3: Neutron angular distribution for elastic scattering from HCNO elements at two different energies 2.45 and 14 MeV (COM system).

The neutron angular distribution in the COM system may be obtained from one of the nuclear library databases [37, 125], the angular distribution for H-C-N-O elements from incident neutron of 2.5 and 14 MeV are indicated in Figure 3.3.

3.2 Neutron inelastic scattering

Inelastic scattering can occur for fast neutrons when the incident neutron energy is greater than the first excitation state of the nucleus (known as the threshold). Most nuclei de-excite to the ground state or to a lower energy state by emitting a gamma photon of certain energy (difference between the two energy levels) [126]. The inelastic neutron interaction is different from radiative capture, but takes a longer time, around 10^{-14} s for most interactions [127-129], e.g., when the 4438 keV level in carbon is excited, the nucleus decays with $T_{1/2} \sim 0.04$ ps. Oxygen can be also detected through inelastic scattering excitations with a number of distinct gamma rays at 7115 keV ($T_{1/2} \sim 8.3$ fs), 6915 keV ($T_{1/2} \sim 4.7$ fs), and 6128 keV ($T_{1/2} \sim 18.4$ ps) [130]. The inelastic interaction threshold of some nuclei starts at few hundreds kilo electronvolts (e.g. ^{115}In has the first transition at ~336 keV).

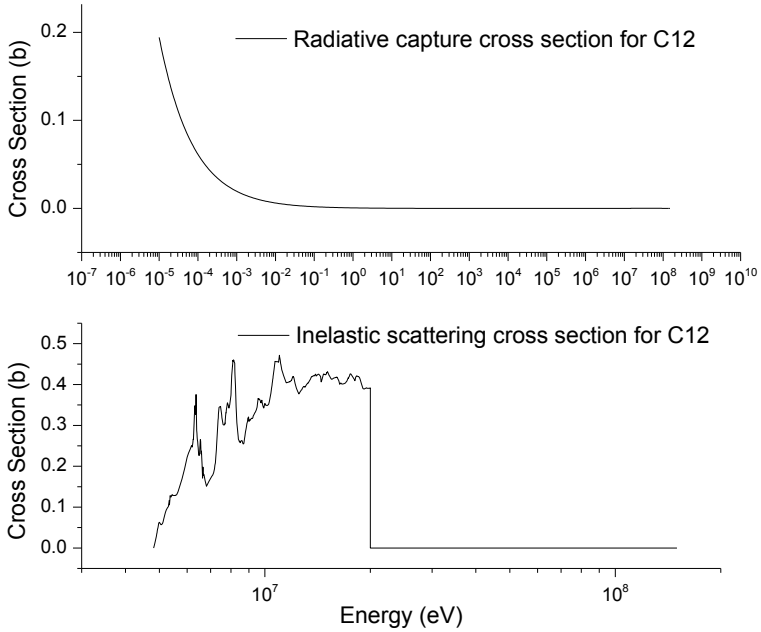

Figure 3.4: Radiative capture and inelastic scattering cross sections for Carbon.

Gamma ray emission from inelastic neutron scattering can be used to identify the isotopic contents of a material. In some cases, the inelastic gamma emission is more useful than the radiative capture gammas, because of the higher cross section, and the ease of constructing a fast neutron source. Figure 3.4 shows the cross section for inelastic scattering of carbon, which reaches 420 mbarn at (E_n=14 MeV). On the other hand, the radiative capture cross section for thermal neutrons (E_n=0.0253 eV) is around 3.5 mbarn only [37, 131].

3.3 Prompt gamma neutron activation analysis

High energy neutrons slow down in a bulk medium, the rate depending on the atomic mass of the elements in the medium. The slowing down process allows the neutrons to enter the energy region where the radiative capture cross section greatly increased. Some elements have radiative capture resonance regions, where the cross section may increase by orders of magnitude. Measuring the prompt gamma rays emitted can give an indication of the material contents. The prompt gamma ray neutron activation analysis (PGNAA) technique has different applications in the manufacturing industry, for contraband detection and in well logging [132-134].

3.4 Signature based radiation scanning

The signature based radiation scanning (SBRS) technique seeks to compare responses from an unknown material to template responses. The responses (called signatures) from a scanned target are compared to the signatures of the template under comparison to see how closely they agree. The templates are characteristic of dangerous material such as hidden explosives. The template signatures may be collected in experimental work or via simulation techniques like Monte-Carlo [135-137].

3.4.1 Figure of merit

A figure of merit (FOM) value, with its standard deviation, is used to differentiate materials. The figure of merit equation is developed along the lines of the Chi squared equation [138-

142]. Let N represent the number of responses under a certain scanning process, R_i be the response of the detector number i, and S_{li} represent the response i for template l. Then begin by defining

$$FOM = \left(\sum_{i=1}^{N} \frac{(R_i - S_{il})^2}{\sigma^2(R_i) + \sigma^2(S_{il})} \right), \qquad \textbf{(3.13)}$$

where $\sigma^2(R_i)$ and $\sigma^2(S_{li})$ are the variances of the sample and template responses, respectively.

In some cases, it is convenient to give a certain detector more importance than others, for the sensitivity, accuracy, signal to noise ratio, or the conditional signal importance, for example, if the process interested in measuring the thermal neutrons, it is better to give the ^{3}He detectors more importance then lithium-iodide ones, because of the higher efficiency to thermal neutrons and lower sensitivity to gamma rays. Another example is to count the target weight or volume as a response or signature; generally this factor is subjected to estimation and may have large error; therefore it is recommended to keep the importance of such response less than the others.

The variable $\boldsymbol{\alpha_i}$ is introduced as an importance factor for detector i. For equal importance, $\alpha_i = 1/N$, in any case the summation of $\boldsymbol{\alpha_i}$ must equal to one. Another important factor that should be taken into account is the geometry and other environmental conditions that may affect the target scanning response; factor $\boldsymbol{\beta_i}$ is used for compensation of such effects. The FOM equation can then be rewritten as

$$FOM = \left(\sum_{i=1}^{N} \alpha_i \frac{(\beta R_i - S_{il})^2}{\sigma_i^{\,2}} \right) \qquad \textbf{(3.14)}$$

where the denominator is $\sigma_i^{\,2} = \beta^2\sigma^2(R_i) + \sigma^2(S_{il})$

It is important to derive the standard deviation for the FOM. For a nonlinear function of independent variables, $\Re(u, v, ..)$, the variance may be found as follows [143]

$$\sigma^2(\Re) = \left(\frac{\partial \Re(u,v)}{\partial u} \right)^2 \sigma^2(u) + \left(\frac{\partial \Re(u,v)}{\partial v} \right)^2 \sigma^2(v) + .. + 2\left(\frac{\partial \Re(u,v)}{\partial u} \right)\left(\frac{\partial \Re(u,v)}{\partial v} \right)\sigma(u,v) + .. \qquad \textbf{(3.15)}$$

In our case, the third term can be neglected as the covariance between the two variables is zero. Using equation (3.15) and substituting in equation (3.14) to find the variance of the FOM.

$$\sigma^2(\mathrm{FOM}) = \left(\frac{\partial \left(\sum_{i=1}^{N} \alpha_i \frac{(\beta R_i - S_{il})^2}{\beta^2 \sigma^2(R_i) + \sigma^2(S_{il})} \right)}{\partial R_i} \right)^2 \sigma^2(R_i)$$

$$+ \left(\frac{\partial \left(\sum_{i=1}^{N} \alpha_i \frac{(\beta R_i - S_{il})^2}{\beta^2 \sigma^2(R_i) + \sigma^2(S_{il})} \right)}{\partial S_{il}} \right)^2 \sigma^2(S_{il})$$

$$+ \left(\frac{\partial \left(\sum_{i=1}^{N} \alpha_i \frac{(\beta R_i - S_{il})^2}{\beta^2 \sigma^2(R_i) + \sigma^2(S_{il})} \right)}{\partial \sigma^2(R_i)} \right)^2 \sigma^2(\sigma^2(R_i)) \qquad \textbf{(3.16)}$$

$$+ \left(\frac{\partial \left(\sum_{i=1}^{N} \alpha_i \frac{(\beta R_i - S_{il})^2}{\beta^2 \sigma^2(R_i) + \sigma^2(S_{il})} \right)}{\partial \sigma^2(S_{il})} \right)^2 \sigma^2(\sigma^2(S_{il}))$$

By differentiating the first two terms, the second and third term assumed to be neglected, then

$$\left(\frac{\partial \left(\sum_{i=1}^{N} \alpha_i \frac{(\beta R_i - S_{il})^2}{\beta^2 \sigma^2(R_i) + \sigma^2(S_{il})} \right)}{\partial R_i} \right)^2 \sigma^2(R_i) \qquad \textbf{(3.17)}$$

,

$$= \left(\sum_{i=1}^{N} \frac{\alpha_i}{\beta^2 \sigma^2(R_i) + \sigma^2(S_{il})} 2\beta(\beta R_i - S_{il}) \right)^2 \sigma^2(R_i)$$

and

$$\left(\frac{\partial \left(\sum_{i=1}^{N} \alpha_i \frac{(\beta R_i - S_{il})^2}{\beta^2 \sigma^2(R_i) + \sigma^2(S_{il})} \right)}{\partial S_{il}} \right)^2 \sigma^2(\mathrm{S}_{il}) \qquad \textbf{(3.18)}$$

$$= \left(\sum_{i=1}^{N} \frac{-\alpha_i}{\beta^2 \sigma^2(R_i) + \sigma^2(S_{il})} 2(\beta R_i - S_{il}) \right)^2 \sigma^2(\mathrm{S}_{il})$$

Combining the two terms in equation (3.17) and (3.18) together and substitute in (3.16) to get the a formula for the variance

$$\sigma^2(\mathrm{FOM}) = 4\beta^2 \left(\sum_{i=1}^{N} \frac{\alpha_i}{\beta^2 \sigma^2(R_i) + \sigma^2(S_{il})} (\beta R_i - S_{il}) \right)^2 \sigma^2(R_i)$$

$$+ 4 \left(\sum_{i=1}^{N} \frac{\alpha_i}{\beta^2 \sigma^2(R_i) + \sigma^2(S_{il})} (\beta R_i - S_{il}) \right)^2 \sigma^2(\mathrm{S}_{il}) \qquad \textbf{(3.19)}$$

$$= 4 \left(\sum_{i=1}^{N} \alpha_i \frac{(\beta R_i - S_{il})}{\beta^2 \sigma^2(R_i) + \sigma^2(S_{il})} \right)^2 \left(\beta^2 \sigma^2(R_i) + \sigma^2(\mathrm{S}_{il}) \right)$$

Simplify equation (3.19) and take the square root to get the standard deviation for the figure of merit.

$$\sigma(\mathrm{FOM}) = 2 \sum_{i=1}^{N} \left(\alpha^2{}_i \frac{(\beta R_i - S_{il})^2}{\beta^2 \sigma^2(R_i) + \sigma^2(S_{il})} \right)^{1/2} . \qquad \textbf{(3.20)}$$

Equations (3.14) and (3.20) give the figure of merit (FOM) and its standard deviation.

A normalization factor was proposed to enhance the span of the FOM values; in equation (3.14), let the response R_i equal to zero, the resulted $FOM|_{R_i=0}$ is then used as a normalization factor for the FOM.

$$NORM = \sum_{i=1}^{N} \alpha_i \frac{(S_{il})^2}{\sigma^2(S_{il})} \qquad \textbf{(3.21)}$$

The FOM and the standard deviation after normalization will be

$$FOM\big|_{norm} = \gamma \left(\frac{\sum_{i=1}^{N} \alpha_i \frac{(\beta R_i - S_{il})^2}{\beta^2 \sigma^2(R_i) + \sigma^2(S_{il})}}{\sum_{i=1}^{N} \alpha_i \frac{(S_{il})^2}{\sigma^2(S_{il})}} \right), \qquad \textbf{(3.22)}$$

and

$$\sigma(\mathrm{FOM})\big|_{norm} = 2\gamma \frac{\sum_{i=1}^{N} \left(\alpha^2{}_i \frac{(\beta R_i - S_{il})^2}{\beta^2 \sigma^2(R_i) + \sigma^2(S_{il})} \right)^{1/2}}{\sum_{i=1}^{N} \alpha_i \frac{(S_{il})^2}{\sigma^2(S_{il})}} . \qquad \textbf{(3.23)}$$

where γ factor was added for scaling purpose, for instance when γ is equal to 100, this gives a FOM range from zero up to ~100 in most of the cases; in this work we used a value of 500.

For target materials under interrogation that have responses close to the template responses, the FOM gives a small number somewhat close to unity; this indicates a dangerous material. For inert materials, the responses are far from the template values, which imply higher FOM values. The value of FOM and the standard deviation of the FOM can be used to establish a suitable cut-off value for each kind of explosive or dangerous material template. An interrogated sample for which the FOM is higher than the cut-off indicates the sample may contain inert (safe) materials. Some materials may give a FOM which is over the cut-off value but within a standard deviation of it; this indicates the sample "MAY BE" contains only inert materials, but to be more certain additional tests should be conducted. A sample for which the FOM is more than a standard deviation below the cut-of value is considered a "match" and thus probably dangerous. In order to address confidence levels, the value that specifies the region occupied by a certain material on the FOM space may be stated as a filter function f *(λ)*

$$f(\lambda) = \mathrm{FOM} \pm \lambda \sigma(\mathrm{FOM}), \qquad \textbf{(3.24)}$$

where the value of λ is used to adjust the safety region, the function *f(λ)* has two boundaries $f_+(\lambda)$ *and* $f_-(\lambda)$, with center at *f(0).* Theoretically, the larger the value of λ, the higher the confidence level of the device decision. Figure 3.5 indicates different cases for the figure of merit, the first case A, the FOM lies in the safe region, however the $f_-(\lambda)$ intersects the proposed cutoff region, which implies more investigations for the case, normally by different type of scan or a direct individual intervention.

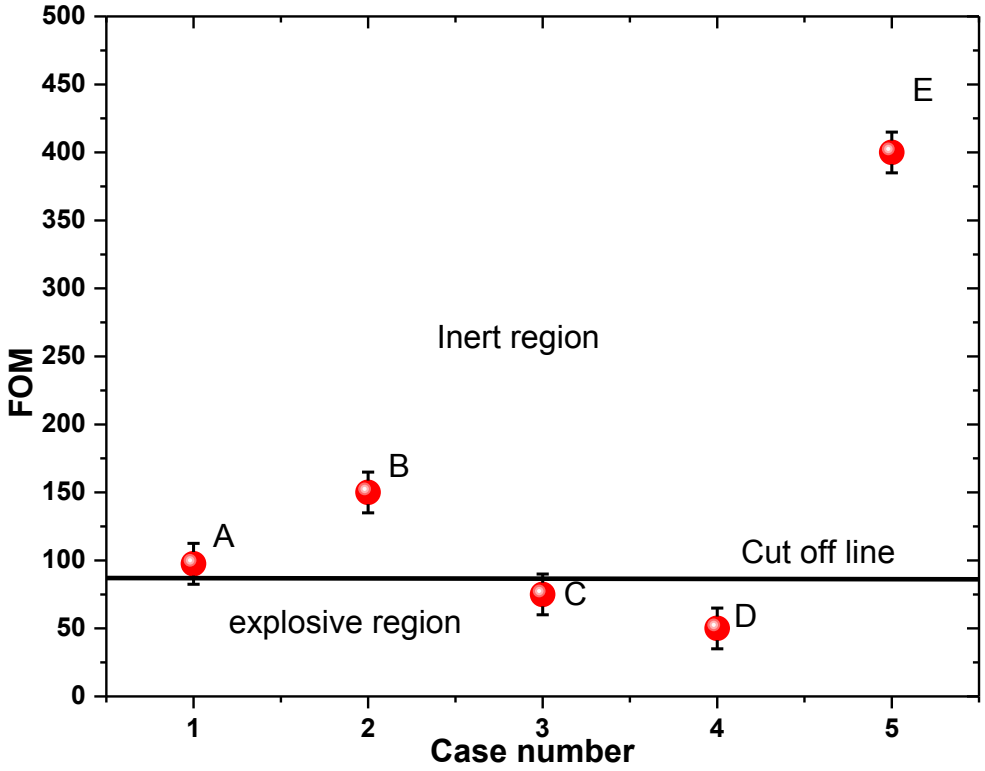

Figure 3.5 : The different cases of the FOM confidence levels.

Case B indicates an inert material with reasonable level of confidence. Case number C indicates an explosive material, but as $f_{+}(\lambda)>$ cutoff level, there may be a chance of being inert material, although, such a case requires more investigation. Case D totally lies in the explosive region, and indicates potentially dangerous material. The last case E is an inert material with high confidence level of safety. The targets in the method of SBRS are intended to be scanned in a linear raster-like pattern [144], where the templates signatures are applied at each region of scanning.

Chapter 4 - **KSU Dense Plasma Focus and Diagnostic System**

4.1 KSU-DPF

The Kansas State University Dense Plasma Focus (KSU-DPF) machine was established in early 2010 as a Mather-type geometry dense plasma focus device, see Figure 4.1. The machine serves as a non-radioactive multi-radiation source at the Department of Mechanical and Nuclear Engineering at Kansas State University.

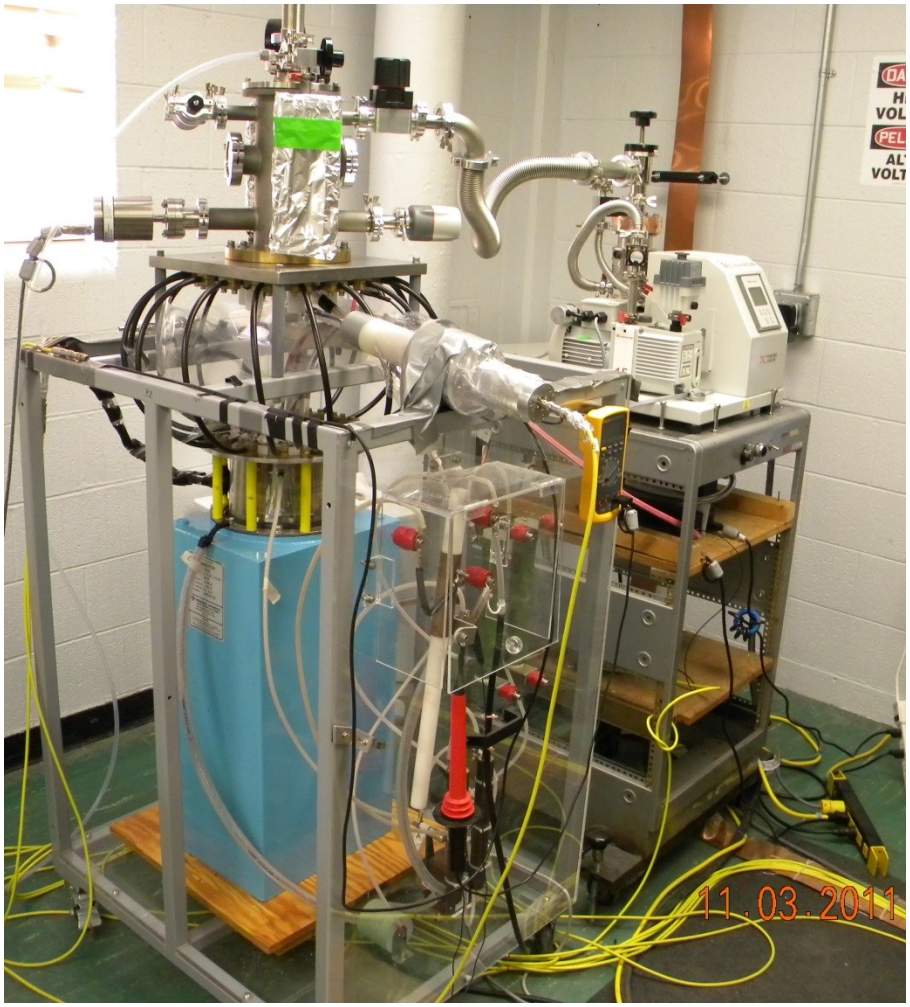

Figure 4.1: KSU Dense Plasma Focus 10 kJ machine and vacuuming system. The capacitor at the bottom is connected to the chamber through the thyratron and sixteen 50 ohm high voltage coaxial cables.

The capacitor bank comprises a General Atomics GA capacitor of 12.5-μF capacitance with rated voltage of 40 kV; the maximum stored energy of the capacitor is 10kJ. The capacitor is charged using a General Atomics power supply with rated voltage of 30 kV and 8 kJ/s. The capacitor is connected to the electrodes through a thyratron TDI1–200 k/25 kV, which acts as a fast switch (Figure 4.2) with < 3 ns jitter time. The thyratron is normally filled with deuterium or hydrogen gas, inside a ceramic body with metal connections.

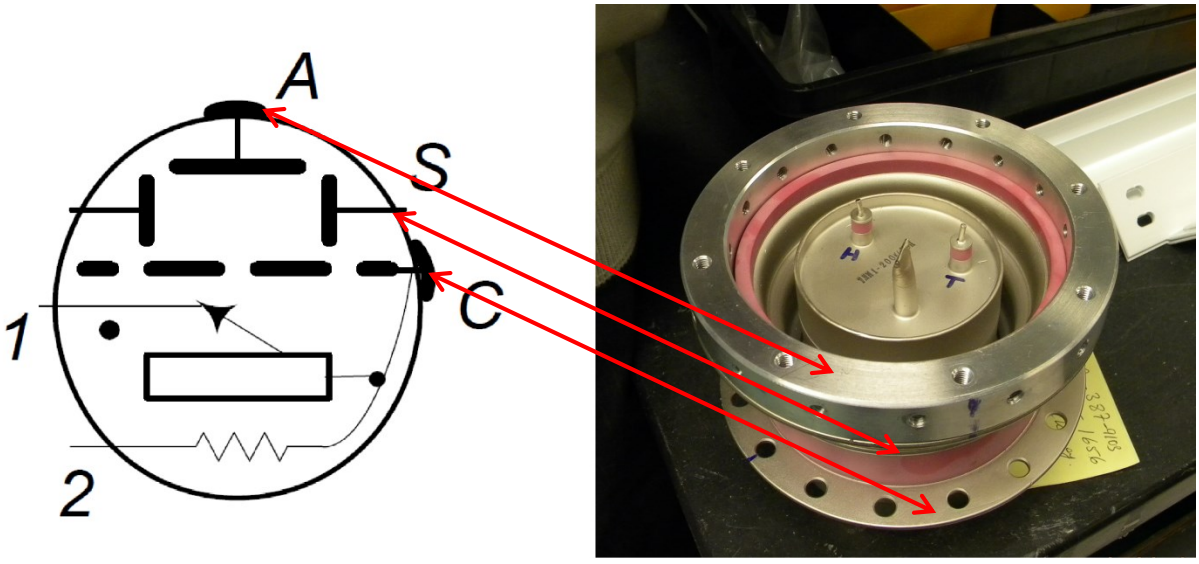

Figure 4.2: Thyratron TDI1200k/25kV, A=anode, S=screen, C=cathode, 1=T=trigger negative signal input, and 2=H=reservoir heater (R_{res}~1 ohm)

Due to limitation of the thyratron typical switch voltage (20 kV) and current (150 kA), the machine is kept working at lower energy; normally at 17 kV capacitor charge, corresponding to 1.8 kJ. The central straight anode is a semi-hollow rod with outer diameter of 15 mm at the base. Different anode configurations of different materials have been fabricated for testing machine performance, Figure 4.3. The main materials used were copper, tungsten-copper alloy, stainless steel (S.S), and graphite. Stainless steel is known as an affordable material with good electric conductivity, high melting point, and resistance to erosion. The copper material is used for its high electric conductivity and better X-ray production than stainless steel, tungsten is a

dense material with a high X-ray mean energy and intensity production, which has very high resistance to erosion and gives the high neutron production when operated as an anode [16, 145]; the tungsten is mixed with a copper in alloy to enhance the machining properties of the anode.

Table 4.1: Properties of some materials that are used for dense plasma focus anode or cathode fabrication.

Material	*Atomic number*	*Density (g/cm^3)*	*Melting point (^oC)*	*Electric conductivity (s/m)*
Stainless steel*	Cr=24, Fe=26, Ni=28	7.5	1400	1.45×10^6
Carbon (graphite)	C=6	2.2	4300	3×10^5
Copper	Cu=29	8.96	1083	5.96×10^7
Tungsten	W=74	19.35	3410	1.79×10^7
	* properties depend on the stainless steel composition			

The anode of the machine is surrounded by a squirrel-cage cathode; the cathode is made of six equally spaced brass rods at a distance of 29 mm from the center of the anode (see Figure 4.3). The anode base is insulated from the cathode by a Pyrex tube of 68-mm length and 1.6-mm wall thickness [146]. Both cathode and anode are mounted inside a stainless steel chamber of 3 mm wall thickness with two glass windows of thickness 10 mm. The chamber has multiple ports with flanges (Figure 4.1) for the vacuum pump connection, gas inlet, pressure gauges, and for test equipment.

4.2 Vacuum system

The working pressure of the KSU-DPF machine in different applications varies between 0.5 mbar and tens of mbars. To achieve this pressure, the stainless-steel chamber must be evacuated to very low pressure (10^{-5} mbar) before supplying the working gas through a fine leak valve (EDWARDS LV10K). The chamber is also evacuated through an EDWARDS Speedivalve which connects the chamber to the vacuum pumping system. The vacuum inside chamber was achieved by two-stage pumping system Edwards-TIC station; the first stage is a 435-Watt rotary backing pump model E2M1.5 that reduces the pressure from atmospheric to $\sim1\times10^{-2}$ mbar. The

second stage is a turbomolecular pump EDWARDS EXT-76DX, the turbomolecular pump can evacuate the chamber to 10^{-5} mbar. A Turbo Instrument Controller (TIC) model D397-21-000 controls the backing and turbomolecular pumps operations.

Three types of pressure gauges with different ranges measure the vacuum pressure inside the chamber. Edwards CG16K capsule dial gauge with range from 0-50 mbar gives the vacuum absolute pressure reading from atmosphere down to one mbar. An Edwards WGR-S Wide Range Gauge is connected to the pumping station; the gauge is a combined inverted magnetron and Pirani gauge in a single unit that measures to very low-pressure (10^{-9} mbar); the gauge is connected to the TIC controller to read the pressure. The third gauge an MKS Baratron capacitance manometer model 627B with absolute pressure transducer, is used to measure the working gas pressure. The gauge has a pressure range from 0.027 mbar up to 1333 mbar with an accuracy of 0.12% of the reading.

4.3 Techniques of diagnostics

The diagnostics of plasma focus requires characterizing the machine performance as a radiation source. The characterization requires measuring the electric impedance of the capacitor bank of the machine, the voltage and current at each single shot. A required measurement is the radiation emission for each shot. This includes the measurement of the electron and ion beam energies and intensities, the soft X-rays from the compressed dense plasma, the hard X-rays from the bremsstrahlung radiation of the anode material, the neutron emission (for deuterium filled gas) energy and flux density in the radial and axial directions. The diagnostic tools should be able to measure the fast event as the short lived plasma lasts for only few nanoseconds (ns) up to hundreds of ns. The diagnostic tools must be protected and shielded against the electromagnetic noise during the time of the pinch; this requires grounding and shielding procedure, using tri-axial cables rather than ordinary coaxial cables.

Figure 4.3: (Up) The machine stainless steel anode and six brass cathode rods supported on the brass base. (Down) Fabricated anodes for the KSU-DPF machine test. From the left side: Two stainless steel and copper semi tapered anodes, four Copper, stainless steel, graphite head, and Tungsten-copper (75/25) alloy straight anodes, two short semi-tapered and round head stainless steel anodes, two full tapered copper and stainless steel anodes, short straight Tungsten-copper (75/25) alloy straight anode.

4.3.1 Current and voltage monitor

The voltage and current of a dense plasma focus device characterize the behavior of the machine, provide information about the energy delivered to the plasma, and determine the speed of the axial and radial phases and the strength of the pinch. The voltage and current can be used to tell whether the machine is running normally or if there may be a failure within the electrical connections and insulation.

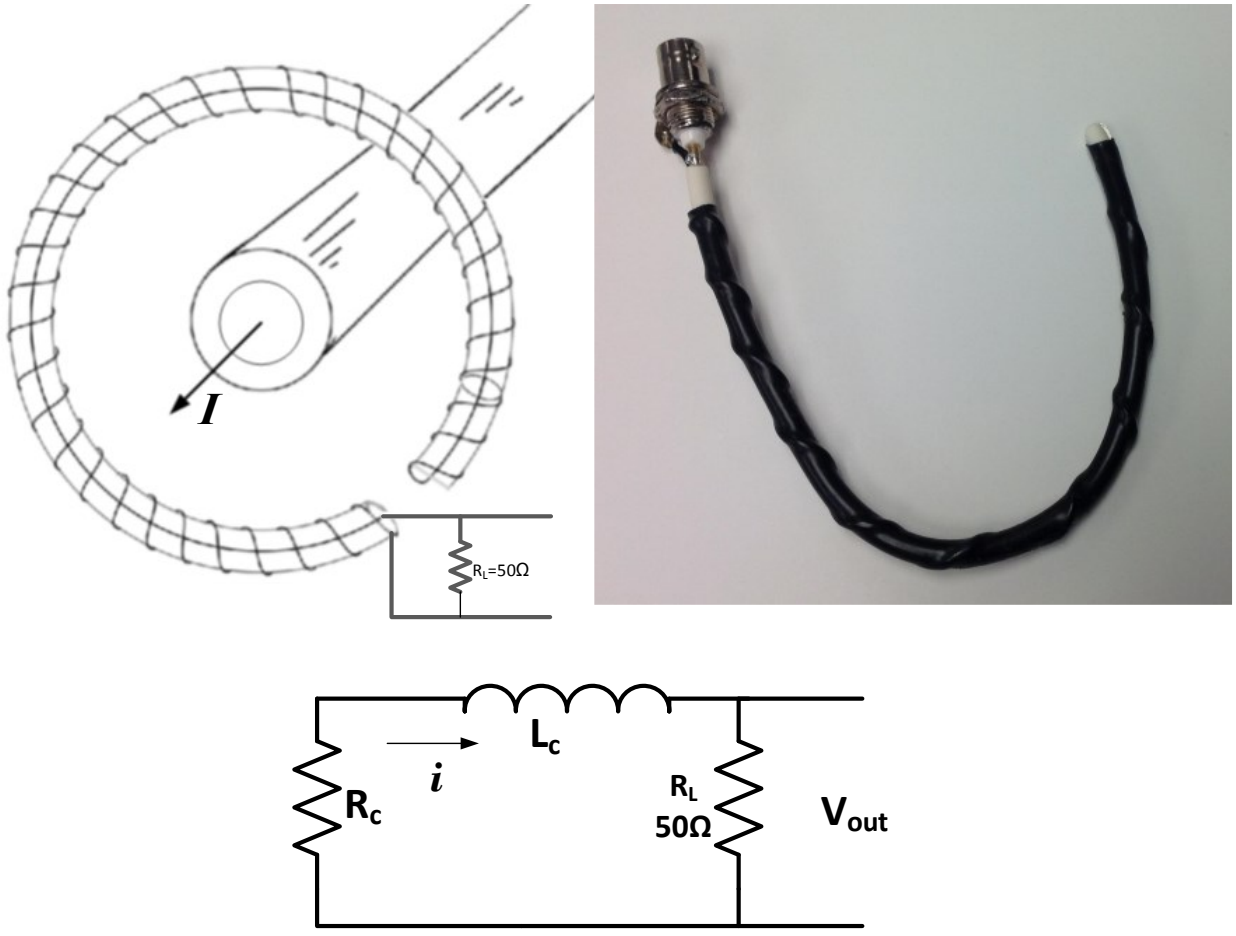

Figure 4.4: Rogowski coil, helical coil bent around a conductor to measure the current *I* passing through.

A North-Star High Voltage probe HV5 60/100 kV DC/AC 80 MHz was used to measure the voltage waveform across the tube. The current is measured using a Rogowski coil; the coil

senses the rate of change of the current in a certain conductor, the coil signal is measured over a 50-ohm resistance, (Figure 4.4). The EMF induced on the coil sides is proportional to *dI/dt*. The equivalent circuit can be described through the equation of Kirchhoff's law

$$L_c \frac{di}{dt} + R_c i + R_L i = k \frac{dI}{dt}, \qquad \textbf{(4.1)}$$

where *k* is constant.

For $L_c \frac{di}{dt} >> (R_c + R_L) i$

$$V_o = iR_L = R_L \frac{k}{L_c} I \ . \qquad \textbf{(4.2)}$$

In such a case the output voltage is proportional to the current *I* through the inductor.

For $L_c \frac{di}{dt} << (R_c + R_L) i$

$$V_o = iR_L = \frac{k\ R_L}{(R_c + R_L)} \frac{dI}{dt} \qquad \textbf{(4.3)}$$

and in this second case, the output voltage is proportional to the time change of current. The coil is used to measure the derivative of the inductor current in such case. The coil signal can be integrated either by electronic (R-C integrator) or by a numerical method. The numerical method of integration has the advantage over the electronic method to give the exact integration plus elimination of noise coming from the strong electromagnetic shock during the plasma movement in the axial rundown and the radial compression phases.

The discharge current waveform obtained from the numerically integrated Rogowski coil signal occasionally shows baseline shift. Electromagnetic pickup and power line interference are potential root causes of the baseline shift [147]; the offset could also result from grounding problems or asymmetrical topology effects with the mounting of the coil so that the coil monitors not only the current that passes inside but also the current that passes outside the coil [148, 149]. The removal of baseline shift in the current signal can be performed numerically [74].

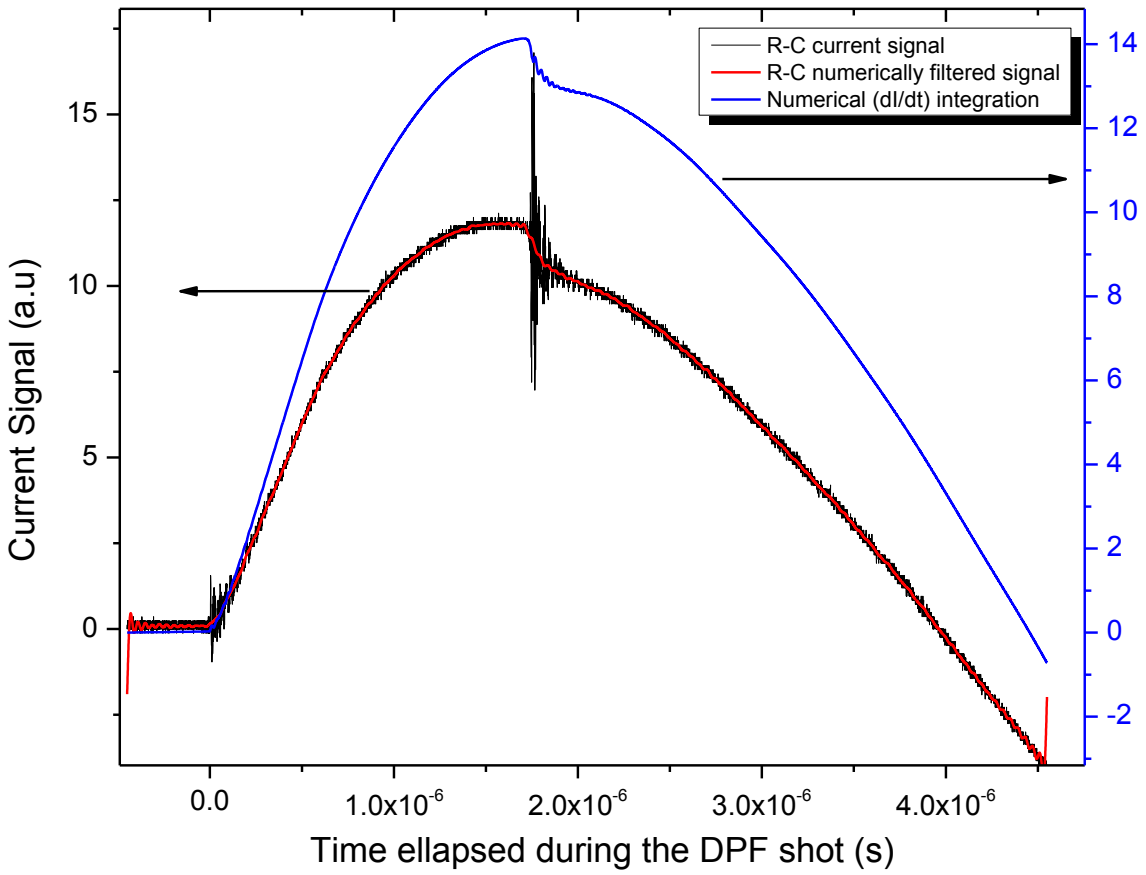

Figure 4.5: DPF current signal obtained by R-C integrator and numerical integrator.

The signals from KSU-DPF machines is recorded in a Tektronix oscilloscope model 7104-DPO that have analogue bandwidth of 1 GHz, and sample rate 5 GS/s - 20 GS/s, it can measure 25M point - 250M point in four channels. The oscilloscope is capable of integrating life signal and applying digital signal processing as well.

4.3.2 Soft X-ray PIN diode

The PIN diode has a wide area of intrinsic semiconductor material sandwiched by *p*- and *n*-doped semiconductor sides, the intrinsic area in the middle acts like an active medium that absorbs photons or charged particles and produces electron-hole pairs, producing a signal through the reversed bias potential, see Figure 4.6.

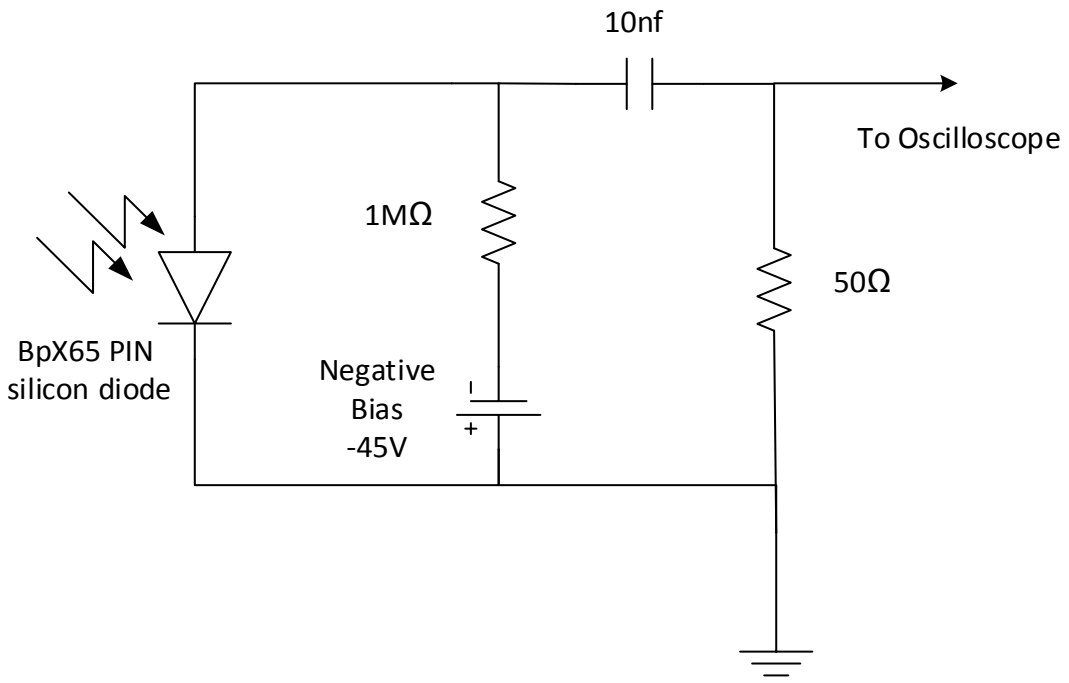

Figure 4.6: BPX-65 biasing circuit for soft x-ray detection.

The PBX-65 is a high speed, high sensitivity PIN silicon photodetector with an active chip area of 1 mm^2; the chip has a 10 μm active layer thickness with an upper dead layer of 0.5 μm. The diode has a rise time of 3.5 ns for R_L=50 ohm [150]. The protective glass of the diode can be removed and different filters can be added to obtain different photon energies. A 16 μm thick Al foil was used to cover the diode window in order to remove visible and UV light. The sensitivity of the device [151]with and without the Al foil is shown in Figure 4.7. The detector then detects low energy X-ray photons. The wide intrinsic region decreases the p-n junction capacitances, thereby increasing the frequency response of the diode. The average photon energy required to produce an electron-hole pair in a semiconductor is three times the band gap energy of the material; this energy for the PIN silicon photodiode is W=3.66 eV [152, 153] at room temperature.

The quantum efficiency of the silicon chip can be calculated as follows

$$\varepsilon_q = \frac{h\nu}{W}\exp(-\mu_{si}\,\mathrm{X}_{dead})\times\left(1-\exp(-\mu_{si}\,\mathrm{X}_{active})\right) \qquad \textbf{(4.4)}$$

,

where μ_{si} is the linear attenuation coefficient for silicon, X_{dead} and X_{active} are the thicknesses of the dead and active zones of the chip.

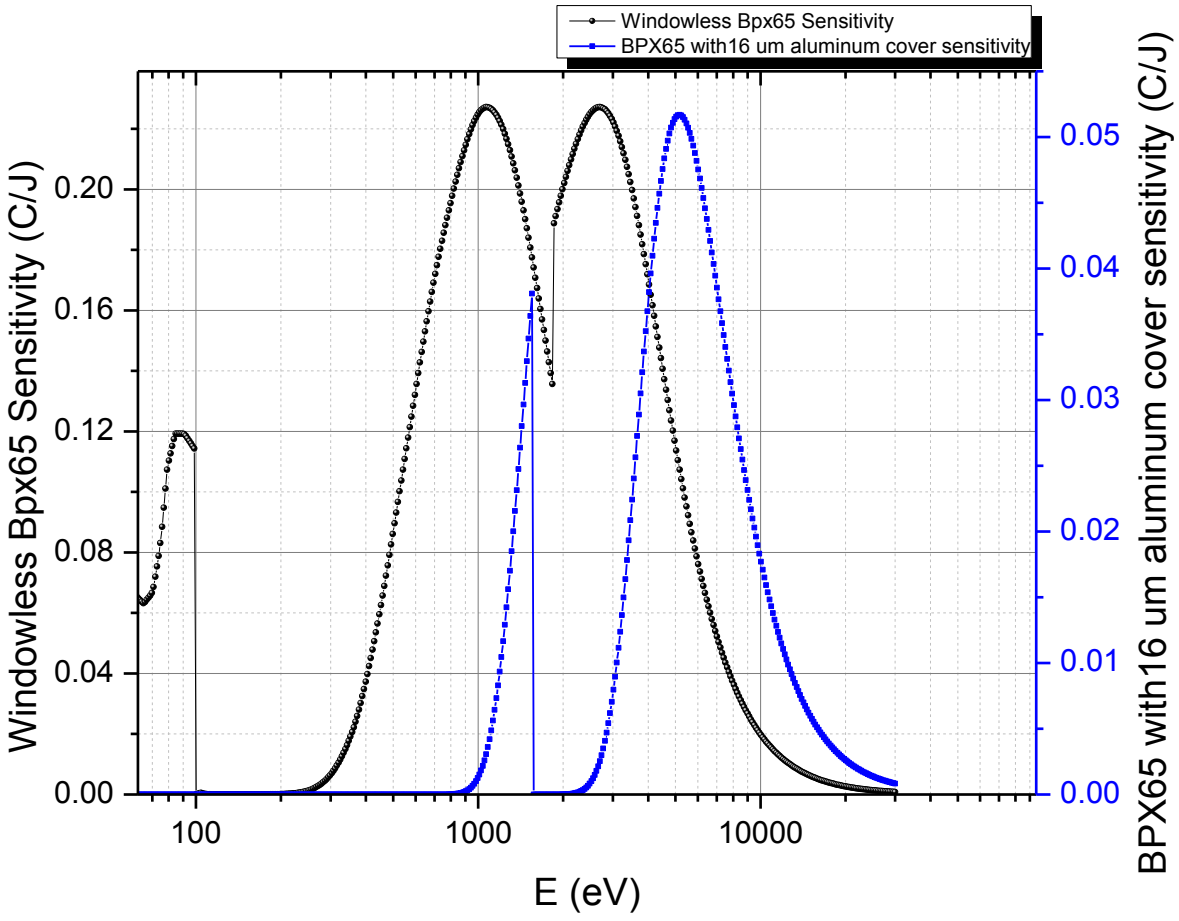

Figure 4.7: Windowless and Aluminum covered Bpx-65 sensitivity to photon energies less than 100 eV to 30 keV.

4.3.3 Ion beam detection (intensity, energy, and angular distribution)

The measurement of ion beam intensity and energy are required to characterize the DPF performance. The energetic deuterons play a big role in the neutron production of the plasma focus machines. The ion beams have various applications in plasma processing, thermal surface treatment, thin film deposition, ion implementation, etc. [154, 155]. The ion energy and intensity measurements require utilizing the time of flight (TOF) method. The method involves recording

the beginning of the ion emission, and the ion signal at a certain distance from the source. A Faraday cup is an efficient charged particle collector; and one was installed for the ion measurement purpose. An ultrafast silicon photodiode model Bpx-65 was used to record the soft X-ray signal accompanying the beginning of radiation emission.

4.3.3.1 Faraday Cup (FC)

The Faraday Cup (FC) is a diagnostic tool for charged particles; it consists of an aperture and an insulator inside a metal cover that surrounds a metal collector in the form of cup. The KSU-DPF faraday cup assembly consists of an SMA female connector, which has a center metal contact surrounded by an insulator. The contact was used as the collector. The SMA connector cap was drilled to form a centered aperture, the exposed collector area is $A = \pi(D/2)^2$, where $D=1$ mm. A copper plate in the form of quarter circle supports four FCs at 0^o, 10^o, 20^o, and 30^o degrees from the axial direction. Usage of SMA connector as a Faraday Cup ensures essentially 50-ohm impedance matching. The FC has the advantage of being a low cost ion diagnostic device with fast signal response. The disadvantage of the FC is the emission of secondary electrons due to the ion bombardment with the collector surface. The spectrum of the secondary electron emission has a peak of few electron volts and over 85% of spectrum lies below 50eV. The electron interference to the ion signal can be suppressed by a negative biased voltage to the collector [156, 157].

The ion analysis of the KSU-DPF by TOF used the Bpx-65 X-ray signal as the flight beginning signal. The FC then records the ion signal voltage as a function of time $V_i(t)$. The relation between time and energy is then used to determine the ion density as a function of ion energy or velocity. The ion energy E_i(t) can be determined from the TOF t as $E_i = 0.5mv^2$, where the speed $v = d/t$. The ion density (/cm^3) from a FC with aperture area A can be determined as follows

$$N_i = \frac{V}{R} \frac{t}{e Z A d}, \qquad \textbf{(4.5)}$$

where V is the peak voltage of ion signal, Z is the atomic number of the ion, e is the electron charge, d and t are the distance and time between the plasma focus and the FC, and R is the resistance across the voltage is measured. The total deuteron flux can be determined by integrating the ion signal over the time period of emission $\int V dt \,/\, Z\, e\, R\, A$ (m^{-2}). The ion energy distribution

can be determined by calculating the quantity $d^2N_i/dE_i d\Omega$ and plotting it versus ion energy, where Ω is the solid angle.

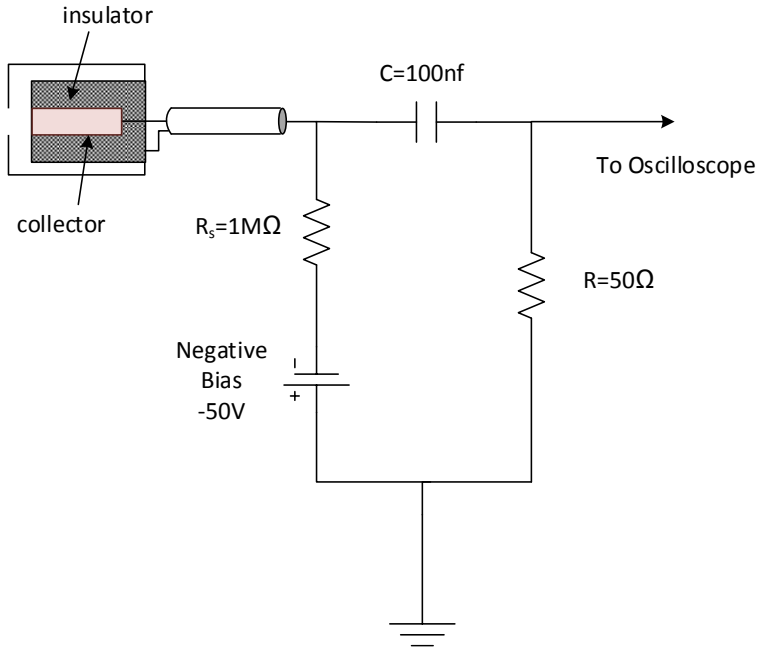

Figure 4.8: Faraday Cup circuit bias for ion measurement.

4.3.3.2 Nuclear track detector

The nuclear track detector is a transparent plastic polymer film ($C_{12}H_{18}O_7$); the charged particles or neutrons hit the film leaving traces on the film surface that can be detected under a microscope. The detector has the advantage of zero sensitivity to photons. The commercial name of the detector is CR-39 and PM355. An Alkali solution (sodium hydroxide) is used to treat the film after being exposed to radiation, hence the tracks can be shown under microscope. The track detector gives a permanent record of the radiation [48].

4.3.4 Neutron detection techniques

The plasma focus device emits a fast pulse of neutrons over a time interval of about a hundred ns. Table 4.2 shows some common detectors used for neutron detection [158]. The neutron detectors used at the KSU-DPF include the 418- plastic scintillator coupled to Hamamatsu-H7195 photomultiplier tube, BTI BD-PND bubble detector, Ludlum LiI(Eu) scintillator, and ^{3}He tube detectors.

Table 4.2: Common neutron detectors and their activation materials and efficiencies.

Detector type	*Size*	*neutron activation material*	*Incident neutron energy*	*Neutron detection efficiency (%)*	*gamma -ray sensitivity (R/h)*
Plastic Scintillator/ Liquid Scintillator	5-cm thick	^{1}H	1MeV	78	0.01
Loaded Scintillator	1.0 cm thick	^{6}Li	thermal	50	1
Methane (7atm)	5.0 cm dia	^{1}H	1MeV	1	1
^{4}He (18atm)	5.0 cm dia	^{4}He	1MeV	1	1
^{3}He(4atm), Ar(2atm)	2.5 cm dia	^{3}He	thermal	77	1
^{3}He(4atm), CO_2 (5%)	2.5 cm dia	^{3}He	thermal	77	10
BF_3 (0.66atm)	5.0 cm dia	^{10}B	thermal	29	10
BF_3 (l.18atm)	5.0 cm dia	^{10}B	thermal	46	10

4.3.4.1 Plastic Scintillator and time of flight

The scintillation phenomenon produces light with a visible or near visible wavelength when the scintillation material is subjected to ionized radiation. The medium of the scintillation detector should be transparent to the produced light wavelength. The scintillator material should have a fast decay time. The plastic scintillator is characterized by fast decay time (few nano-seconds) and low density (around 1.02 g/cm^3).

The plastic scintillator BC-418 was used for X-ray and neutron detection. The BC-418 has a Polyvinyl-toluene base ($C_{27}H_{30}$), the hydrogen-to-carbon atom ratio in the BC-418 is 1.1. Neutron detection in plastic scintillators is indirect as the neutrons have neutral charge and are not able to ionize the medium directly. The neutrons lose kinetic energy when they collide with a proton or a carbon nucleus in the scintillator medium. The recoil proton and carbon ion act as the ionizing radiation source for the scintillator. Figure 4.9 shows the results of a Monte-Carlo simulation of the recoil protons created inside a 2 inch plastic scintillator crystal. More scintillation light comes from proton ionization because the heavy carbon nuclei acquire low velocities in interactions with neutrons. The range and relative light output for protons are shown in Figure 4.10, the light output of the recoil proton is a nonlinear function, while it is linear in case of photons or electrons. The light output was measured as a function of deposited neutron energy in the crystal and fit to a quadratic function [159].

$$L = 0.036E_n^2 + 0.125E_n, \qquad \textbf{(4.6)}$$

where L is the light output in MeVee (MeV electron equivalent).

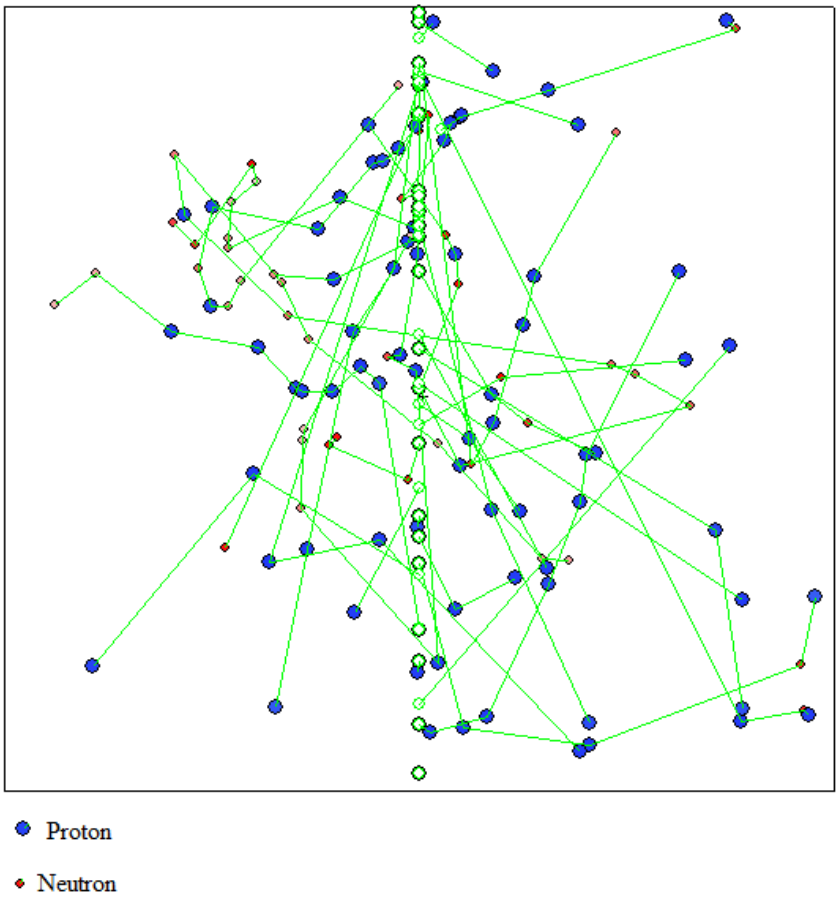

Figure 4.9: Monte Carlo simulation for neutron elastic collision and recoil protons production for 0.5MeV neutron beam in 2-inch × 1.18-inch plastic scintillator.

The light of the scintillator is converted to electrons through a photocathode at the surface of the PMT tube. The number of electrons is magnified by passing through multiple dynodes. The charge collected at the end of the PMT tube can be calculated as follows

$$Q = \frac{N\,G}{\tau_s}\exp\left(-t/\tau_s\right) \qquad (4.7)$$

where N is the number of photoelectrons at the photocathode, G is the gain of the photomultiplier (which depends on the applied voltage and number of dynodes stages), and τ_s is the scintillator time constant. The decay time constant for the BC-418 plastic scintillator is 1.4 ns. The output voltage over a resistance R from the PMT anode is

$$V_o = \frac{N e G}{\tau - \tau_s} \mathrm{R}\left(\exp\left(-t/\tau_s\right) - \exp\left(-t/\tau\right)\right), \qquad \textbf{(4.8)}$$

where e is the electron charge, and τ is the circuit time constant. The Hamamatsu-H7195 is an ultrafast PMT that is used in TOF measurements; it has a typical gain of 3×10^6 with a rise time of 2.7 ns. In the neutron TOF technique, the neutron energy is determined by measuring the flight time of a neutron through a certain distance [160]; in DPF, the pinch is used as a start time of the neutron pulse.

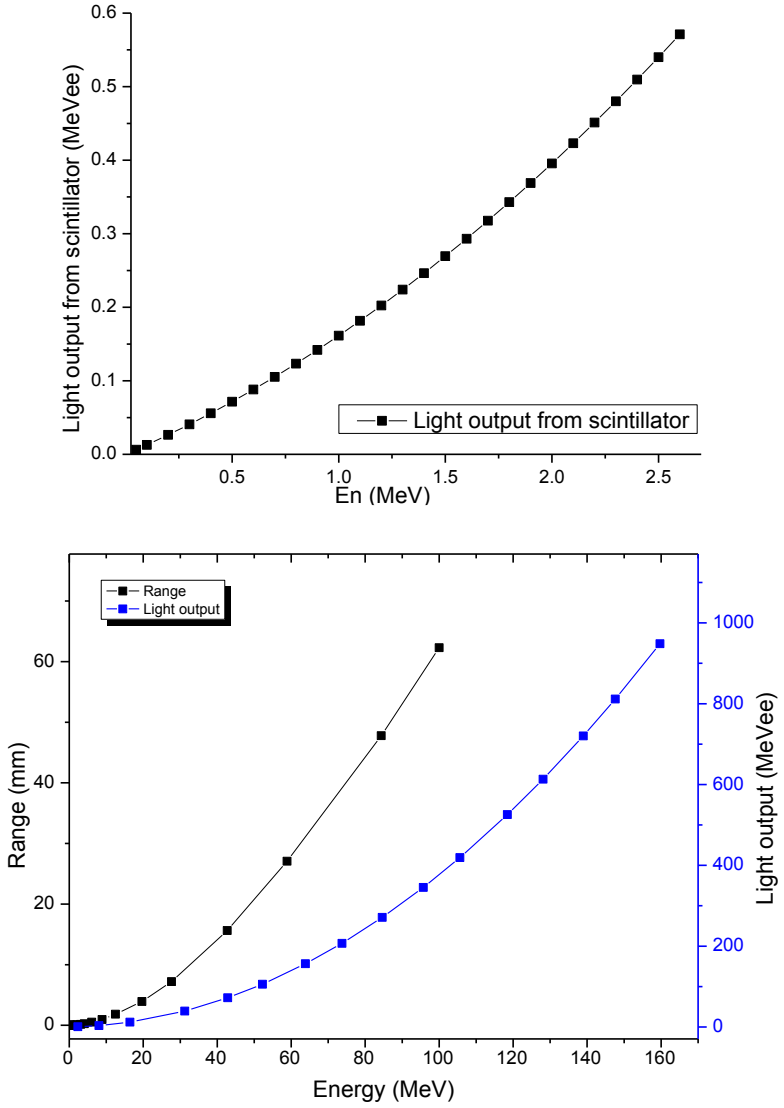

Figure 4.10: Range and relative light output in BC-418 plastic scintillator, (upper curve) from 0 to 2.5 MeV, and (lower curve) from 0 to 160 MeV.

Figure 4.11 shows signals that are used in the neutron time of flight (nTOF) technique to find the mean energy of a neutron pulse from the KSU-DPF. Two BC-418 scintillators were positioned at 5 m and 7.5 m apart from the KSU-DPF anode. The voltage spike, current dip and hard X-ray signals are shown to be synchronized together, the neutron signal comes after 230 ns, and 345 ns, respectively. The anode material in the shot was a tungsten-copper alloy, the chamber pressure was adjusted to 9 mbar of deuterium gas. The neutron energy was around 2.4-2.5 MeV.

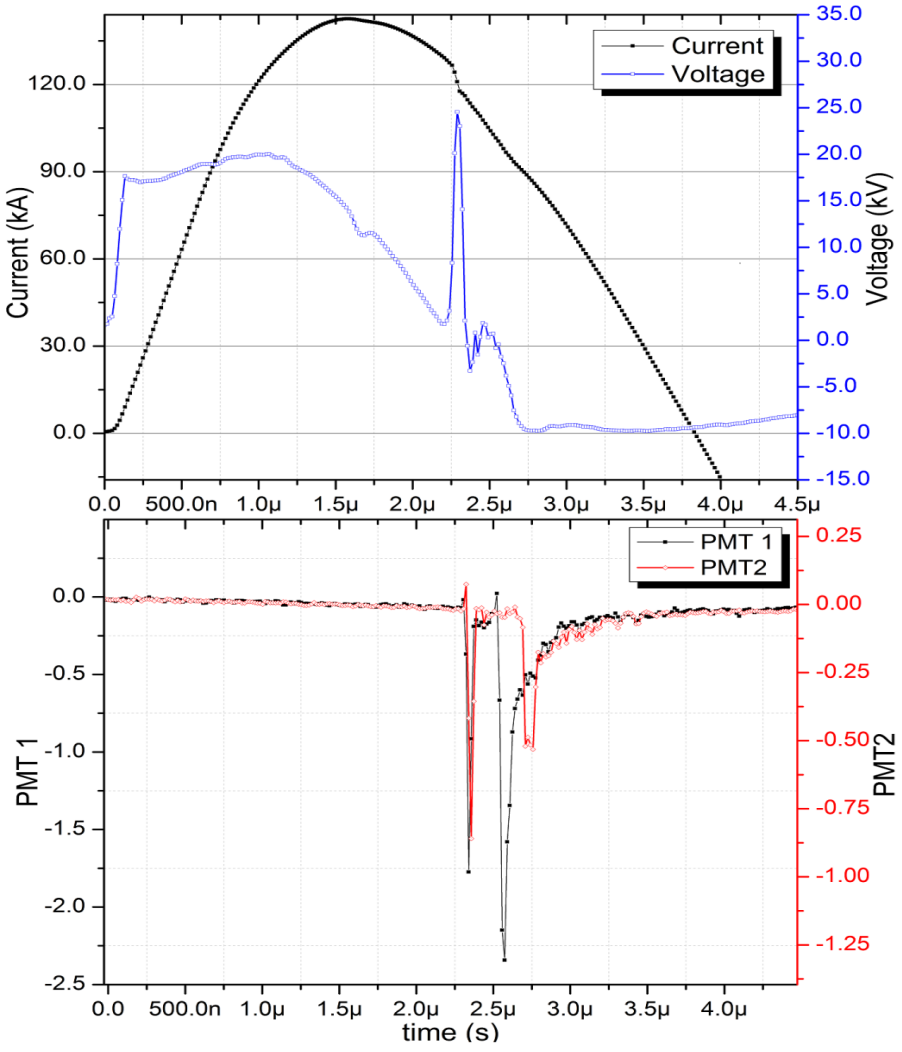

Figure 4.11: KSU-DPF shot at 9 mbar, the current, voltage, and corresponding hard X-ray (first spike) and neutron TOF pulses (second spike) between two PMTs.

4.3.4.2 Bubble detector

The bubble detector contains a droplet of superheated liquid, which is dispersed through a transparent liquid polymer [161, 162]. The bubble detectors provide instant indication of the neutron dose. Three BTI- bubble detectors model BD-PND with sensitivity 6.7 bubble/mrem, were used to characterize the neutrons from the KSU-DPF device. The detectors are 145 mm in length and 19 mm in diameter. A neutron collides elastically with a droplet, leading to instant vaporization to form a trapped bubble in the clear polymer, as shown in Figure 4.12. The neutron source strength (S_n) was calculated (assuming isotropic source) from the bubble detector set on the DPF in the radial direction as follows

$$S_n = 4\pi r^2 \times N_{bubbles} \times 1/(\text{sensitivity}) \times (1/\text{R}) \qquad \textbf{(4.9)}$$

where $N_{bubbles}$ is the number of bubbles, R is a response function, according to ICRP [123, 163], R ~ 425×10^7 mrem cm^2/neutron. The bubble detector was fixed at 17.5 cm apart from the anode, so $S_n = 1.35\times10^7 N_{bubble}$.

Figure 4.12: BTI neutron bubble detector of 6.7 bubble/mrem; the figure shows the detector before and after irradiation.

The bubble detector can be reset easily by applying a light pressure to the inside liquid by the detector cap for about 30 minutes. Unlike other detection devices, bubble detectors are not

affected by electromagnetics from the DPF machine during operation. Bubble detectors have the advantage of zero sensitivity to X rays and gamma rays, which may be present with the neutron radiation. The disadvantage of the bubble detector is the limited lifetime; the manufacturer recommends replacing the detector every six months or the reading may be inaccurate.

4.3.4.3 ^{6}LiI scintillator detector (Bonner sphere neutron detector)

Highly enriched ^{6}LiI (Eu) crystals have a high detection efficiency for thermal neutrons. The cross section for the ^{6}Li(n,t)α reaction is 955 barns with 4.78 MeV kinetic energy for the triton and alpha particle. The high detection efficiency makes the ^{6}LiI (Eu) crystal very powerful in detecting illicit nuclear weapons by detecting ^{239}Pu, and ^{235}U [164]. For fast neutron detection, a spherical moderator is used to slow down the neutrons to the thermal region.

KSU-DPF used a Ludlum model 464 Bonner Sphere LiI(Eu) neutron detector plus a Ludlum model 2200 reading unit was used to characterize the KSU-DPF device. Different sizes of moderators come with the detection unit. The moderator spheres contain a polyethylene material of density ~ 0.92 g/cm^3 [165]. The 4 mm × 4 mm scintillator and a magnetic shielded PMT deliver the signal to the Ludlum 2200 counter unit. The six moderators provided by the manufacturer vary in diameter, from 5.1 cm to 30.5 cm. The detector has a sensitivity of 45 cpm/mrem/hr for an Am-Be neutron source [166]. The KSU-DPF lab uses the 30.5 cm moderator sphere; it has the maximum efficiency at 2.5 MeV neutrons.

4.3.4.4 ^{3}He detector

The ^{3}He is the first (lowest mass) isotope of helium; it has one of the highest absorption cross sections for thermal neutron; the thermal absorption cross section for the ^{3}He(n, p)^{3}H reaction is ~5319 barns. Proportional counters filled with ^{3}He gas have been widely used for thermal neutron detection purposes. The ^{3}He(n, p)^{3}H reaction induces kinetic energy of 764 keV shared between the proton and triton products. A Ludlum ^{3}He model 42-30H neutron detector, which contains ^{3}He gas under pressure of 2-atm, is also used with the KSU-DPF device.
The detector uses a polyethylene moderator sphere of 25.4 cm diameter. The 42-30H detector has sensitivity 200 cpm/mrem/hr (for the AmBe source) the operating voltage is 1100 V [167].

Ludlum Inc. calibrated the ^{3}He detector and bubble detector in June 2010. The Bonner sphere and ^{3}He were cross-calibrated afterwards using the AmBe neutron source at Kansas State University Nuclear Reactor Facility to ensure their adjustment and agreement. Figure 4.13 shows the calibration of ^{3}He and Bonner sphere. The sensitivity of the Bonner sphere detector at 600 V to Cs-137 gamma source @ 100 mR/hr was zero.

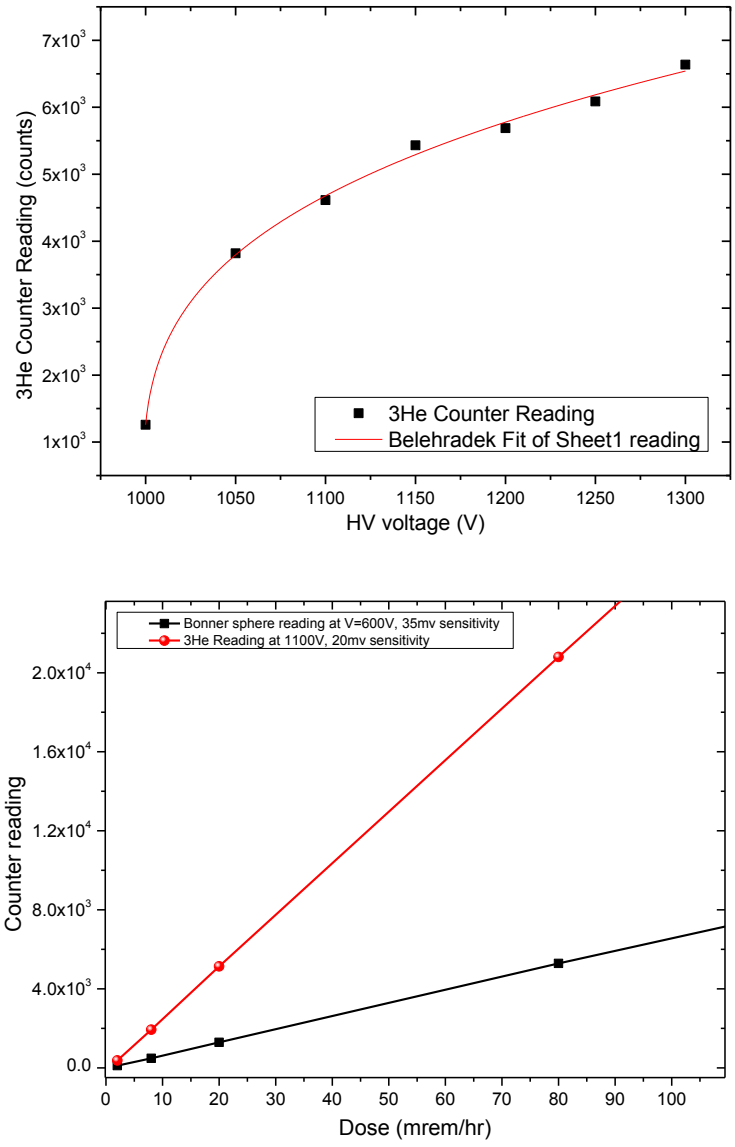

Figure 4.13: (top) ^{3}He counter reading as a function of tube voltage, (bottom) the calibration of the Bonner sphere at 600 V and ^{3}He detector at 1100 V, 60 seconds counts.

4.3.5 Hard X-ray detection

The hard X-ray energy spectrum is one of the most important characteristics of DPF machines. Hard X rays from DPF devices have many industrial applications because the pulse is short and the emission is bright. The energy spectrum depends on the anode material, the filling gas and gas pressure, and the stored energy of the capacitor [32]. The hard X-ray spectrum can be determined by a set of detectors with different filters. For a filter of thickness *d*, the intensity *I(E$_o$)* at energy *E$_o$* is calculated from $I_i(E_o)/I_0(E_o)=\exp(-\mu_j(E_o)\times d_{i,j})$, where the subscript *i* denotes the filter thickness and the subscript *j* denotes the material and μ is the linear attenuation coefficient[168, 169]. The used detector may be a sodium iodide scintillator, a Thermo-luminesce dosimeter (*TLD*), or a conventional X-ray film. Depending on the type of the detector and purpose of experiment, the detector may record the time variation of the spectrum or only integrate the whole spectrum over the exposure time.

4.3.5.1 Filtered X-ray radiography

Radiography image can be displayed directly in digital radiography or after treatment of a film for analogue radiography. The radiography system includes a source of X rays, which in our case is the DPF, an intensifying screen that transforms the X-ray photons to a visible light photon which is efficiently detected by a film. The intensifying screen is protected inside a cassette.
The film itself often has low sensitivity (less than 1%) to the X-ray photons, which is the reason for the intensifying screen. Screens typically contain a high *Z* material like gadolinium Gd or tungsten W, and a visible wavelength fluorescent material, usually a rare earth element such as terbium or europium [170]. Most of the commercial green screens contains Gd2O2S:Tb, which absorbs X-ray photons and emits green light at peak of 545 nm, as shown in Figure 4.14, with 1.5 ms decay to 10% [171].
The intensifying screen thickness is set to allow efficient absorption of X-ray photons and transparency of the visible light; thick screens also lead to blurred images. The sensitivity of the film-screen couple is expressed as the exposure required to produce a density on the film of a unit after the fog level, see

Table 4.3 [172]. Manufactures also use the term "speed", which is just the inverse of the sensitivity measured in mR, [173]. The actual sensitivity of the radiography equipment depends on the X-ray energy spectrum. Figure 4.15 shows the number of visible photons generated by ionizing photons of various energies for a typical intensifier. The film density can be read by a densitometer device.

Table 4.3: Film density and corresponding transmission.

Transmittance (I_t/I_0)	*Percent Transmittance*	*Inverse of Transmittance* (I_0/I_t)	*Film Density* ($Log(I_0/I_t)$)
1.0	100%	1	0
0.1	10%	10	1
0.01	1%	100	2
0.001	0.1%	1000	3
0.0001	0.01%	10000	4
0.00001	0.001%	100000	5
0.000001	0.0001%	1000000	6
0.0000001	0.00001%	10000000	7

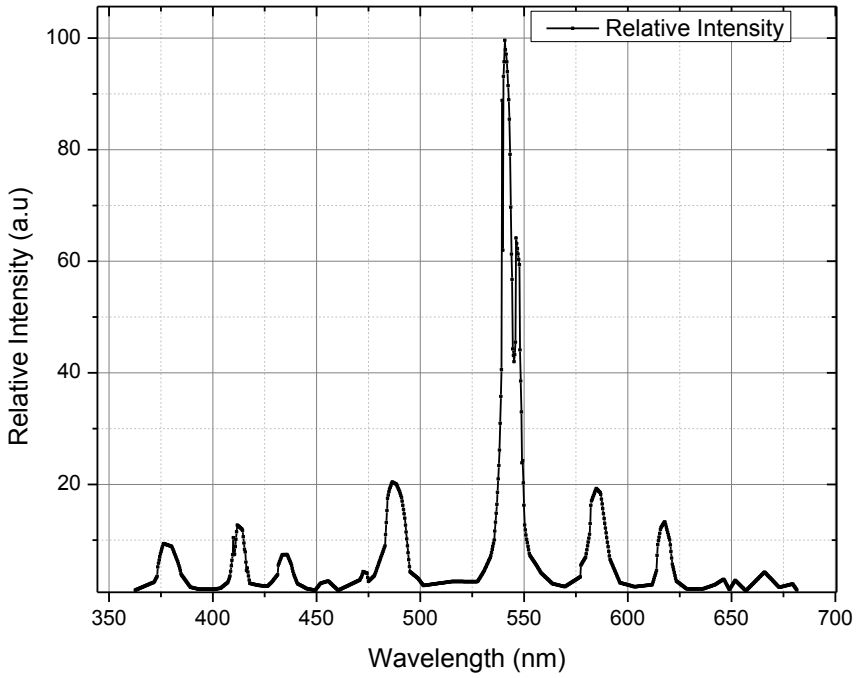

Figure 4.14: Gd2O2S:Tb Green intensifying screen wavelength emission.

The KSU-DPF experiment uses 100, 400 and 600 speed green cassettes of dimensions 8 inch × 10 inch. The manufacturer describes the cassette as Aluminum Pushbutton X-Ray Cassette w/o ID Window in combination with High Contrast Green (HR-T) 8×10 Fuji X-ray films. Densitometer X-Rite model 301 is used to read the X-ray film density. A calibrated tablet with 15 density steps (Denstep) is used to calibrate the densitometer.

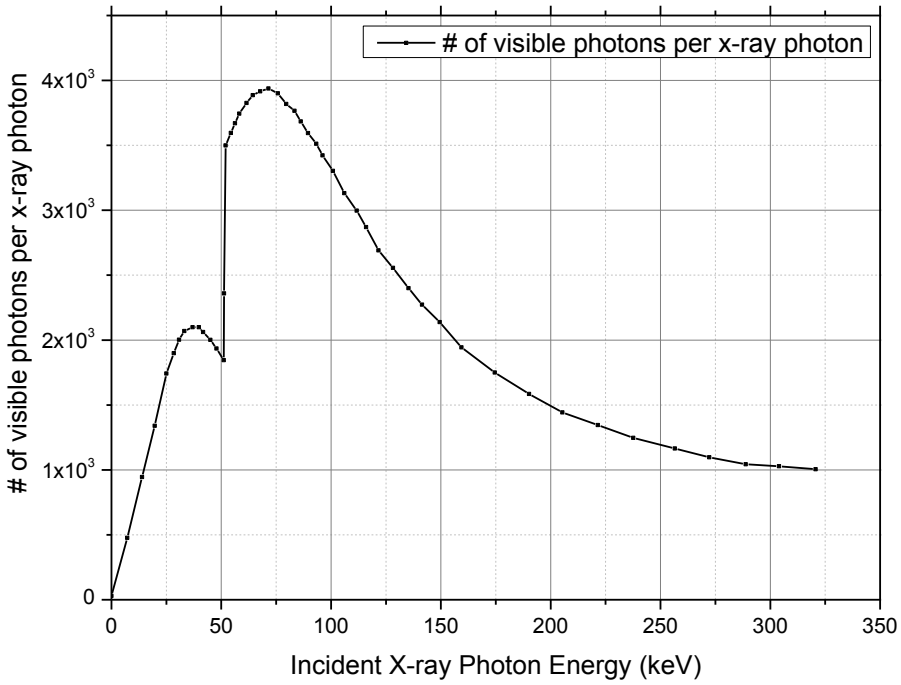

Figure 4.15: number of emitted visible photons from the Gd2O2S:Tb (GOS) intensifying screen per photon.

Assume the X-ray spectrum after the DPF window is S*(E)* , and $\eta(\mathrm{E})$ is the energy response function of the intensifying screen, namely screen conversion efficiency. Then the screen output under a filter of thickness *D* will be

$$I(D) = \int_o^\infty \varepsilon\, S(\mathrm{E})\, \eta(\mathrm{E})\, e^{-\mu(\mathrm{E})D} dE \quad , \qquad \textbf{(4.10)}$$

where ε is the X-ray photon fluence (#/cm^2) and μ is the linear attenuation coefficient of the filter material. The ratio of filtered to non-filtered screen output will be

$$R_i^j = \frac{\int_o^\infty S(\mathrm{E})\,\eta(\mathrm{E})\,e^{-\mu_i(\mathrm{E})D_i^j}\,dE}{\int_o^\infty S(\mathrm{E})\,\eta(\mathrm{E})\,dE}\,, \qquad \textbf{(4.11)}$$

where *i and j* denote filter material and filter thickness respectively. The ratio R_i^j expresses the transmission coefficient for the filter (*i,j*) [174] which is measured experimentally. Equation (4.11) is then solved numerically for the spectrum *S*(*E*).

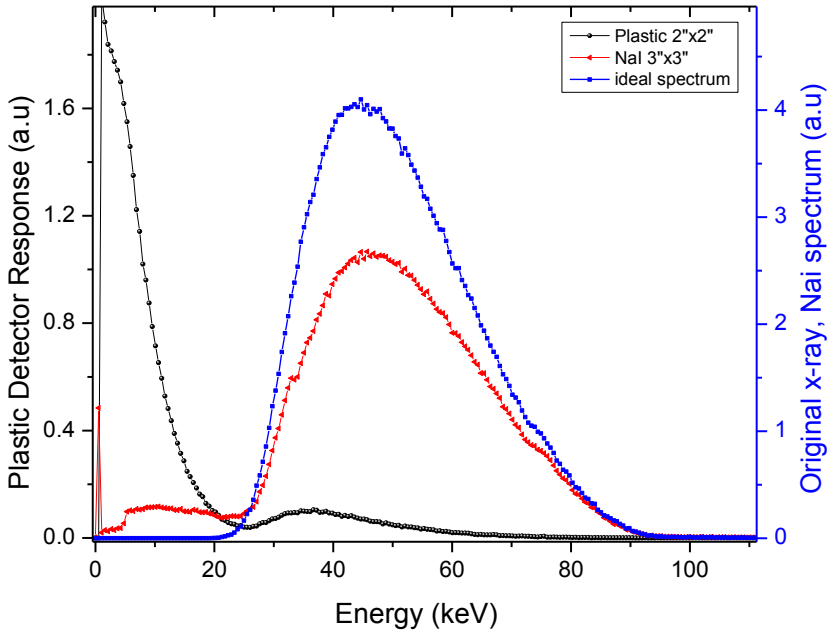

Figure 4.16: 3x3 inch NaI and 2x2 inch plastic scintillator response for an X-ray spectrum.

4.3.5.2 Gamma ray scintillation detection

The scintillation detection of x-ray and gamma ray photon is one of the most reliable detection methods. The Sodium iodide (NaI(Ti)) scintillator is one of the most reliable and commercial scintillators in the field of nuclear detection and spectroscopy. The NaI(Ti) is inorganic scintillator of high density 3.67 g/cm^3., the high Z of iodine ($^{127}_{53}I$) plus the high density of the crystal ensure high absorption for photons of tens of eV up to several MeV. Figure (5.16) shows

an MCNP comparison between a 3"×3" NaI and a 2"×2" plastic detector to detect an X-ray energy spectrum. The photoelectric cross section for the NaI is dominant up to 260 keV whereas only 20 keV in the plastic scintillator, see Figure 4.17.

The NaI(Ti) has a wavelength peak of visible light at 415 nm (blue-violet region) and high refractive index 1.85. The visible light yield is $38{,}000$ photon/MeV of x-ray/gamma ray photon. It has decay time of 230 ns at room temperature. Similar to the plastic scintillator, equation (4.8) describes the voltage output of the PMT connected to the scintillator.

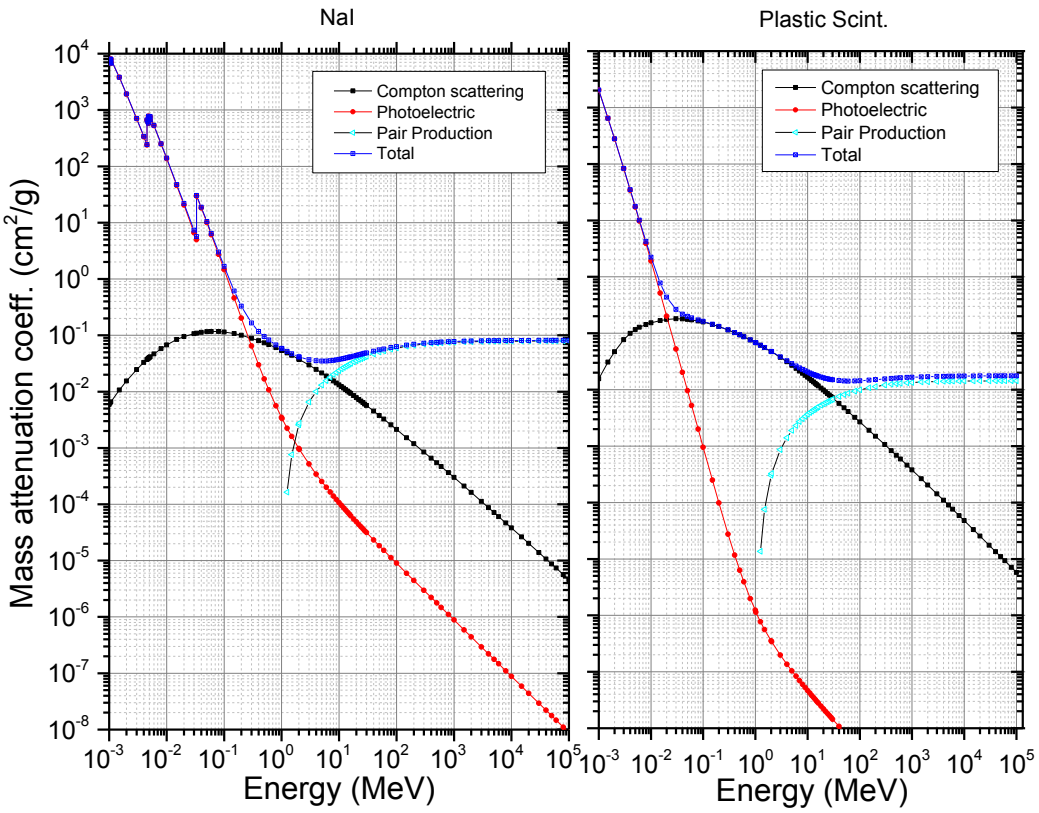

Figure 4.17: Mass attenuation coefficients for the NaI and plastic scintillator materials.

Canberra model 802 is a 3×3 inch NaI(Ti) scintillator combined with ten stages PMT is used for x-ray /gamma ray analysis for the DPF radiation. The preamplifier of the unit, model 2007P was replaced by an RC circuit to decrease the time response of the unit. A ceramic capacitor of 100 nF and a resistance of 50 ohm were used for that purpose, the PMT is working at HV supply of 700-1000 V.

Chapter 5 - **Experimental Work**

5.1 Introduction

The experimental research using the KSU-DPF device is discussed in this chapter. First, tests to determine the static parameters of the machine, and the characteristics of the X-ray, neutron and ion radiation are described. Then, experimental work with the KSU-DPF for material detection using the SBRS technique is discussed.

5.2 Measurement of electric circuit parameters of the KSU-DPF

The static impedance of the dense plasma focus capacitor bank is an important parameter in determining the behavior of the current waveform supplied to the machine. Hence, it affects the neutron yield and X-ray emission of such machines [175, 176]. The KSU-DPF machine was tested to find the static electrical parameters, i.e., the resistance R_o, the inductance L_o and capacitance C_o. The dense plasma focus circuit is shown in Figure 5.1. The plasma focus electric circuit is modeled as follow

$$\frac{1}{C_o}\int_{t_o=0}^{t} Idt + R_o I + L_o \frac{dI}{dt} + R_p I_p + \frac{d(L_p I_p)}{dt} - V_0 = 0 \quad , \qquad \textbf{(5.1)}$$

where V_o is the initial capacitor charging voltage, I is the current passing through the capacitor, I_p, L_p, and R_p are the current, inductance and resistance of the tube, respectively, in which the plasma propagates. The tube is recognized as a coaxial conductor, and the inductance of the tube at the axial and radial phases are

$$L_p(z) = \frac{\mu_o}{2\pi} z \ln(b/a) \quad , \qquad \textbf{(5.2)}$$

and

$$L_p(\mathrm{r}_p) = \frac{\mu_o}{2\pi} z_a \ln(b/r_p) \quad , \qquad \textbf{(5.3)}$$

where b, and a are the distances from the center of anode to the cathode and to the circumference of the anode, respectively, r_p is the radius of the plasma column in the radial phase, and z is the length from the anode base to the plasma sheet position.

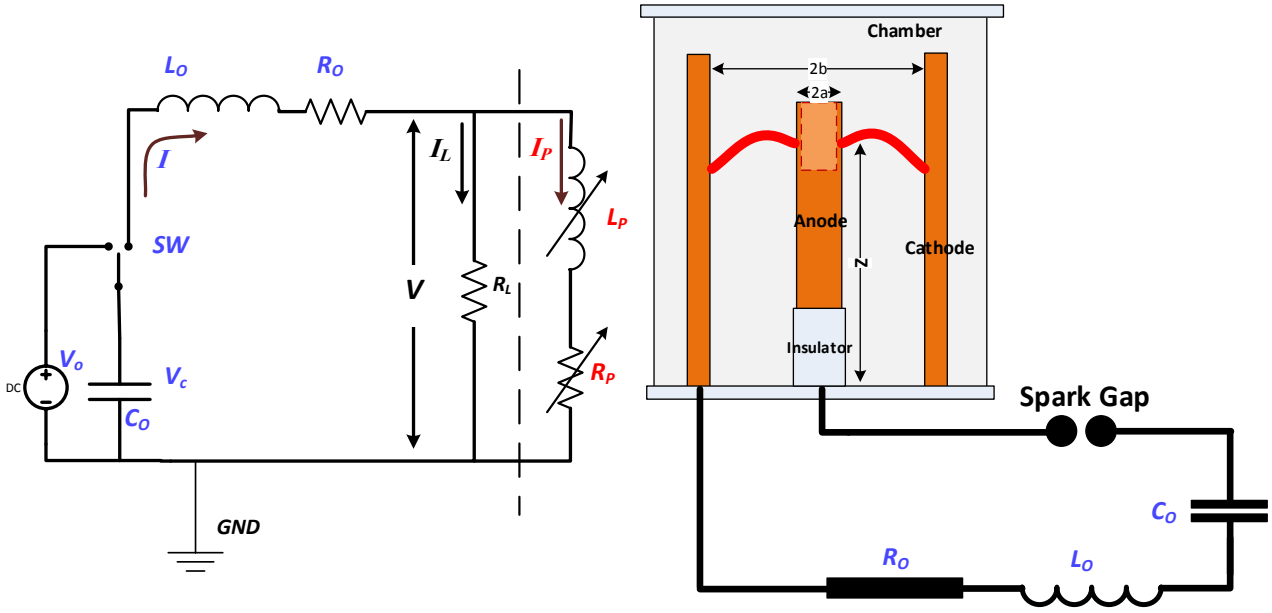

Figure 5.1: KSU Dense Plasma Focus machine connections, and electrical equivalent circuit.

5.2.1 Short circuit test

The most reliable method to determine the DPF static parameters C_o, L_o, and R_o is the short-circuit (SC) test. The calibration of the Rogowski coil is essential to find the exact amplitude of the current; the calibration procedure can be performed through fixing the Rogowski coil in a simple RLC circuit and then measuring the current through the circuit.

In the SC test, the DPF machine anode and cathode were eliminated. A metal connector was used to connect the plates of the anode and cathode, and to compensate for the impedance change due to removal of the real anode and cathode. The circuit then contains the machine capacitor plus the coaxial cables and other connections that can be described as a resistance, inductance and capacitance (RLC) in series. In the SC test, the capacitor was charged to the required voltage V_o then switched on to the circuit. The transient response of the circuit was recorded, the voltage $V_c(t)$ by the voltage probe and current $I(t)$ by the Rogowski probe. As C_o is known to be 12.5 μF,

and the charging voltage is V_o, the analysis of an *RLC* circuit was then used to determine the electrical parameters L_o and R_o adding to the Rogowski coil calibration.

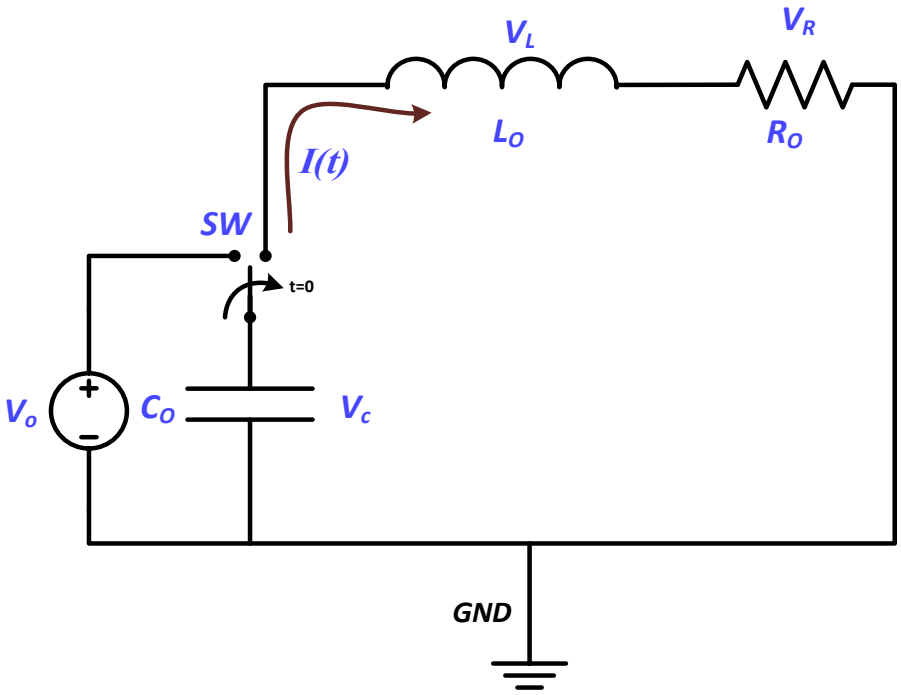

Figure 5.2: The DPF equivalent circuit for the short circuit test.

When the switch turns on, the circuit is described as

$$L_o \frac{dI(t)}{dt} + I(t)R_o + \frac{1}{C_o}\int I(t)dt = \mathrm{V} \qquad \textbf{(5.4)}$$

Differentiating the equation results in

$$\frac{d^2I}{dt^2} + \frac{R_o}{L_o}\frac{dI}{dt} + \frac{1}{L_oC_o}I = 0 \qquad \textbf{(5.5)}$$

Therefore, the characteristic equation would be

$$\mathrm{S}^2 + \frac{R_o}{L_o}S + \frac{1}{L_oC_o} = 0, \qquad \textbf{(5.6)}$$

the solution of which is

$$\mathrm{S}_{1,2} = -\alpha \pm \sqrt{\alpha^2 - \omega_d^2}, \qquad \textbf{(5.7)}$$

where α is the exponential damping coefficient $\frac{R_o}{2L_o}$, ω_d is the resonant radial frequency for the circuit $\frac{1}{\sqrt{L_o C_o}}$, and the natural angular frequency is $\omega_n = \sqrt{\omega_d^2 - \alpha^2}$. In plasma focus devices $\omega_d^2 > \alpha^2$, and the circuit goes in under-damped response, therefore the periodic time of the waveform *T* is

$$T = \frac{2\pi}{\omega_n} = 4\pi L_o \sqrt{\frac{C_o}{4L_o - R_o^2 C_o}} \qquad \textbf{(5.8)}$$

and the current *I(t)* is

$$I(t) = \frac{V_o}{\omega_n L_o} e^{-\alpha t} \sin(\omega_n t) \qquad \textbf{(5.9)}$$

.

To get V_1, V_2 … which are the positive and negative peaks of the damped current curve, the equation is differentiated with respect to time and set equal to zero. The eigenvalues of time corresponding to the peak points can be calculated to be

$$t_m = \frac{1}{\omega_n}(\beta + m\,\pi)\ ,\ m = 0,1,2,... \qquad \textbf{(5.10)}$$

,

where

$$\beta = \arctan(\frac{\omega_n}{\alpha}) \qquad \textbf{(5.11)}$$

.

From Equations (5.10) and (5.11), the first positive peak of the current signal is at

$$t_{\max} = \frac{1}{\omega_n}\arctan(\omega_n / \alpha) \qquad \textbf{(5.12)}$$

.

The static inductance can then be calculated from

$$L_o = \frac{T^2}{4\pi^2 C_o (1 + (1/\chi^2))} \qquad \textbf{(5.13)}$$

,

where

$$\chi = \tan(\beta) = \tan(\frac{2\pi t_{max}}{T}) \qquad \textbf{(5.14)}$$

.

The reversal damping ratio is $f = I_{n+1} / I_n$; hence $f = \exp(-\frac{\alpha\pi}{\omega_n})$, we can obtain a formula for the static resistance R_o

$$R_o = \frac{-\ln(f)}{\pi}\sqrt{\frac{4L_o - R_o^2 C_o}{C_o}}, \qquad \textbf{(5.15)}$$

or simply

$$R_o = 2\sqrt{\frac{L_o}{C_o}} \times \sqrt{\frac{1}{1+[\pi/\ln(f)]^2}}. \qquad \textbf{(5.16)}$$

The maximum current peak can be obtained as

$$I_o = \frac{V_o}{L_o\,\omega_d}\exp\left(-\frac{\alpha\beta}{\omega_n}\right) = V_o\sqrt{\frac{C_o}{L_o}}\,(f)^{\frac{\beta}{\pi}}. \qquad \textbf{(5.17)}$$

Equation (5.17) is used to obtain the calibration of the Rogowski coil.

5.2.2 High pressure gas test

In some cases the SC test is technically difficult to perform, especially in high current machines, so it may be preferred to perform a high pressure (HP) test to get approximate values for the static parameters. The assumption is that at high pressures, the current sheet hardly moves as the high gas density suppresses the current sheet motion; the gas density in the high pressure regime is about 5 to 30 times more than the optimum gas work density. The discharge current predominantly goes through a diffusive ohmic regime rather than an electromagnetic regime, see Figure 5.3.

Although the high pressure gas greatly slows down the motion of the current sheet, a small displacement still exists, which adds an amount of inductance and resistance to the circuit. This causes an over-estimation of the static parameters. The error in estimation was calculated from the high pressure test. In the high-pressure regime the chamber was filled with gases at high pressures in the range of 30, 40, 50, and 60 mbar. , Different gases were used e.g., argon, neon, helium, deuterium and hydrogen. The capacitor was charged to 17 kV before each shot, the anode used was copper of length 10 cm. The voltage and current were recorded on the oscilloscope for data analysis. The effect of pressure and gas were studied to determine the error propagation of calculated resistance and inductance under various working conditions.

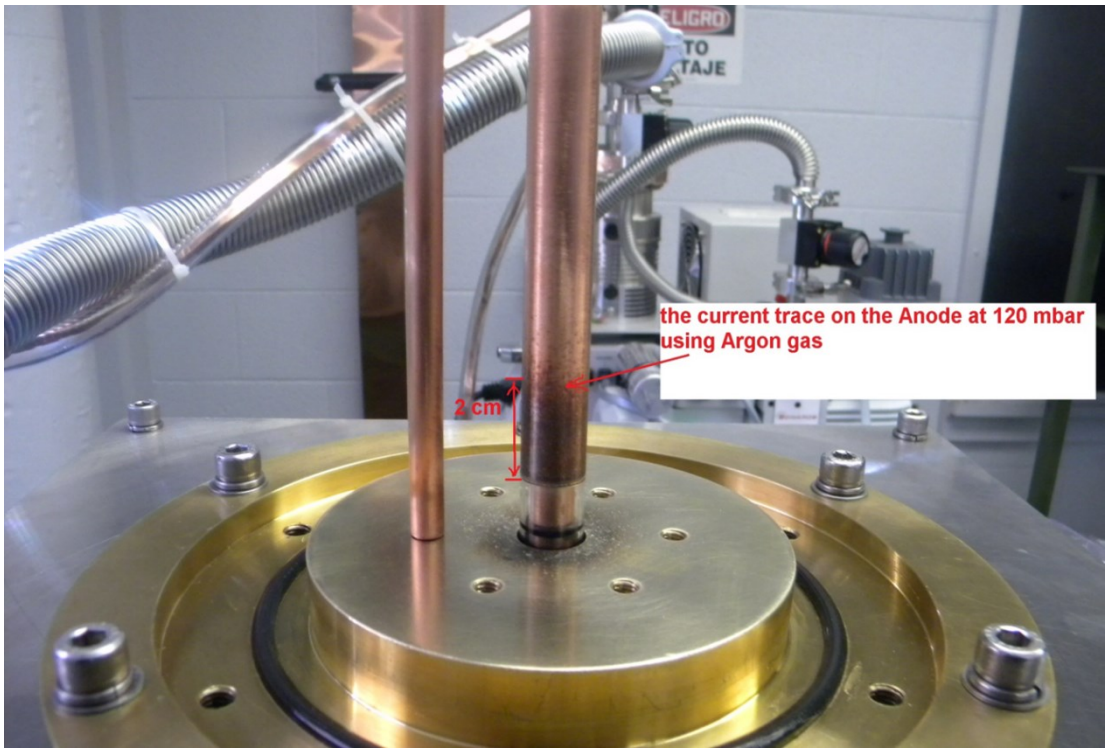

Figure 5.3: The trace of the current sheet shows diffusive discharge rather than electromagnetic mode.

The snow-plow equations were used to describe the axial motion of the current sheet and to calculate the inductance induced during the current sheet motion [18]. Assuming a one dimensional model, with a planar current sheet perpendicular to the axis of the electrodes (an approximation that is nearly true at high pressure), the change of momentum equation due to the force from $j \times B$ is

$$\frac{dmv_z}{dt} = \frac{d}{dt}\left[f_m \rho\pi(b^2 - a^2) z \frac{dz(t)}{dt}\right] = \int_a^b \frac{\mu_o (f_c I)^2 2\pi r\, dr}{2(2\pi r)^2} \quad , \qquad \textbf{(5.18)}$$

where a and b are the radii of the anode and cathode respectively. ρ is the initial density of gas, μ_0 is the permeability of the free space, f_m, and f_c are the snowplow mass swept up factor and the current factor, respectively. Therefore,

$$z(t)\frac{dz(t)}{dt} = \frac{\mu \ln(b/a)}{4\pi^2 f_m \rho(b^2 - a^2)} \int (f_c I)^2 dt \quad . \qquad \textbf{(5.19)}$$

Let $I_{norm}=I/Io$, be the normalized current waveform, integrate to find the displacement of the current sheet $z(t)$.

$$z(t)=\sqrt{2}\,U\left(\int\left(\int I_{norm}^2 dt'\right)dt\right)^{1/2}, \qquad \textbf{(5.20)}$$

where U is the characteristic axial transient speed

$$U=\sqrt{\frac{\mu\ln(b/a)(f_c I_o)^2}{4\pi^2(f_m\rho)(b^2-a^2)}}. \qquad \textbf{(5.21)}$$

Then the axial speed is given by

$$v(t)=\frac{dz}{dt}=\frac{U^2}{z}\int I_{norm}^2 dt\ . \qquad \textbf{(5.22)}$$

The axial position *z(t),* and axial speed *v(t),* can take the final form of

$$z(t)=\frac{U}{2\alpha(\alpha^2-\omega^2)}\begin{pmatrix}\alpha^4 e^{-2\alpha t}(1-\cos(2\omega t))+\alpha^2\omega^2 e^{-2\alpha t}(2+\cos(2\omega t))\\ +2\alpha^3\omega e^{-2\alpha t}\sin(2\omega t)+\omega^4(e^{-2\alpha t}-1)-3\alpha^2\omega^2\\ +2\alpha^3\omega^2 t+2\alpha\,\omega^4\end{pmatrix}^{1/2} \qquad \textbf{(5.23)}$$

$$v(t)=\frac{dz}{dt}=\frac{U^2}{4z(t)}\left(\frac{1-e^{-2\alpha t}}{\alpha}+\frac{\alpha e^{-2\alpha t}\cos(2\omega t)-\omega e^{-2\alpha t}\sin(2\omega t)-\alpha}{(\alpha^2+\omega^2)}\right). \qquad \textbf{(5.24)}$$

The equations (5.21), (5.23), and (5.24) show that there is still motion for the current sheet which is suppressed by the higher gas density. This motion leads to an error in the calculated values of static resistance and inductance of the machine, as it is affected by the addition of R_p and L_P.

5.2.3 Pressure scan for current characteristics

The machine was investigated to find the pressure at the time that the current sheet reaches the radial phase at maximum current value. A stainless steel (SS) straight cylindrical anode of radius 7.5 mm and 100 mm length beyond the Pyrex glass insulator was used. The anode has a hole in the top of 4 mm radius and 20 mm depth. The voltage probe and Rogowski coil were used to measure the voltage and current. The chamber was first evacuated of air, then filled with deuterium gas at pressure from 1 mbar up to 8 mbar. The capacitor was charged to 17 kV for each shot. Six shots were taken at each pressure before the chamber was evacuated of used gas and new gas was injected into the chamber for the next pressure test. In this experiment, the

current waveform was recorded by an oscilloscope; the oscilloscope data acquisition was adjusted at 500 ns/div (5 μs signal time), and 400 ps/pt. The oscilloscope trigger was connected to the output of the Rogowski coil through 50 ohm termination resistance., The oscilloscope was adjusted to automatically capture the signals when the shot starts, the data were then saved in an excel file for further signal processing. The average time of the axial phase, the time of the radial phase and the average current waveform were calculated.

5.3 Ion energy and neutron investigation

In this section, the deuteron beam energy and density were measured during the pinch time, the associated neutron emissions were measured in the axial and radial directions.
Two different experiments were performed to measure the ion energy and density of deuterons. The first experiment included fixing three ion collectors inside a stainless steel axial tube that was 60 cm long and 4 cm in diameter. A copper disk with a pinhole in the center of diameter 2 mm was supported at the bottom opening of the tube to allow the axial ion beam to pass and prevent the shock wave of the gas, and other hysteresis. A composite shape copper anode (the lower half is straight and the upper half is tapered) of 10 cm length, 1.5 cm base diameter, and 1 cm end diameter was used in the experiment. The copper anode has central hole of 5 mm diameter and 3 cm length, a Pyrex glass tube of 1.5 cm outer diameter and 1.3 cm inner diameter was used as an anode insulator.
The three ion collectors were axially distributed at 28 cm, 56 cm, and 70 cm from the top of the anode, see Figure 5.4. The first two ion collectors are hollow cylinders made of 100 μm copper sheet and have 15 mm and 10 mm diameter, respectively. The third ion collector was a copper disk of 10 mm diameter. The ion detectors were -50 V biased through an RC circuit of 100 nF capacitor, and 50 ohm termination resistance and connected to the oscilloscope. A soft X-ray (SXR) detector consisting of a windowless BPX-65 photodiode covered by a 16 μm aluminum foil sheet was placed above the anode tip, 15 cm radially apart. The SXR detector was connected to the oscilloscope through an RC circuit of 10 nF capacitance and a termination resistance of 50 ohm. The SXR, voltage, and current (dI/dt) signals were used to correlate with the ion emission. The energy of the deuterons was simply calculated from $E=0.5mv^2$, where m and v are the mass and velocity of the deuterons, respectively.

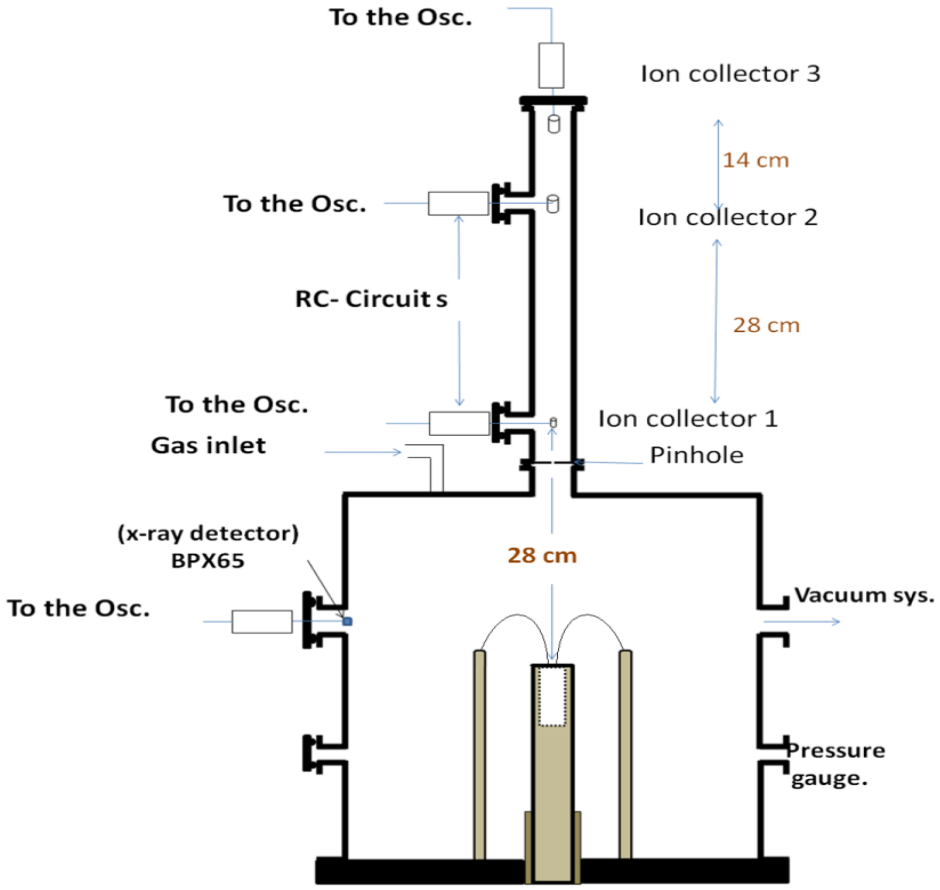

Figure 5.4: KSU dense plasma focus configuration for axial ion energy measurement by the TOF method.

The second part of the experiment was to measure the spatial distribution of the energy and density of the beam ions. For this purpose, four faraday cups (FCs) that were fixed on a copper arc support and distributed at 0º, 10º, 20º, and 30º, see Figure 5.5. The FCs assembly was fixed 14 cm from the top of the composite shape copper anode (lower half is straight, tapered from the upper half). Each FC has an aperture of 1 mm diameter that works as a collimator. The FCs were biased to -50 V and connected to the oscilloscope through an RC circuit of 100 nF capacitance, and 50 ohm termination resistance, see Figure 5.6.The negative biased voltage was connected for two purposes: to repel any electrons accompanying the ion beam and to remove the secondary electrons generated by ion beam bombardment with the surface of the FC collector. The BPx-65 photodiode was used as a Soft X-ray sensor to correlate to the beginning of the emission.

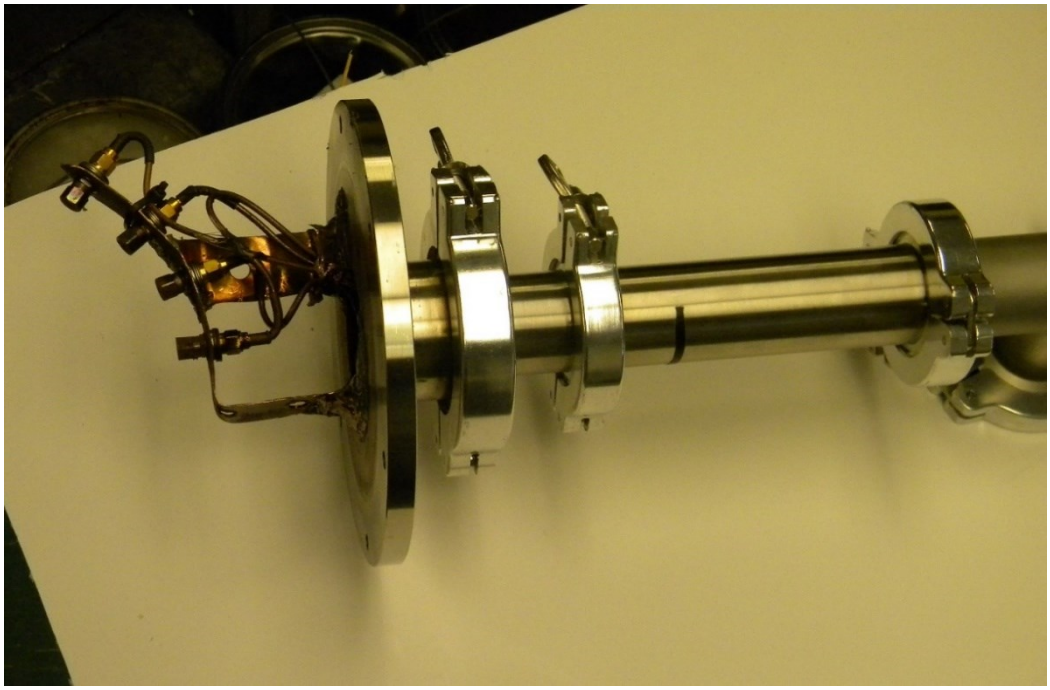

Figure 5.5: Faraday cups configuration for ion spatial distribution measurements.

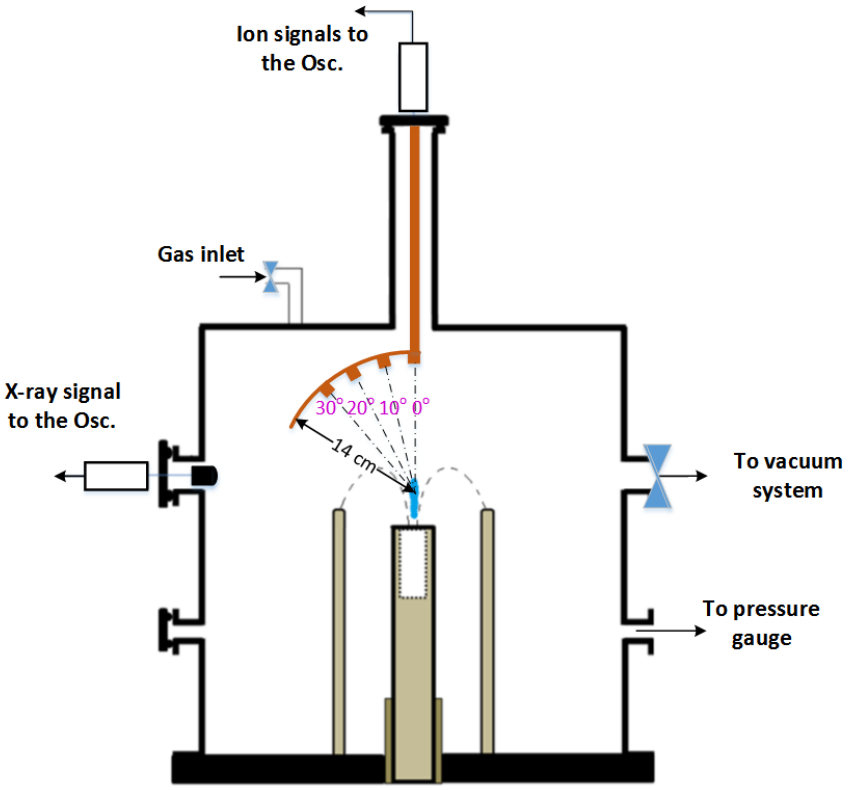

Figure 5.6: KSU dense plasma focus configuration for measurements of spatial ion energy and density distribution.

In the ion beam investigation, the chamber was evacuated through the vacuum system and filled with deuterium gas at pressures 0.5 mbar up to 10 mbar. The capacitor was charged to 17kV before each shot; six shots were taken at each pressure for statistical purposes. The associated neutron emission was measured in the axial and radial directions by a ^{3}He detector and a LiI detector with Bonner spheres of 25.4 cm, and 30.5 cm diameter respectively. The center of the LiI Bonner sphere was set 100 cm from the anode center at the same elevation level of the DPF anode tip to detect radial emission. The Bonner sphere counter model-2200 had a voltage power of 600 V, 1x gain, off window, and 30 mV threshold.

The ^{3}He detector was set on the top of the experiment, 60 cm apart from the anode tip. The ^{3}He counter model 2200 had supply voltage of 1100 V, 1x gain, off window, and 20 mV threshold. The calibration of both detectors are shown in Figure 4.13 at the theses values of adjustment. The neutron emission from the DPF machine was assumed to be at 2.5 MeV, hence a calibration factor from dose to mrem was calculated according to the ICRP [163] to be ~41.5×10^{-6} mrem cm^{2}/n. The two detectors were used to find the ratio of neutron axial and radial emission.

5.4 Hard X-ray measurement

This section focuses on investigating the hard X-ray capabilities as a fast pulsed X-ray source and the X-ray spectrum from the electron beam bombardment with the anode material. X-ray filters of different materials (copper, lead, aluminum, and cadmium), with different thicknesses were used in front of an X-ray film. The step filters used are shown in Figure 5.7, the number of steps and thicknesses are indicated in to read the film image after treatment.

Table 5.1. The step filters were supported on a Fuji 8"×10" Speed-100 intensifying screen, a high contrast Fuji HR-T-Green film was used to record the X-ray image. A certified denstep of 15 steps was attached with the film inside the screen to calibrate the film image. A calibrated densometer X-Rite model X-301 was used to read the film image after treatment.

Table 5.1: Filters materials and thicknesses used for X-ray spectrum construction.

Filter Material	*Step Thickness*	*No of steps*
Aluminum (Al1)	3.12mm	4
Aluminum (Al2)	1.6mm	8
Copper (Cu1)	330µm	6
Copper (Cu2)	130µm	21
Cadmium (Cd)	600µm	4
Lead (Pb)	74.2µm	12

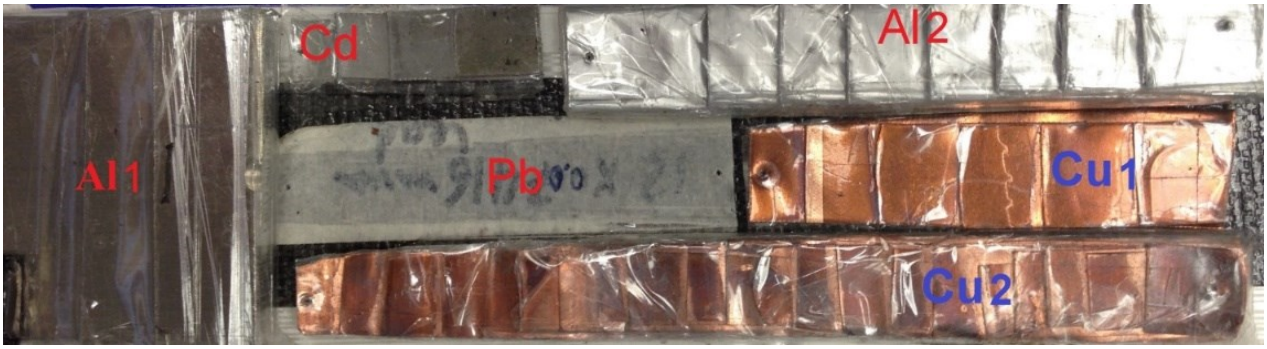

Figure 5.7: Filters used on the X-ray cassette include aluminum, copper, cadmium and lead sheets arranged in step thicknesses.

A Matlab code was written to predict the X-ray incident spectrum; a raw spectrum equation was introduced and used to substitute in the numerical form of equation (4.11) and get calculated values for R_i^j . The initial spectrum of X-ray [177] was chosen as

$$\varphi(E) = A_n \,\mathrm{Sin}\left(\frac{\pi(E - E_{\min})}{E_{\max} - E_{\min}}\right)\exp(0.03(E - E_{\min})), \qquad \textbf{(5.25)}$$

where A_n is a normalization factor for the spectrum, and $E_{\min}$, and $E_{\max}$ are the minimum and maximum energies of the spectrum, respectively. The minimum energy was estimated from the glass window shield of 1 cm thickness to be 20 keV. The maximum energy was expected to be

below 140 keV [169]. A successive iteration method was run to reduce the difference between the calculated and measured R_i^j as low as possible.

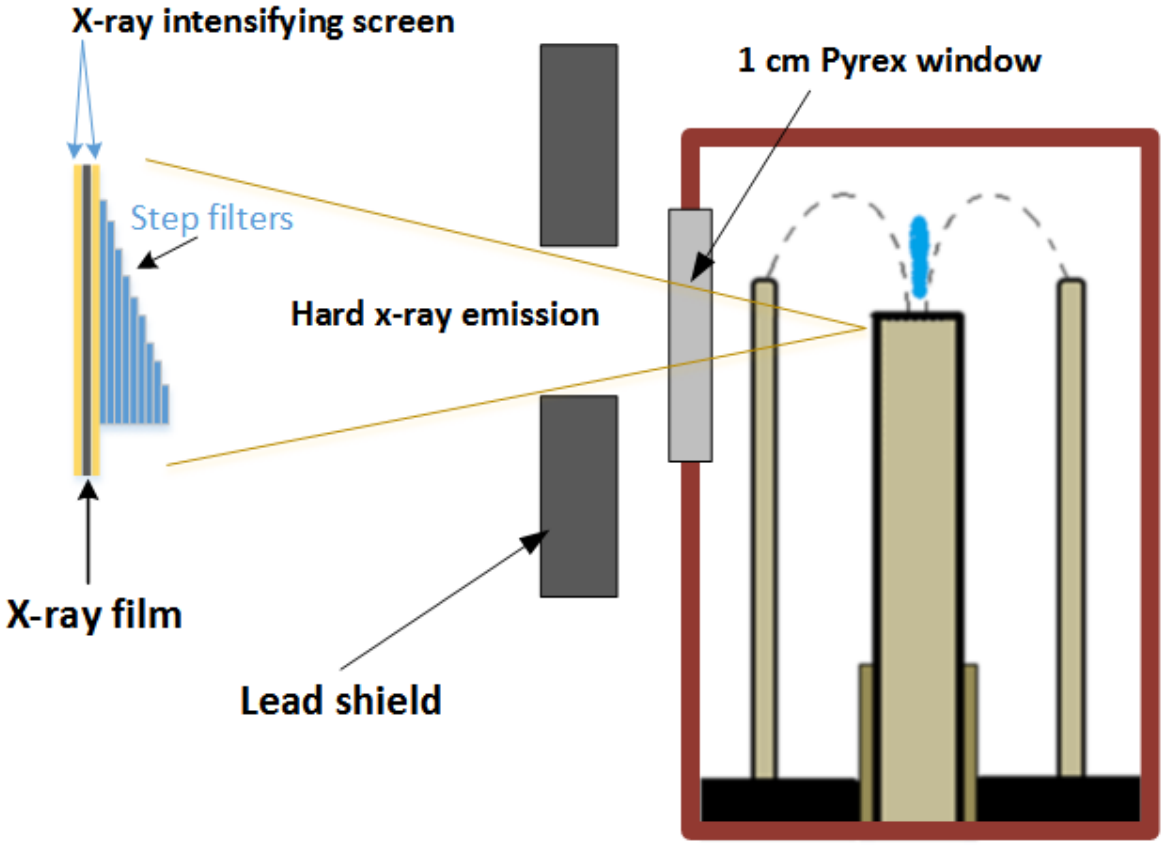

Figure 5.8: Hard X-ray spectrum measurement setup, a conventional filtered X-ray was set in front of the machine window.

For the X-ray regime, the chamber was evacuated and filled with neon gas, at 1 mbar. The copper anode was used; the anode was 10 cm long and had a 1.5 cm base with a glass insulator. The capacitor was charged to 17 kV before each shot. Lead bricks of 5 cm thickness were used to shield the DPF chamber except the glass window, as shown in Figure 5.8. The current and voltage signals were registered in the oscilloscope.

5.5 Material detection by neutron scattering

In this section the machine was used as a mono-energetic pulsed neutron source for the purpose of explosive or harmful material detection. A tungsten straight anode of length 5 cm was used. Tungsten anode was found to have higher neutron emission due to low erosion during the shot. It also has low sputtering and a high melting point. A sheet of 4 mm thickness was wrapped around the cathode and a cover sheet was set on the top of the chamber. The lead shield plus the walls of the device allow X-ray attenuation of ~ 99% at 200 keV. The chamber was shielded, except the glass window, by 12 inch successive layers of steel and high density borated polyethylene sheets (1/2 inch of steel + 2 inch of polyethylene). The Monte Carlo code MCNPx was used to study the shielding and angles of neutron elastic scattering for the neutrons. The simulation indicated that a 12 inch of shielding was able to reduce a neutron beam by more than 97%.

A previous gas pressure scan was performed from 3 mbar to 40 mbar to find the optimum pressure for the neutron emission. Ten shots were taken at each pressure for statistical evaluation. A ^{3}He neutron detector was set 1 m and 90^{o} from the anode axis to measure neutron emission, and to choose the optimum pressure for the detection experiment. Figure 5.9 shows the experimental setup of the neutron based explosive detection. The target is an iron cylindrical can which has a capacity of one gallon or five gallons. Each can was filled with different material. The can center was adjusted 45 cm from the anode, in front of the unshielded neutron source window, Figure 5.10. A Ludlum bare ^{3}He tube detector was set in front of the target to detect the thermalized neutrons scattered from the target; the tube was connected to a Ludlum counter model 2200. The counter and connection cables were shielded with aluminum foil and connected to ground to overcome noise from electromagnetic waves. The counter was reset before testing each target.

Four 2" BC-418 scintillators coupled to H7195 Hamamatsu PMTs were adjusted to detect directly emitted neutrons, and fast scattered neutrons from the target. The BC-418 is an efficient detector with 78% efficiency at 1MeV, the H7195 PMT has 12 stages of amplification, and is 6 cm in diameter. Each PMT was coupled to a high voltage power supply, ORTEC model 2592, which was adjusted at -2000V. The collection of scintillator detectors was shielded from electromagnetic waves by aluminum foil and connected to an oscilloscope through 50 ohm tri-axial cables.

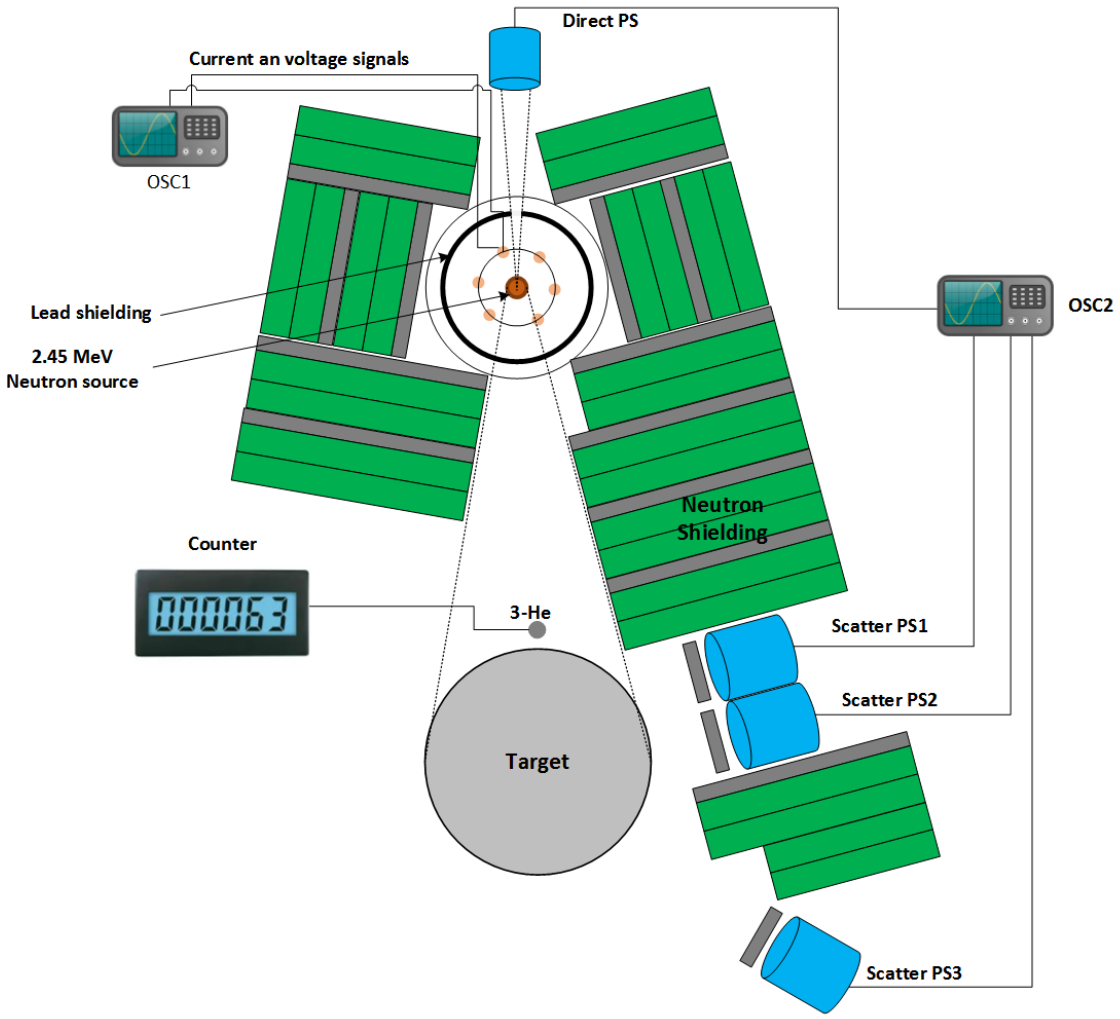

Figure 5.9: KSU-DPF machine experimental setup for material detection. The chamber is shielded by steel and polyethylene, except the target and direct plastic scintillator (PS).

Two plastic scintillators were set at 110 degree with the anode-target axis 20 cm apart from the target center to detect backscattering neutrons. One plastic scintillator was set at 70 degree and 25cm from the target center to detect forward scattering. The forth plastic scintillator was adjusted on the other side 1 m apart from the anode in case of the five gallons target and 2 m for the one gallon target experiment to detect the direct neutron emission for the purpose of shot-to-shot normalization, see Figure 5.9. The internal lead shield inside the chamber had a 10 mm

hole in front of the direct scintillator to detect the beginning of the X-ray pulse. The plastic scintillators were side shielded using 10 mm lead to reduce stray gamma-ray interference. Filters were adjusted in front of the scintillators; the first and second had 0.5 mm cadmium plus 2 mm of lead, and 2.5 cm polyethylene, respectively, and the third scintillator had 2 mm of lead shield. The forth reference scintillator had 130 μm of copper shield to allow the measurement of X-rays and neutron pulses.

Nine materials were used as targets for the five gallon cans. Three *explosive surrogates* consisted of a 35% nitrogen fertilizer denoted as Fert-A, a 28% nitrogen fertilizer denoted as Fert-B, and a 50/50 mixture of both fertilizers, known as Fert-Mix. The other targets were called *inert materials* and consisted of sand, water, chalk, rubber mulch, polyethylene and aluminum (Al). The one gallon targets included the same materials used for the five gallons, plus three extra materials consisting of ammonium-nitrate (AN) as an *explosive surrogate*, and graphite and sugar as *inert materials*. The neutron signals of the ^{3}He bare detector and the BC-418 scintillators were tested with no target to ensure that the background is below significance, and that there is no X-ray scattering that affects the detectors.

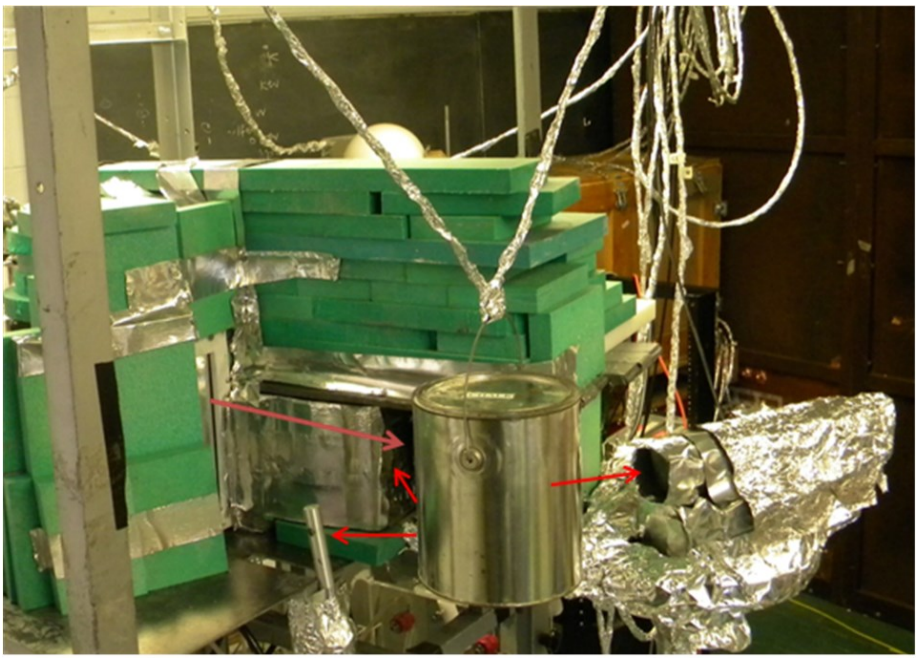

Figure 5.10: One gallon target can held in front of the DPF, three plastic scintillators and a ^{3}He tube are arranged and shielded around the target.

The plastic scintillator response to gamma rays is known to decay faster than the neutron signal, and thus the response to gamma ray photons has a narrow pulse. On average, it was found during the experiment that the FWHM of the gamma ray is ~7 ns. Those gamma photons are either stray or thermal capture/inelastic photons. Fortunately, the plastic scintillator is less efficient for the gamma rays as it contains only hydrogen and carbon, and it has a density of ~1.02 g/cm^3. The gamma photon pulse was subtracted from the neutron signal using peak recognition software and averaging techniques. The neutron signal was integrated and the area of the neutron signal was recorded for each shot. Ten KSU-DPF neutron shots were taken at each target, the results were averaged for statistical calculations. For each can size, the SBRS technique was applied, the integration of the neutron signal and the ^{3}He response were considered as target signatures. The Fert-mix was taken as an explosive template to compare the other materials and try to differentiate the other two fertilizers from the inert materials. The FOM plus error values were calculated from equations (3.22), (3.23), and (3.24) assuming uniform weight factors (equal importance of the signatures).

Chapter 6 - **Results and discussion**

6.1 Measurement of KSU-DPF parameters

This section includes the results of the short circuit and high pressure tests.

6.1.1 Short circuit (SC) results

Using the current waveform signal of the SC test, and by using equations (5.13), (5.16), and (5.17), certain parameters were determined as described in the following. The GA capacitance is known to be $C_o = 12.5\,\mu F$, and the capacitor charging voltage is $V_o = 17\,kV$. Figure 6.1 shows the current waveform during the short circuit test. The corresponding peaks (measured by oscilloscope as voltages V_1, V_2, V_3 …etc) were used to determine the reversal damping ratio.

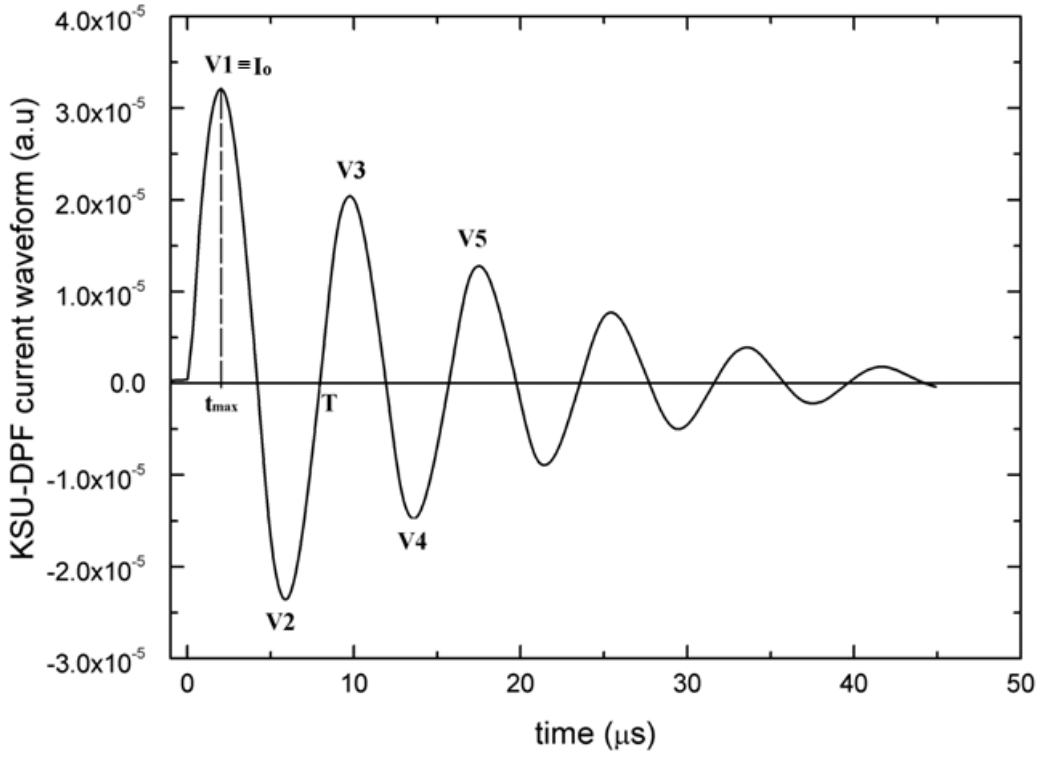

Figure 6.1: An example of the short circuit current waveform for the KSU-DPF, obtained from the Rogowski coil signal. The values of V_1, V_2, V_3 … are the current signal peaks values measured on the oscilloscope, I_o is the corresponding current peak flows through the anode.

The average reversal ratio f_{av} was determined by averaging the first five peak value ratios of the current waveform signal, as follows $(V_1/V_2+V_2/V_3+V_3/V_4+V_4/V_5)/4$. The value obtained was $f_{av} = 0.82 \pm 0.03$. The average time to reach the peak, $t_{\max}$ was $1.79\,\mu s$. The periodic time of the signal T was calculated as $6.65 \pm 0.03\,\mu s$. The values of β and χ in equations (5.11) and (5.14) were 1.64 and -33.1, respectively. The machine parameters of the KSU-DPF machine were then determined to be $L_o = 89.80 \pm 1.00\,nH$, $R_o = 10.48 \pm 0.42\,m\Omega$, $I_o = 179.32 \pm 6.98\,kA$. The Rogowski calibration factor was calculated as the ratio (I_o/V_1) (I_o is the discharge current peak value, and the V_1 is the corresponding current peak signal as measured on the oscilloscope), and was found to be $(4.95 \pm 0.08) \times 10^6$ kA/V.

6.1.2 High pressure (HP) results

The same equations as were used in the SC test were applied to the current waveform signals of the HP test for each gas. The data were compared to the short circuit (SC) static parameters. The differences in *L* and *R* were calculated as a percentage deviation of value.

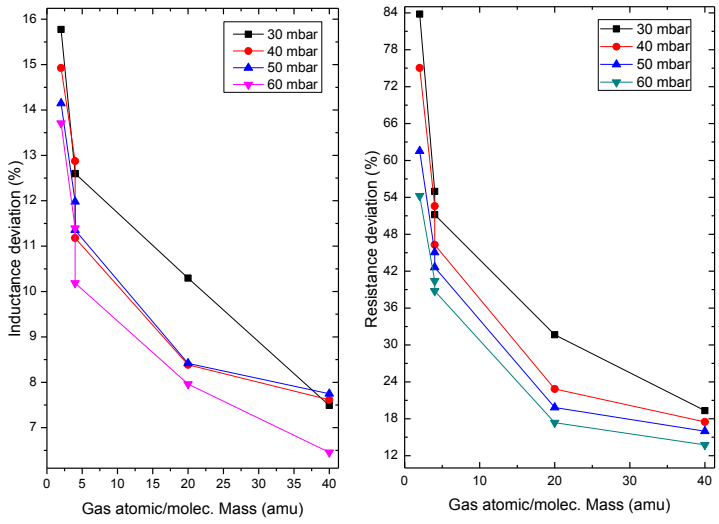

Figure 6.2: Inductance and resistance deviation of the HP test for different gases at different pressures.

Figure 6.2 shows the deviation values. The inductance shows high deviation, in excess of 15%, for low atomic/molecular mass gases; the deviation quickly decreases as atomic/molecular

gas mass increases. The lowest inductance deviation was noticed for argon gas at 60 mbar to be 6.5%. The resistance deviation shows a similar behavior with a high deviation of 84% for hydrogen at 30 mbar and a low deviation of 13% for argon at 60 mbar. The heavy gases like argon were found to give the most accurate parameters L, and R. Increasing gas pressure over 30 mbar for heavy gases gives no effective improvement of the computed static impedance. The calculations of axial position and speed of the current sheet were listed in Table 6.1. The data show that the average axial speed in argon was 0.79 cm/μs. This speed is inversely proportional to the gas atomic/ molecular mass and to the gas pressure. In hydrogen, it reaches about 1.6 cm/μs. The tube inductance that caused the deviation of the calculated inductance was calculated. The tube adds an inductance of about 7 nH at 60 mbar of argon, and more for the lighter elements reaching 19 nH for hydrogen at 30 mbar pressure. The axial motion of the current sheet (over a 10 cm straight anode of 1.5 cm in diameter) shows a motion of 2.8cm with average speed of 0.79 cm/μs for argon. Those values changes for hydrogen up to 7.4 cm with speed in excess of 1.7 cm/μs.

Table 6.1: Axial position and velocity values at different gas pressures for different gases.

Gas	Pressure (mbar)	Average tube inductance *Lp* (nH)	*Z* (cm)	Expected v ($cm/\mu s$)	Average velocity (cm/ μ s)
Argon	60	07.36	2.83	0.70	0.79
	50	08.95	3.44	0.84	
	40	08.70	3.35	0.82	
	30	08.56	3.30	0.80	
Neon	60	09.32	3.58	0.87	0.96
	50	09.91	3.81	0.92	
	40	09.85	3.79	0.93	
	30	12.22	4.70	1.13	
Helium	60	12.20	4.70	1.13	1.25
	50	13.50	5.17	1.24	
	40	13.25	5.20	1.26	
	30	15.00	5.70	1.37	
Deuterium	60	13.39	5.15	1.23	1.32
	50	14.22	5.47	1.31	
	40	14.48	5.57	1.33	
	30	15.19	5.84	1.40	
Hydrogen	60	16.70	6.43	1.52	1.60
	50	17.09	6.58	1.55	
	40	17.70	6.80	1.60	
	30	19.18	7.38	1.73	

The snow plow model was used to plot the axial position, and speed in the high pressure regime. The model equations used the current equation $I(t) = I_o \exp(-\alpha t)\sin(\omega t)$ and was compared to a simpler non-damped form $I(t) = I_o \sin(\omega t)$. Figure 6.3 shows the model output for the two current equations. The solid lines show the decayed current model and the dotted lines shows the sinusoidal current model during the first half cycle of the current waveform.

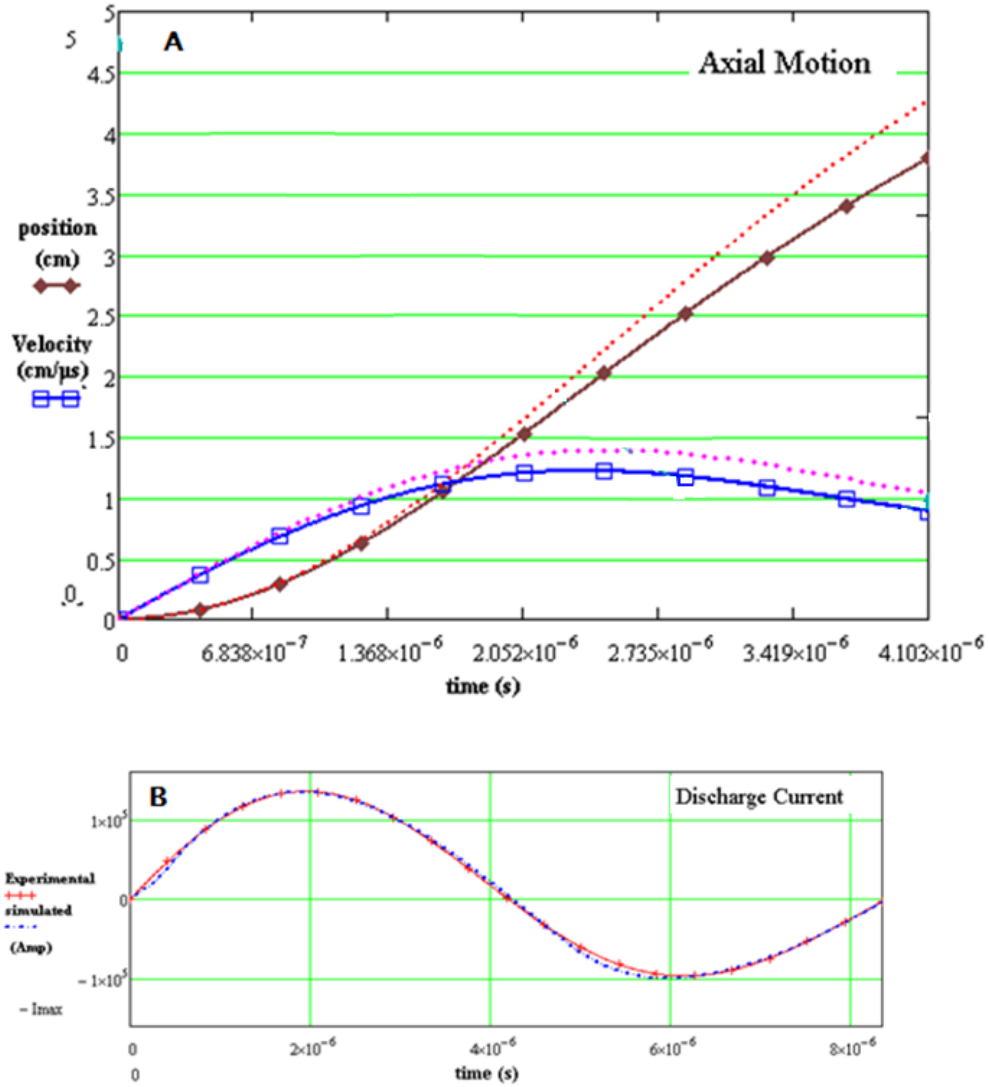

Figure 6.3: Top: the position, and velocity of the current sheet using the snowplow equations (data for neon at 40 mbar, 17kV). Bottom: the experimental vs theoretical current waveform used in the simpler model.

During the HP test, a tiny pinch was noticed in hydrogen at 30 mbar during the second half of the first cycle at 7.6 μs, where the first cycle period was 4.25 μs. This means that it took only 3.35 μs

for the second half current sheet to reach the top of the axial phase, which is a shorter time than it took at the first half. This behavior can be interpreted as follows. After the discharge current peaks and starts to drop towards zero, the tube voltage drops to zero. As the voltage drops to zero the plasma current (which is still above zero) decouples from the capacitor bank by forming a closed loop with the front end of the loop being the original current sheet and the back end being near the starting insulating end. The current of the next half cycle then starts flowing from z=0 in the reversed direction. This new and growing current sheet then pushes the decoupled current loop down the axial direction. Moreover after the first current sheet moves, it pushes the gas forward, hence rarefying the pressure behind it [178]. This low pressure allows the second half of the cycle to have a higher speed. Therefore, the second CS is running into reduced pressure gas and hence moves faster than the first CS even though the current amplitude is lower.

6.2 Pressure scan and pinch time

The most important characteristic of the machine is the current sheet behavior. It was found that the magnetic piston that pushes the gas to compress depends on the square of the current value, and determines the duration and strength of the machine radiation.

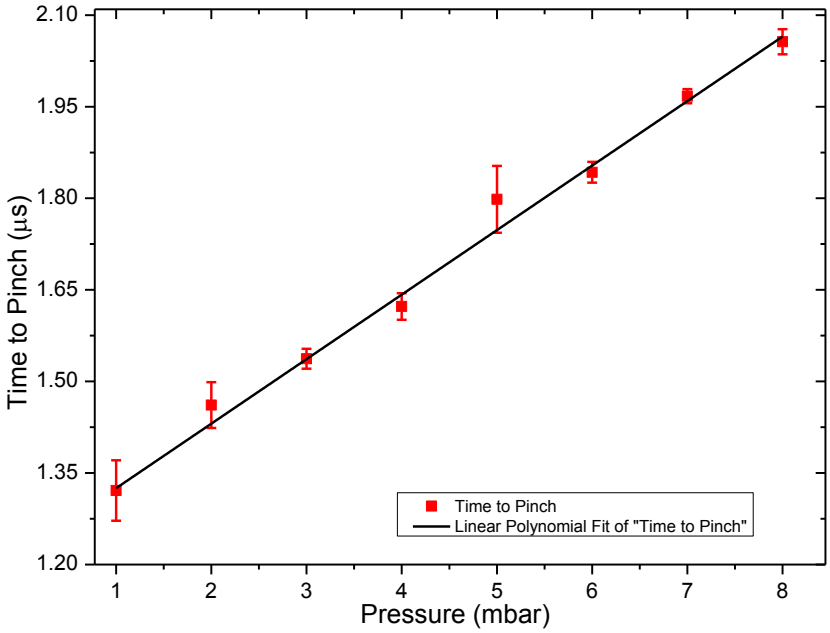

Figure 6.4: Pressure scan for time to pinch, using deuterium gas, stainless steel cylindrical regular anode.

The discharge current waveform measurement during the pressure scan of deuterium indicated details about the behavior of the machine. Figure 6.4 shows the time that the current starts to grow to the beginning of pinch. The time to pinch increases with pressure; due to the pressure increase, the density of the gas increases. Hence it takes a longer time to push the excess amount of gas at the same condition of charging voltage and anode geometry.

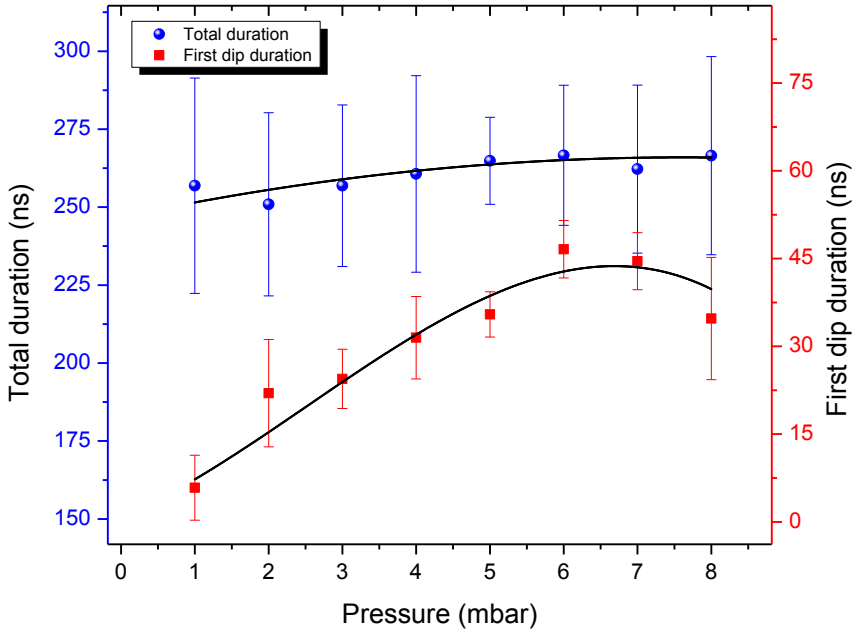

Figure 6.5: Pressure scan for the first dip duration, using deuterium gas, and stainless steel cylindrical regular anode.

The total duration of the radial phase, shown in Figure 6.5, exhibits a slight increase over the pressure range; it has an average value of 260 ns. The high inductance machine, such as the KSU-DPF, show multiple dips during the radial phase. The first dip in Figure 6.5 was affected by the pressure change. The duration of the current dip was about 6 ns at 1 mbar and gradually increased up to 46 ns at 6 mbar and then moderately decreased at the high pressure side to 34 ns at 8 mbar. This change affects both radiation strength and radiation duration of the burst. Figure 6.6 shows the change of discharge current signal over the pressure range for a 17 kV capacitor charge, while all other parameters remained constant. Each current curve is an average of six

curves at the same pressure. The graph indicates that the discharge current increased in magnitude from 1 mbar to ~6 mbar then saturated beyond that pressure. The dip also delayed with pressure increment as it took more time to end the axial phase and start the radial phase.

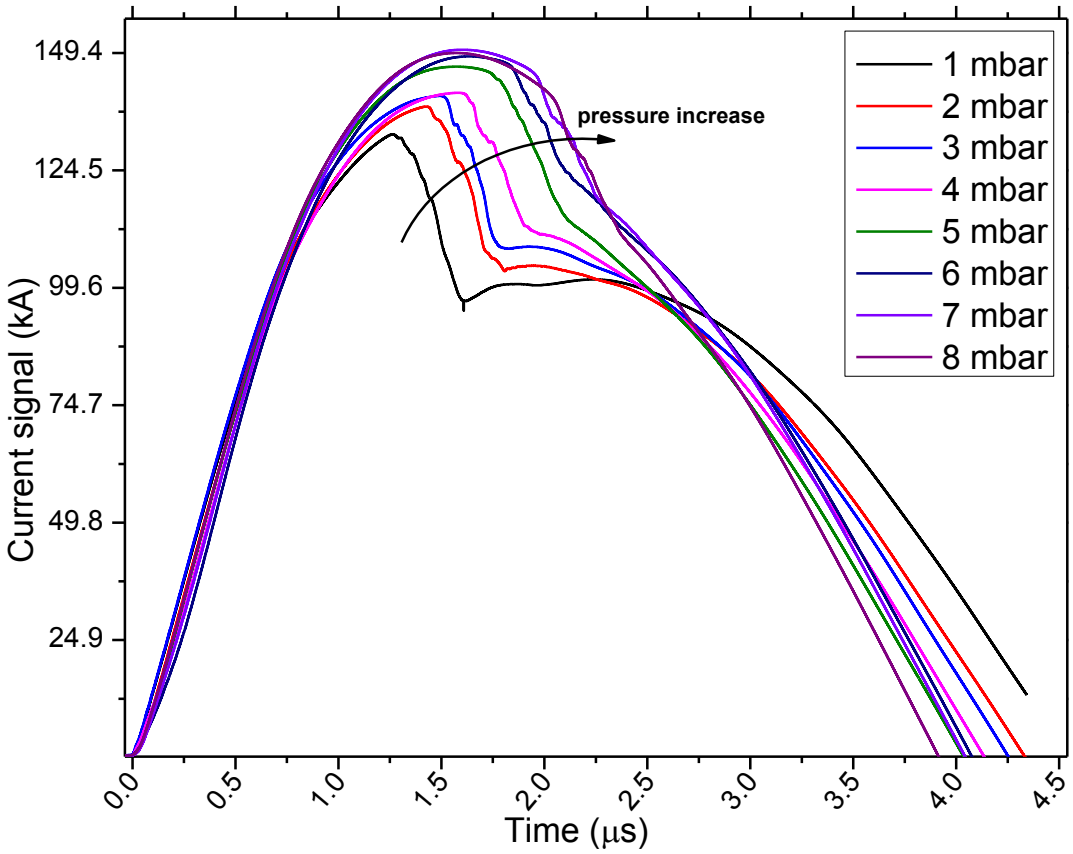

Figure 6.6: Pressure scan, current dip change with pressure.

6.3 X-ray results

The X-ray treated film was digitally scanned, Figure 6.7 shows an X-ray image for one shot from the KSU-DPF machine, with a copper anode. The film for these images was set 35 cm from the anode tip on the top of the chamber, and used an aluminum window of 10 mm width. The pictures show some electronic components, BNC connector, and staples. The resolution of the image is high enough to identify each element. The intensity of the X-ray source is shown to provide good radiographic images. The KSU-DPF machine produces X-ray pulses of tens – hundreds of nanoseconds. This short period makes the machine an excellent source for moving targets.

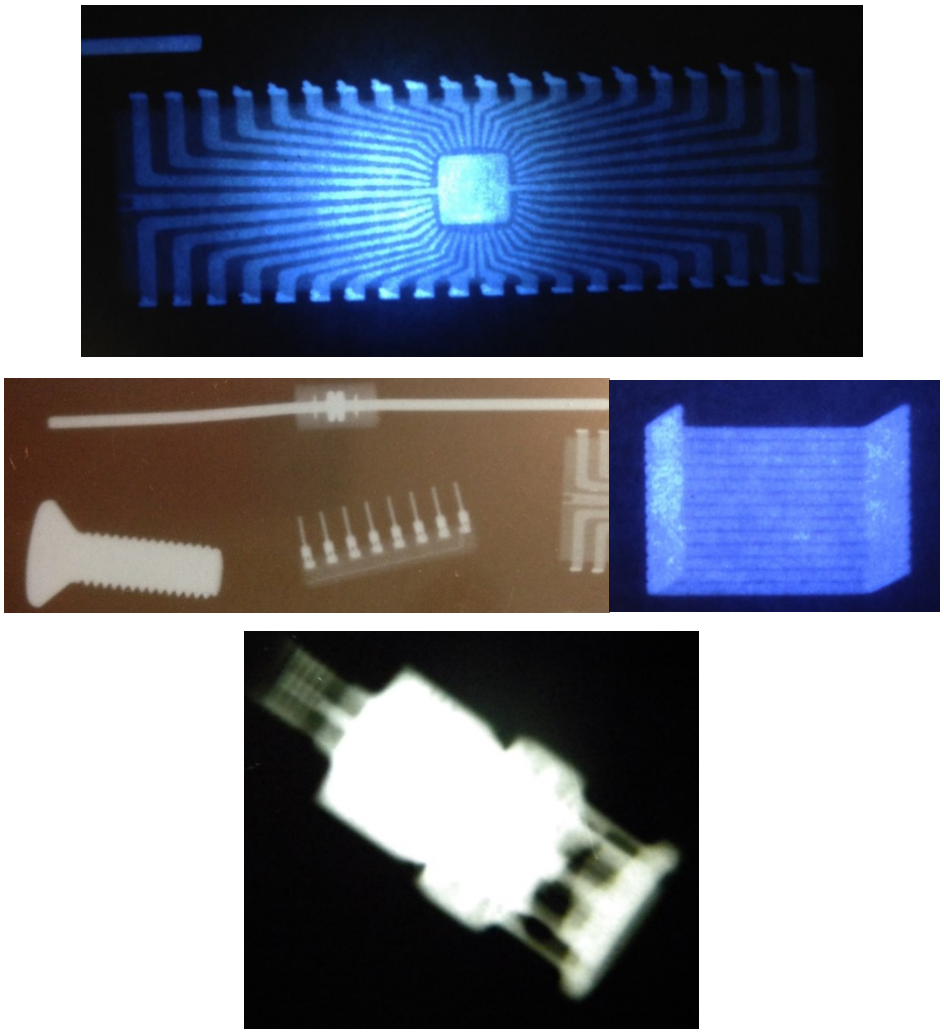

Figure 6.7: KSU-DPF one-shot radiograph images using neon gas, 1mbar, V=16kV (1.6kJ).

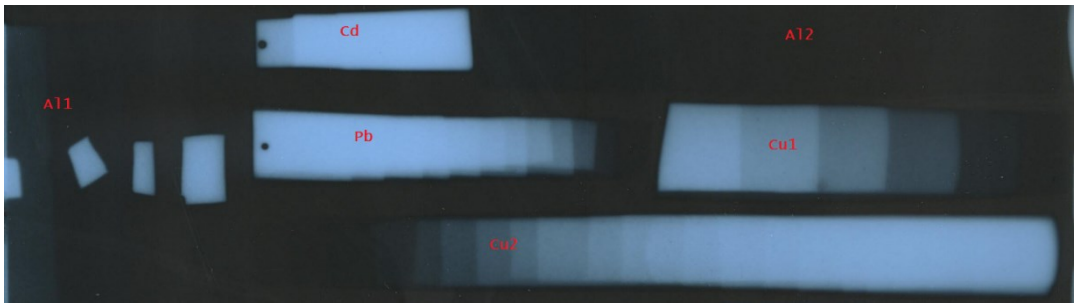

Figure 6.8: Example of one KSU-DPF shot over step-filtered cassette (in Figure 5.7), for neon gas at 1 mbar pressure, 17kV (1.8kJ), speed-100 Fuji film.

The radiographic image for the step filters is shown in Figure 6.8. In general, the aluminum filters Al1 and Al2 did not work well (it works better for lower energy spectrum). Only two out of four steps of cadmium were identified, while multiple steps of the lead were identifiable. The copper filter gave multiple steps above the fog level and under the film saturation level. The copper filter had 27 different steps.

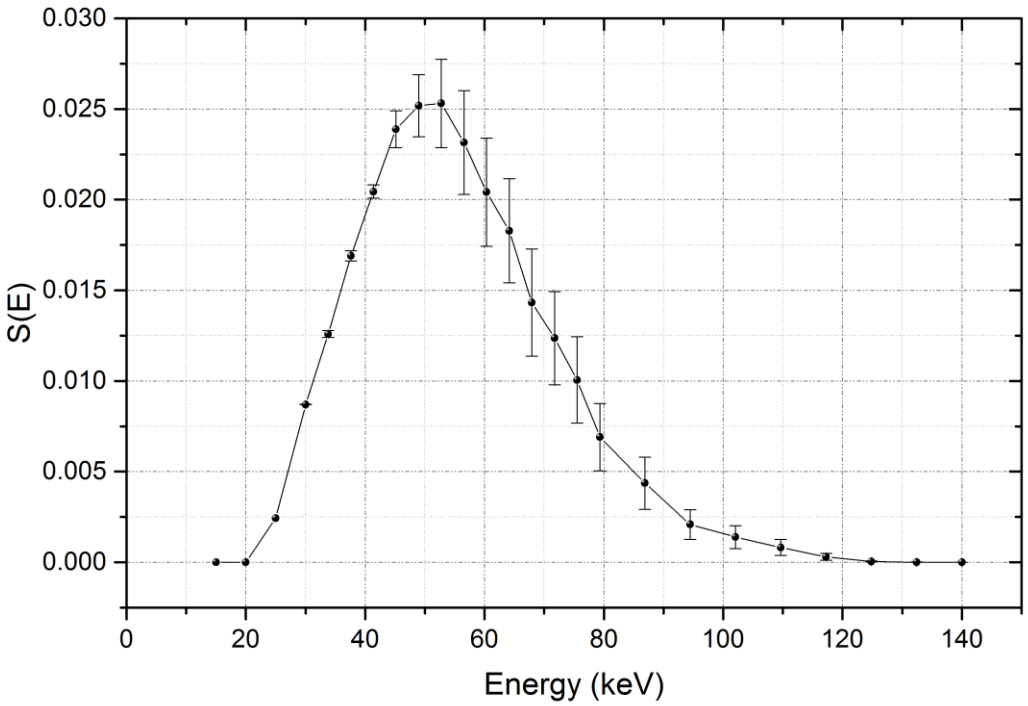

Figure 6.9: X-Ray constructed approximate spectrum for neon 1mbar.

The copper also has its K-edge at 8keV, which will not affect the spectrum calculation, while the lead (Pb) has its K-edge at 74keV, which may raise some error around this energy. Figure 6.9 shows the approximate constructed energy spectrum for the X-ray emission of the KSU-DPF at 1 mbar neon pressure and 17 kV capacitor voltage using the copper anode. The minimum energy of the spectrum is above 20 keV because of the 1 cm glass window. The most probable energy is around 50 keV and the average energy is ~57keV. Further results of the KSU-DPF X-ray was studied in reference [179].

6.4 Ion results

The ion beam plays a big role in the neutron emission of the KSU-DPF machine. The ion beam TOF technique was used to measure the deuteron energies of the ion beam emission of the KSU-DPF. The signals of the soft X-rays the voltage probe Rogowski coil (dI/dt) are shown in Figure 6.10.A. The three ion collectors in the axial direction correlated to the soft X-ray signal are shown in Figure 6.10.B, the graph shows an example of the system of diagnostics for deuterium at 0.5 mbar, 17 kV capacitor charge, and copper anode of composite shape (half straight and half tapered). The pinch started at 1.15μs, the Rogowski signal d*I*/d*t* and voltage signal indicated the FWHM of the signal to be ~40 ns, the voltage in figure shows a voltage peak (from the high voltage probe) ~78 kV. The Bpx-65 X-ray signal was used as the TOF starting signal. For the part B of the figure, the three axial ion collectors at distances of 28, 56, 70 cm. The figure shows two main ion bursts. The first one is smaller in magnitude and corresponds to an energy of 130 keV; the second peak is higher in magnitude but corresponds to a lower energy of 72 keV.

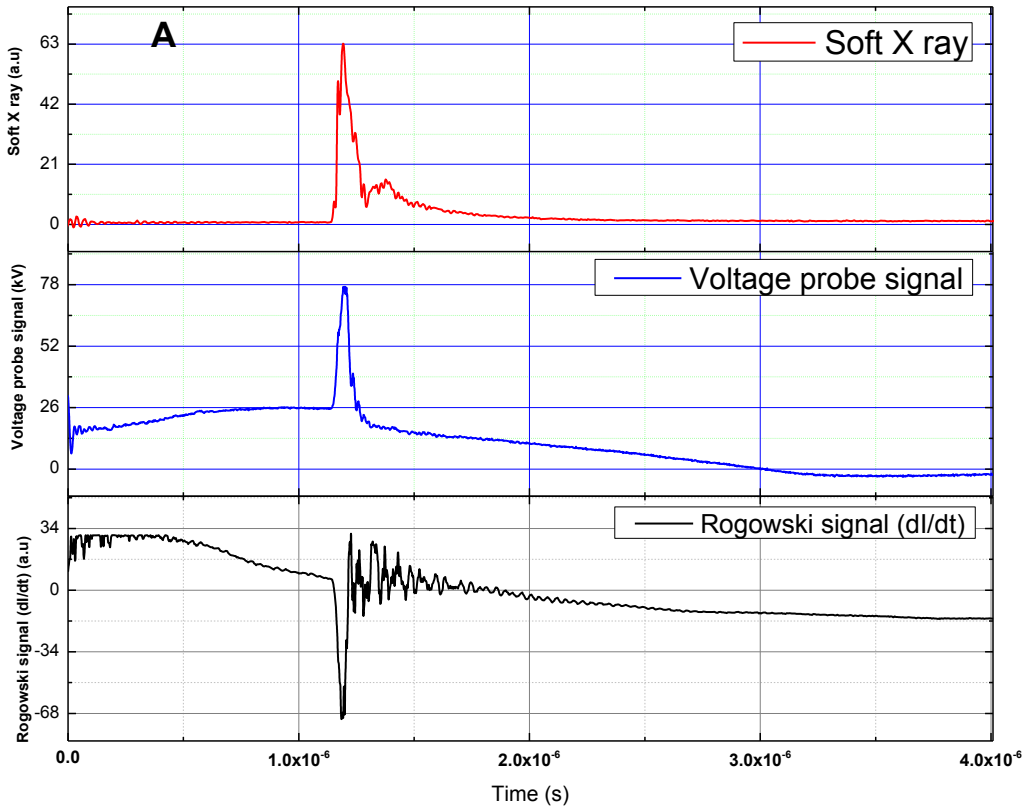

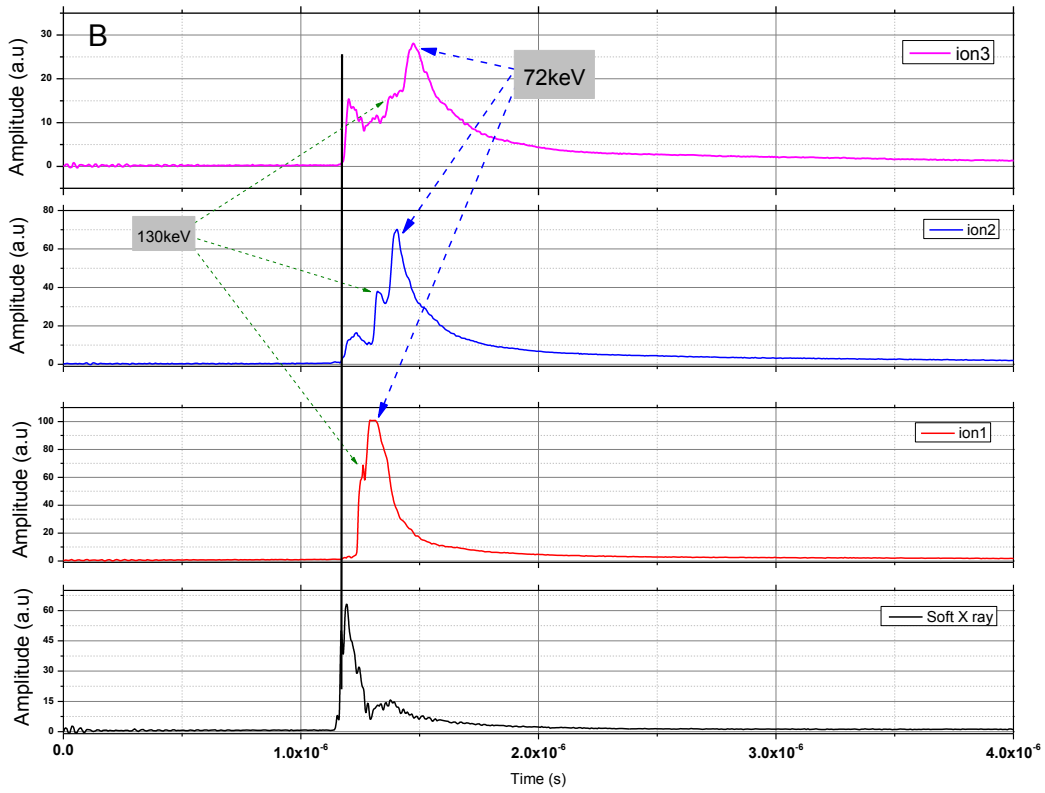

Figure 6.10: (Top: A) KSU-DPF correlated signals of the Bpx-65 photodiode, voltage probe and Rogowski coil. (Bottom: B) three deuteron beam signals correlated to the soft X-ray.

It was observed that the ion collectors pick up signals at the same time as the Bpx65 signal is initiated. It is thought to be due to soft X-rays. This may be taken as an initiation signal for the purpose of time correlation. The separation of overlapped ion peaks is possible by peak recognition techniques, Originlab was used to separate the multiple peaks; the signal was first smoothed by digital filter, the software was then used to recognize overlapped peaks.

6.4.1 Deuteron beam energy and density results

The axial deuteron peak density, total beam intensity, and peak energy were calculated at different deuterium pressures, at 17 kV capacitor voltage. Figure 6.11 shows the deuteron flux density (/cm^3) corresponding to the most probable energy of the ion signal, and the total ion

beam intensity (/m^2) integrated over time. The deuteron peak density and the total beam intensity change with pressure in the shape of an inverted parabola. The beam intensity of about 2.8×10^{18} m^{-2} was measured at a low pressure of less than 1 mbar. The intensity increases as the gas density increases and hits a peak around 4~5 mbar to record more than 3.2×10^{18} m^{-2}. The compression at this pressure is the maximum as the discharge current reaches its maximum value. The intensity of deuterons then decreases as the pressure increases and the compression phase occurs at a lower current value. This region for the anode configuration is characterized by slower speed of the shockwave and weak compression of the pinch. One other reason for the decrease in deuteron intensity at the high pressure (>5 mbar) is the interaction of deuterons with the gas molecules.

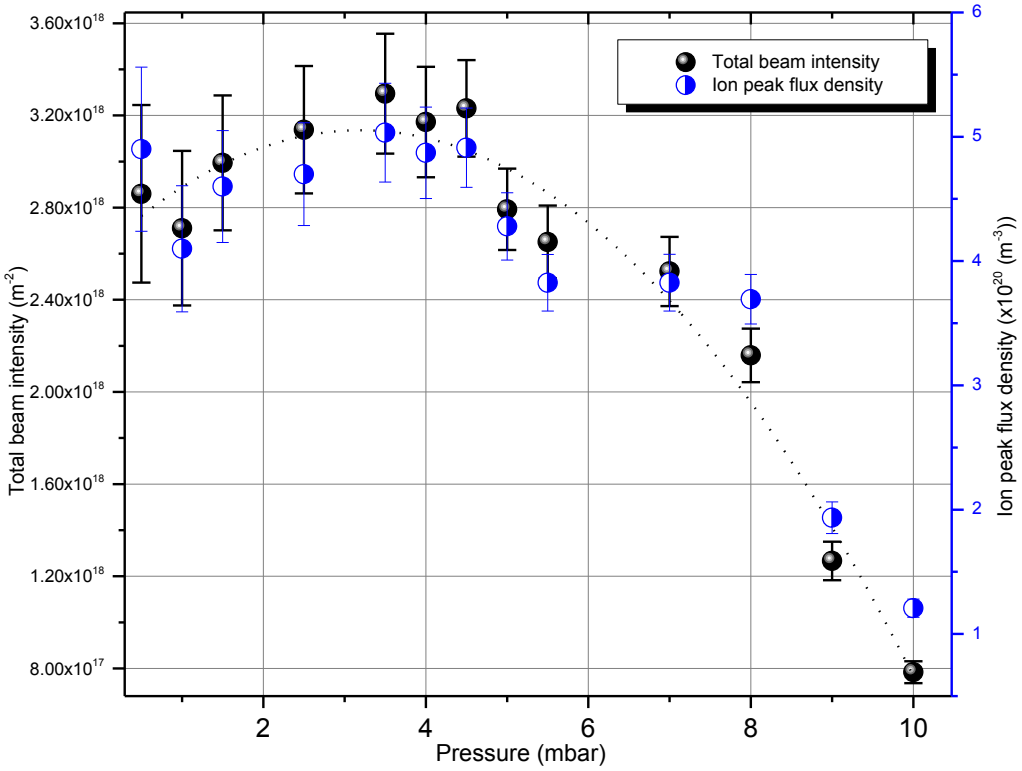

Figure 6.11: Variation of the total beam intensity, and the peak density in the axial direction with pressure, 17kV (1.8kJ).

A similar behavior was noticed to the peak energy (the energy at the peak deuteron TOF signal) of the deuteron burst. The deuteron energy was high at low pressure, about 85 keV at 0.5

mbar. The energy increased with pressure as the gas density increased and the compression occurred at higher discharge current values. The energy reached ~105keV at 1.5mbar; this value reached 200keV in some shots characterized by better compression, higher values of dI/dt and voltage in the radial phase, the radial phase also had one pinch and one burst of ions. The ion peak energy slightly decreased from 4 to 6mbar, and reaches 85keV then decreases moderately with the pressure to reach 30keV at 10mbar. The radial phase frequently shows multiple spikes of radiation with a separate period of tens of nanoseconds, this phenomena is attributed to a developed anomalous resistivity during the pinch compression [180, 181].

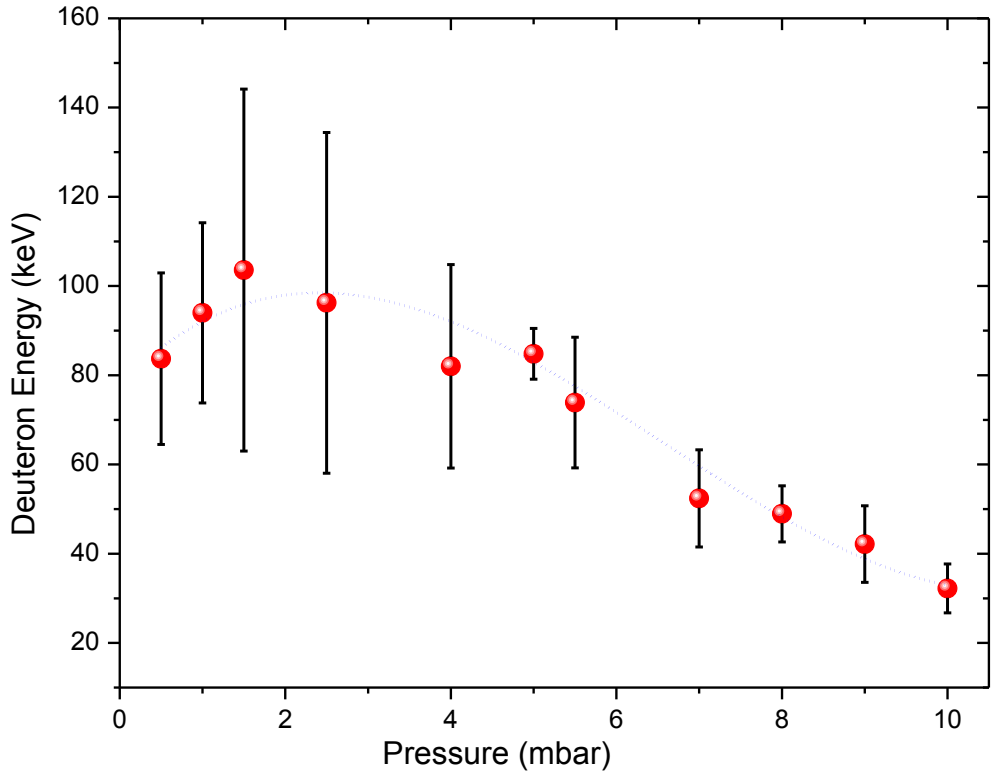

Figure 6.12: variation of deuteron beam energy with the pressure, 17kV (1.8kJ).

6.4.2 Deuteron energy distribution

The energy spectrum of the deuterons was calculated from the TOF using the ion collector. The energy spectra were normalized in order to compare the behavior with respect to energy for different pressures. Figure 6.13 shows the energy distributions of the deuterons for gas pressures from 0.5 mbar up to 10 mbar. The spectra show exponential-like tails with ion energy and the peak energies varied for different gas pressures. Generally, the slope of the energy spectrum

tail is inversely proportional to the pressure. This tail plays a big role neutron production. For instance, the spectrum density decays quickly at 10 mbar pressure, with a tail value of 5% at an energy lower than 200 keV. At 5 mbar the spectrum has one tenth of the maximum value over ~0.45MeV, where the cross section for neutron production is ~ 80 mbarn. For the low pressure region the spectrum has higher energy peak, and energetic tail of over 700 keV for one tenth of the spectrum magnitude. The spectrum tail is tightly related to the peak energy, as both increase and decrease together.

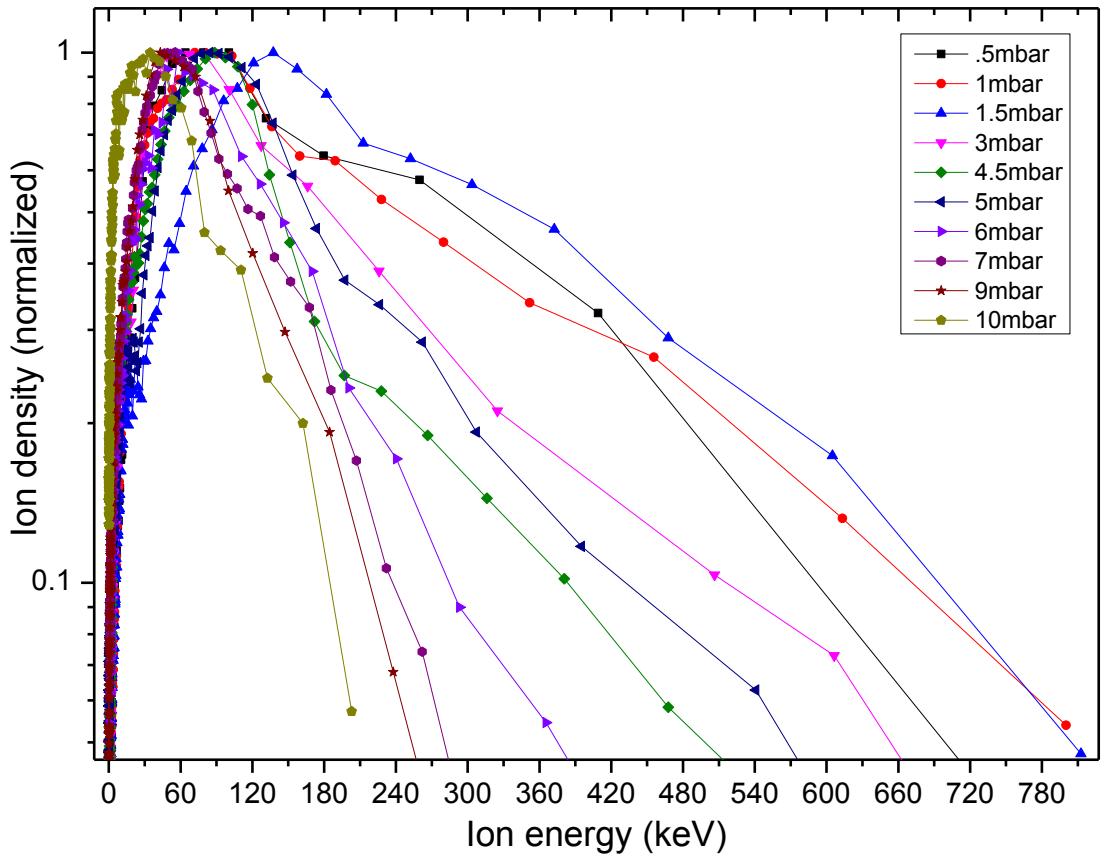

Figure 6.13: Deuteron energy distribution in the axial direction, 17kV (1.8kJ)

6.4.3 Spatial distribution of ion beam

The spatial variation of the beam intensity was measured by four FCs on 0, 10, 20 and 30 degrees w.r.t the anode axis (vertical direction). The ion intensity varies with axial direction, Figure 6.14, the deuteron total intensity in the axial direction (0^o) reaches about 3×10^{18} m^{-2} at 5mbar pressure. The intensity decreases to 2.8×10^{18} m^{-2} at 10^o, and decays to 2.4×10^{18} m^{-2} then 2×10^{18}

m^{-2}at 20^{o} , 30^{o} respectively. The data show a reduction in the deuteron beam with a maximum in the axial direction. This divergence of the beam may be attributed to the structure of the focused plasma in the pinch [52] as it is not an ideal cylindrical shape that axially accelerates ions in the axial direction. Instead, it is a funnel shape with the pinch current extending from the pinch roots into the cathode rods. This shape develops a non-axial electric field that diverges the trajectory of the ions. The other cause of the change in ion intensity with angle is the gyration of the ions inside the pinch as it is subjected to a developed magnetic field [182, 183]. The ion gyration adds a radial component to the ion axial velocity, which was formerly developed by the electric field.

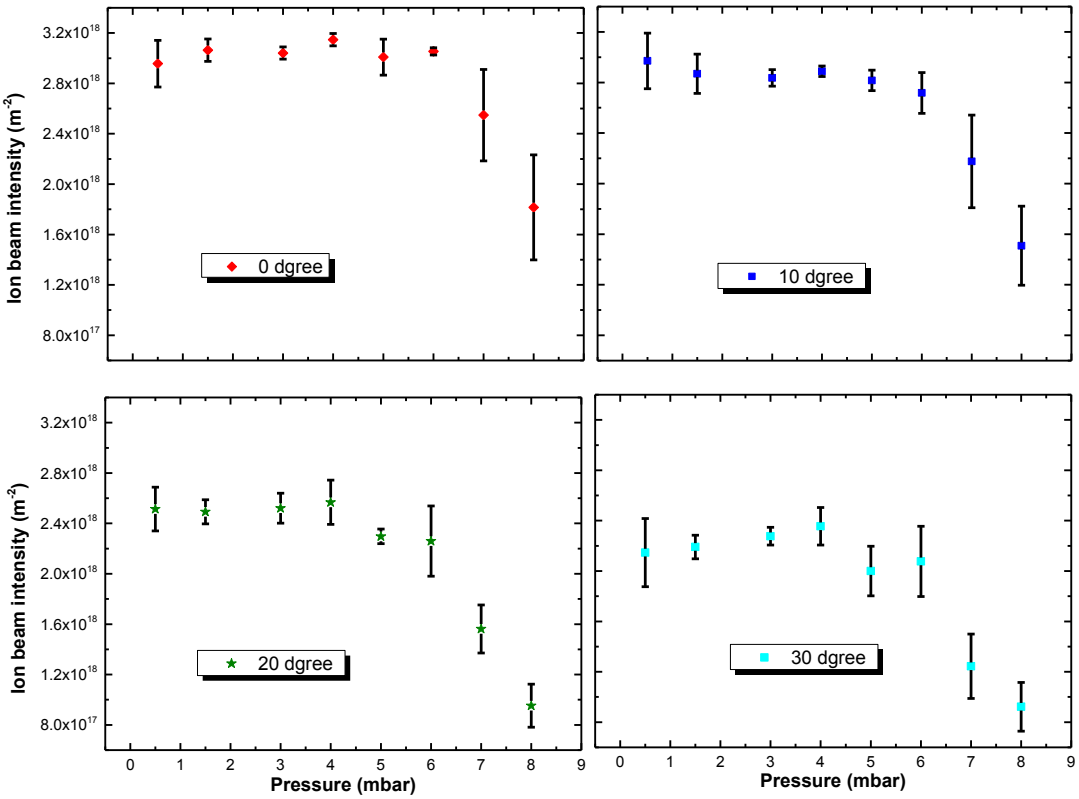

Figure 6.14: Total Ion beam intensity at 0, 10, 20, 30 degrees with the axial direction, 17kV (1.8kJ).

The four FC signals were very close in shape with different amplitudes as previously discussed. The peak energy of the beam was found to have no spatial difference. The spatially distributed FCs give more reliable data as the positions of the FCs are closer to the anode than the

ion collectors in the previous part of the experiment are, and hence there are fewer interactions with gas molecules, affecting the accuracy of the density and energy results.

6.5 Neutron yield results

The 3-He and Bonner sphere neutron results in the axial and radial directions are shown this section. The neutron production in the axial direction is always greater as the beam target mechanism adds an axial component of the neutron production. Figure 6.15 shows that the average neutron yield is relatively low; at low pressure around 1 mbar the yield is 10^7 n/pulse in the axial direction, and 3×10^6 n/pulse in the radial direction. The neutron yield increases as the gas density increases; at 5 mbar it reaches a maximum value of about 1.2×10^7 n/pulse for the axial direction and 7×10^6 n/pulse in the radial direction. The neutron yield decreases at high pressure to 10^7 n/pulse and 6×10^6 n/pulse in the axial and radial directions, respectively.

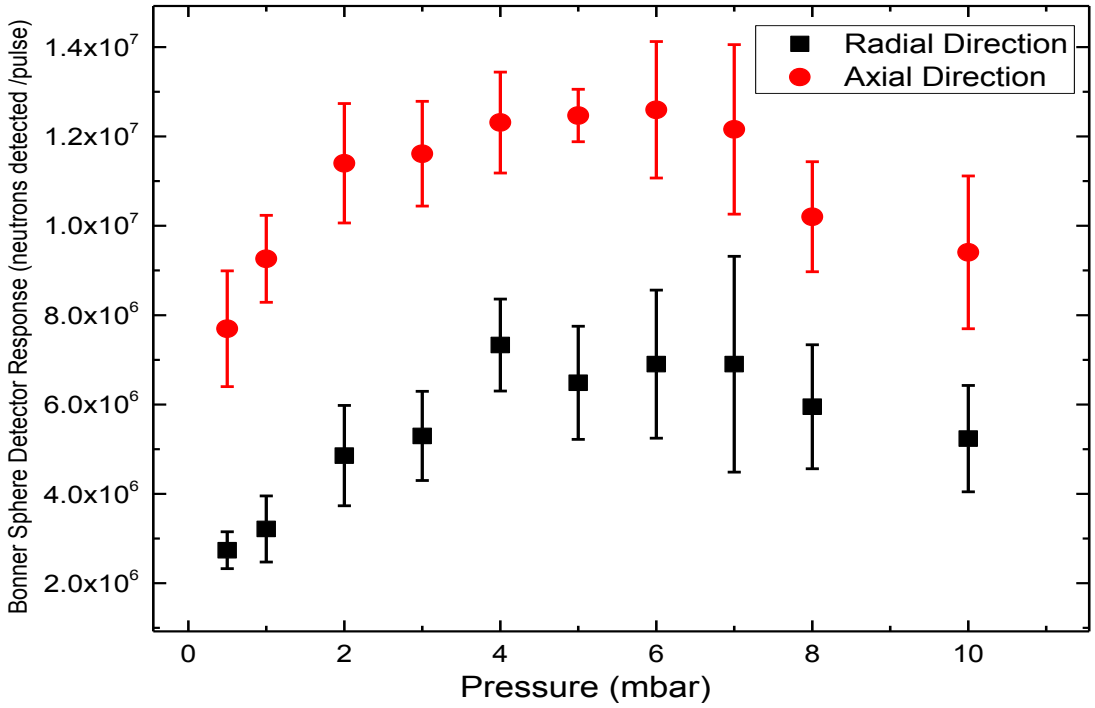

Figure 6.15: Axial and radial neutron yield emission from the KSU-DPF for composite shape copper anode, at 17 kV.

The neutron yield anisotropy, or the ratio of the axial to the radial neutron yields, is given in Figure 6.16. The ratios were formed for each shot and then averaged over the total number of

shots at each pressure. At low pressure, the anisotropy is high and the ratio reaches 2.3 at 1 mbar, which means the neutron yield is dominated by the beam target mechanism. The anisotropy decreases as the pressure increases to reach an average value of 1.3 in the pressure range from 5 to 10 mbar. In this pressure region, the ion beam average energy and density decreased, but on the other side the neutron production was found to increase as shown before. This phenomenon can be interpreted as follows. The neutron yield in the higher pressure region is dominated by the energized deuterons inside the pinch. The ions acquires energy by either ohmic heating or developed magnetic field through the gyro-motion inside the pinch. This pressure region is characterized by high neutron production and lower energy and density of the ions beam [183]. The thermonuclear fusion neutron production is thought to contribute to the total neutron yield by a small amount [184].

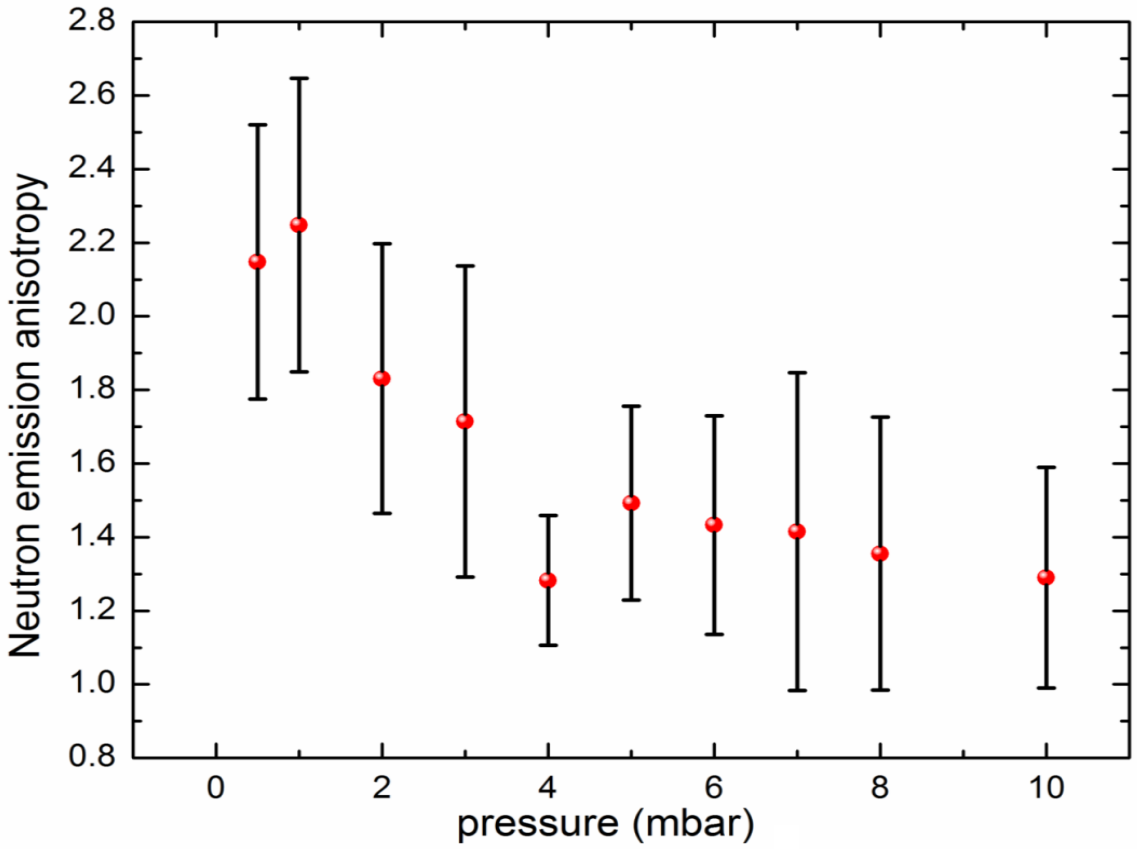

Figure 6.16: Neutron yield anisotropy, the ratio between axial and radial neutrons recorded from shot to shot, 17 kV.

6.6 Neutron based explosive detection results

For the application of the KSU-DPF as a source of neutrons for explosive detection, the DPF was configured using a tungsten anode because previous publications claimed better performance and neutron yield with such an anode material [16, 145]. The neutron yield in the radial direction from the 5 cm tungsten-copper alloy anode was measured.

6.6.1 Neutron source configuration

The neutron yield using a short tungsten anode was plotted in Figure 6.17 over the wide pressure range from 3 to 40 mbar. Around (the chosen pressure for detection experiment) 6 mbar, the neutron yield reached $\sim 5\times10^{7}$ neutron per shot. The yield slightly changed from 5 to 35 mbar and is expected to decrease at higher pressure. Most of the shots on the low pressure side showed one spike of radiation, whereas by increasing the pressure, multiple bursts of radiation were seen.

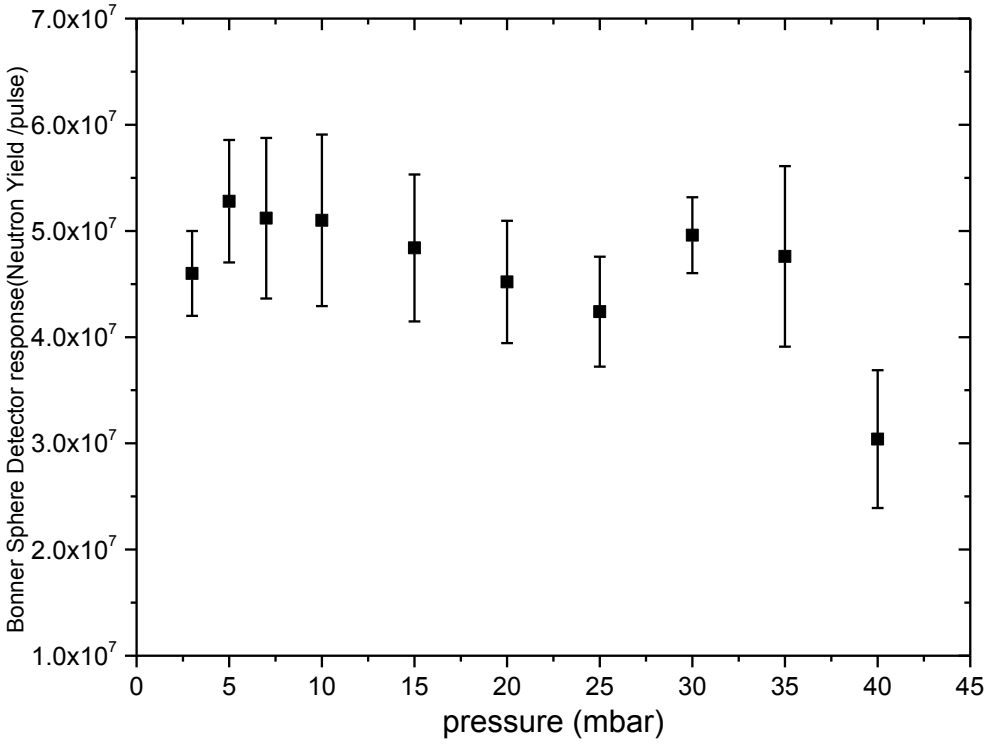

Figure 6.17: Neutron yield of the tungsten-copper alloy straight anode, anode length 5 cm.

The deuterium gas pressure during the explosive detection process was 7 mbar. In the radial direction the neutron energy is always around 2.4-2.5 MeV as the ion beam has no significant energy contribution in the radial direction. The neutron signal is picked up by the BC-418 plastic scintillators. Figure 6.18 shows four signals, one for the direct neutron emission and three for neutrons scattered from the target, as described previously. The left figure is the original signal, and the right figure shows the signals after removing gamma signal overlap.

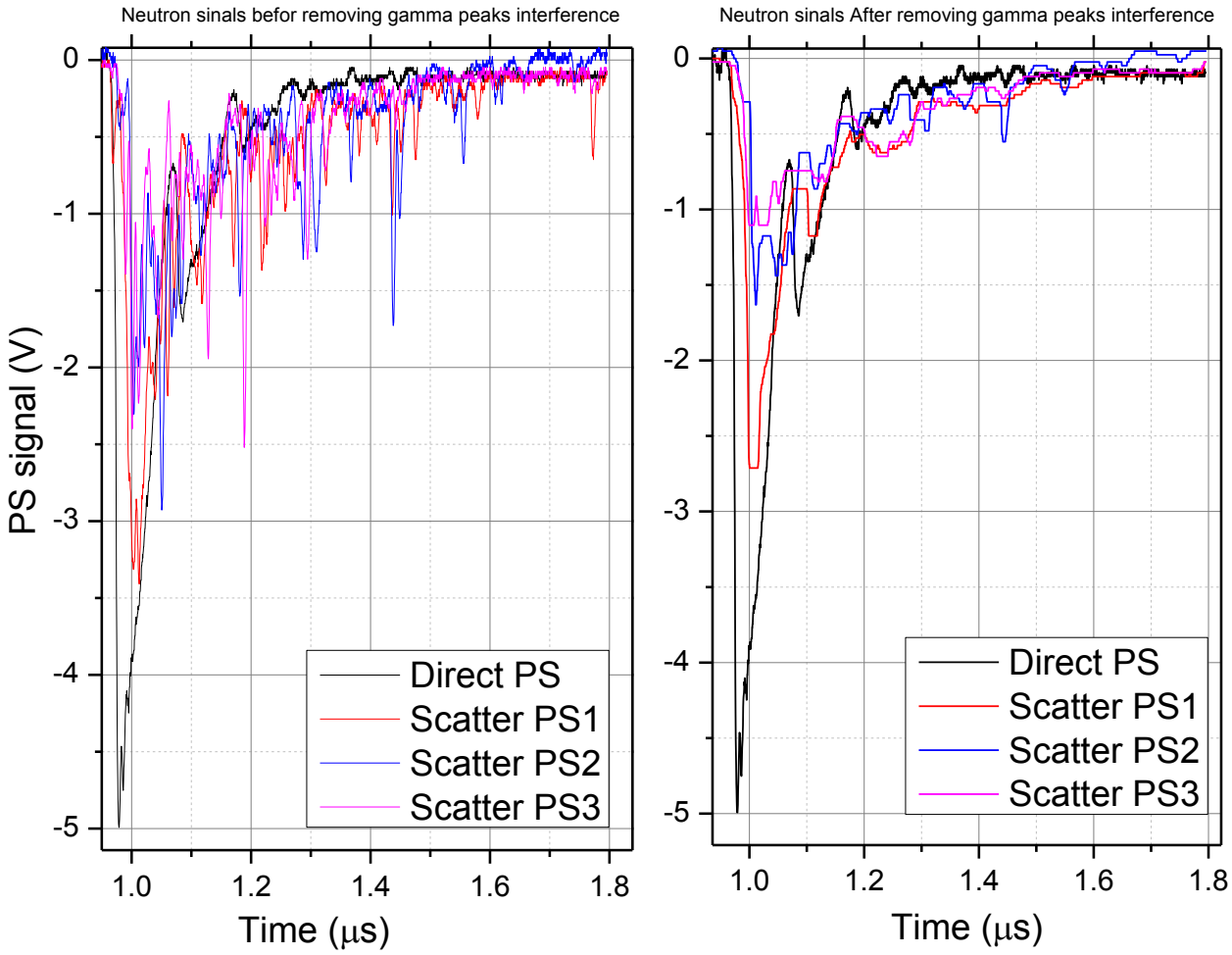

Figure 6.18: Example for plastic scintillators neutron signal, for five gallons sand. The graph shows the signal before and after removing gamma ray interference from PS1, 2, and 3.

A bare ^{3}He tube was also used to sense thermal neutrons only. The reading of the ^{3}He counter was accumulated for ten shots using different one gallon target cans. The counts in Figure 6.19 shows a background of 38 counts, the aluminum (Al) target gave the minimum number of counts as 40 counts followed by 47 counts for chalk, this response is expected as the aluminum and chalk don't significantly slow down the energetic neutrons. The fertilizers A, B and mixture fell in the region between 50 and 60 counts, this higher response was attributed to the average contents of the hydrogen, carbon, oxygen and nitrogen in the fertilizers. The organic materials and hydrogen-rich materials gave higher response above 80 counts. The graph shows that the bare ^{3}He detector can differentiate between inorganic, and organic materials; in other words, it is sensitive to the hydrogen content of the material.

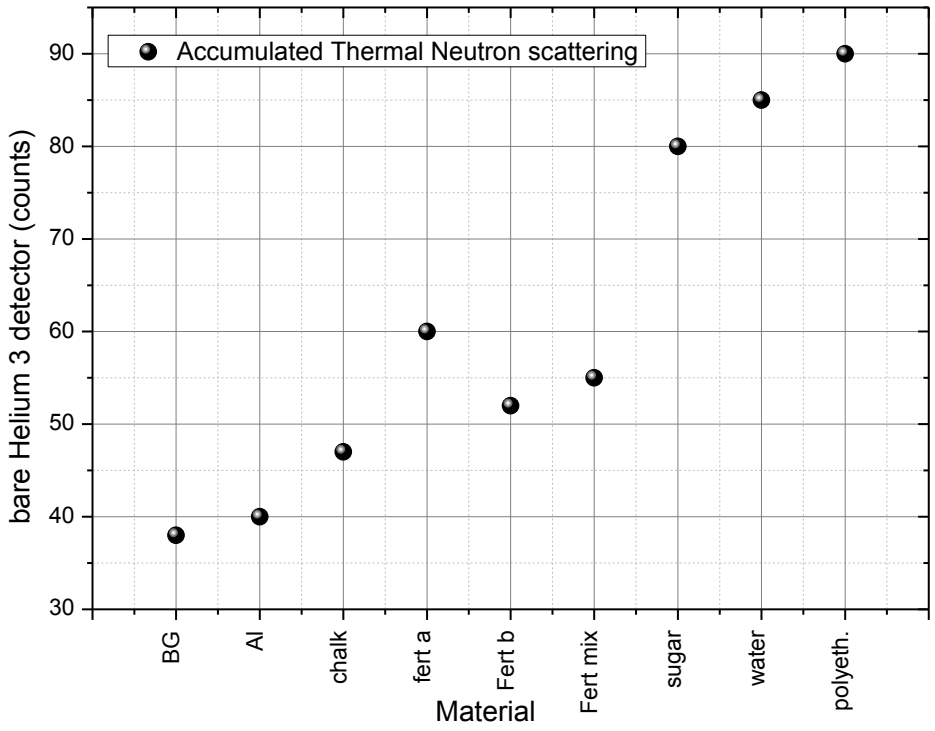

Figure 6.19: The accumulated counts for ten shots trial to configure the ability bare ^{3}He detector to respond to different targets.

6.6.2 Signature measurements and SBRS results

For the target cans of five gallons, the signatures of each material were measured using three plastic scintillators and one bare ^{3}He tube detector. The three plastic scintillator signals for

neutron scattering were normalized by the signal of the direct plastic scintillator. The signatures for the three types of fertilizers, chalk, sand, water, rubber, polyethylene and aluminum were plotted for each signature kind. The average counts per shot of the ^{3}He tube was below three counts. The materials are ordered in average nucleus mass (total molecule mass/ number of nucleus), from the higher to the lower. Figure 6.20 shows that the water target gave the highest response of 12.6, followed by the polyethylene can 10.5, which is expected because of the high hydrogen contents of both materials. The rubber mulch gave an average of 6.7 counts as it is a low density organic material. The fertilizers A, B and mix had relatively low responses, around 5.5 counts. The sand gave a comparable response as the fertilizer targets. Chalk had a lower value, around 5.0 counts, as it contains a high percentage of the relatively high mass calcium and also has no hydrogen content. The lowest response of 4.97 was for aluminum, which is a metal and neutrons are not easily moderated inside.

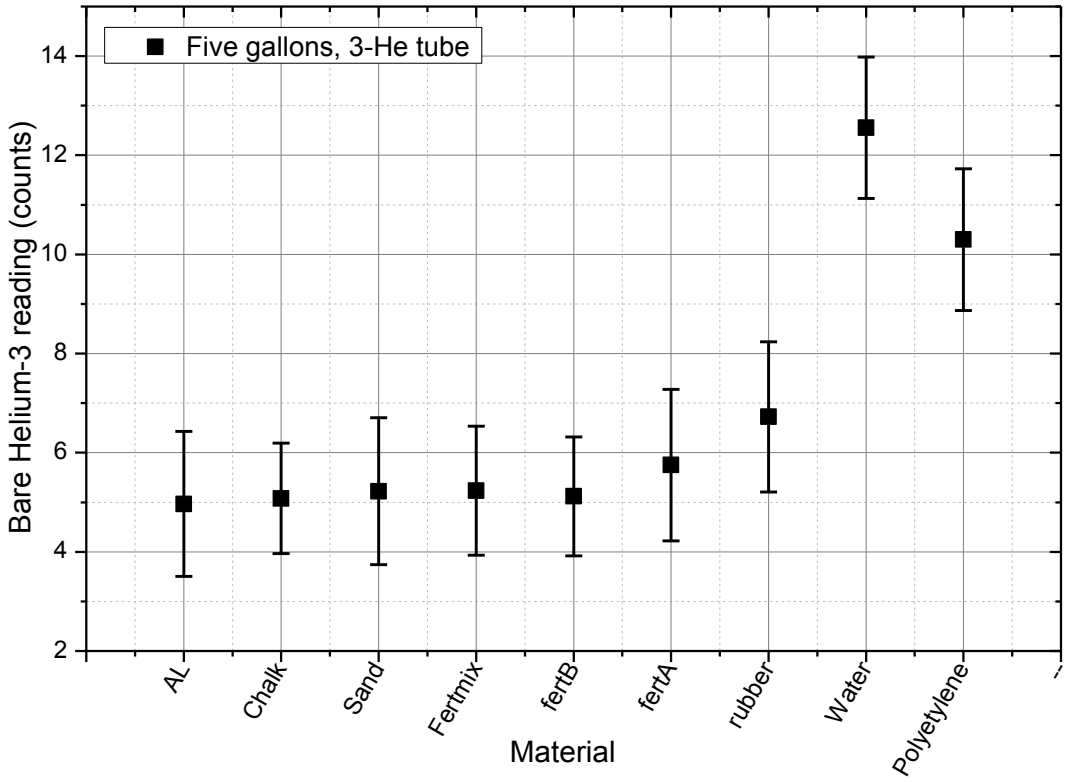

Figure 6.20: average counts per neutron pulse of the bare ^{3}He detector.

The three plastic scintillators gave responses that were similar in behavior, because the distance between the source and target was ~45 cm and the distance between the each plastic

scintillator and the center of the target can was short, only ~20cm. The solid angle is not small enough to allow the plastic scintillators to get different scattered neutron signals. The filters in front of the scintillators helped to obtain somewhat different responses for the target. The signatures of the first scintillator in Figure 6.21 shows that the water and polyethylene had responses under 0.25, while the rubber had a little higher response of 0.25. The three fertilizers had a response range between 0.2 and 0.3. The sand and chalk gave much higher responses, over 0.35. The highest response was for aluminum and reached 0.6. The plastic scintillator measures the fast neutrons; previous research indicated that it doesn't work well for neutrons under 50keV. The most effective neutrons are the single-scattered neutrons, which greatly depends on the material nucleus size and the scatter angle.

This scintillator response was similar to the other ones in Figure 6.22, and Figure 6.23; in both figures, the discrepancy between the three fertilizers and the other materials was clear. The second scintillator had a one-in. polyethylene filter, which attenuated the fast neutrons. Results for this scintillator are shown in Figure 6.22. In the scintillators with 2mm lead and 0.5mm cadmium shields, there was no significant attenuation.

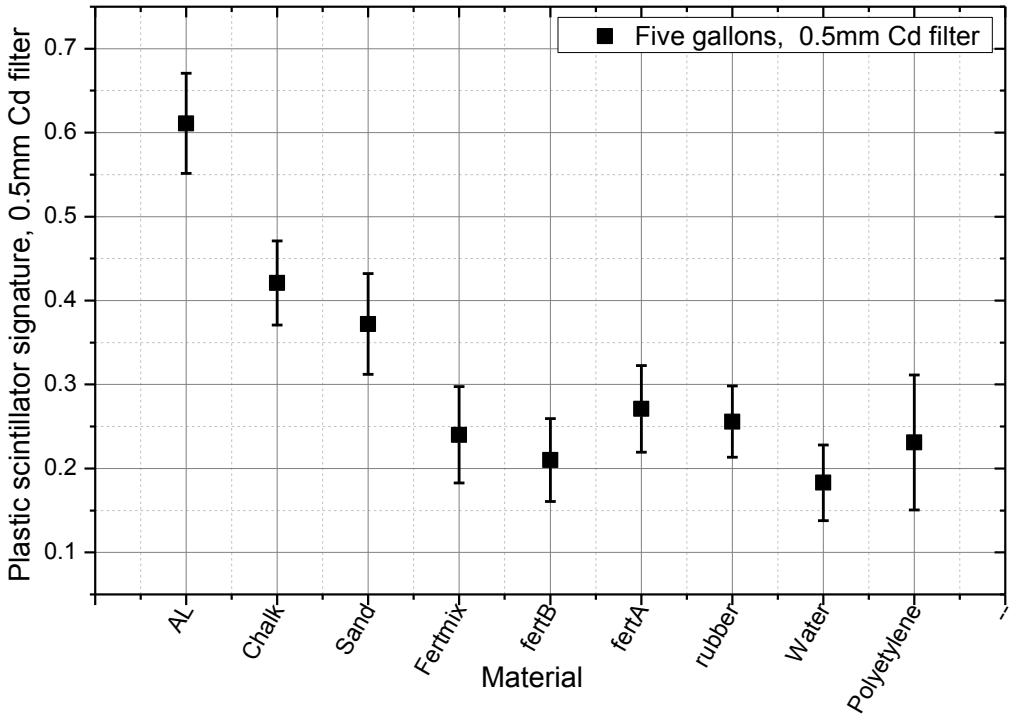

Figure 6.21: Plastic scintillator-1 signature, using filter of 0.5mm cadmium.

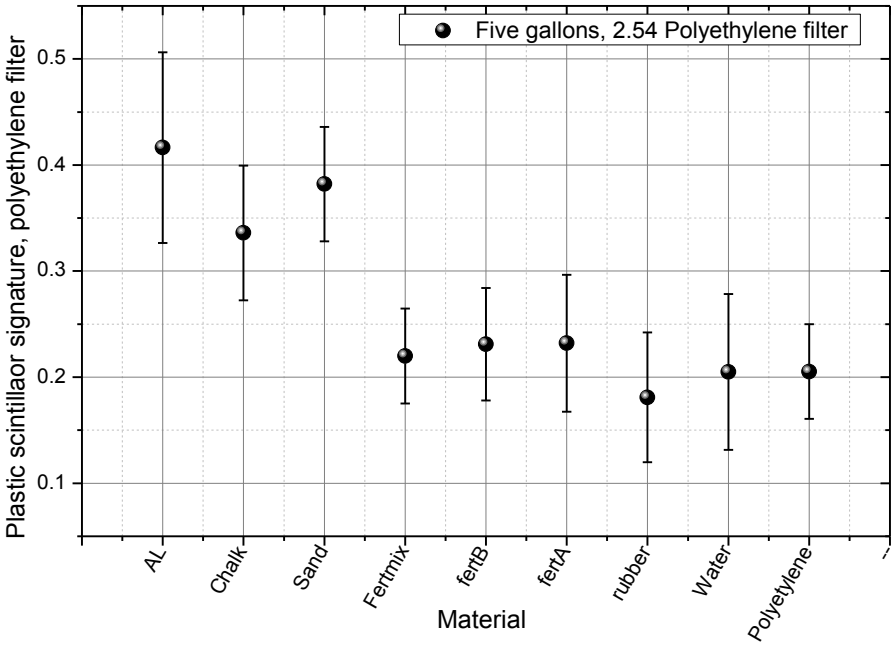

Figure 6.22: Plastic scintillator-2 signature, using filter of one inch polyethylene.

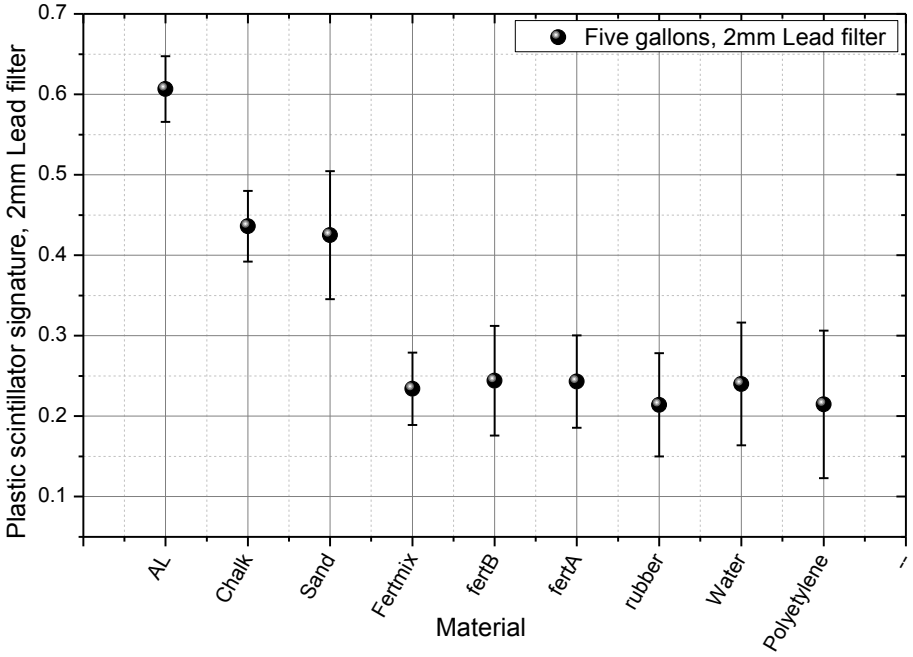

Figure 6.23: Plastic scintillator-3 signature, using filter of 2mm lead.

Using the four previous signatures for the five gallons targets, one can calculate the figure-of-merit, FOM, for each sample used and the standard deviation using equations (3.22), and (3.23). The normalized FOM for the five gallons targets is shown in Figure 6.24. Using the responses

from the Fertilizer-mix as a template, the Fertilizers A and B, which are the two explosive surrogates, have very low values of the FOM. Using a suitable cut-off value, the user can decide if a sample is explosive, inert or suspect, as indicated before. In our case a cutoff of 20 was chosen. The chalk, sand, and water appear to be inert materials, with FOM values in the range of 30 to 100. The metal target, namely aluminum, was the best to discriminate as an inert target with, with a FOM in excess of 300. The FOM failed to distinguish the rubber mulch as an inert material as it gave a low value of 10. The polyethylene sample had a FOM above 20 but at one standard deviation below, the value was below the cutoff line, meaning that this material may need extra investigation.

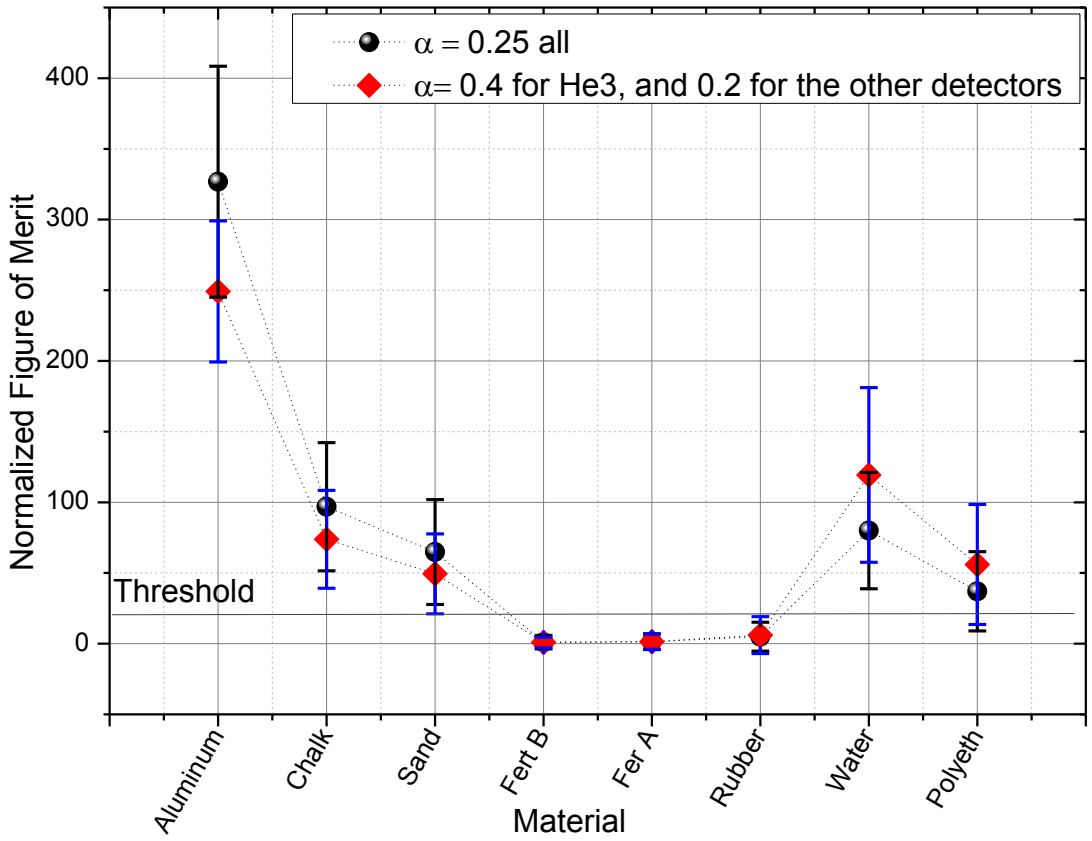

Figure 6.24: Figure of Merit for the five gallons target using four signatures, Fertilizer-mix was used as a template.

The figure indicated two calculations of the FOM, for equal importance of detectors (α=0.25), and for He-3 with higher importance (α=0.4) than the plastic scintillators (α=0.2), this

change increased the FOM for materials like narcotics and organic materials, while the first calculated FOM was better to differentiate metals and non-organic dense materials. The indication of Fert-A and Fert-B as explosive samples is called True Positives (TP), indicating the non-surrogates as inert material is called True Negative (TN), while mistakenly indicating the rubber as an explosive, is called false positive (FP). In case an explosive was indicated as an inert, this case is called a False Negative (FN).

Twelve one gallon cans were also investigated' Nine of the materials were the same as for the five gallon cans and sugar, ammonium nitrate, and graphite were also tested. One gallon cans are relatively small, limiting the number of reflected neutrons. The materials tested have average densities and nuclear masses as shown in Figure 6.26. These two factors plus the elements' neutron cross sections control the scattering response for each target.

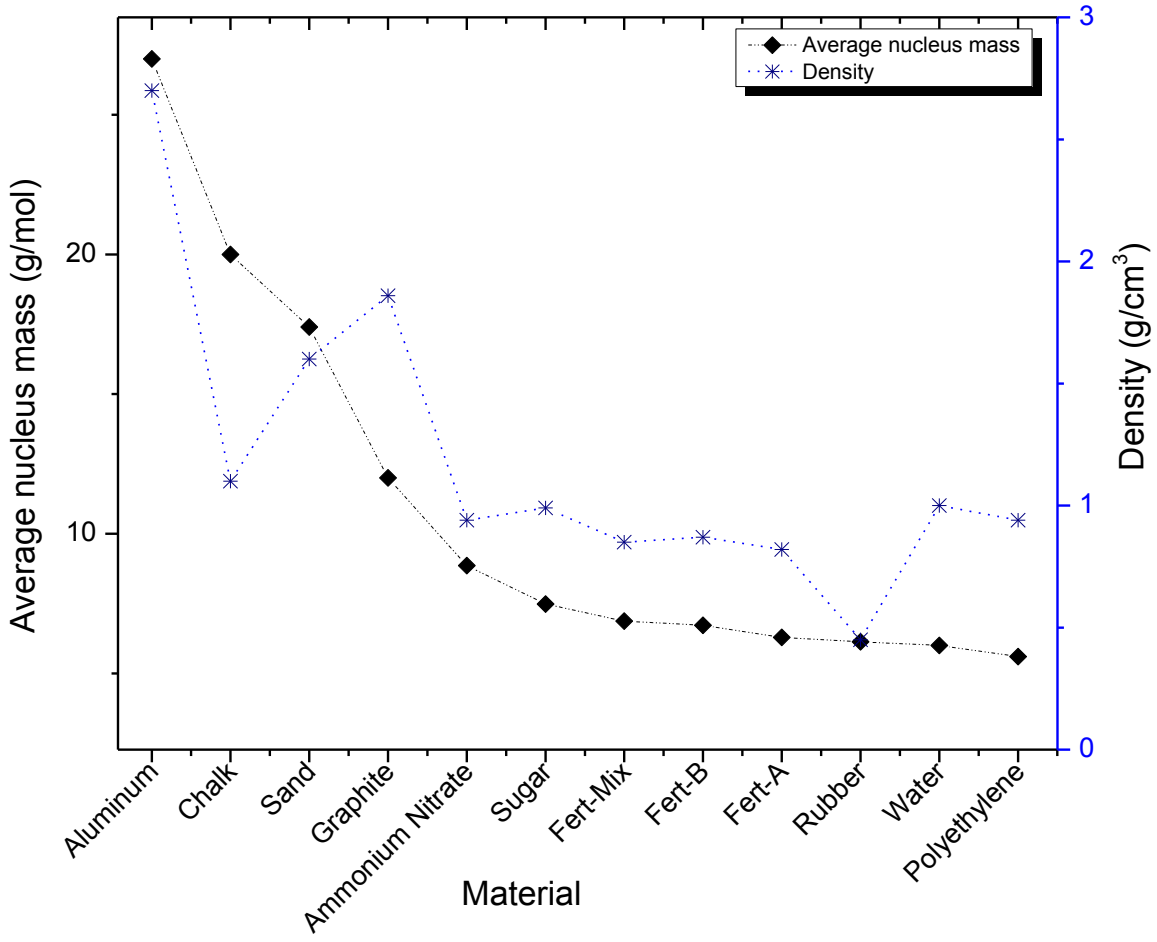

Figure 6.25: Average nucleus mass and density for the twelve target materials.

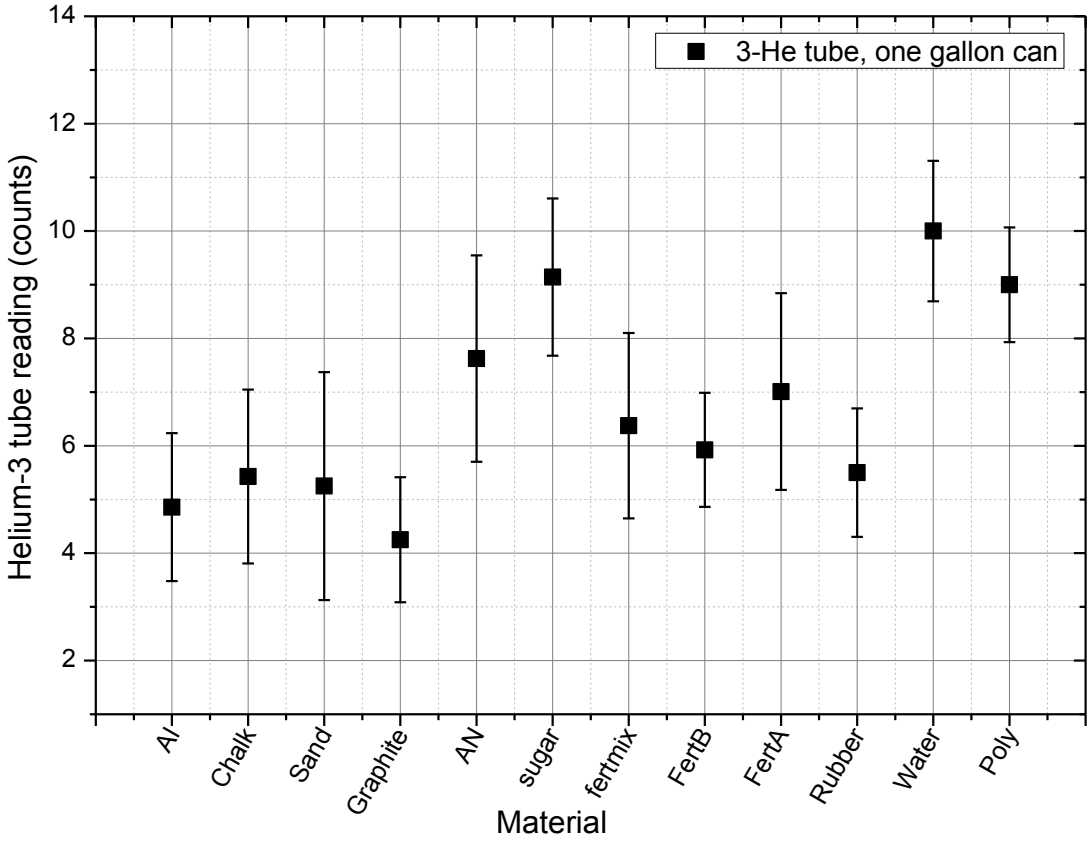

Figure 6.26: ^{3}He tube average counts per neutron pulse.

The bare ^{3}He reading was recorded for ten shots and averaged for each material. Figure 6.26 shows that the aluminum, chalk, sand and graphite gave the lowest values in the range between four to six counts. The ammonium nitrate, fertilizer A, B, and mix gave a response between six and eight counts. Sugar, water, and polyethylene then gave the highest responses between eight and ten counts. Note that sugar, an organic material (C12H22O11), gave a higher response than the ones with similar mass numbers. As described before, the three plastic scintillators had different filters and one was placed at an angle of 70 degrees and two were placed at 110 degrees. Figure 6.27, Figure 6.28, and Figure 6.29 show similar behavior as the five gallon cans but the relative error was higher as the reflected flux was lower than the previous case. The materials in the graphs are arranged according to average nuclear mass, from higher to smaller. The tendency of the response value seems to be directly proportional to the nucleus average mass.

The fast neutron response level can be divided into three categories. The first level is for high mass materials including metals and high density non-organic materials, i.e., aluminum, chalk, sand and graphite; these materials gave responses from 0.3 to 0.4. The second category is for average nucleus mass, i.e., the fertilizers A, B, mix, and ammonium nitrate, where the responses are between 0.25 and 0.3. The third category is for the organic and hydrogen rich materials including rubber, water and polyethylene; the responses for this category are relatively low compared to the first and second categories, ranging between 0.2 and 0.25.

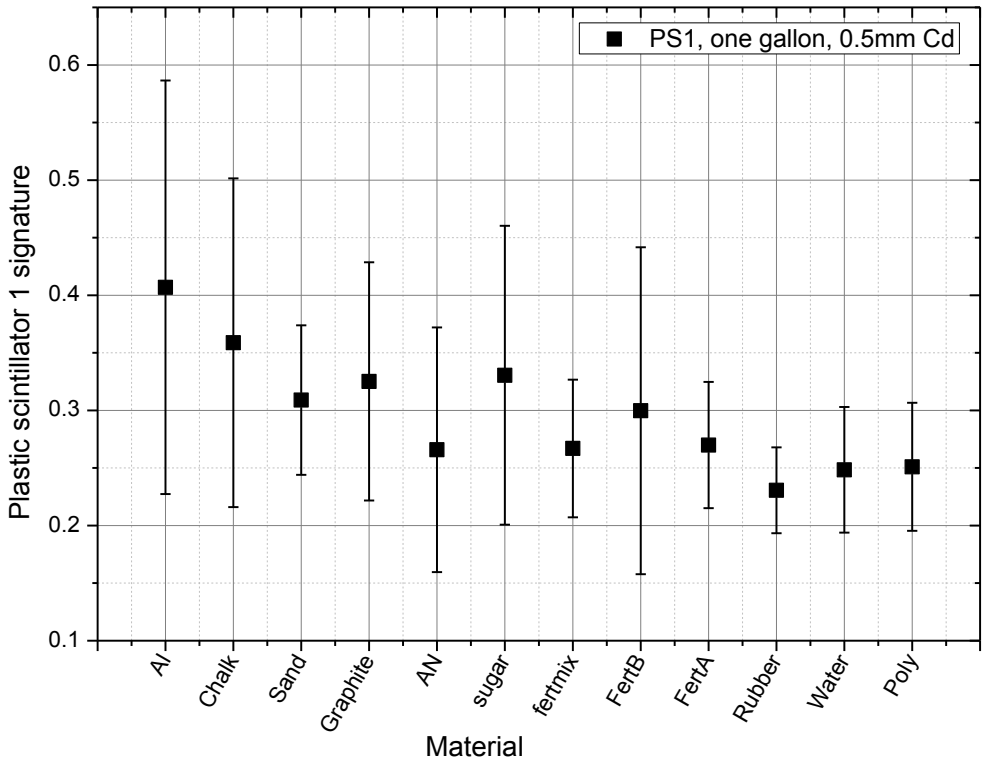

Figure 6.27: Plastic scintillator-1 signature, using filter of 0.5mm cadmium, at 70 degree.

The other two plastic scintillators had similar responses that differ in exact values according to the supply voltage, distance from the source, and the angle of measurement. It was noticed that the polyethylene response in the second plastic scintillator was higher than expected. It may be that this response is high because of electromagnetic noise interference. The four responses were used to get the normalized FOM for the one gallon targets.

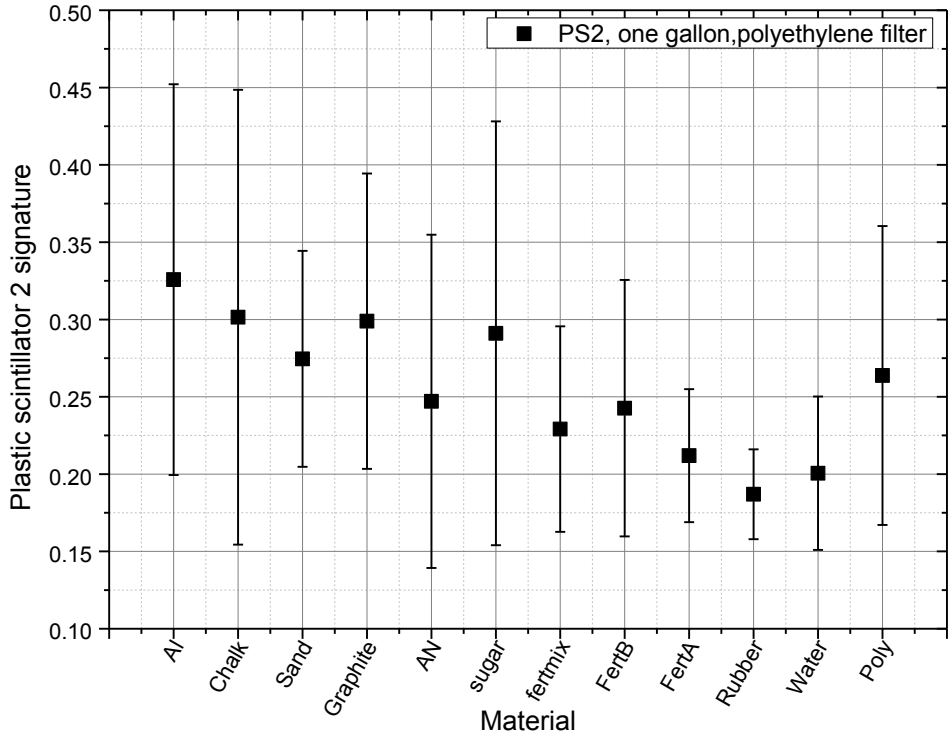

Figure 6.28: Plastic scintillator-2 signature, using filter of one inch polyethylene, 110 degree.

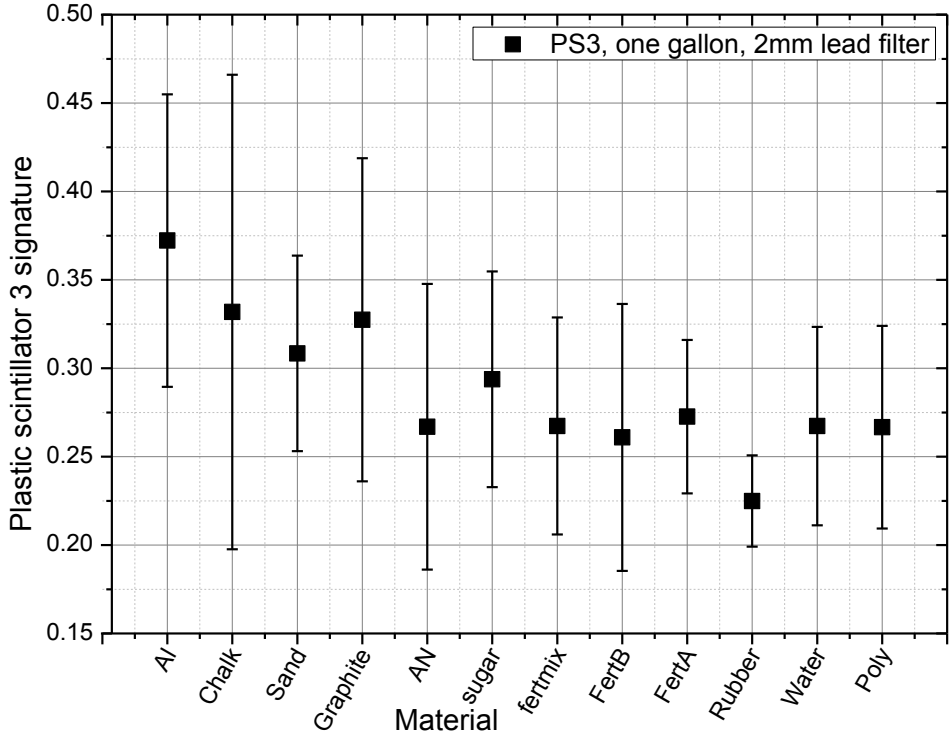

Figure 6.29: Plastic scintillator-3 signature, using filter of 2 mm lead, 70 degree.

The normalized figure of merit was calculated and plotted as shown in Figure 6.30. The error bar is high as the error propagation calculation used the standard deviation of the four signatures which was high as well. It was mentioned before that this is due to the weak scattered flux. This error may be reduced by increasing the power of the machine, hence increasing the neutron flux.

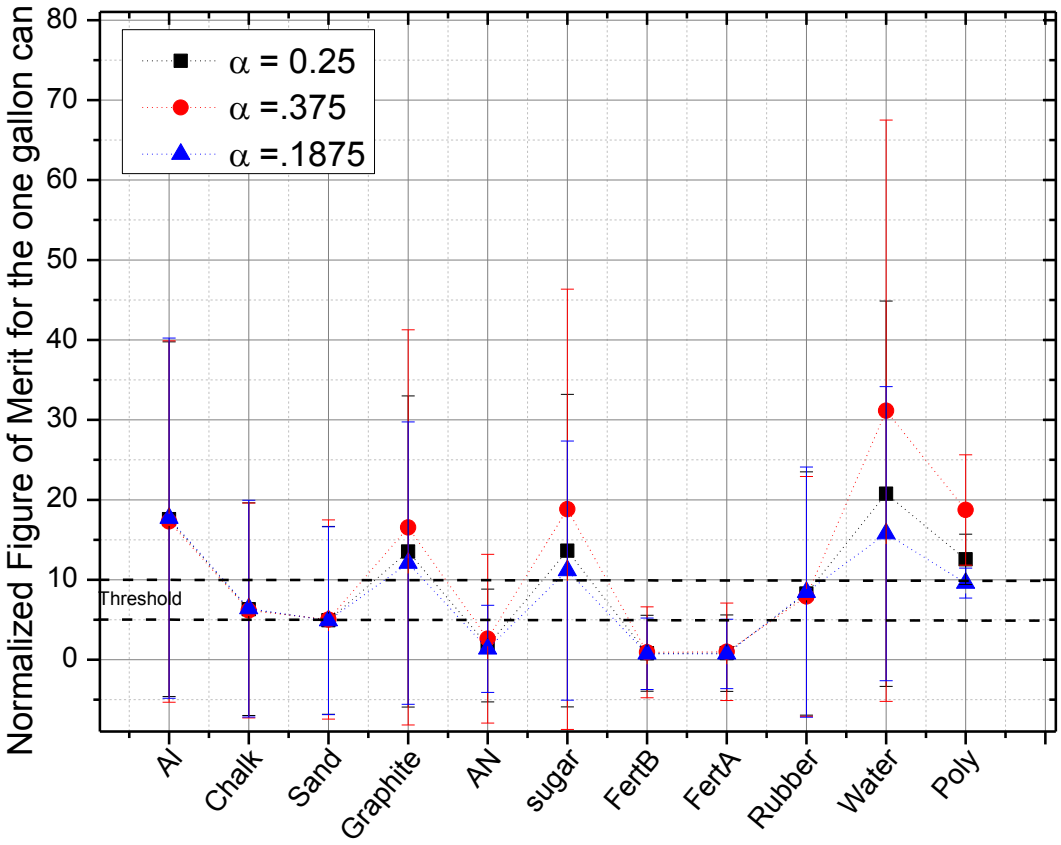

Figure 6.30: Normalized Figure of merit for the one gallon cans for different values of importance (α) for the ^{3}He detector.

If we look at the mean value of the FOM, the value for the Fert-A, and B were very small (less than unity), which means to the signatures matched the used template, for Fert-mix in our case. The FOM for ammonium nitrate was closest to the values for the fertilizer samples; the value was near unity, as AN is close in mass and density to the Fert-mix. The chalk, sand and rubber have much higher FOM values, within the range five to ten. The aluminum, graphite, sugar, water, and polyethylene had FOM values above ten. It is difficult to establish a cutoff line with the high standard deviations. However, assuming smaller error values could be achieved

with higher neutron flux, we may use the FOM values and assume a cutoff. The assumption of lower error at high flux is strengthened by the results of the Monte Carlo simulations presented in the next chapter. The change in weighting of the detectors gave some differences in the FOM values for some materials as shown in Figure 6.30. Choosing a cutoff value of five and using the FOM values with no error bars gives the ability to distinguish three materials as True Positive explosives (or surrogates), namely Fert-A, B and ammonium nitrate, the rest of materials are inert (True Negative). Having a higher value of the cutoff in Figure 6.30 increases the False Positive materials to include chalk, sand, and rubber. We may claim that if the KSU Dense Plasma Focus reaches full energy (10 kJ), this may increase the neutron flux by two orders of magnitude. In this case, the target-detector distance can be increased, shrinking the solid angle, and the TOF technique can be used to provide an extra signatures.

Chapter 7 - **Theoretical Model**

7.1 MCNP/X code introduction

The MCNP/X code is a Monte Carlo code that was developed at Los Alamos National Laboratory. The code uses Monte Carlo method to simulate the transport of radiation particles. The Monte Carlo method allows one to treat complex geometries, energy dependence, and time dependence for problems that are difficult to solve analytically [185]. The Monte Carlo method can simulate the transport of real particles according to the particle transport equation and cross section tables.

The early versions of MCNP simulated the transport of neutrons, photons, and electrons. The MCNPX code is simulates transport of these particles but is able to simulate charged particles as well (e.g.), protons, deuterons, alpha particles, and so forth. . The recent version MCNP6.1.x also simulates charged particle transport and the main three particles [186-188]. The code can simulate neutrons in the energy range from 10^{-11} to 20 MeV by default, the energy can be increased to 150 MeV using non-tabular cross sections and tabular data, when available. The range over 150MeV uses non-tabular data only. The code simulates photon energies in the range of 1 keV to 100 GeV, and electrons from 1 keV to 1 GeV.

There are three main categories in the MCNP/X code input. The first identifies the surfaces in the geometry that define the 3-D shapes. The second part is the cell definition, where the user defines cells bounded by surfaces, and assigns a material to each cell [189, 190]. A cell is defined as the volume bounded by multiple surfaces. The third part of the code input identifies the sources and tallies. The source is defined mainly by position, type of radiation, energy, and direction of radiation. These variables may be defined as constants or functions. The tallies are responsible for measuring different radiation quantities in the problem space. Table 7.1 shows common tallies that are used to measure various nuclear quantities for various particles. The F1tally records the average current at a surface, while F2 is used for the average flux at a surface. The F4 tally is used to measure the flux in a cell. The F5 is a special point detector tally that measures the radiation flux at a certain point in the problem space. The F6 tally records the absorbed energy in a cell; this tally depends on the assigned material of the cell. The F8 tally is a

pulse height tally that is used in photon spectroscopy. The new MCNP6/X code has the capability to use the F8 tally with neutrons or other particles by adding special treatment to the tally [191].

Table 7.1: Common MCNP/X tallies.

Tally	*Tally type*	*measured particle*	*F_n/history*
F1	surface current	N or P or N,P or E,T,h	#
F2	average surface flux	N or P or N,P or E, T,h	#/cm^2
F4	average flux in a cell	N or P or N,P or E, T,h	#/cm^2
F5	flux at a point or ring	N or P	#/cm^2
F6	energy deposition	N or P or N,P, T,h	MeV/g
F8	pulse height distribution in a cell	P or E or P,E, N, T,h (with combined special tally treatment)	pulses

7.2 MCNPX problem simulation

Since it is hard to use real explosives in the laboratory to prove the explosive detection technique, it is recommended to simulate experiments that have explosives and validate the code with an experimental work that uses explosive surrogates.

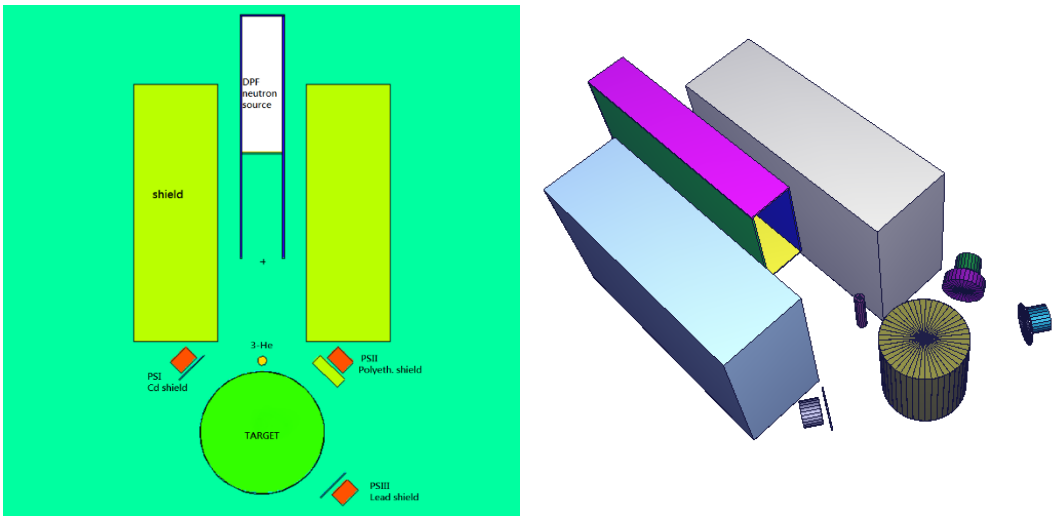

Figure 7.1: Problem geometry, the DPF source emits 2.45MeV neutrons.

An MCNPx simulation was performed for the one-gallon and five- gallons samples using MCNPX 2.7.x version. The code includes a monoenergetic neutron source of 2.45 MeV that emits neutrons from inside a stainless steel chamber with a 1 cm glass window, as shown in Figure 7.1. The

chamber is shielded with a high density polyethylene neutron shield. Cylindrical iron cans of two sizes were used as targets, the sizes of can were 26 cm long and 30 cm in diameter for the five gallon cans with a 1-mm wall thickness, and 19 cm long and 16 cm diameter for the one gallon can with 0.2 mm wall thickness. These cans were filled with various investigated materials, and were set in front of the chamber glass window at a distance of 50 cm from the source position. Nineteen materials were used in this investigation: seven real explosive materials, three fertilizer materials, and nine organic and inorganic inert materials. Table 7.2 identifies the materials simulated.

Table 7.2: Target materials used for MCNP simulation.

Target Material	*Average nucleus mass (u)*	*Density (g/cm3)*
Polyethylene	4.6495	0.94
Water	5.97383	1.00
Rubber	6.12934	0.45
Fertilizer-A	6.29186	0.82
Fertilizer-B	6.71857	0.87
Fertilizer-Mix	6.86675	0.85
Sugar	7.47538	0.99
Ammonium nitrate	8.86158	0.95
Nitrocellulose	10.35388	1.66
RDX	10.55009	1.81
HMX	10.55009	1.90
TNT	10.79138	1.65
EGDN	10.8356	1.49
PETN	10.87483	1.77
Nitroglycerin	11.33005	1.13
Graphite	12	1.86
Sand	17.40568	1.70
Chalk	20.00799	1.10
Aluminum	26.982	2.69

Three plastic polyvinyl toluene cylinders of diameter 2 inch were set at angles 70^{o} and 110^{o} (similar to the experimental work), at 25 cm from the target center, three shields of cadmium, polyethylene and lead were set in front of the three plastic detectors. A ^{3}He tube was set between the source and the target to measure thermalized neutrons. The particle designator mode in the problem included neutrons, protons, and tritium. The tally F6 which registers the energy deposited in a cell was used to measure the detector responses as indicated in the next section.

7.2.1 Plastic scintillator modeling

The plastic detector response to fast neutron radiation is an indirect response; the fast neutrons transfer their energy to the crystal through a scattering collisions between the neutrons and the protons and carbon nuclei in the target. Most of the response comes from the neutron-proton collisions as the masses are very close and so the incident neutron loses more energy, on average, in collisions with protons than with carbon nuclei. The crystal light generated by the recoil protons is also greater than the light generated by carbon nuclei, as discussed in section 4.3.4. An MCNPX input file was written for the purpose of finding the energy deposited by recoil protons in a 2-in. plastic scintillator crystal versus the total energy deposited in the crystal. Figure 7.2 shows that most of the incident neutron deposited energy goes to the crystal protons from low energy <300 keV up to 2.5 MeV.

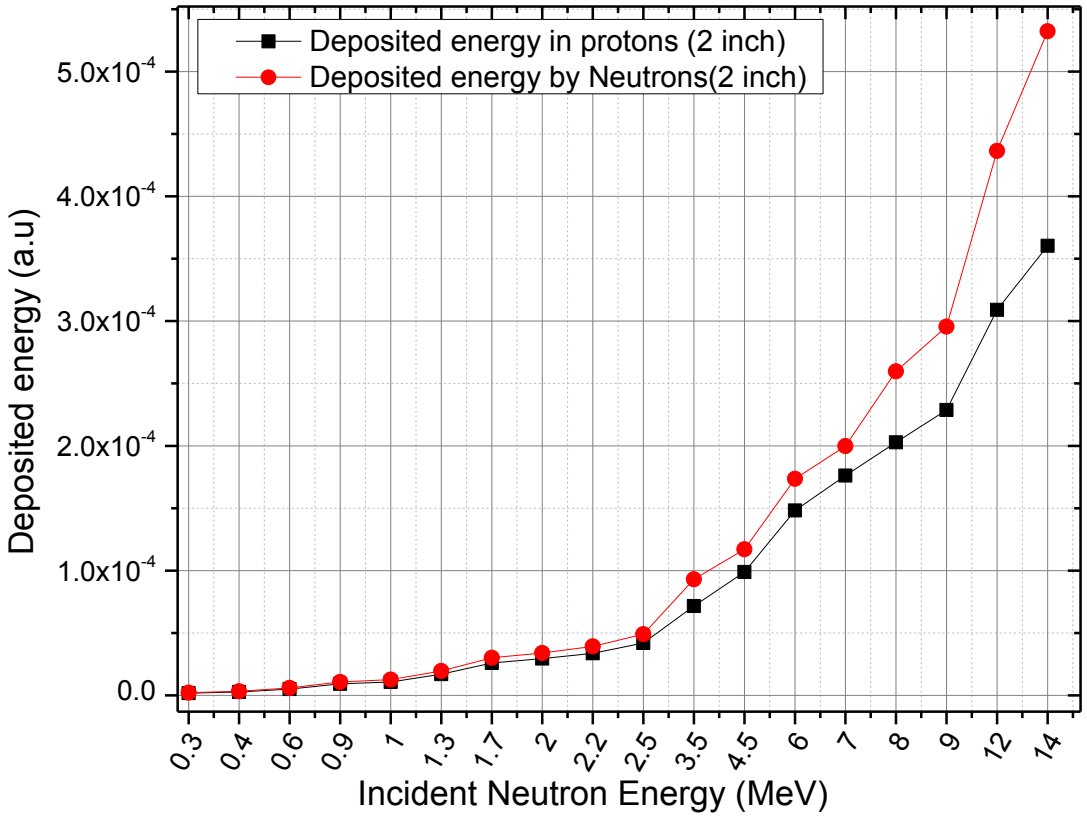

Figure 7.2: Neutron energy deposited in the 2-in. crystal through the neutron-proton elastic collision.

The recoil proton energy-to-light conversion is not a linear process [159, 192, 193]. The MCNPX command DE/DF was used for the purpose of light conversion. The conversion process converts the recoil proton energy deposited from MeV to MeVee (MeV electron equivalent). Equation (4.6) was used to establish the measured light output from the plastic scintillator crystal. The light output from carbon converts by the equation $L = 0.02E_p$ [194], this amount of carbon light represents 1.6% of the total light developed inside the crystal at an incident neutron energy of 2.5 MeV. It increases to 4.5% at a neutron energy of 14 MeV. Overall, the majority of crystal light output is produced by the recoil protons.

7.2.2 Helium-3 detector modeling

The ^{3}He tube is responsible for detecting thermal neutrons through the following reaction

$$n + {}^3He \rightarrow T + P + 0.764\ MeV \qquad \textbf{(7.1)}$$

Some or all of the kinetic energy of the proton and triton products is deposited in the tube and gives a signal indicating a neutron capture. The ^{3}He was tube modeled as a cylinder filled with ^{3}He at 2 atm pressure; the tube is 10 cm long and 2 cm in diameter. The tube was set behind the target to detect scattered thermal neutrons from the target. It was assumed that the ^{3}He detector had zero sensitivity to gamma rays. The response was recorded in two ways. The triton product was recorded using tally F6 and the special tally treatment (FT) with coincidence capture (CAP). The second method is offered in MCNP6 or MCNPX V-2.7E only, the first method is offered in MCNPX V2.2. The material compositions were listed at the end of the code, the "Compendium of material composition data for radiation transport modeling" [195] reference was used for the explosive composition and other materials when available.

7.3 MCNPX code results

First, a study was performed to examine the effect of different target materials and angles of neutron scattering. Then the real experiment was simulated and the FOM method was applied on the signatures from the materials under investigation.

7.3.1 MCNPX scattering method validation

Initially, a set of detectors was arranged around the target, as shown in Figure 7.3 the flux recorded by each detector indicated that the flux at different angles is an efficient way to differentiate among different materials, as each material has its own scattering fingerprint.

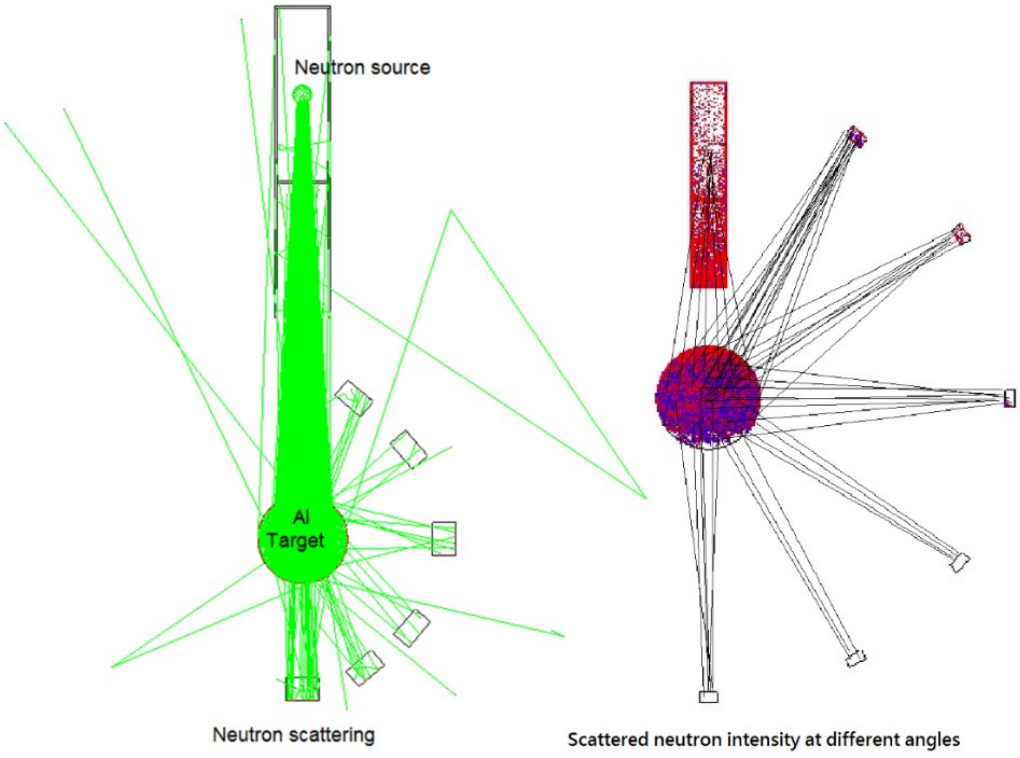

Figure 7.3: Neutron flux scattering, measured at different angles, aluminum on the left, water to the right.

Figure 7.4 shows scattering responses for detectors at different angles for an imaginary material that contains carbon, nitrogen, and oxygen (C-N-O). The highest response was noticed at the largest angle, namely 150^{o}. The response decreases with decreasing angle. The figure shows three spikes with different intensities at each angle, those spikes correspond to scattering from each of the C-N-O nuclei. It is easy to tell that the higher energy peak corresponds to the lower mass (carbon in this case), and vice versa. Each examined material will have its own response according to the elements of composition and their concentration in the material.

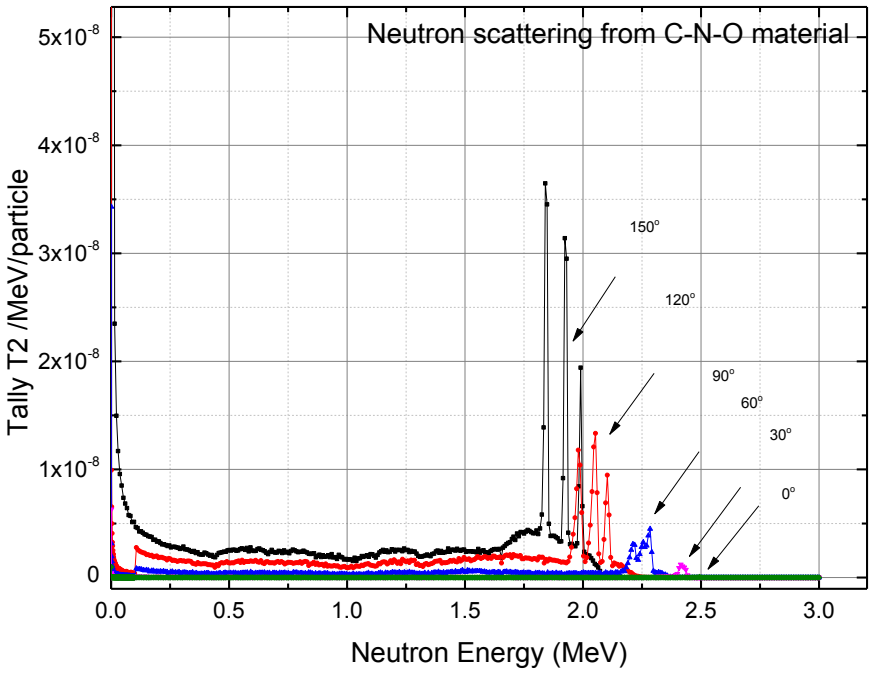

Figure 7.4: Angular dependent response for a C-N-O content material.

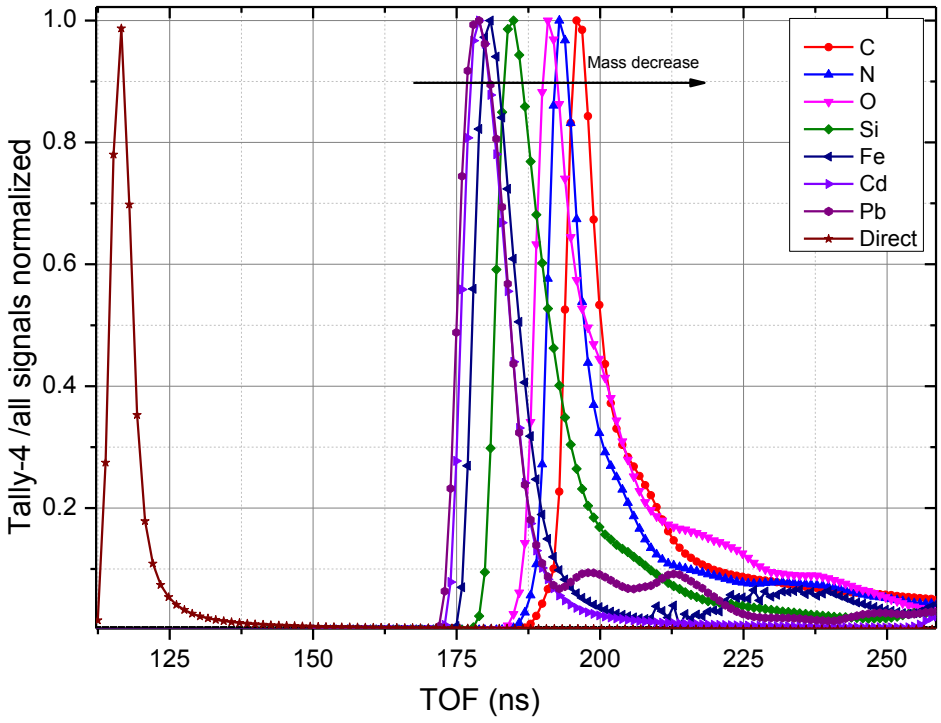

Figure 7.5: TOF simulation for different elements, the detector was set at three meters from the target can, and the angle of scattering was 140°; the source energy was 2.5 MeV.

The TOF technique will be an advantage to measure responses in the time domain if we have a pulsed and monoenergetic neutron source. For example, for a 2.5 MeV neutron source a distance of ~3 meters is needed to be able to separate the energies in the response. A high neutron flux of at least 10^9 n/pulse is also needed. The times of flight corresponding to different elements, including light and heavy ones, are shown in Figure 7.5. The source of neutrons was set at (0,0,0), the target material was set at (0, -80,0) and the backscattering detector was at (200,-150,0). This gives a target-detector distance of ~3 m, and a scattering angle of 140°. The signals show a TOF difference according to the mass of the element. The neutron source was modeled as a pulse with 5 ns FWHM.

7.3.2 MCNPX simulation code results

In our experiment simulations, we neglected the time of flight measurement as the KSU-DPF neutron flux does not allow the measurement of TOF. The responses for the five gallons targets are shown in Figure 7.6 and Figure 7.7. The three responses of the plastic scintillators in the first figure were recorded by the modified F6 tally. In general the response is directly proportional to the average nuclear mass of the material.

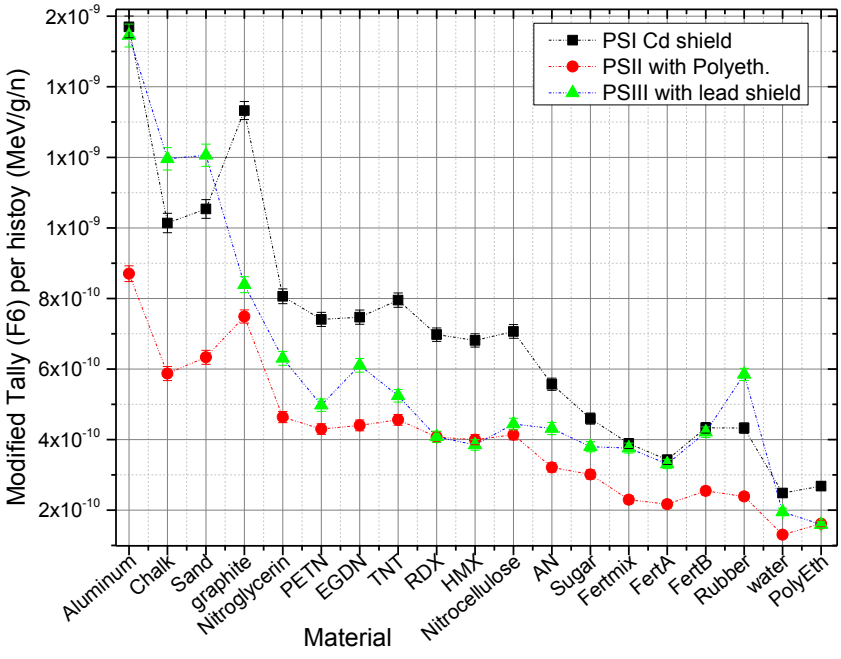

Figure 7.6: Five gallons target MCNPX simulation, the three plastic scintillators responses.

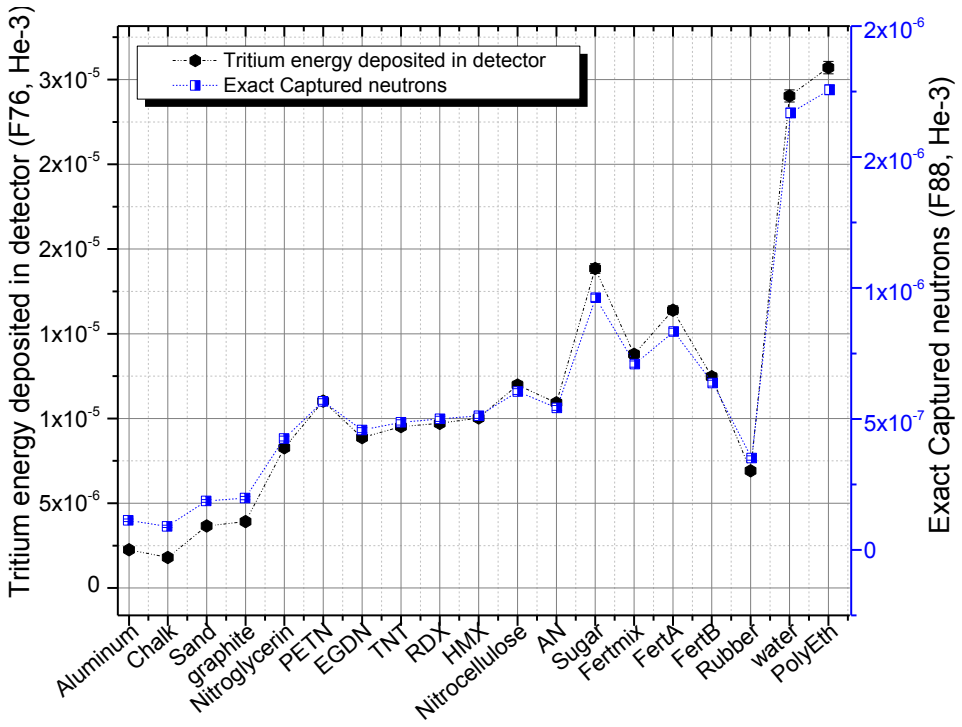

Figure 7.7: Five gallons target MCNPX simulation, ^{3}He detector response.

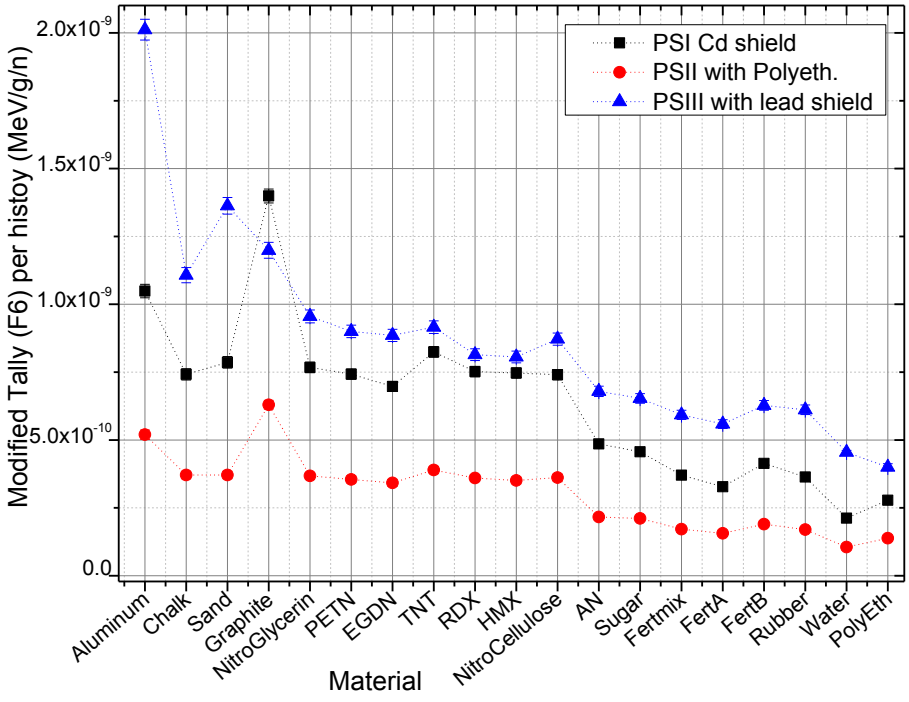

Figure 7.8: One gallons target MCNPX simulation, the three plastic scintillators responses.

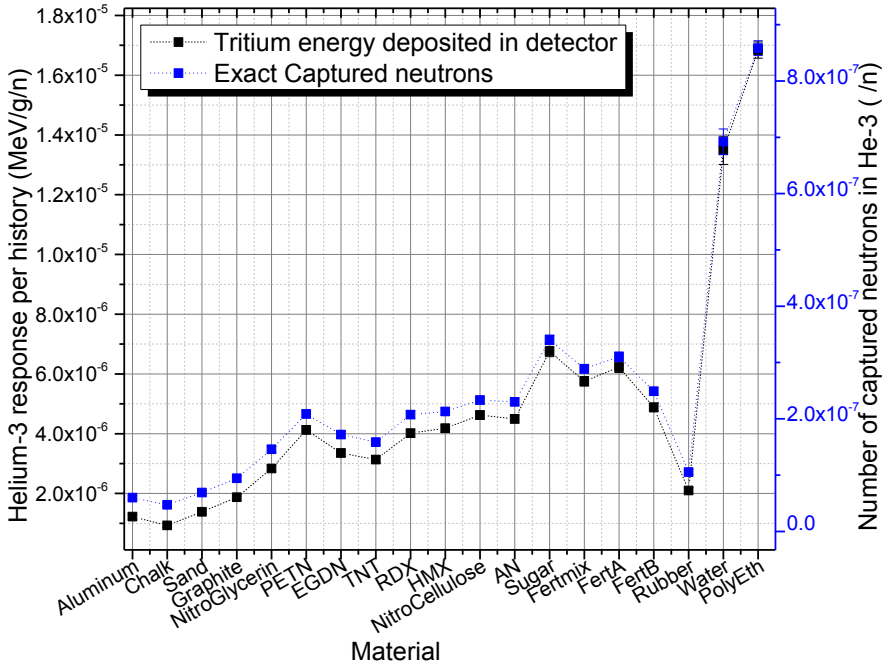

Figure 7.9: One gallon target MCNPX simulation, ^{3}He detector response.

The bare ^{3}He tube responses recorded by the two methods are consistent and show a relationship between the hydrogen contents and the response value. Irregular points from samples like graphite or rubber come from both density effects and the scattering cross section of the material elements. The polyethylene shield was shown to reduce the response as it is a good absorber for neutrons. The responses of the one gallon cans are shown in Figure 7.8, and Figure 7.9. The responses have similar behavior to the responses from the five gallons cans. The graphs of simulation results show reasonable agreement between experiment and simulation.

7.3.3 Tally error reduction

The tally error was recorded as a function of the number of particles simulated (NPS). The simulation was performed with a PC machine with Intel® Xeon® Processor E3-1225 (6M Cache, 3.10 GHz), and 8GB DDRIII ram. The error was recorded for biased (directed) and non-biased (isotropic) neutron sources.

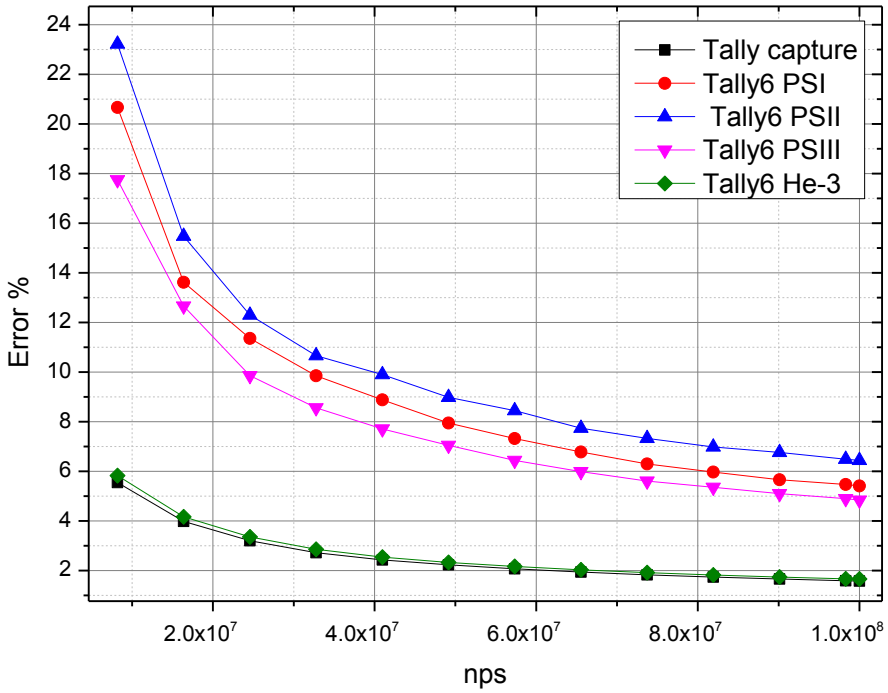

Figure 7.10: Non-biased source tally error for the 5 gallons target, simulation time 470 minutes.

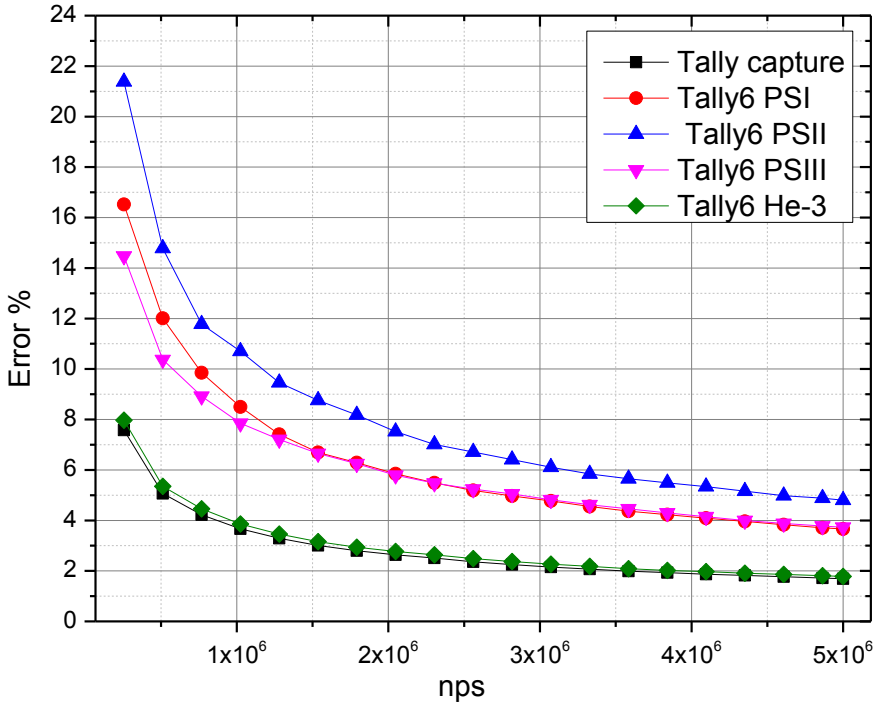

Figure 7.11: Biased source tally error for the 5 gallons target, simulation time 118 minutes.

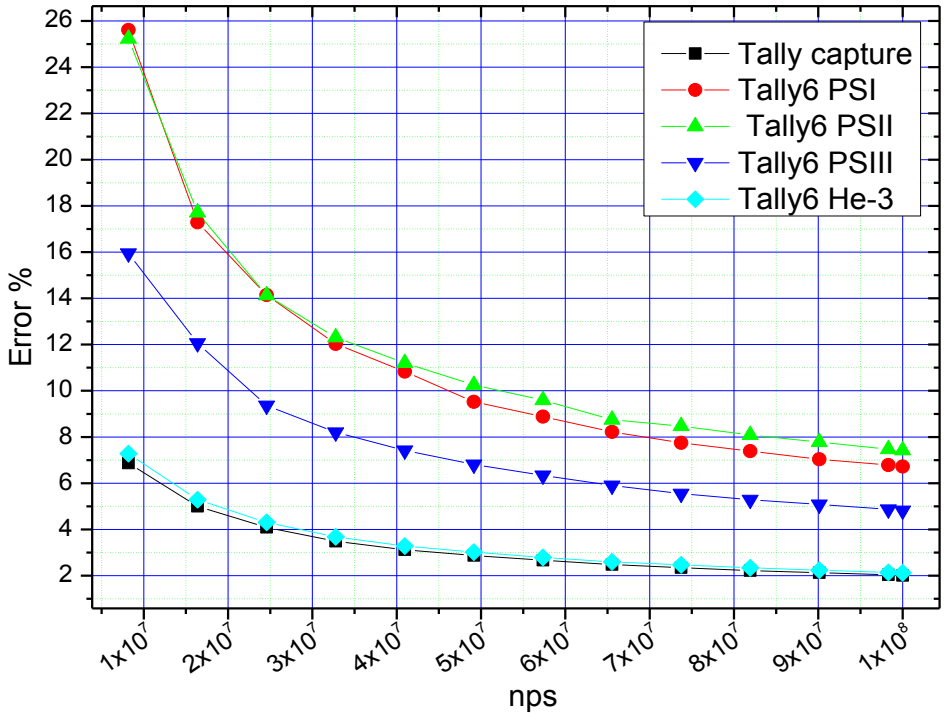

Figure 7.12: Non biased source tally error for the one gallon target, simulation time 464 minutes.

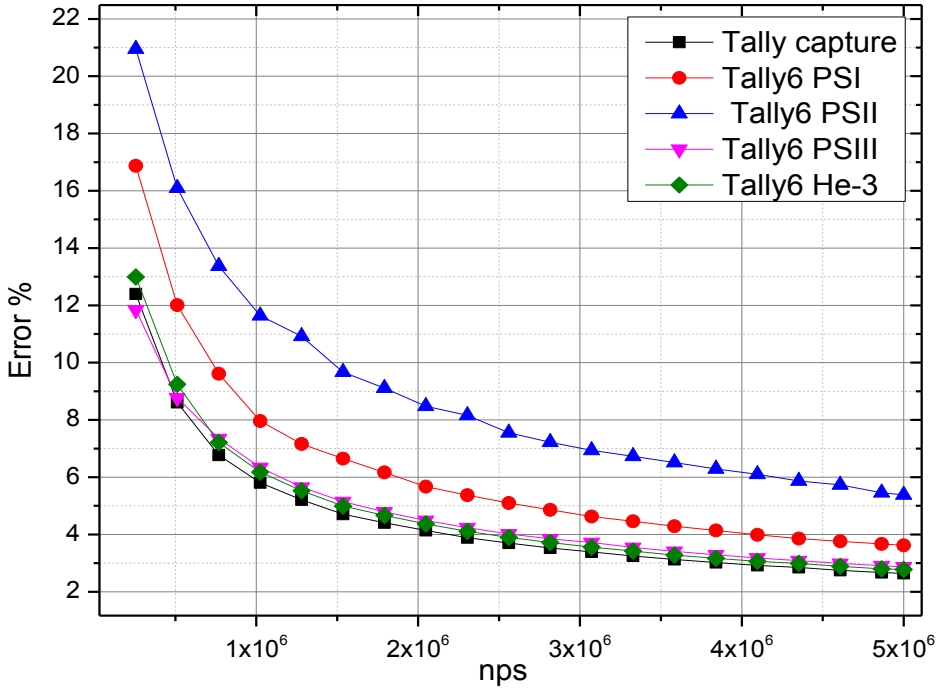

Figure 7.13: Biased source tally error for the one gallon target, simulation time 93 minutes.

The error results for Fert-mix shows better results and smaller error percentage for the biased source even though the NPS for the biased case is lower by twenty times. The simulation time for the five gallon cans was reduced four times by the source biasing, and five times for the one gallon simulations.

7.4 Figure of Merit results

The Figure of Merit FOM and its standard deviation was calculated in the same as for the experimental work through equations (3.22) and (3.23), respectively. A Matlab code written for that purpose gave the results below. The Fertilizer-mi and TNT explosive were used a templates.

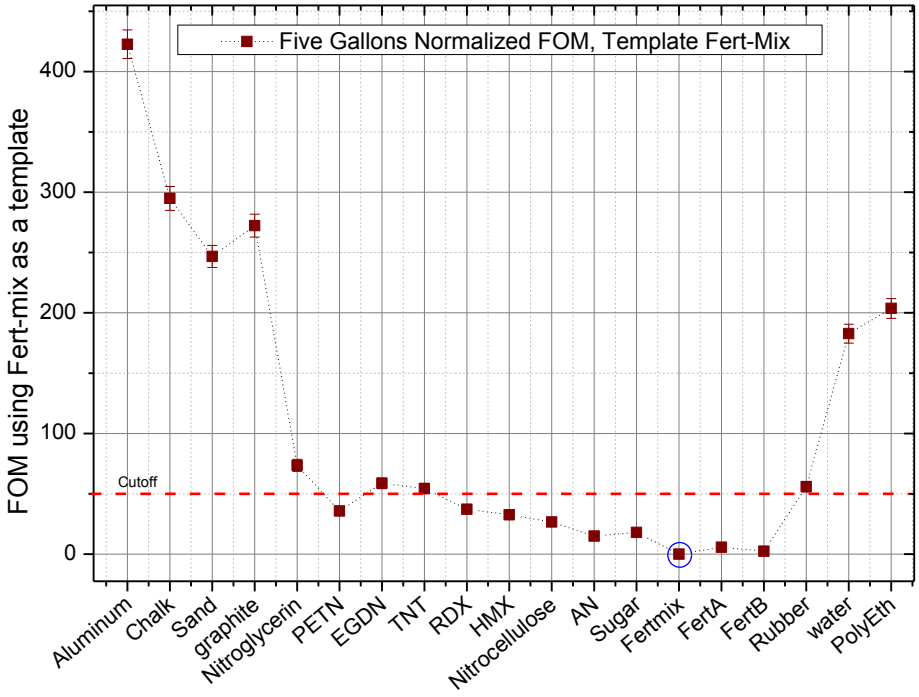

Figure 7.14: FOM for the five gallons target, Fert-Mix was used as a template.

The FOM in Figure 7.14 shows that the three kinds of fertilizers were differentiated with an FOM ~ equal to zero. Using a threshold of 50, six materials were differentiated as explosive like (similar to the Fert-Mix), five were true positive TP and one (sugar) was identified as a false positive FP. Three explosives (TNT, EGDN, and nitroglycerin) were indicated as false negative FN, The rest of the materials were true negative TN, while the rubber material was near the

threshold line. Using TNT as a real explosive template, the FOM was able to identify all the seven explosives, as shown in Figure 7.15. The valued of the FOM for all explosives were less than seven. The ammonium nitrate was identified by a FOM value of 13. Using a threshold of 50, Fert A was identified as an inert material, which in reality it is. The nine inert materials were identified as true negatives. Fert-Mix and Fert-B lied on the threshold and may be considered as suspect; that is because the fertilizer has a relatively similar construction to the explosives but with different density.

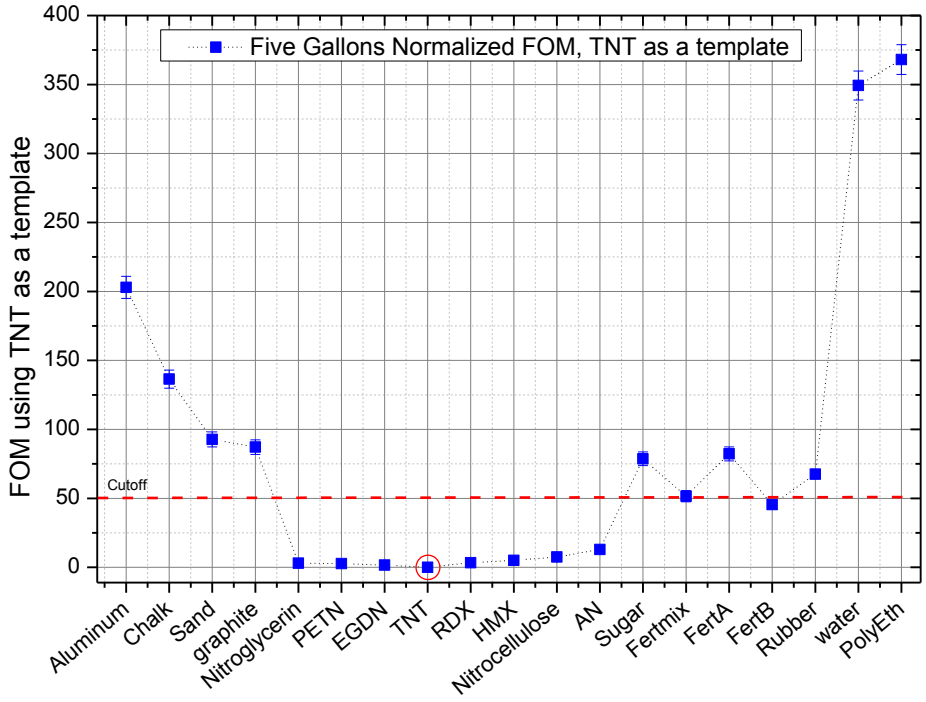

Figure 7.15: FOM for the five gallons target, TNT was used as a template.

The FOM for the one gallon cans is shown in Figure 7.16, where the responses from Fert-Mix are used as the template. The FOM was able to identify the Fert-A and B, and ammonium nitrate as like materials. The sugar was identified as a FP; all the other materials are identified as TN except rubber was a suspect. The FOM when TNT was used as a template is shown in in Figure 7.17. The seven explosives again were identified as TP with an FOM less than seven. The ammonium nitrate was also identified as a TP with a higher value of 37, the chalk and sand could not be identified as inert in the small cans and gave FP signals. All other materials were identified successfully as TN, except Fert-B may be considered as suspect.

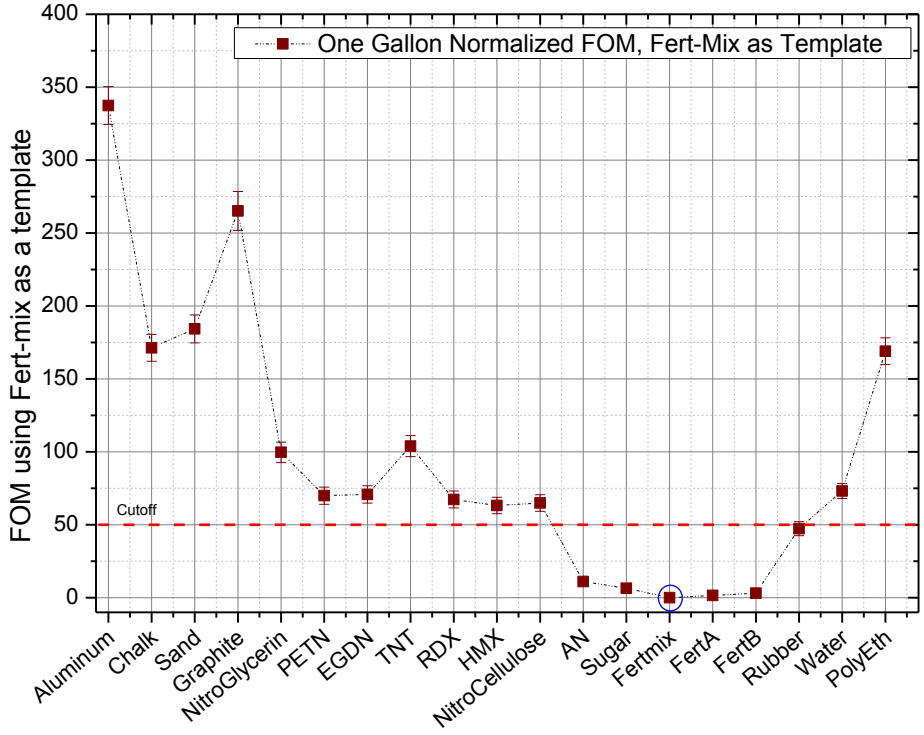

Figure 7.16: FOM for the one gallons target, Fert-Mix was used as a template.

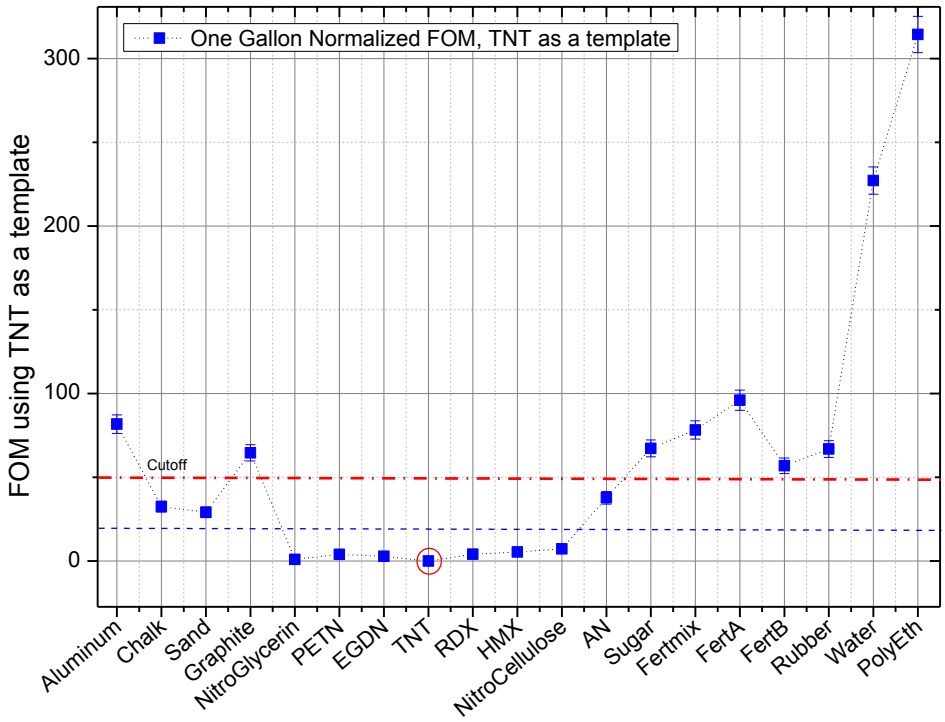

Figure 7.17: FOM for the one gallons target, TNT was used as a template.

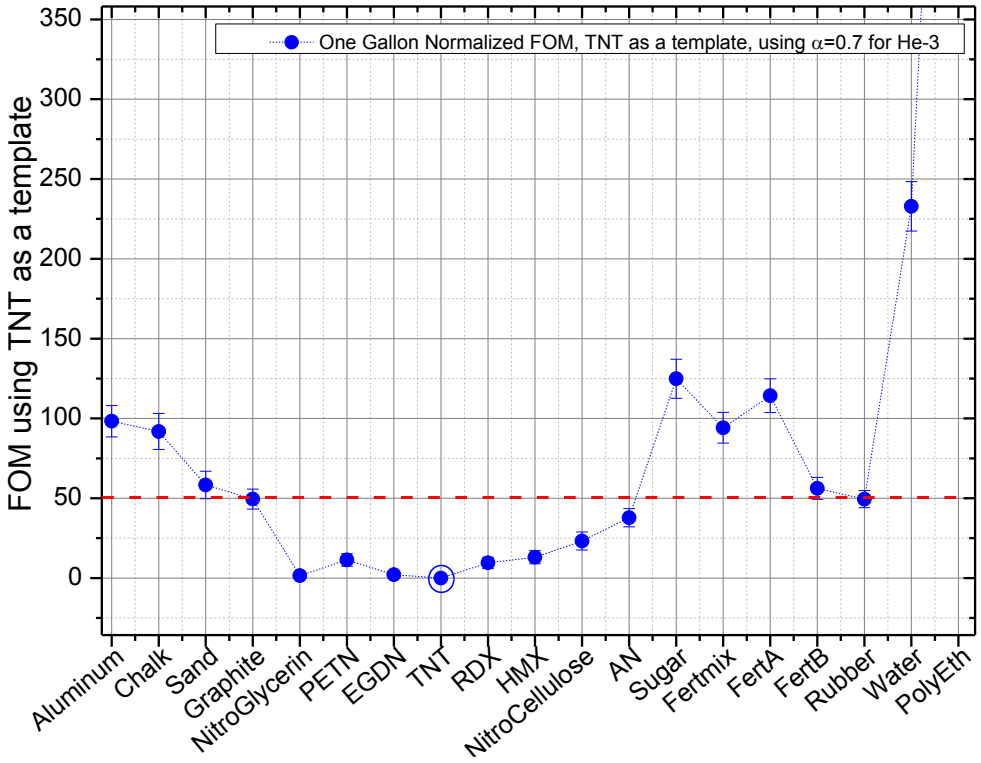

Figure 7.18: FOM for the one gallons target, TNT was used as a template, alpha for 3-HE =0.7, other detectors have alpha=0.1 each.

A change of the weight factor (α value) can change the FOM identification of the materials. By giving the ^{3}He tube higher importance of 0.7 instead of equal importance, the FOM construction changed a little. The explosives in Figure 7.18 were still identified as TP including ammonium nitrate, while sand and chalk had higher values and escaped to the TN region. On the other hand, the graphite and rubber fell down to touch the threshold and gave suspect signals.

Chapter 8 - **Conclusions and Future Work**

In this dissertation we described the construction and performance of a nuclear radiation source device that contributed to the nuclear program at Kansas State University. The machine is known as the Kansas State University dense plasma focus (KSU-DPF) device. The KSU-DPF machine was designed and operated in early 2010 as a 2.5 kJ device. After a failure of the initial capacitor, we redesigned the capacitor connection part of the machine using a new GA 12.5 μF capacitor, which upgraded the maximum energy to 10 kJ. The machine was diagnosed to determine the optimum performance as a radiation source for X rays, ions and monoenergetic neutrons of ~2.5MeV. The machine as a neutron source was used for the purpose of neutron based material detection. The SBRS method was used to investigate materials and identify the materials that match a certain predefined template.

In this chapter we give our conclusion about the performance of the machine, the use of the SBRS technique for material detection, and the use of MCNP simulations as a trusted and powerful means to assess the DPF device for the purpose of material detection. Future suggested work is mentioned in the second part of the chapter.

8.1 KSU-DPF machine performance

The KSU-DPF was successfully designed and operated as a Mather type plasma focus machine. The machine has a size of 28” (W) × 34” (L) × 72” (H), and is mounted on a movable base. The machine is connected to a vacuum system of rotary and turbo-molecular pumps, and is electrically connected to a 40kV GA power supply. These characteristics give the capability for the machine to be a movable machine or carried on a truck for field applications.

The short circuit analysis for the machine electric circuit was successful to determine the machine’s basic static electric parameters. The period time was calculated to be 6.65 μs, from which the first quarter reaches a maximum current at ~1.66 μs. At this time the maximum compression of the plasma is expected. The inductance of the machine was measured to be ~90 nH. This is a relatively high inductance compared to other similar machines. This inductance is thought to be responsible for a longer compression region and for producing multiple dips in the compression region [181, 196]. The Rogowski coil was found to be efficient in measuring the

discharge current waveform. The dI/dt signal was integrated at the beginning by an R-C circuit but was noisy. Later, we found it was easier to numerically integrate the signal. This gave a good current signal. The powerful Tektronix digital oscilloscopes provided the ability to follow the fast signals of the plasma focus.

The high pressure test was performed as an alternative to the SC test for the machine. The test is important for the high discharge current machines (>0.2 MA) where the short circuit test is hard to perform. The induced error percentage due to the motion of the current sheet was calculated. These results can be used to correct the values calculated with HP tests, and can be applied fairly well on other dense plasma focus machines with different geometries and energy scales. The resulting values for the inductance and resistance incorporate contributions due to the motion of the current sheet. This motion has a dependence on the pressure and gas molecular weight. In the high pressure regime the KSU-DPF is operating as a low speed device and has a low shock wave speed. In such a regime, the coupling of energy provided to the plasma is predominantly through diffusive electrical discharge rather than electromagnetic piston-like discharge. The HP regime speed is about one fourth of the current sheet speed during the normal operational conditions.

In the high pressure regime the KSU-DPF is operating at low shock wave speed; in such a regime the coupling of energy provided to the plasma is predominantly through diffusive electrical discharge rather than electromagnetic piston-like discharge. Nevertheless the data indicate that there is downstream motion of the diffusive structure, which we interpret as due to electromagnetic drive. Moreover the data for the average speed are found to be proportional to $(1/\rho)^{0.5}$. We presented this technique as a useful alternative method to the short circuit (SC) test in order to find out the static parameters for the machine where SC is hard to be performed. The deviation in L and R is proportional also to $(1/\rho)^{0.5}$ where ρ is the gas density. The snow plow equation was easy to imply and efficient to describe the behavior of the current sheet during the high pressure regime, it should be noted that it is still an approximation when compared to other methods of using the equation of motion coupled to the circuit equation [197].

The time to pinch shows a linear relation with the filling gas density. This gives an average axial speed of the current sheet of 6 cm/μs at a pressure of 5 mbar deuterium. When the capacitor is charged to 17 kV, the current peak was around 145 kA at a pressure of 3.37 torr. The

speed factor ($I_p/r_a/P_t$) of the machine is 105 kA/cm/torr D_2, where I_p is the peak of the current, r_a is the anode radius, and P_t is the pressure in torr. This value is believed to control the speed of the current sheet in the axial and radial phases and is responsible for the strength of neutron emission [22]. The calculated speed factor is a little higher than reported for other machines around the world with values between 82-100 kA/cm/torr D_2. The radial phase duration was longer and characterized by multiple compressions. The first compression duration gave an indication about the average radial speed. The average radial speed at 5 mbar gas pressure was about 18 cm/μs. This is three times more than the axial speed. The multiple compressions may be attributed to a stored energy beyond the magnetic piston that exerts further compressions. Others have postulated the existence of anomalous resistance formed during the pinch time [45, 181]. The multiple pinches phenomena was rare in the low pressure region, below 2.5 mbar and the compression was more efficient.

The machine has excellent capability to develop a hard X-ray pulse on the nanoseconds scale. Radiographic images for a variety of objects exhibited good spatial resolution and high contrast, even with a single shot. The facts that good images can be obtained with a single shot and that each shot is so short makes the DPF device ideal for imaging objects in motion. It was possible to estimate the energy spectrum of the hard X rays by the step-filter method. For a neon filling gas and a copper anode, the average energy of the spectrum was 57 keV and the high energy tail reached 120 keV, characteristics that make the machine a good radiographic source for various applications. Using the tungsten anode will enhance the intensity and raise the average energy of the emitted spectrum [198]. Using neon as filling gas is responsible for the high X-ray intensity, as the full ionization of neon produces ten times the number of electrons than would be produced with deuterium or hydrogen as the gas. On the other hand, one would expect that the X-ray energy range for deuterium would be higher as the axial and radial speeds are much higher for light gases. One could consider mixing a small percentage of high Z gas into a light filling gas, to increase plasma density and increase the pinch stability. This would increase the number of free electrons in the plasma medium but still allow high speed motion of the current sheet at the same time to get strong compression [199].

The faraday cup or ion collector coupled to the R-C circuit was fast enough to follow the fast ion pulse. The TOF is a useful technique in diagnosing a dense plasma focus device. The

start time can be caught from the soft X ray signal, or the current or voltage signals, or even by using multiple ion collectors at different positions. Nevertheless, this technique faces some difficulties when multiple pinches occur and signals overlap. The use of ion spectrometers or nuclear track detectors may help if used in combination with the faraday cup.

The ion beam and hard X-ray emissions occur simultaneously; hence the ion and electron acceleration in the pinch have the same electric field and are subjected to the same conditions. The optimum pressure in the DPF has two modes, depending on the desired output radiation. The optimum pressure for ion emission usually occurs in the low pressure regime, where the gas density is low and the shock speed is high. The pinch is characterized by a high electric field and hence produces high energy deuterons. The energy tail of the ion spectra plays a role in the neutron production as it reaches several hundreds of keV. The second mode of pressure optimization is the neutron production mode, which occurs at a higher pressure level. A higher density of the filling gas and optimum compression of the pinch which meets the highest current peak, increases neutron production. The neutron anisotropy is high at low pressure. The neutron yield is low and comes mostly from the beam target interaction. The neutron yield is high at high pressure and comes mainly from the gyro-motion acceleration and thermonuclear fusion.

The neutron yield was enhanced using the short tungsten anode instead of the copper anode. The average maximum neutron yield measured with the copper anode was 1.2×10^7, and for the short tungsten anode was about 5.0×10^7. The tungsten anode lifetime is much longer than the previously used stainless steel or copper anodes. The erosion of the tungsten anode from joule heating and the plasma and electron beam bombardment was not noticeable after hundreds of shots, this anode is suggested when using the machine in repetitive manner.

The pinch in the short anode with the low pressure side was usually sharp and limited to one pinch instead of multiple pinches. This may be because the low value of inductance added to the circuit as $L_p \propto z\,(t)$, where L_p is the plasma inductance and $z(t)$ is the distance between the conductive base of the anode and the position of the current sheet. The neutron radiation at the lower pressure side was characterized by single neutron pulse most of the time, this makes it suitable for applications related to TOF and time related neutron scattering.

8.2 Neutron based SBRS material detection

The SBRS method using neutron generated signatures was able to identify the targets which are close in composition and density to the target that was used to generate the template. The signatures depend on the contents of the material and especially on the average nuclear mass of the elements, the hydrogen content of the material, and the material density. Other factors such as the neutron scattering cross section are important for elements with unusual cross-section values. The suppression of inelastic gamma rays picked up by the plastic scintillator was a powerful method using digital filters as the gamma signal has faster decay time than neutron signal. The bare ^{3}He detector was the best to determine hydrogen content of the material as it is not sensitive to X rays and gamma rays and has almost zero sensitivity to fast neutrons. Most hydrogen-rich compounds, for which the ^{3}He detector gives high relative counts, are non-explosive, however narcotics contain hydrogen and templates could be developed to detect drugs. When using an explosive surrogate to generate the template, other explosive surrogates were identified as true positives using the SBRS methodology. Non-organic/metals and organic targets were generally identified as true negatives, with some exceptions. The density of the material plays a role in determining the responses. In the case of rubber mulch, the low density leads to a low ^{3}He response. The detector responses were also sensitive to induced radiation emitted from radiation interactions with the shielding of the machine, but this would have been fairly repeatable and induced less than four counts background for the ^{3}He detector.

The plastic scintillators suffered from electromagnetic interference and stray neutrons and gamma rays coming from the shielding and the surroundings. This signal-to-noise ratio was acceptable in the case of the five gallon targets, but was poor in the case of the one gallon cans.

Because the plastic scintillators were placed only about 20 cm from the target, the neutron TOF technique was difficult to use. The neutron TOF technique to measure the scattered neutron energy requires placement of detectors at large distances. But a larger detector area is required to compensate for the reduction in the solid angle of the detector from the target. Fortunately plastic scintillators are produced in different sizes and may reach several feet in diameter and a few inches in thickness [200, 201]. This should be taken into consideration in future research. The value of alpha (signature weight) can be used to adjust the importance of certain signatures. For instance, when the ^{3}He weight was higher, this helped differentiating organic materials or water.

8.3 MCNP/X calculations

The MCNP/X code was used for the simulation of a d-d neutron source. Scattering from both the experiment shielding and the target was modeled. The MCNP/X code was successfully used to convert neutron energy deposited in the plastic scintillator into a corresponding light signal. This complex process is complex includes kinetic energy transfer between the incident neutron and the recoil proton. The proton energy deposition and conversion into light in the crystal was shown to be a nonlinear process and needed a DE/DF card for modelling.

Two kinds of neutron source biasing were used, the isotropic source and a direction biased source. Both gave similar results. The calculated error in the tally when the biased source was used was smaller by two orders of magnitude. The code was able to simulate real explosives, which we could not investigate in the laboratory. By comparing simulation and laboratory results for explosive surrogates and getting good agreement, we can then confidently use simulation results to establish predicted templates for real explosives or other materials to be detected. The simulation indicated that the error can be greatly decreased by avoiding the sources of noise and modifying the source strength and detector size. The simulation showed that the used explosives have similar structures from the nuclear point of view, although it may have different chemical structure. The FOM from the MCNP/X results is useful in determining the threshold line that separates inert from explosive targets.

The MCNP/X code is a powerful tool to predict the signature values. It can be used to determine the optimum source-target and target-detector distances, detector size and position to obtain the highest responses. It can also be used to determine the detector separation from the target that will allow real detectors to accurately measure TOF. The MCNP model used for measuring the neutron TOF indicated that neutron backscattered radiation at 150^{o} needed at least 3 meters distance between target and detector. This minimum distance will increase for 14MeV neutrons in case of a D-T neutron source. The neutron scattering calculations in MCNP indicated that the best peak separation for the neutron TOF occurs at the highest possible scattering angle.

One problem with MCNP/X calculations occurs when materials are porous. The best approach is to adjust the density of the material but this is only an approximate fix. The environmental background from electromagnetic noise and stray particles is not accounted for in the MCNP simulations.

The neutron based screening and explosive detection is not yet commercialized to work in ports and borders like the X-ray based techniques are. This is partially because the neutron sources produce activation in the targets and are often radioactive materials themselves. Neutron-based techniques are sometimes difficult to implement [101, 202] because of cost or complexity. These problems can be addressed in three ways. First, fabricate a stable nonradioactive neutron source, like the d-d or d-t sources. Second, develop an effective combination of responses, including neutron responses and secondary induced particle/gamma rays responses that is shown to be effective in discriminating explosives from inerts. Third, suitable shielding must be designed that reduces dose to levels acceptable for commercial use.

8.4 Future research

The future research should focus on four areas. First, enhancement of the DPF neutron intensity and speed of the pulse. Second, detector enhancement by using larger detectors with faster response times. It would also be good to add more kinds of signatures than only the fast and thermalized scattered neutrons. Third, more complex geometries should be considered that include "clutter" (materials other than the container and a single material as contents) in order to find the effect of interference on the material interrogation signatures. Fourth, use MCNP for simulation of more materials and more geometries using d-d or d-t sources. We suggest some steps that may enhance the system of interrogation.

- The KSU-DPF should be upgraded to work at a full power of 10 kJ to provide one to two orders of magnitude higher neutron intensity. High neutron emission gives a higher capability to detect material at greater stand-off and hence in a safer mode. The existing jitter-thyratron should be replaced and the electric insulation should be modified to comply with the new energy dissipated by the machine. The pulse duration of the DPF should be as short as possible for the TOF technique to work. The stainless steel KSU-DPF chamber needs to change to separate the capacitor and main components from the chamber in order to reduce neutron scattering by the equipment. An aluminum chamber may be preferred as it will interfere less with the neutrons.

  Using different anode tips to increase or decrease X- rays according to the required application. In neutron based material interrogation it may be required to suppress

the X-ray emission so as not to interfere with the neutron signals. A suggestion is to use a graphite anode tip and/or hollow tube anodes and measure the effect on the neutron production and X-ray suppression. This may limit the shielding needed for the X- rays and hence limit the inelastic scattering between the neutrons and such shields. This also removes a component of the unwanted gamma rays induced by the surrounding components.

- Combine the neutron scattering signatures with gamma ray signatures. These signatures will enhance the capability to interrogate for special nuclear materials. The utilization of prompt gamma activation analysis (PGAA) and inelastic gamma measurements as new signatures will increase the detection efficiency and provide additional capabilities such as quantitative analysis. The signatures of the PGAA and inelastic gamma rays were discussed briefly in paragraphs 3.3, and 3.3. If the machine is working in a repetitive mode a timing configuration will be needed to measure the inelastic gamma rays at the time of the neutron pulses, and the prompt gamma rays that come hundreds of nanoseconds after. A fast gamma ray detector with good efficiency will be needed for such purpose. The new $LaBr_3$(Ce) scintillators [203, 204] have better resolution, faster response and higher light yield than the conventional NaI(Tl) detectors, but are also more expensive.

- The Monte Carlo technique should be used to build new templates in order to detect more types of explosives and other threatening materials. These templates should be contained in a database and updated periodically.

- Investigate targets with clutter present, and determine the change in signatures corresponding to such clutter. This should be performed both experimentally and by Monte Carlo simulation.

Finally the DPF machine is a multi-radiation source that is fairly simple to design and operate and can be used for various applications. The pulsed X rays can be used to radiograph moving targets. The machine also can be used as a neutron source in applications such as measuring moisture content of samples and oil well logging. Efforts are being made to replace dangerous

radiological sources with machine sources. The oil industry has long used radioisotope neutron sources and DPF devices offer a safer alternative neutron source for well logging applications.

REFERENCES

[1] J. W. Mather and P. J. Bottoms, "Characteristics of the dense plasma focus discharge," *Phys. Fluids,* vol. 11, pp. 611, 1968.

[2] S. Lee, "Plasma focus radiative model: Review of the Lee model code," *J. Fusion Energy,* vol. 33, pp. 319-335, 2014.

[3] J. Marshall, "Acceleration of plasma into vacuum," *Journal of Nuclear Energy (1954),* vol. 7, pp. 276-276, 1958.

[4] J. Mather, "15. Dense Plasma Focus," *Methods in Experimental Physics,* vol. 9, pp. 187-249, 1971.

[5] W. Stygar, G. Gerdin, F. Venneri and J. Mandrekas, "Particle beams generated by a 6–12.5 kJ dense plasma focus," *Nucl Fusion,* vol. 22, pp. 1161, 1982.

[6] A. Bernard, P. Cloth, H. Conrads, A. Coudeville, G. Gourlan, A. Jolas, C. Maisonnier and J. Rager, "The dense plasma focus—A high intensity neutron source," *Nucl. Instrum. Methods,* vol. 145, pp. 191-218, 1977.

[7] U. J. a. H. Herold, "Fast ion kinetics and fusion reaction mechanism in the plasma focus," *Nucl Fusion,* vol. 27, pp. 407, 1987.

[8] F. Castillo, M. Milanese, R. Moroso and J. Pouzo, "Evidence of thermal and non-thermal mechanisms coexisting in dense plasma focus DD nuclear reactions," *J. Phys. D,* vol. 33, pp. 141, 2000.

[9] K. Frank, E. Boggasch, J. Christiansen, A. Goertler, W. Hartmann, C. Kozlik, G. Kirkman, C. Braun, V. Dominic, M. A. Gundersen, H. Riege and G. Mechterscheimer, "High-power pseudospark and BLT switches," *Plasma Science, IEEE Transactions On,* vol. 16, pp. 317-323, 1988.

[10] J. Urban and K. Frank, "Cold cathode thyratron development for pulsed power applications," in *Power Modulator Symposium, 2002 and 2002 High-Voltage Workshop. Conference Record of the Twenty-Fifth International,* 2002, pp. 217-220.

[11] F. F. Chen and A. Trivelpiece, "Introduction to plasma physics," *Phys Today,* vol. 29, pp. 54, 1976.

[12] M. A. Lieberman and A. J. Lichtenberg, "Principles of plasma discharges and materials processing," *MRS Bull,* vol. 30, pp. 899-901, 1994.

[13] K. Burm, "Calculation of the Townsend discharge coefficients and the Paschen curve coefficients," *Contributions to Plasma Physics,* vol. 47, pp. 177-182, 2007.

[14] M. Zakaullah, I. Ahmad, G. Murtaza, M. Yasin and M. M. Beg, "Effect of insulator sleeve contamination on the low energy plasma focus performance," *Fusion Eng. Des.,* vol. 23, pp. 359-365, 1, 1994.

[15] M. Zakaullah, T. J. Baig, S. Beg and G. Murtaza, "Effect of insulator sleeve length on neutron emission in a plasma focus," *Physics Letters A,* vol. 137, pp. 39-43, 5/1, 1989.

[16] A. Shyam and R. Rout, "Effect of anode and insulator materials on Plasma Focus sheath (pinch) current," *Plasma Science, IEEE Transactions On,* vol. 25, pp. 1166-1168, 1997.

[17] M. Sadowski and M. Scholz, "The main issues of research on dense magnetized plasmas in PF discharges," *Plasma Sources Sci. Technol.,* vol. 17, pp. 024001, 2008.

[18] N. Tsagas, G. Mair and A. Prinn, "Motion and shape of snowplough sheets in coaxial accelerators," *J. Phys. D,* vol. 11, pp. 1263, 1978.

[19] A. Prinn and B. Ricketts, "Experimental study of a continuous flow pinch," *J. Phys. D,* vol. 5, pp. 2026, 1972.
[20] M. Scholz, B. Bieńkowska, I. Ivanova-Stanik, L. Karpiński, R. Miklaszewski, M. Paduch, W. Stępniewski, K. Tomaszewski and M. Sadowski, "The physics of a plasma focus," *Czechoslovak Journal of Physics,* vol. 54, pp. C170-C185, 2004.
[21] L. Soto, "New trends and future perspectives on plasma focus research," *Plasma Phys. Controlled Fusion,* vol. 47, pp. A361, 2005.
[22] P. Lee and A. Serban, "Dimensions and lifetime of the plasma focus pinch," *Plasma Science, IEEE Transactions On,* vol. 24, pp. 1101-1105, 1996.
[23] A. Toepfer, D. Smith and E. Beckner, "Ion heating in the dense plasma focus," *Phys. Fluids,* vol. 14, pp. 52, 1971.
[24] M. Haines, "A review of the dense Z-pinch," *Plasma Phys. Controlled Fusion,* vol. 53, pp. 093001, 2011.
[25] J. D. Jackson and R. F. Fox, "Classical electrodynamics," *American Journal of Physics,* vol. 67, pp. 841-842, 1999.
[26] J. Bittencourt, "The pinch effect," in *Fundamentals of Plasma Physics*Anonymous Springer, 2004, pp. 325-350.
[27] J. D. Huba, "NRL Plasma Formulary The Office of Naval Research," *NRL: Plasma Formulary,* 2004.
[28] T. Green and G. Niblett, "Rayleigh-Taylor instabilities of a magnetically accelerated plasma," *Nucl Fusion,* vol. 1, pp. 42, 1960.
[29] O. A. Anderson, W. R. Baker, S. A. Colgate, J. Ise and R. V. Pyle, "Neutron Production in Linear Deuterium Pinches," *Phys.Rev.,* vol. 110, pp. 1375-1387, Jun, 1958.
[30] F. Castillo-Mejía, M. M. Milanese, R. L. Moroso, J. O. Pouzo and M. A. Santiago, "Small plasma focus studied as a source of hard X-ray," *Plasma Science, IEEE Transactions On,* vol. 29, pp. 921-926, 2001.
[31] P. Knoblauch, F. Di Lorenzo, V. Raspa, A. Clausse and C. Moreno, "Design, hard x-ray source characterization and applications of a plasma focus tailored for flash hard x-ray imaging," *Phys. Scripta,* vol. 2008, pp. 014033, 2008.
[32] M. Barbaglia, L. Soto and A. Clausse, "Dependence of Hard X-ray Emissions with the Charging Pressure in a Small Plasma Focus," *J. Fusion Energy,* vol. 31, pp. 105-108, 2012.
[33] H. Bruzzone, H. Acuña and A. Clausse, "Neutron correlations with electrical measurements in a plasma focus device," *Brazilian Journal of Physics,* vol. 38, pp. 117-122, 2008.
[34] H. Bhuyan, M. Favre, E. Valderrama, H. Chuaqui and E. Wyndham, "Experimental studies of ion beam anisotropy in a low energy plasma focus operating with methane," *J. Phys. D,* vol. 39, pp. 3596, 2006.
[35] J. K. Shultis and R. E. Faw, *Fundamentals of Nuclear Science and Engineering Second Edition.* CRC Press, 2007.
[36] R. Eisberg and R. Resnick, "Quantum physics of atoms, molecules, solids, nuclei, and particles," 1974.
[37] M. Chadwick, P. Obložinský, M. Herman, N. Greene, R. McKnight, D. Smith, P. Young, R. MacFarlane, G. Hale and S. Frankle, "ENDF/B-VII. 0: Next generation evaluated nuclear data library for nuclear science and technology," *Nuclear Data Sheets,* vol. 107, pp. 2931-3060, 2006.

[38] E. Sindoni and C. Wharton, *Diagnostics for Fusion Experiments: Proceedings of the Course, Varenna, Italy, 4-16 September 1978.* Elsevier, 2013.
[39] C. Moreno, H. Bruzzone, J. Martínez and A. Clausse, "Conceptual engineering of plasma-focus thermonuclear pulsors," *Plasma Science, IEEE Transactions On,* vol. 28, pp. 1735-1741, 2000.
[40] S. Lee, "Current and neutron scaling for megajoule plasma focus machines," *Plasma Phys. Controlled Fusion,* vol. 50, pp. 105005, 2008.
[41] S. Lee and S. Saw, "Neutron scaling laws from numerical experiments," *J. Fusion Energy,* vol. 27, pp. 292-295, 2008.
[42] M. J. Bernstein and G. G. Comisar, "Neutron Energy and Flux Distributions from a Crossed- Field Acceleration Model of Plasma Focus and Z- Pinch Discharges," *Phys. Fluids,* vol. 15, pp. 700-707, 1972.
[43] M. J. Bernstein. Acceleration mechanism for neutron production in plasma focus and z - Pinch discharges. *Physics of Fluids (1958-1988) 13(11),* pp. 2858-2866. 1970. . DOI: http://dx.doi.org/10.1063/1.1692871.
[44] S. Moo, C. Chakrabarty and S. Lee, "An investigation of the ion beam of a plasma focus using a metal obstacle and deuterated target," *Plasma Science, IEEE Transactions On,* vol. 19, pp. 515-519, 1991.
[45] R. A. Behbahani and F. M. Aghamir. Anomalous resistivity effect on multiple ion beam emission and hard x-ray generation in a mather type plasma focus device. *Physics of Plasmas (1994-Present) 18(10),* 2011. . DOI: http://dx.doi.org/10.1063/1.3647958.
[46] M Zakaullah and Ijaz Akhtar and A Waheed and Khalid Alamgir and Anwar Z Shah and,G.Murtaza, "Comparative study of ion, x-ray and neutron emission in a low energy plasma focus," *Plasma Sources Sci. Technol.,* vol. 7, pp. 206, 1998.
[47] F L Curzon and R T Hodgson and,R.J.Churchill, "Excitation of m = 0 instabilities in a Z - pinch discharge," *Journal of Nuclear Energy.Part C, Plasma Physics, Accelerators, Thermonuclear Research,* vol. 6, pp. 281, 1964.
[48] S. Springham, S. Lee and S. Moo, "Deuterium plasma focus measurements using solid state nuclear track detectors," *Brazilian Journal of Physics,* vol. 32, pp. 172-178, 2002.
[49] G. Decker, L. Flemming, H. Kaeppeler, T. Oppenlander, G. Pross, P. Schilling, H. Schmidt, M. Shakhatre and M. Trunk, "Current and neutron yield scaling of fast high voltage plasma focus," *Plasma Physics,* vol. 22, pp. 245, 1980.
[50] S. Lee, "Neutron yield saturation in plasma focus: A fundamental cause," *Appl. Phys. Lett.,* vol. 95, pp. 151503-151503-3, 2009.
[51] S. Lee and S. Saw, "Pinch current limitation effect in plasma focus," *Appl. Phys. Lett.,* vol. 92, pp. 021503, 2008.
[52] V. Gribkov, A. Banaszak, B. Bienkowska, A. Dubrovsky, I. Ivanova-Stanik, L. Jakubowski, L. Karpinski, R. Miklaszewski, M. Paduch and M. Sadowski, "Plasma dynamics in the PF-1000 device under full-scale energy storage: II. Fast electron and ion characteristics versus neutron emission parameters and gun optimization perspectives," *J. Phys. D,* vol. 40, pp. 3592, 2007.
[53] S. Saw and S. Lee, "Scaling laws for plasma focus machines from numerical experiments," *Energy and Power Engineering,* vol. 2, pp. 65, 2010.
[54] Mandrekas,W.Stygar and G.Gerdin and F.Venneri and J., "Particle beams generated by a 6–12.5 kJ dense plasma focus," *Nucl Fusion,* vol. 22, pp. 1161, 1982.

[55] M. Sadowski, Ż, J. ebrowski, E. Rydygier, H. Herold, U. Jäger and H. Schmidt, "Multi-spike structure of ion pulses generated by plasma focus discharges," *Physics Letters A,* vol. 113, pp. 25-31, 11/25, 1985.
[56] B. B. Nayak, B. S. Acharya, S. R. Mohanty, T. K. Borthakur and H. Bhuyan, "Surface nitriding of graphite substrate by plasma focus device towards synthesis of carbon nitride coating," *Surface and Coatings Technology,* vol. 145, pp. 8-15, 8/1, 2001.
[57] R. Rawat, P. Lee, T. White, L. Ying and S. Lee, "Room temperature deposition of titanium carbide thin films using dense plasma focus device," *Surface and Coatings Technology,* vol. 138, pp. 159-165, 2001.
[58] C. R. Kant, M. Srivastava and R. Rawat, "Dense plasma focus energetic ions based fullerene films on a Si (111) substrate," *Physics Letters A,* vol. 239, pp. 109-114, 1998.
[59] M. Srivastava, S. Mohanty, S. Annapoorni and R. Rawat, "Diode like behaviour of an ion irradiated polyaniline film," *Physics Letters A,* vol. 215, pp. 63-68, 1996.
[60] E. Angeli, A. Tartari, M. Frignani, D. Mostacci, F. Rocchi and M. Sumini, "Preliminary results on the production of short-lived radioisotopes with a Plasma Focus device," *Applied Radiation and Isotopes,* vol. 63, pp. 545-551, 2005.
[61] M. Descalle, D. Manatt and D. Slaughter, "Analysis of manifests for containerized commodities imported through US ports," in *Nuclear Science Symposium Conference Record, 2006. IEEE,* 2006, pp. 275-280.
[62] (2015). *FedEX Fact Sheet, Quarter ended December 17, 2014.* Available: http://about.van.fedex.com/our-story/company-structure/corporate-fact-sheet/.
[63] A. K. Novakoff, "FAA bulk technology overview for explosives detection," in *Applications in Optical Science and Engineering,* 1993, pp. 2-12.
[64] A. Guermazi, D. Hayashi, S. E. Smith, W. Palmer and J. N. Katz, "Imaging of blast injuries to the lower extremities sustained in the Boston Marathon bombing," *Arthritis Care & Research,* vol. 65, pp. 1893-1898, 2013.
[65] L. GRODZINS, "Photons in- photons out: Non-destructive inspection of containers using x ray and gamma ray techniques," in *FAA, Proceedings of the First International Symposium on Explosive Detection Technology P 201-231(SEE N 93-21856 07-03),* 1992, .
[66] S. Singh and M. Singh, "Explosives detection systems (EDS) for aviation security," *Signal Process,* vol. 83, pp. 31-55, 2003.
[67] R. G. Ewing, M. J. Waltman, D. A. Atkinson, J. W. Grate and P. J. Hotchkiss, "The vapor pressures of explosives," *TrAC Trends in Analytical Chemistry,* vol. 42, pp. 35-48, 1, 2013.
[68] K. Wells and D. A. Bradley, "A review of X-ray explosives detection techniques for checked baggage," *Applied Radiation and Isotopes,* vol. 70, pp. 1729-1746, 8, 2012.
[69] J. CLIFFORD, R. MILLER, W. MCCULLOUGH and K. HABIGER, "An explosive detection system for screening luggage with high energy x rays," in *FAA, Proceedings of the First International Symposium on Explosive Detection Technology P 237-251(SEE N 93-21856 07-03),* 1992, .
[70] M. HURWITZ, W. NORONHA and T. ATWELL, "Airport testing of a new thermal neutron analysis explosives detection system," in *FAA, Proceedings of the First International Symposium on Explosive Detection Technology P 388-395(SEE N 93-21856 07-03),* 1992, .
[71] Y. Yang, T. Li and Y. Li, "Explosives detection using dual energy X-ray imaging and photoneutron analysis," in *Nuclear Science Symposium Conference Record (NSS/MIC), 2009 IEEE,* 2009, pp. 876-878.

[72] T. Gozani, R. E. Morgado and C. C. Seher, "Nuclear-based techniques for explosive detection," *Journal of Energetic Materials,* vol. 4, pp. 377-414, 1986.
[73] Committee on the Review of Existing and Potential Standoff Explosives Detection Techniques,National Research Council, *Existing and Potential Standoff Explosives Detection Techniques.* The National Academies Press, 2004.
[74] G. VOURVOPOULOS, F. Schultz and J. Kehayias, "A pulsed fast-thermal neutron interrogation system," in *FAA, Proceedings of the First International Symposium on Explosive Detection Technology P 104-115(SEE N 93-21856 07-03),* 1992, .
[75] G. Nebbia and J. Gerl, "Detection of buried landmines and hidden explosives using neutron, X-ray and gamma-ray probes," *Europhys. News,* vol. 36, pp. 119-123, 2005.
[76] P. Mächler, "Detection technologies for anti-personnel mines," in *Proceedings of the Autonomous Vehicles in Mine Countermeasures Symposium, Monterey, CA, USA,* 1995, pp. 6.150-6.154.
[77] N. A. Diakides and J. D. Bronzino, *Medical Infrared Imaging.* CRC press, 2007.
[78] C. Bauer, A. Sharma, U. Willer, J. Burgmeier, B. Braunschweig, W. Schade, S. Blaser, L. Hvozdara, A. Müller and G. Holl, "Potentials and limits of mid-infrared laser spectroscopy for the detection of explosives," *Applied Physics B,* vol. 92, pp. 327-333, 2008.
[79] M. Todd, R. Provencal, T. Owano, B. Paldus, A. Kachanov, K. Vodopyanov, M. Hunter, S. Coy, J. Steinfeld and J. Arnold, "Application of mid-infrared cavity-ringdown spectroscopy to trace explosives vapor detection using a broadly tunable (6–8 μm) optical parametric oscillator," *Applied Physics B,* vol. 75, pp. 367-376, 2002.
[80] D. HENDERSON, E. SILBERMAN and F. SNYDER, "Fourier-transform infrared spectroscopy applied to explosive vapor detection," in *FAA, Proceedings of the First International Symposium on Explosive Detection Technology P 604-617(SEE N 93-21856 07-03),* 1992, .
[81] J. S. Caygill, F. Davis and S. P. Higson, "Current trends in explosive detection techniques," *Talanta,* vol. 88, pp. 14-29, 2012.
[82] John F Federici and Brian Schulkin and Feng Huang and Dale Gary and Robert Barat and Filipe Oliveira and,David Zimdars, "THz imaging and sensing for security applications—explosives, weapons and drugs," *Semiconductor Science and Technology,* vol. 20, pp. S266, 2005.
[83] B. Piosczyk, O. Braz, G. Dammertz, C. T. Iatrou, S. Kern, M. Kuntze, A. Mobius, M. Thumm, V. Flyagin and V. Khishnyak, "A 1.5-MW, 140-GHz, TE 28, 16-coaxial cavity gyrotron," *Plasma Science, IEEE Transactions On,* vol. 25, pp. 460-469, 1997.
[84] G. R. Neil, G. Carr, J. F. Gubeli III, K. Jordan, M. C. Martin, W. R. McKinney, M. Shinn, M. Tani, G. Williams and X. Zhang, "Production of high power femtosecond terahertz radiation," *Nuclear Instruments and Methods in Physics Research Section A: Accelerators, Spectrometers, Detectors and Associated Equipment,* vol. 507, pp. 537-540, 2003.
[85] F. Huang, B. Schulkin, H. Altan, J. F. Federici, D. Gary, R. Barat, D. Zimdars, M. Chen and D. Tanner, "Terahertz study of 1, 3, 5-trinitro-s-triazine by time-domain and Fourier transform infrared spectroscopy," *Appl. Phys. Lett.,* vol. 85, pp. 5535-5537, 2004.
[86] H. Liu, Y. Chen, G. J. Bastiaans and X. Zhang, "Detection and identification of explosive RDX by THz diffuse reflection spectroscopy," *Optics Express,* vol. 14, pp. 415-423, 2006.
[87] D. FALCONER and D. WATTERS, "Explosive detection using microwave imaging," in *FAA, Proceedings of the First International Symposium on Explosive Detection Technology P 486-492(SEE N 93-21856 07-03),* 1992, .

[88] B. L. Henke, E. M. Gullikson and J. C. Davis, "X-Ray Interactions: Photoabsorption, Scattering, Transmission, and Reflection at< i> E= 50-30,000 eV,< i> Z= 1-92," *Atomic Data and Nuclear Data Tables,* vol. 54, pp. 181-342, 1993.
[89] L. Gerward, N. Guilbert, K. Bjørn Jensen and H. Levring, "X-ray absorption in matter. Reengineering XCOM," *Radiat. Phys. Chem.,* vol. 60, pp. 23-24, 2001.
[90] J. D. Baldeschwieler, *Detection of Explosives for Commercial Aviation Security.* Natl Academy Pr, 1993.
[91] D. Dance and G. A. Carlsson, "Interactions of Photons with Matter," *Handbook of Radiotherapy Physics: Theory and Practice,* pp. 57, 2007.
[92] N. Murray and K. Riordan, "Evaluation of automatic explosive detection systems," in *Security Technology, 1995. Proceedings. Institute of Electrical and Electronics Engineers 29th Annual 1995 International Carnahan Conference On,* 1995, pp. 175-179.
[93] E. M. A. Hussein and E. J. Waller, "Review of one-side approaches to radiographic imaging for detection of explosives and narcotics," *Radiat. Measur.,* vol. 29, pp. 581-591, 12, 1998.
[94] B. Achmad and E. M. A. Hussein, "An X-ray Compton scatter method for density measurement at a point within an object," *Applied Radiation and Isotopes,* vol. 60, pp. 805-814, 6, 2004.
[95] S. Yuk, K. H. Kim and Y. Yi, "Detection of buried landmine with X-ray backscatter technique," *Nuclear Instruments and Methods in Physics Research Section A: Accelerators, Spectrometers, Detectors and Associated Equipment,* vol. 568, pp. 388-392, 11/30, 2006.
[96] R. D. Evans, *Compton Effect.* Springer, 1958.
[97] E. Ali and D. Rogers, "Functional forms for photon spectra of clinical linacs," *Phys. Med. Biol.,* vol. 57, pp. 31, 2012.
[98] G. Harding, "X-ray scatter tomography for explosives detection," *Radiat. Phys. Chem.,* vol. 71, pp. 869-881, 2004.
[99] Z. Asa'd, M. Asghar and D. Imrie, "The measurement of the wall thickness of steel sections using Compton backscattering," *Measurement Science and Technology,* vol. 8, pp. 377, 1997.
[100] L. Tavora and W. Gilboy, "Study of Compton scattering signals in single-sided imaging applications using Monte Carlo methods," *Nuclear Instruments and Methods in Physics Research Section B: Beam Interactions with Materials and Atoms,* vol. 213, pp. 155-161, 2004.
[101] A. Buffler and J. Tickner, "Detecting contraband using neutrons: Challenges and future directions," *Radiat. Measur.,* vol. 45, pp. 1186-1192, 12, 2010.
[102] Z. Chen, Y. Zheng, B. R. Abidi, D. L. Page and M. A. Abidi, "A combinational approach to the fusion, de-noising and enhancement of dual-energy x-ray luggage images," in *Computer Vision and Pattern Recognition-Workshops, 2005. CVPR Workshops. IEEE Computer Society Conference On,* 2005, pp. 2-2.
[103] R. C. Runkle, T. A. White, E. A. Miller, J. A. Caggiano and B. A. Collins, "Photon and neutron interrogation techniques for chemical explosives detection in air cargo: A critical review," *Nuclear Instruments and Methods in Physics Research Section A: Accelerators, Spectrometers, Detectors and Associated Equipment,* vol. 603, pp. 510-528, 5/21, 2009.
[104] T. GOZANI, "Principles of nuclear-based explosive detection systems," in *FAA, Proceedings of the First International Symposium on Explosive Detection Technology P 27-55(SEE N 93-21856 07-03),* 1992, .

[105] J. Overley, M. Chmelik, R. Rasmussen, R. Schofield and H. Lefevre, "Explosives detection through fast-neutron time-of-flight attenuation measurements," *Nuclear Instruments and Methods in Physics Research Section B: Beam Interactions with Materials and Atoms,* vol. 99, pp. 728-732, 1995.
[106] T. Gozani and D. Strellis, "Advances in neutron based bulk explosive detection," *Nuclear Instruments and Methods in Physics Research Section B: Beam Interactions with Materials and Atoms,* vol. 261, pp. 311-315, 8, 2007.
[107] A. Buffler, "Contraband detection with fast neutrons," *Radiat. Phys. Chem.,* vol. 71, pp. 853-861, 2004.
[108] M. Litz, C. Waits and J. Mullins, "Neutron-Activated Gamma-Emission: Technology Review," *U. S. Army Research Laboratory, Adelphi, MD 20783-1197,* 2012.
[109] G. Molnar, *Handbook of Prompt Gamma Activation Analysis: With Neutron Beams.* Springer, 2004.
[110] R. Speller, "Radiation-based security," *Radiat. Phys. Chem.,* vol. 61, pp. 293-300, 6, 2001.
[111] R. C. Runkle, T. A. White, E. A. Miller, J. A. Caggiano and B. A. Collins, "Photon and neutron interrogation techniques for chemical explosives detection in air cargo: A critical review," *Nuclear Instruments and Methods in Physics Research Section A: Accelerators, Spectrometers, Detectors and Associated Equipment,* vol. 603, pp. 510-528, 2009.
[112] B. H. Hui, *Study of Gamma Rays from Neutron Inelastic Scattering.,* 1970.
[113] D. R. Brown and T. Gozani, "Cargo inspection system based on pulsed fast neutron analysis," *Nuclear Instruments and Methods in Physics Research Section B: Beam Interactions with Materials and Atoms,* vol. 99, pp. 753-756, 5/5, 1995.
[114] E. Rhodes, C. Dickerman, A. DeVolpi and C. Peters, "APSTNG: radiation interrogation for verification of chemical and nuclear weapons," *Nuclear Science, IEEE Transactions On,* vol. 39, pp. 1041-1045, 1992.
[115] A. Buffler, "Contraband detection with fast neutrons," *Radiat. Phys. Chem.,* vol. 71, pp. 853-861, 0, 2004.
[116] F. D. Brooks, A. Buffler, M. S. Allie, K. Bharuth-Ram, M. R. Nchodu and B. R. S. Simpson, "Determination of HCNO concentrations by fast neutron scattering analysis," *Nuclear Instruments and Methods in Physics Research Section A: Accelerators, Spectrometers, Detectors and Associated Equipment,* vol. 410, pp. 319-328, 6/11, 1998.
[117] P. C. Womble, F. J. Schultz and G. Vourvopoulos, "Non-destructive characterization using pulsed fast-thermal neutrons," *Nuclear Instruments and Methods in Physics Research Section B: Beam Interactions with Materials and Atoms,* vol. 99, pp. 757-760, 5/5, 1995.
[118] K. Norrish and B. Chappell, "X-ray fluorescence spectrometry," *Physical Methods in Determinative Mineralogy,* pp. 201-272, 1977.
[119] R. Tertian and F. Claisse, *Principles of Quantitative X-Ray Fluorescence Analysis.* Heyden, 1982.
[120] J. R. Lamarsh, *Introduction to Nuclear Reactor Theory.* Addison-Wesley Reading, MA, 1966.
[121] W. M. Stacey, *Nuclear Reactor Physics.* John Wiley & Sons, 2007.
[122] J. J. Duderstadt, "Nuclear reactor analysis," 1976.
[123] J. K. Shultis, R. E. Faw and K. R. Kase, *Radiation Shielding.* Prentice Hall PTR, 1996.
[124] J. K. Shultis, R. E. Faw and M. Dekker, *Fundamentals of Nuclear Science and Engineering.* Marcel Dekker New York, 2002.

[125] N. Soppera, M. Bossant, H. Henriksson, P. Nagel and Y. Rugama, "Recent upgrades to the nuclear data tool JANIS," in *Proc. of the International Conference on Nuclear Data for Science and Technology,* 2010, pp. 26-30.
[126] B. Sowerby, "Elemental analysis by neutron inelastic scatter gamma rays with a radioisotope neutron source," *Nucl. Instrum. Methods,* vol. 166, pp. 571-579, 1979.
[127] M. Hosoe and S. Suzuki, "Gamma Rays from Neutron Inelastic Scattering of Magnesium, Aluminum, Iron and Bismuth," *Journal of the Physical Society of Japan,* vol. 14, pp. 699-707, 1959.
[128] P. M. Walker and J. J. Carroll, "Nuclear isomers: Recipes from the Past and Ingredients for the Future," *Nuclear Physics News,* vol. 17, pp. 11-15, 2007.
[129] S. Kailas, "Nuclear isomers revisited," *Current Science (Bangalore),* vol. 77, 1999.
[130] R. Hertzog and R. Plasek, "Neutron-excited gamma-ray spectrometry for well logging," *Nuclear Science, IEEE Transactions On,* vol. 26, pp. 1558-1567, 1979.
[131] Z. Révay and T. Belgya, "Principles of the PGAA method," in *Handbook of Prompt Gamma Activation Analysis*Anonymous Springer, 2004, pp. 1-30.
[132] M. Lone, R. Leavitt and D. Harrison, "Prompt gamma rays from thermal-neutron capture," *Atomic Data and Nuclear Data Tables,* vol. 26, pp. 511-559, 1981.
[133] A. Naqvi, "A Monte Carlo comparison of PGNAA system performance using< sup> 252 Cf neutrons, 2.8-MeV neutrons and 14-MeV neutrons," *Nuclear Instruments and Methods in Physics Research Section A: Accelerators, Spectrometers, Detectors and Associated Equipment,* vol. 511, pp. 400-407, 2003.
[134] A. A. Naqvi, F. A. Al-Matouq, F. Z. Khiari, M. A. Gondal, K. Rehman, A. A. Isab, M. Raashid and M. A. Dastageer, "350 keV accelerator based PGNAA setup to detect nitrogen in bulk samples," *Nuclear Instruments and Methods in Physics Research Section A: Accelerators, Spectrometers, Detectors and Associated Equipment,* vol. 729, pp. 8-13, 11/21, 2013.
[135] W. L. Dunn, K. Banerjee, A. Allen and J. van Meter, "Feasibility of a method to identify targets that are likely to contain conventional explosives," *Nuclear Instruments and Methods in Physics Research Section B: Beam Interactions with Materials and Atoms,* vol. 263, pp. 179-182, 10, 2007.
[136] K. W. Loschke and W. L. Dunn, "Detection of chemical explosives using multiple photon signatures," *Applied Radiation and Isotopes,* vol. 68, pp. 884-887, 0, 2010.
[137] J. D. Lowrey and W. L. Dunn, "Signature-based radiation scanning using radiation interrogation to detect explosives," *Applied Radiation and Isotopes,* vol. 68, pp. 893-895, 0, 2010.
[138] M. Johll, "MCNP simulations for standoff bomb detection using neutron interrogation," *Kansas State University, Master, Nuclear Engineering,* 2009.
[139] R. L. Brewer, "Neutron and neutron-induced gamma ray signatures as a template matching technique for explosives detection," *Kansas State University,* 2009.
[140] K. W. Loschke, "Photon signatures for standoff bomb detection," *Master, Nuclear Engineering, Kansas State University,* 2008.
[141] S. A. Heider, "An MCNP study of fast neutron interrogation for standoff detection of improvised explosive devices," *Kansas State University, Master, Nuclear Engineering,* 2012.
[142] C. P. Matthew, "Design studies for stand off bomb detection," *Master, Nuclear Engineering, Kansas State University,* 2010.

[143] N. Tsoulfanidis and S. Landsberger, *Measurement and Detection of Radiation.* CRC press, 2010.
[144] R. Brewer, W. Dunn, S. Heider, C. Matthew and X. Yang, "The signature-based radiation-scanning approach to standoff detection of improvised explosive devices," *Applied Radiation and Isotopes,* vol. 70, pp. 1181-1185, 2012.
[145] R. Rout, A. Garg, A. Shyam and M. Srinivasan, "Influence of electrode and insulator materials on the neutron emission in a low energy plasma focus device," *Plasma Science, IEEE Transactions On,* vol. 23, pp. 996-1000, 1995.
[146] M. Ismail, A. Abodou, A. Mohamed, S. Lee and S. Saw, "Kansas state university dense plasma focus (KSU-DPF) initial neutron results," in *Plasma Science (ICOPS), 2011 Abstracts IEEE International Conference On,* 2011, pp. 1-1.
[147] D. A. Ward and J. L. T. Exon, "Using Rogowski coils for transient current measurements," *Engineering Science & Education Journal,* vol. 2, pp. 105-113, 1993.
[148] A. E. Mohamed, A. E. Abdou, M. I. Ismail, S. Lee and S. H. Saw, "Current Sheet Axial Dynamics of 2.5-kJ KSU-DPF Under High-Pressure Regime," *Plasma Science, IEEE Transactions On,* vol. 40, pp. 2736-2740, 2012.
[149] Lee, S and Saw, SH and Rawat, RS and Lee, P and Verma, R and Talebitaher, A and Hassan, SM and Abdou, AE and Ismail, Mohamed and Mohamed, Amgad and others, "Measurement and processing of fast pulsed discharge current in plasma focus machines," *J. Fusion Energy,* vol. 31, pp. 198-204, 2012.
[150] OSRAM Opto Semiconductors, "Silicon photodetector BPX65 V1.1 ," 2010.
[151] P. Martinez, *A Practical Guide to CCD Astronomy.* Cambridge University Press, 1998.
[152] R. Alig and S. Bloom, "Electron-hole-pair creation energies in semiconductors," *Phys. Rev. Lett.,* vol. 35, pp. 1522, 1975.
[153] F. Scholze, H. Rabus and G. Ulm. Mean energy required to produce an electron-hole pair in silicon for photons of energies between 50 and 1500 eV. *J. Appl. Phys. 84(5),* pp. 2926-2939. 1998. . DOI: http://dx.doi.org/10.1063/1.368398.
[154] S. R. Mohanty, H. Bhuyan, N. K. Neog, R. K. Rout and E. Hotta, "Development of multi faraday cup assembly for ion beam measurements from a low energy plasma focus device," *JAPANESE JOURNAL OF APPLIED PHYSICS PART 1 REGULAR PAPERS SHORT NOTES AND REVIEW PAPERS,* vol. 44, pp. 5199, 2005.
[155] S. R. Mohanty, N. K. Neog, B. B. Nayak, B. S. Acharya, P. Lee, T. L. Tan and R. S. Rawat, "Energetic ion irradiation of American diamond in a plasma focus device and characterization of irradiated material," *Nuclear Instruments and Methods in Physics Research Section B: Beam Interactions with Materials and Atoms,* vol. 243, pp. 113-118, 1, 2006.
[156] J. Harasimowicz and C. Welsch, "Faraday cup for low-energy, low-intensity beam measurements at the USR," *Proc.BIW, Santa Fe, NM, USA,* 2010.
[157] R. A. Baragiola and C. A. Dukes, "Plasmon-assisted electron emission from Al and Mg surfaces by slow ions," *Phys. Rev. Lett.,* vol. 76, pp. 2547, 1996.
[158] B. S. Tomar, T. C. Kaushik, S. Andola, Ramniranjan, R. K. Rout, A. Kumar, D. B. Paranjape, P. Kumar, K. L. Ramakumar, S. C. Gupta and R. K. Sinha, "Non-destructive assay of fissile materials through active neutron interrogation technique using pulsed neutron (plasma focus) device," *Nuclear Instruments and Methods in Physics Research Section A: Accelerators, Spectrometers, Detectors and Associated Equipment,* vol. 703, pp. 11-15, 3/1, 2013.

[159] S. A. Pozzi, J. A. Mullens and J. T. Mihalczo, "Analysis of neutron and photon detection position for the calibration of plastic (BC-420) and liquid (BC-501) scintillators," *Nuclear Instruments and Methods in Physics Research Section A: Accelerators, Spectrometers, Detectors and Associated Equipment,* vol. 524, pp. 92-101, 2004.
[160] F. Brooks and H. Klein, "Neutron spectrometry—historical review and present status," *Nuclear Instruments and Methods in Physics Research Section A: Accelerators, Spectrometers, Detectors and Associated Equipment,* vol. 476, pp. 1-11, 2002.
[161] BTI, "Bubble detectordors neutrons dosimeters," BTI BUBBLE TECHNOLOGY INDUSTRIES, http://www.bubbletech.ca/pdfs/BTI_BUBBLE_General_May72009.pdf, 2009.
[162] N. Smirnova, N. Semaschko and Y. Martinuk, "Bubble detectors in fusion dosimetry," *Radiat. Prot. Dosimet.,* vol. 44, pp. 347-349, 1992.
[163] A. Klett and B. Burgkhardt, "The new remcounter LB6411: Measurement of neutron ambient dose equivalent H*(10) according to ICRP60 with high sensitivity," in *Nuclear Science Symposium, 1996. Conference Record., 1996 IEEE,* 1996, pp. 132-134 vol.1.
[164] A. Syntfeld, M. Moszynski, R. Arlt, M. Balcerzyk, M. Kapusta, M. Majorov, R. Marcinkowski, P. Schotanus, M. Swoboda and D. Wolski, "/sup 6/LiI (Eu) in neutron and/spl gamma/-ray spectrometry-a highly sensitive thermal neutron detector," *Nuclear Science, IEEE Transactions On,* vol. 52, pp. 3151-3156, 2005.
[165] M. Awschalom and R. S. Sanna, "*Applications of Bonner Sphere Detectors in Neutron Field Dosimetry*
," *Applications of Bonner Sphere Detectors in Neutron Field Dosimetry,* 1983.
[166] I. LUDLUM MEASUREMENTS, "LUDLUM MODEL 42-5 NEUTRON BALL CART," LUDLUM Inc. http://www.ludlums.com/multisites/medphys/images/stories/product_manuals/M42-5.pdf;, April, 2011.
[167] I. LUDLUM MEASUREMENTS, "LUDLUM MODEL 42-30H NEUTRON DETECTOR," LUDLUM MEASUREMENTS, INC, Sweetwater, Texas 79556, Apr 2014.
[168] L. Silberstein, "Determination of the spectral composition of X-ray radiation from filtration data," *JOSA,* vol. 22, pp. 265-278, 1932.
[169] V. Raspa, C. Moreno, L. Sigaut and A. Clausse, "Effective hard x-ray spectrum of a tabletop Mather-type plasma focus optimized for flash radiography of metallic objects," *J. Appl. Phys.,* vol. 102, pp. 123303, 2007.
[170] G. Ludwig and J. Prener, "Evaluation of Gd2O2S: Tb as a phosphor for the input screen of x-ray image intensifier," *Nuclear Science, IEEE Transactions On,* vol. 19, pp. 3-8, 1972.
[171] C. M. Michail, I. G. Valais, A. E. Toutountzis, N. E. Kalyvas, G. P. Fountos, S. L. David, I. S. Kandarakis and G. S. Panayiotakis, "Light emission efficiency of (GOS: Eu) powder screens under x-ray mammography conditions," *Nuclear Science, IEEE Transactions On,* vol. 55, pp. 3703-3709, 2008.
[172] (). *NDT-Non Destructive Test, Radiographic Density, NDT Education Resource Center, 2001-2014, The Collaboration for NDT Education, Iowa State University, www.ndt-ed.org.*
[173] P. Sprawls, *Physical Principles of Medical Imaging.* Medical Physics Pub., 1995.
[174] V. Raspa and C. Moreno, "Radiographic method for measuring the continuum hard X-ray output spectrum of a Plasma Focus device," *Physics Letters A,* vol. 373, pp. 3659-3662, 2009.

[175] A. Mohamed, A. Abdou, M. Ismail, S. Lee and S. Saw, "Short circuit test-complete analysis for the dense plasma focus," in *Plasma Science (ICOPS), 2011 Abstracts IEEE International Conference On,* 2011, pp. 1-1.
[176] S. Saw, S. Lee, F. Roy, P. Chong, V. Vengadeswaran, A. Sidik, Y. Leong and A. Singh, "In situ determination of the static inductance and resistance of a plasma focus capacitor bank," *Rev. Sci. Instrum.,* vol. 81, pp. 053505, 2010.
[177] S. Sawchuk, "Monte carlo estimate to improve photon energy spectrum reconstruction," in *Advanced Monte Carlo for Radiation Physics, Particle Transport Simulation and Applications*Anonymous Springer, 2001, pp. 383-388.
[178] S. Lee, "Transverse Ionizing Shock Waves in a Planar Electromagnetic Shock Tube," *Australian National Univ. , Canberra,* 1969.
[179] Mohamed Ismail, "Rapid material interrogation using x-rays from a Dense Plasma focus device." 2015.
[180] A. E. Mohamed, M. I. Ismail, W. Dunn and A. Abdou, "Deuteron beam characteristics of 2.5 kJ KSU-DPF as a high inductance dense plasma focus machine," in *IEEE Pulsed Power & Plasma Science Conference – PPPS 2013,* San Francisco, CA, June, 2013, .
[181] S. Lee, S. Saw, A. Abdou and H. Torreblanca, "Characterizing plasma focus devices—role of the static inductance—instability phase fitted by anomalous resistances," *J. Fusion Energy,* vol. 30, pp. 277-282, 2011.
[182] H. Schmidt, P. Kubes, M. J. Sadowski and M. Scholz, "Neutron emission characteristics of pinched dense magnetized plasmas," *Plasma Science, IEEE Transactions On,* vol. 34, pp. 2363-2367, 2006.
[183] M. V. Roshan, P. Lee, Z. Pan, R. Verma, R. S. Rawat and S. V. Springham, "Correlation analysis of intense and high-energy deuteron beam, pinch images, and neutron yield," *Plasma Science, IEEE Transactions On,* vol. 38, pp. 2434-2438, 2010.
[184] S. V. Springham, S. P. Moo, P. Lee, R. S. Rawat, A. C. Patran and S. Lee, "Imaging of fusion protons from a 3 kJ deuterium plasma focus," *Japanese Journal of Applied Physics,* vol. 44, pp. 4117, 2005.
[185] W. L. Dunn and J. K. Shultis, *Exploring Monte Carlo Methods.* Elsevier, 2011.
[186] F. B. Brown, R. Barrett, T. Booth, J. Bull, L. Cox, R. Forster, T. Goorley, R. Mosteller, S. Post and R. Prael, "MCNP version 5," *Trans.Am.Nucl.Soc,* vol. 87, pp. 02-3935, 2002.
[187] G. McKinney, J. Durkee, J. Hendricks, M. James, D. Pelowitz, L. Waters and F. Gallmeier, "MCNPX–New Features Demonstrated," 2007.
[188] L. S. Waters, "MCNPX user's manual," *Los Alamos.(Accesed in Apr 15, 2012 at Http://Mcnpx.Lanl.Gov/Opendocs/Versions/v230/MCNPX_2.3.0 _Manual.Pdf),* 2002.
[189] J. K. Shultis and R. E. Faw, "An MCNP primer," *Dept.of Mechanical and Nuclear,* 2011.
[190] J. S. Hendricks, G. W. McKinney, M. L. Fensin, M. R. James, R. C. Johns, J. W. Durkee, J. P. Finch, D. B. Pelowitz, L. S. Waters and M. W. Johnson, "MCNPX 2.6. 0 Extensions," *Los Alamos National Laboratory, LA-UR-08-2216,* 2008.
[191] D. B. Pelowitz, "MCNP6 User's Manual, Version 1," 2013.
[192] B. H. Daub, V. Henzl, M. A. Kovash, J. L. Matthews, Z. W. Miller, K. Shoniyozov and H. Yang, "Response of BC-418 plastic scintillator to low-energy protons," *Nuclear Instruments and Methods in Physics Research Section A: Accelerators, Spectrometers, Detectors and Associated Equipment,* vol. 701, pp. 171-175, 2/11, 2013.

[193] H. Klein and F. D. Brooks, "Scintillation detectors for fast neutrons," in *Proceedings of the Conference FNDA2006, International Workshop on Fast Neutron Detectors, University of Cape Town, South Africa,* 2006, .
[194] S. A. Pozzi and L. UT-Battelle, *Recent Developments in the MCNP-PoliMi Postprocessing Code.* United States. Department of Energy, 2004.
[195] R. McConn Jr, C. J. Gesh, R. T. Pagh, R. A. Rucker and R. Williams III, "Compendium of material composition data for radiation transport modeling," *PNNL-15870 Rev,* vol. 1, 2011.
[196] S. Lee and S. Saw, "Joint ICTP-IAEA Workshop on Dense Magnetized Plasma and Plasma Diagnostics," 2010.
[197] S. Lee, "Scaling of the plasma focus – viewpoint from dynamics," in **Invited Paper to be Presented at International Plasma Focus Symposium,* Kudowa, Poland, 1998, .
[198] A. Mohamed E. MCNP simulation to hard X-ray emission of KSU dense plasma focus machine. *Http://Arxiv.Org/Abs/1503.02930* 2014.
[199] R. Verma, P. Lee, S. Lee, S. Springham, T. Tan, R. Rawat and M. Krishnan, "Order of magnitude enhancement in neutron emission with deuterium-krypton admixture operation in miniature plasma focus device," *Appl. Phys. Lett.,* vol. 93, pp. 101501-101501-3, 2008.
[200] J. Neal, J. Mihalczo, M. Hiatt and J. Edwards, "Large plastic scintillation detectors for the nuclear materials identification system," in *Institute of Nuclear Materials Management Annual Meeting, Orlando, Florida,* 2004, .
[201] D. V. Jordan, P. L. Reeder, L. C. Todd, G. A. Warren, K. R. McCormick, D. L. Stephens, B. D. Geelhood, J. M. Alzheimer, S. L. Crowell and W. A. Sliger, *Advanced Large-Area Plastic Scintillator Project (ALPS): Final Report.* Pacific Northwest National Laboratory, 2007.
[202] B. Sowerby, N. Cutmore, Y. Liu, H. Peng, J. Tickner, Y. Xie and C. Zong, "Recent developments in fast neutron radiography for the interrogation of air cargo containers," in *IAEA Conference, Vienna,* 2009, pp. 4-8.
[203] P. R. Menge, G. Gautier, A. Iltis, C. Rozsa and V. Solovyev, "Performance of large lanthanum bromide scintillators," *Nuclear Instruments and Methods in Physics Research Section A: Accelerators, Spectrometers, Detectors and Associated Equipment,* vol. 579, pp. 6-10, 2007.
[204] A. Favalli, H. Mehner, V. Ciriello and B. Pedersen, "Investigation of the PGNAA using the LaBr 3 scintillation detector," *Applied Radiation and Isotopes,* vol. 68, pp. 901-904, 2010.

Appendix A - Matlab Coding for SBRS Method

Matlab program, written for determining the figure of merit (FOM) and the standard deviation for the SBRS method of detection.

V.1: Manually data entry

```
clear all
sample = input('please enter number of samples :  ');
response = input('please enter number of responses :  ');
response_array =zeros(sample,response);
response_array_error =zeros(sample,response);
template_array=zeros(1,response);
template_array_error=zeros(1,response);
Name_of_material=zeros(sample,1);
% kind = input('For x-ray press 1, for neutron press 2 :  ');
beta=ones(sample,response);
alpha=ones(sample,response);
alpha =alpha/response;
%
for i=1:sample
   Name_of_material(i,1)=input('');
   for j=1:response
      str = sprintf('response no %d for sample %d: ',j,i);
      disp(str);
      response_array(i,j)= input('');
      disp('Response error: ')
      response_array_error(i,j)= input('');
   end
end
disp('For the template')
   for j=1:response
     str = sprintf('For response no %d: ',j);
      disp(str);
      template_array(1,j)= input('');
      disp('Error: ');
      template_array_error(1,j)= input('');
   end
fig_merit_each=zeros(sample,response);
figure_of_merit=zeros(sample,1);
fig_merit_error_each=zeros(sample,response);
figure_of_merit_error=zeros(sample,1);
for i=1:sample
   for j=1:response
      % FOM calc.
    fig_merit_each(i,j)=alpha(i,j)*(((response_array(i,j)- template_array(1,j))^2)/(((response_array_er-
ror(i,j))^2)+((template_array_error(1,j)^2))));
    figure_of_merit(i,1)=figure_of_merit(i,1)+fig_merit_each(i,j);
    % FOM error calc.
    fig_merit_error_each(i,j)=(alpha(i,j)^2)*(((response_array(i,j)- template_array(1,j))^2)/(((response_array_er-
ror(i,j))^2)+((template_array_error(1,j)^2))));
```

```
    figure_of_merit_error(i,1)=figure_of_merit_error(i,1)+fig_merit_error_each(i,j);
   end
figure_of_merit_error(i,1)=2*((figure_of_merit_error(i,1))^0.5);
fplus(i,1)=figure_of_merit(i,1)+figure_of_merit_error(i,1);
fminus(i,1)=figure_of_merit(i,1)-figure_of_merit_error(i,1);
end
```

V.2: Automatic reading from pre-saved data.

```
clear all
% the r4esponses data must be saved in the MAT worksheet file.
load('Exp_interrogation_tables.mat')
sample = input('please enter number of samples :  ');
response = input('please enter number of responses :  ');
beta=ones(sample,response);
alpha=ones(sample,response);
alpha =alpha/response;
% Name_of_material=zeros(sample,1);
% kind = input('For x-ray press 1, for neutron press 2 :  ');
% beta=ones(sample,response);
% alpha =alpha/response;
fig_merit_each=zeros(sample,response);
figure_of_merit=zeros(sample,1);
normalization_factor=zeros(sample,1);
normalization_factor_each=zeros(sample,response);
fig_merit_error_each=zeros(sample,response);
figure_of_merit_error=zeros(sample,1);
for i=1:sample
   for j=1:response
      % FOM calc.
    fig_merit_each(i,j)=alpha(i,j)*(((response_array(i,j)- template_array(1,j))^2)/(((response_array_er-
ror(i,j))^2)+((template_array_error(1,j)^2))));
    figure_of_merit(i,1)=figure_of_merit(i,1)+fig_merit_each(i,j);
    % FOM error calc.
    fig_merit_error_each(i,j)=(alpha(i,j)^2)*(((response_array(i,j)- template_array(1,j))^2)/(((response_array_er-
ror(i,j))^2)+((template_array_error(1,j)^2))));
    figure_of_merit_error(i,1)=figure_of_merit_error(i,1)+fig_merit_error_each(i,j);
    %
    normalization_factor_each(i,j)=alpha(i,j)*((0- template_array(1,j))^2)/(0+((template_array_error(1,j)^2)));
    normalization_factor(i,1)=normalization_factor(i,1)+normalization_factor_each(i,j);
   end
   FOM_normalized=500*figure_of_merit./normalization_factor; % a range factor of 500 was added to adjust the
range of data
   FOM_normalized_error=500*figure_of_merit_error./normalization_factor;
figure_of_merit_error(i,1)=2*((figure_of_merit_error(i,1))^0.5);
fplus(i,1)=figure_of_merit(i,1)+figure_of_merit_error(i,1);
fminus(i,1)=figure_of_merit(i,1)-figure_of_merit_error(i,1);
end
```

Appendix B - MCNP coding for the problem*, **

* These codes to compile under the MCNPX2.4 compiler, some physics cards may need to be changed to work under MCNP6.x.

** Please give credit to the author if you use the code or part of the code in your work.

I. The MCNP program used for the detection of neutron signatures, and the material used in simulation at the end of the program.

```
Plasma focus  device, neutron emission for explosive detection
c --- the program includes neutron source , three plastic scintillators, and one bare helium 3 detector.
c --- the target can is either 5 gallons or one gallons of different materials
c ********************block one: cells*************************
1   1  -7.8212   -1   imp:h=1 imp:n=1 imp:t=0 $ side of chamber imp:t=0
2   1  -7.8212   -2   imp:h=1 imp:n=1 imp:t=0  $ side of chamber
3   1  -7.8212   -3   imp:h=1 imp:n=1 imp:t=0  $ side of chamber
4   1  -7.8212   -4   imp:h=1 imp:n=1 imp:t=0  $ side of chamber
5   8  -2.4      -5      imp:h=0 imp:n=1 imp:t=0  $ Glass plate window
6   1  -7.8212   -6      imp:h=1 imp:n=1 imp:t=0  $ side of chamber
7   0           -7      imp:h=1 imp:n=1 imp:t=0  $ gas inside chamber
8   4 -0.0012   #1 #2 #3 #4 #5 #6 #7 -9 11
     13 14 15 16 18 17 19 20 21 imp:h=1 imp:n=1 imp:t=0  $ lab room contains natural air.
10 3 -2.3  9  -10      imp:h=0 imp:n=1 imp:t=0  $ walls of concrete composition to studyreflection effects.
11 10 -1.032    -11      imp:h=1 imp:n=1  imp:t=0 $ plastic  DETECTOR IN scatter
12 44  -0.99    -12      imp:h=1 imp:n=1  imp:t=0 $ Target Can
13 34 -7.874 12 -13      imp:h=1 imp:n=1 imp:t=0  $ Can wall of iron
14 27 -1.2      -14      imp:h=1 imp:n=1 imp:t=0  $ POLYETHYLENE shield
15 10 -1.032    -15      imp:h=1 imp:n=1 imp:t=0  $ plastic  DETECTOR IN scatter
16 33 -11.35    -16      imp:h=1 imp:n=1 imp:t=0  $ LEAD shield
17 10 -1.032    -17      imp:h=1 imp:n=1 imp:t=0  $ plastic DETECTOR IN scatter
18 33 -11.35    -18      imp:h=1 imp:n=1 imp:t=0  $ LEAD shield
19 49 -0.0002677 -19     imp:h=1 imp:n=1 imp:t=1  $ Helium-3 detector tube of 2 atm pressure from manual.
c 20 27 -1.2      -20      imp:h=1 imp:n=1 imp:t=0  $ Polyethe shield
c 21 27 -1.2      -21      imp:h=1 imp:n=1 imp:t=0  $ Polyethe shield
20 27 -1.2      -20      imp:h=1 imp:n=1 imp:t=0  $ Polyethe shield changed density for testing only
21 27 -1.2      -21      imp:h=1 imp:n=1 imp:t=0  $ Polyethe shield changed density for testing only
30 0            10      imp:h=0 imp:n=0 imp:t=0  $ Void outside

c ******************block two: surfaces ******************
1   Rpp -5  -4.6  -40  15.6    0    22   $ walls of chamber -x -direction
2   Rpp 4.6  5    -40   15.6   0    22   $ walls of chamber  x -direction
3   RPP -5   5    -40   16     -0.3  0   $ walls of chamber -z -direction
4   Rpp -5   5    -40   16     22   22.4 $ walls of chamber  z -direction
5   RPP -4.6 4.6  -16   -15.6  0    22   $ walls of chamber  -y -direction
6   RPP -5   5    15.6  16.0   0    22   $ walls of chamber  y -direction
7   RPP -4.6 4.6  -15.6 15.6   0    22
9   RPP -100  500 -800  150  -130   200  $ room concrete size 1
10  Rpp -110  510  -810 160  -150   220  $ room concerete size 2
11  RCC 23.0 -71 8 -3 -2.0 0  2.5      $ back scatter detector
c 12 RCC 0 -80  0    0 0 18     8       $ the 1 gallon can
c 13 RCC 0 -80 -0.04 0 0 18.08 8.04      $ the can walls
12  RCC  0 -80 -4    0 0 24     14       $ the 5 gallon can
```

```
13  RCC  0 -80 -4.1  0 0 24.2  14.1      $ the can walls
c
14  RCC  19  -73.5 8 -2.2 -1.3 0 4.0     $ polyethylene shield
15  RCC  23.0 -90  8 -3  2 0 2.5 $ forward scatter detector
16  RCC  19.0 -88  8 .17  -.115 0 4.0   $ lead shield
17  RCC -23.0 -71  8 3  -2 0 2.5 $ back scatter detector
18  RCC -19 -73.5  8 0.185   -0.115 0 4.0   $ lead shield
19  RCC  0   -63.5 3  0   0  10  1       $ He3 detector tube of 10cm length
20 RPP 10 29 -59 0 -15 20               $ polyethylene shield
21 RPP -29 -10  -59 0 -15 20             $ polyethylene shield

c ******************block 3 data card*********************
mode n h t
c PHYS:N emax ean iunr dnb tabl fism recl  (ex: PHYS:N J 100 3J -1. for capture)
PHYS:N    3    0   0    0  -1    0    2
c PHYS:H emax ean tabl J istrg J  recl j j j efac
phys:H    3    0  -1   J   0   J   0  $ j j j 0.95
phys:t    3    0  -1   J   0   J   0  $ j j j 0.95
cut:n 2j 0 0
cut:h j .001
cut:t j .001
nps 5000000  $ stop after this number emitted from source
SDEF  POS = 0 0 8 PAR=1  Erg=2.45 axs= 0 0 1  dir=d5 vec= 0 -1 0 tme= d1
si1 A 0     0.3   0.6   0.9  1.2   1.5  1.8  2.1  2.4
sp1   0.015 20.8 36.20 36.5 21.14 9.89  4.3  1.5  0.09
si5  -1  0.987   1
sp5   0  0.987  .001
sb5   0    0      1
c xxxxxxxxxxxxxxxxxxxxxxxxxxxxxxxxxxxxxxxxxxxxxxxxxxxxxxxxxxxxx
c F6:n   17
c t6  0 100i 40
c E6 0.05 200i 2.5
c F16:n  11
c t16 0  100i 40
c E16 0.05 200i 2.5
c F26:n  15
c t26 0  100i 40
c E26 0.1 20i 2.5
c F36:n  19
c t36 0  100i 1000
c E36 0  100i 0.0001
c xxxxxxxxxxxxxxxxxxxxxxxxxxxxxxxxxxxxxxxxxxxxxxxxxxxxxxxxxxxxx
F46:h  17        $ this tally converts neutron to light production inside plastic scintillator
DE46 LIN  0 0.05 0.1 0.2 0.3 0.4 0.5 0.6 0.7
         0.8 0.9 1 1.1 1.2 1.3 1.4 1.5 1.6
         1.7 1.8 1.9 2 2.1 2.2 2.3 2.4 2.5 2.6
DF46 LIN  0.0 0.00634 0.01286 0.02646 0.04078 0.05582
         0.0716 0.0881 0.10534 0.1233 0.14198 0.1614
        0.18154 0.20242 0.22402 0.24634 0.2694 0.29318
         0.3177 0.34294 0.3689 0.3956 0.42302 0.45118
         0.48006 0.50966 0.54 0.57106
t46 0  50i 90
F56:h  11
DE56 LIN  0 0.05 0.1 0.2 0.3 0.4 0.5 0.6 0.7
         0.8 0.9 1 1.1 1.2 1.3 1.4 1.5 1.6
```

```
        1.7 1.8 1.9 2 2.1 2.2 2.3 2.4 2.5 2.6
DF56 LIN  0.0 0.00634 0.01286 0.02646 0.04078 0.05582
        0.0716 0.0881 0.10534 0.1233 0.14198 0.1614
        0.18154 0.20242 0.22402 0.24634 0.2694 0.29318
        0.3177 0.34294 0.3689 0.3956 0.42302 0.45118
        0.48006 0.50966 0.54 0.57106
t56 0  50i 90
F66:h  15
DE66 LIN  0 0.05 0.1 0.2 0.3 0.4 0.5 0.6 0.7
        0.8 0.9 1 1.1 1.2 1.3 1.4 1.5 1.6
        1.7 1.8 1.9 2 2.1 2.2 2.3 2.4 2.5 2.6
DF66 LIN  0.0 0.00634 0.01286 0.02646 0.04078 0.05582
        0.0716 0.0881 0.10534 0.1233 0.14198 0.1614
        0.18154 0.20242 0.22402 0.24634 0.2694 0.29318
        0.3177 0.34294 0.3689 0.3956 0.42302 0.45118
        0.48006 0.50966 0.54 0.57106
t66 0  50i 90
c xxxxxxxxxxxxxxxxxxxxxxxxxxxxxxxxxxxxxxxxxxxxxxxxxxxxxxxxxx
F76:t  19   $ helium 3 detector, measures tritons induced inside.
t76 0  50i 3e5
c E76 0 10i 2.9
c
f88:n 19
ft88 CAP 2003 GATE $ 0.01 1e5 $ neutron capture tally in Helium-3 ; Events measured inside the He-3 chamber
t88 0  50i 3e5
c E88 0 100i 2.9
Print
c f78:n 19
c ft78 PHL 1 76 1
c t78 0  50i 3e5
c E78 0 200i 2.9
c
c ********************NATERIAL DEFINITION*****************
c -------------the stinless steel  rho = 7.92
m1        24000 -0.190 $ Cr
          25055.50c -0.020 $ Mn
          26000 -0.695 $ Fe
          28000 -0.095 $ Ni
c ************************************************************
c ------------ Hydrogen
m2     1001.50c   1.00000
c ************************************************************
c ------------ Concrete composition rho = 2.30
m3    1001.50c -0.022100
          6000 -0.002484
          8016.50c -0.574930
         11023.50c -0.015208
         12000 -0.001266
         13027.50c -0.019953
         14000 -0.304627
         19000 -0.010045
          20000 -0.042951
          26000 -0.006435
c ************************************************************
c Air composition   rho = 0.001205
```

```
m4     7014.50c    -0.7558
         8016.50c       -0.2314
        18000      -0.0128
c ************************************************************
c ------Aluminum composition   rho=2.6989
m5     13027.50c   -1.00000
c ************************************************************
c ------Tungsten  rho = 19.3
m6     074000   -1.00000
c ************************************************************
c ----- copper-----  rho=8.960
m7     29000     -1.00000
c ************************************************************
c ----- plate glass     rho=2.4
m8       8016.50c -0.459800
          11023.50c -0.096441
          14000 -0.336553
          20000 -0.107205
c ************************************************************
c ------Steel rho= 7.82 ----
m9     6000     -0.005000
      26000    -0.995000
c ************************************************************
c ----Plastic Scintillator1.032( g / cm3 ) Polyvinyl toluene
m10    1001.50c  -0.085000
          6000  -0.915000
c ************************************************************
c     SOIL: [Jacob, Radn. Prot. Dos. 14, 299, 1986]**** 1.625 g/cm^3
m11     1001.50c  -0.021
        6000  -0.016
        19000  -0.013
        26000  -0.011
        20000  -0.041
        13027.50c  -0.050
        14000 -0.271
        8016.50c  -0.577
c ************************************************************
c Carbon, Graphite, rho = 1.70 g/cc
m12  6000 1.00
c ************************************************************
c Explosive Compounds
c ************************************************************
c TNT, rho = 1.654
m13 1001.50c  -0.022189
         6000 -0.370160
        7014.50c  -0.185004
        8016.50c  -0.422648
c ************************************************************
C RDX rxplosive C 3  H 6  N 6  O 6 --- rho=1.806
m14 1001.50c  -0.027227
         6000 -0.162222
         7014.50c -0.378361
         8016.50c -0.432190
c ************************************************************
c HMX Density ( g / cm3 )= 1.902
```

```
m15 1001.50c  -0.027227
        6000 -0.162222
        7014.50c -0.378361
        8016.50c -0.432190
c ************************************************************
c NG ( Nitroglycerin) Density ( g / cm3 )= 1.13
m16 1001.50c  -0.022193
        6000 -0.158671
       7014.50c  -0.185040
       8016.50c  -0.634096
c ************************************************************
c PETN Density ( g / cm3 )= 1.773
m17 1001.50c  -0.025506
        6000 -0.189961
       7014.50c  -0.177223
       8016.50c  -0.607310
c ************************************************************
c EGDN (Ethylene Glycol Dinitrate) Density ( g / cm3 )= 1.490
m18 1001.50c  -0.026514
        6000 -0.157970
        7014.50c -0.184222
        8016.50c -0.631294
c ************************************************************
c AN (Ammonium Nitrate) Density ( g / cm3 )= 1.730
m19 1001.50c   -0.050370
        7014.50c  -0.349978
        8016.50c  -0.599652
c ************************************************************
c NC (Nitrocellulose) Density ( g / cm3 )= 1.660
m20 1001.50c -0.028320
        6000 -0.289258
        7014.50c -0.168664
        8016.50c -0.513758
c ************************************************************
c Fertilizer Density (Fert B) ( g / cm3 )= 0.990
m21     1001.50c  -0.0000504
       8016.50c  -0.0007176
       11023.50c -0.0087350
       12000 -0.0002058
       16000 -0.0001590
       17000 -0.4778000
       19000 -0.5117000
       20000 -0.0002758
       35000 -0.0003303
c ************************************************************
c Gasoline, rho = 0.6837
m22 1001.50c   -0.160000
        6000  -0.840000
c ************************************************************
c Oil
c Crude Oil Density ( g / cm3 )= 0.973
m23 1001.50c   -0.120000
        6000  -0.850000
        7014.50c  -0.010500
        8016.50c  -0.007750
```

```
      16000 -0.030250
c ************************************************************
c Hydraulic Oil Density ( g / cm3 )= 1.28
m24 1001.50c    -0.040509
        6000   -0.585083
        8016.50c   -0.078042
        15000 -0.037771
        17000 -0.258941
c ************************************************************
c Lard Oil  Density ( g / cm3 )= 0.915
m25  1001.50c   -0.117673
         6000  -0.779024
         8016.50c  -0.103657
c ************************************************************
c Paraffin Wax Density ( g / cm3 )= 0.930
m26       1001.50c -0.148605
         6000 -0.851395
c ************************************************************
c Polyethylene Density ( g / cm3 )              = 0.94
m27       1001.50c -0.143716
        6000 -0.856284
c ************************************************************
c Polyethylene Terephthalate    Density      = 1.380
m28 1001.50c -0.041960
        6000 -0.625016
        8016.50c -0.333024
c ************************************************************
c UREA: Density (g/cm3)                      = 1.323
m29         1001.50c    -0.067131
          6000    -0.199999
          7014.50c    -0.466459
          8016.50c     -0.266411
c ************************************************************
c WATER, LIQUID: Density (g/cm3) 1.00
m30    1001.50c     -0.111894
      8016.50c     -0.888106
c ************************************************************
c PARAFFIN WAX: Density (g/cm3)   0.93
m31  1001.50c    -0.148605
         6000   -0.851395
c ************************************************************
c Cadmium   Density ( g / cm3 )= 8.65
m32  48000 -1.000000
c
c *** Lead (density 11.35 g/cc)
M33   82000  -1.0   $elemental Pb and atomic abundance
c ************************************************************
C Iron (density (7.874 g/cc)
c -------------------------
M34   26000  -1.0   $elemental Fe and atomic abundance
c ********************************************************
c            Ceramic (2.403)
c -------------------------------------------------------
M35   8016    0.6364  $Oxygen
     13027   0.1818  $Al
```

```
     14000   0.1818  $Si
c ***************************************************
c    Granite (2.73 g/cc)
c ---------------------------------------------------
M36   1001   0.027122  $Hydrogen
      6012   0.000502  $Carbon
      8016   0.607735  $Oxygen
      11023   0.025866  $Sodium
      12000   0.018081  $Magnesium
      13027   0.062783  $Alumminum
      14000   0.205927  $Silicon
      19000   0.013939  $Potassium
      20000   0.018960  $Calcium
      26000   0.019086  $Iron
c ***************************************************
c    Limestone (2.35 g/cc)
c ---------------------------------------------------
M37   6000   0.2       $Carbon
       8016   0.6       $Oxygen
       20000   0.2       $Calcium
c ***************************************************
c      Ash (0.641 g/cc) General Wood wrong components
c ---------------------------------------------------
M38    6000   0.1300  $Carbon
      8016   0.4200  $Oxygen
     12000   0.0100  $Magnesium
     13027   0.0200  $Aluminum
     19000   0.0800  $Potassium
     20000   0.3400  $Calcium
c ---------------------------------------------------
c Acetone  C3H6O  Density (g/cm3) = 0.789900
m39  1001.50c  -0.104122
        6000  -0.620405
        8016.50c  -0.275473
c ---------------------------------------------------
c Ammonia  NH3 Density (g/cm3) = 0.771
m40  1001.50c  -0.177547
       7014.50c -0.822453
c ---------------------------------------
c Asphalt  (the black glue only) Density (g/cm3) = 1.3
m41  1001.50c    -0.103725
     6000    -0.848050
       7014.50c    -0.006050
      8016.50c    -0.004050
      16000    -0.037700
      23000   -0.000393
       28000   -0.000034
c ---------------------------------------
c  Asphalt Pavement, blacktop. rho=2.5784
m42  1001.50c            -0.007781
       6000           -0.076175
        7014.50c           -0.000363
       8016.50c           -0.459103
         11023.50c         -0.011659
          12000         -0.021757
```

```
         13027.50c         -0.051009
          14000          -0.231474
           16000          -0.002804
          19000          -0.017058
            20000          -0.084471
          22000          -0.003403
            23000          -0.000024
            25055.50c          -0.000362
           26000          -0.031375
          28000          -0.000002
         82000          -0.001179
c -------------------------------------------------
c  ----     Sand 1.7 g/c3 -----------------------------
m43  1001.50c   -0.007833
        6000   -0.003360
        8016.50c   -0.536153
       11023.50c  -0.017063
       13027.50c  -0.034401
       14000  -0.365067
      19000   -0.011622
      20000   -0.011212
     26000    -0.013289
c -------------------------------------------------
c         Sugar (1.54 g/cc)
c -------------------------------------------------
M44  1001    -0.067134702
        6012    -0.400017318
        8016    -0.532847979
c     NaI crystal (density 3.67 g/cm^3)
c -------------------------------------------------------
M45    11023.50c  .425   $elemental Na and atomic abundance
         53000  .425   $elemental I and atomic abundance
         81000  .15   $elemental Tl and atomic abundance
c ********************************************************
c     rubber rho=0.45
m46    1001   -0.118371
        6012   -0.881629
c ******** Ethanol    density = 0.80 g/cc
c ---------------------------------------------------------------------------
m47    1001   0.66667
         6012   0.22222
         8016   0.11111
c ***************************
c Fert A approximation Rho=0.82
m48   1001   -0.100        $Hydrogen
       6012   -0.280        $28% carbon
       7014   -0.280        $28% nitrogen
        8016  -0.150        $ oxygen
       14000  -0.050        $Si
       15000  -0.045        $phosphorus P
       16000  -0.070        $Sulphor S
       19000  -0.025        $Potassium K
c **********Helium-3 ********************
m49  2003.60c  1.000
c -------------------------------------------------------
```

```
c  Fert B ------------ approximation ---------- Rho =0.87
m50   1001    -0.0750     $Hydrogen
        6012    -0.2780     $28% carbon
        7014    -0.3175     $30% nitrogen
        8016    -0.1255     $ oxygen
        14000  -0.0500     $Si
        15000  -0.0440     $phosphorus P
        16000  -0.0500     $Sulphor S
        19000  -0.0336     $Potassium K
        5000    -0.0002     $Boron
        25000  -0.0005     $Mangnese Mn
        26000  -0.0257     $Iron Fe
c   Fert mix ---------- approximation ---------- Rho=0.84
m51    1001   -0.0870
         6012  -0.2700
         7014  -0.2980
         8016  -0.1370
        14000  -0.0500
        15000  -0.0440
        16000  -0.0600
        19000  -0.0283
        25000  -0.0005
        26000  -0.0250
        5000   -0.0002
c ---------------------------------
c Nylon ( type 6 ) ****** Composition by atom fraction
c   rho = 1.14 g/cc
c -------------------------------------
m52  1001.66c 0.58
        6012.50c 0.32
        7014.66c 0.05
        8016.66c 0.05
c -------------------------------------
c Cotton ----- density=0.2 g/cc
c ----------------------
m53     1001.74c   0.47
       6000.74c   0.29
       8016.74c   0.24
c ----------------------------
c Polyester----------- 1.38
m54   1001  -0.04
     6000  -0.63
     8016  -0.33
```

II. Time of flight (nTOF) technique using d-d neutron pulse and measure the TOF at different angles. (Material card is not shown here)

```
Plasma focus  device, neutron emission for explosive detection
c --- the program includes neutron source , three plastic scintillators, and one bare helium 3 detector.
c --- the target can is either 5 gallons or one gallons of different materials
c ******************block one: cells*************************
c 1   0   -1        imp:p=1 imp:n=1 $ side of chamber imp:t=0
c 2   0   -2        imp:p=1 imp:n=1  $ side of chamber
c 3   0   -3        imp:p=1 imp:n=1  $ side of chamber
c 4   0   -4        imp:p=1 imp:n=1  $ side of chamber
c 5   0   -5        imp:p=1 imp:n=1  $ Glass plate window
c 6   0   -6        imp:p=1 imp:n=1  $ side of chamber
c 7   0   -7        imp:p=1 imp:n=1  $ gas inside chamber
8   0     -9 11  15  17 imp:p=1 imp:n=1   $ lab room contains natural air.
10 0         9  -10      imp:p=0 imp:n=0   $ walls of concrete composition to studyreflection effects.
11 10 -1.032    -11      imp:p=1 imp:n=1  $ plastic  DETECTOR IN scatter
c 12 57  -6     -12      imp:p=1 imp:n=1   $ Target Can
c 13 0          12  -13      imp:p=1 imp:n=1  $ Can wall of iron
c 14 0          -14      imp:p=1 imp:n=1   $ POLYETHYLENE shield
15 10 -1.032    -15      imp:p=1 imp:n=1   $ plastic  DETECTOR IN scatter
c 16 0          -16      imp:p=1  imp:n=1  $ LEAD shield
17 10 -1.032    -17      imp:p=1 imp:n=1  $ plastic DETECTOR IN scatter
c 18 0          -18      imp:p=1 imp:n=1  $ LEAD shield
c 19 49 -0.0002677 -19   imp:p=1 imp:n=1  $ Helium-3 detector tube of 2 atm pressure from manual.
c 20 27 -1.2       -20    imp:p=1 imp:n=1  $ Polyethe shield
c 21 27 -1.2       -21    imp:p=1 imp:n=1   $ Polyethe shield
c 20 27 -1.2       -20    imp:p=1 imp:n=1   $ Polyethe shield changed density for testing only
c 21 27 -1.2       -21    imp:p=1 imp:n=1   $ Polyethe shield changed density for testing only
30 0              10    imp:p=0 imp:n=0   $ Void outside

c ******************block two: surfaces ******************
1   Rpp -5  -4.6  -40  15.6    0    22   $ walls of chamber -x -direction
2   Rpp 4.6  5    -40   15.6   0    22   $ walls of chamber  x -direction
3   RPP -5   5    -40   16     -0.3  0   $ walls of chamber -z -direction
4   Rpp -5   5    -40   16     22   22.4 $ walls of chamber  z -direction
5   RPP -4.6 4.6  -16   -15.6  0    22   $ walls of chamber  -y -direction
6   RPP -5   5    15.6  16.0   0    22   $ walls of chamber  y -direction
7   RPP -4.6 4.6  -15.6 15.6   0    22
9   RPP -100  500 -800  550  -130   200  $ room concrete size 1
10  Rpp -110  510  -810 560  -150   220  $ room concerete size 2
11  RCC 200.0 150 8 -3 -5.5 0  10      $ back scatter detector
c
12 RCC 0 -80  6    0 0 12     6        $ the 1 gallon can
13 RCC 0 -80 5.99 0 0 12.08 6.04       $ the can walls
c
14  RCC  36.0 -45  8 -1.8 -1.8 0 4.0     $ polyethylene shield
15  RCC  270 -170  8 -2.5 2.5 0 5       $ forward scatter detector
16  RCC  59.0 -129  8 .15    -.15 0 4.0   $ lead shield
17  RCC -19.0 -62  8 2.5      -2.5 0 2.5 $ back scatter detector
18  RCC -16.0 -65  8 .15    -.15 0 4.0   $ lead shield
19  RCC  0   -63.5 3  0   0  10  1       $ He3 detector tube of 10cm length
20 RPP 10 29 -59 0 -15 20               $ polyethylene shield
21 RPP -29 -10  -59 0 -15 20            $ polyethylene shield
```

```
c ****************** block 3 data card **********************
mode n p
c PHYS:N emax ean iunr dnb tabl fism recl  (ex: PHYS:N J 100 3J -1. for capture)
c PHYS:N    3    0   0    0  -1    0    2
c cut:n 2j 0 0
nps 1e8  $ stop after this number emitted from source
SDEF  POS = 0 0 8 PAR=1  Erg=2.45  tme=d1  Axs= 0 0 1  dir=d5 vec= 0 -1 0
si1 A   0  0.1    0.2  0.3 0.4
sp1     0 158.4  40  17   0
c si5  -1  0.998   1
c sp5   0  0.998  .001
c sb5   0    0      1
c xxxxxxxxxxxxxxxxxxxxxxxxxxxxxxxxxxxxxxxxxxxxxxxxxxxxxxxxxxxx
F4:n   17
t4  0 400i 12
FQ4 t E
c
F14:n  11
t14 0  400i 55
FQ14 t E
c
F5:n 480 -74 8  20
t5 0 400i 44
FQ5 t E
c
F24:n  15
t24 0 400i 35
FQ24 t E
```

III. A code used for checking the shielding against a pulse of 2.5MeV neutron source.

```
Shielding against neutrons including plastic scintillator proton response with time TOF and energy
c ******************block one: cells*********************
   1    1 -7.92 -1  $ side of chamber
   2    1 -7.92-2  $ side of chamber
   3    1 -7.92 -3  $ side of chamber
   4    1 -7.92 -4  $ side of chamber
   5    1 -7.92 -5  $ side of chamber opened
   6    1 -7.92 -6  $ side of chamber
   7    0        -7  $ gas inside chamber
   8    4 -0.00129 #1 #2 #3 #4 #5 #6 #7 -9 $ lab room contains natural air.
           11 12 13 14 15 16 17 18
  10    3   -2.3 9 -10  $ walls of concrete composition
  11   47   -0.87 -11  $ SHIELD imp:H=1 imp:p=1
  12   34   -0.87 -12  $ SHIELD
  13   47   -0.93 -13  $ SHIELD
  14   34   -0.87 -14  $ SHIELD
  15   47   -0.93 -15  $ SHIELD
  16   34   -0.87 -16  $ SHIELD
  17   34   -0.87 -17  $ SHIELD
c -------------------------------------------------------------
  18   10  -1.032 -18  $ plastic detector
  30    0        10  $ Void outside

c ******************block two: surfaces ******************
   1      rpp -5 -4.6 -40 15.6 0 22  $ walls of chamber -x -direction
   2      rpp 4.6 5 -40 15.6 0 22  $ walls of chamber  x -direction
   3      rpp -5 5 -40 16 -0.3 0  $ walls of chamber -z -direction
   4      rpp -5 5 -40 16 22 22.4  $ walls of chamber  z -direction
   5      rpp -4.6 4.6 -16 -15.6 0 22  $ walls of chamber  -y -direction
   6      rpp -5 5 15.6 16 0 22  $ walls of chamber  y -direction
   7      rpp -4.6 4.6 -15.6 15.6 0 22  $ open wall side of chamber
   9      rpp -100 500 -800 150 -130 200  $ room concrete size 1
  10      rpp -110 510 -810 160 -150 220  $ room concerete size 2
  11      rpp -40 40 -100 -78 -20 40  $ SHIELD1
  12      rpp -40 40 -78 -76 -20 40  $ SHIELD2
  13      rpp -40 40 -76 -74 -20 40  $ SHIELD3
  14      rpp -40 40 -74 -72 -20 40  $ SHIELD4
  15      rpp -40 40 -72 -70 -20 40  $ SHIELD5
  16      rpp -40 40 -70 -68 -20 40  $ SHIELD6
  17      rpp -40 40 -68 -65 -20 40  $ SHIELD7
c ---------------------------------------------------------------
  18      rcc 0 -103 8 0 -7.14 0 5  $ scatter detector
c ---------------------------------------------------------------
  20      rpp -6 6 -42.25 -41 -5 25  $ lead shield to simulate the experiment.

mode  n h
c t14 0.1 100i 1 200i 200
c ******************NATERIAL DEFINITION**********************
c -the stinless steel  rho = 7.92
m1    24000.          -0.19  $ Cr
      25055.          -0.02 26000.          -0.695 28000.          -0.095
c ***********************************************************
c ------------- Concrete composition rho = 2.30
m3    1001.          -0.0221
      6000.        -0.002484 8016.         -0.57493 11023.        -0.015208
      12000.       -0.001266 13027.        -0.019953 14000.       -0.304627
      19000.       -0.010045 20000.        -0.042951 26000.       -0.006435
c ***********************************************************
c Air composition   rho = 0.001205
m4    7014.          -0.7558
      8016.          -0.2314 18000.         -0.0128
c ***********************************************************
c ------Aluminum composition   rho=2.6989
m5    13027.              -1
c ***********************************************************
```

```
c ------Tungsten  rho = 19.3
m6    74000.              -1
c ***********************************************************
c ----- copper-----  rho=8.960
m7    29000.              -1
c ***********************************************************
c ------lead rho= 11.35---
m9    82000.              -1
c ***********************************************************
c ----Plastic Scintillator1.032( g / cm3 ) Polyvinyl toluene
m10   1001.            -0.085
      6000.            -0.915
c Paraffin Wax Density ( g / cm3 )= 0.930
m26   1001.          -0.148605
      6000.          -0.851395
c ***********************************************************
c Polyethylene Density ( g / cm3 )               = 0.94
m27   1001.          -0.143716
      6000.          -0.856284
c ***********************************************************
c WATER, LIQUID: Density (g/cm3) 1.00
m30   1001.          -0.111894
      8016.          -0.888106
c ***********************************************************
c Cadmium   Density ( g / cm3 )= 8.65
m32   48000.              -1
c ***************************************************
c Iron (density (7.874 g/cc)
c --------------------------
m34   26000.              -1  $elemental Fe and atomic abundance
c ***************************************************
c ---------------------------------------------------
c ----sodium iodide scintillator 3.66 g/cm3
m46   11023.         -0.153373
      53127.         -0.846627
c  ---------------------------------------------------------
c    5% Borated Polyethylene: [from R/X Catalog 24, 1992]
c       Density 0.93 g/cm^3
c  ---------------------------------------------------------
m47   1001.            -0.116
         5010.             -0.01 5011.             -0.04 6012.             -0.834
imp:n   1 16r        0             $ 1, 30
imp:h   1 16r        0             $ 1, 30
c ******************block 3 data card*********************
c PHYS:H emax ean tabl J istrg J recl
phys:n 5 0 0 -1 -1 0 1
phys:h 5 0 -1 J 0 J 0
cut:h j 0
c nps 400000000  $ stop after this number emitted from source
ctme 15
sdef  POS = 0 0 8 PAR=1  Erg=2.5 $ DIR=1 VEC= 0 -1 0 ARA=1 tme= d1
c si1 0 0.1 0.2 0.3 0.4 0.5 0.6 0.7 0.8
c sp1 0 1    2   3   2   1  0.5  0.1 0
c SI2 A   0.1    0.5   1  1.5  2   2.5  2.65    $ tabulated energies E1 ... E7
c SP2     0.1   .15   .2  .25  .3  .7    0.15   $ distrbution values f(Ei)
c ***********************************************************
f4:n 18
e4: 0 100i 0.1 400i 3
c t4 0.1 100i 1 200i 200
f14:h 18
e14: 0 100i 0.1 400i 3
c ---------------------------------------------------------
```